
**Analysis of $J/\psi \rightarrow \phi\eta\eta$ at BESIII and
Calibration of the
Temperature Monitoring System for
the $\overline{\text{PANDA}}$ Electromagnetic Calorimeter**

Dissertation zur Erlangung des Grades eines
Doktors der Naturwissenschaften
in der Fakultät für Physik und Astronomie
der Ruhr-Universität Bochum

vorgelegt von
Miriam Kümmel
geboren in
Fulda

Bochum, Dezember 2018

1. Gutachter: Prof. Dr. Ulrich Wiedner
 2. Gutachter: PD Dr. Fritz-Herbert Heinsius
- Lehrstuhl für experimentelle Hadronenphysik, Ruhr-Universität Bochum

Tag der Disputation: 29. April 2019

Abstract

A data sample of $1.31 \cdot 10^9$ J/ψ events recorded by the BESIII experiment has been used to analyze the hadronic decay $J/\psi \rightarrow \phi\eta\eta$. Events of this decay pattern with a final state consisting of a pair of charged kaons and four photons have been selected with an efficiency of about 12.5%. A partial wave analysis was performed and the information criteria BIC and AIC were used in an iterative approach to determine the hypotheses which optimally describe the data. The dynamics of scalar contributions are parameterized by a K -matrix with fixed pole positions and coupling strengths according to previous measurements. Utilizing Breit-Wigner functions to parameterize the dynamics of all other resonances, the hypothesis consisting of a $(\pi\pi)_S$ wave contribution as well as $f'_2(1525)$, $f_2(1810)$, $\omega_2(1975)$, $\phi(1690)$, and $h_1(2215)$ resonances yields the best results. Additionally, hypotheses which use a K -matrix with released pole positions and coupling strengths to parameterize the dynamics of tensor contributions are tested. Scattering data from different measurements are used to constrain the K -matrix to reasonable parameter values. The best result is obtained for the hypothesis consisting of a K -matrix with three poles, $(\pi\pi)_S$ wave, $\omega_2(1975)$, $\phi(1680)$, and $h_1(1965)$ contributions. Product branching fractions are determined for all contributions, most of them for the first time. For the $f'_2(1525)$ resonance, the branching fraction $\mathcal{B}(J/\psi \rightarrow \phi f'_2(1525)) = (10.5 \pm 0.6_{\text{stat}} \pm 2.3_{\text{sys}}) \cdot 10^{-4}$ is obtained, which is compatible with the result obtained by DM2 but not with the only other published value obtained by MARKII.

The electromagnetic calorimeter of the $\overline{\text{P}}\text{ANDA}$ detector, which is currently under construction and will start data taking in 2025, is based on lead tungstate crystal scintillators. The operating temperature is chosen to be -25°C in order to increase the light yield. To ensure the envisaged energy resolution, the temperature must be regulated precisely and monitored with a relative accuracy of 0.02°C . Customized sensors and dedicated readout electronics have been developed to fulfill the strong requirements and are produced at Ruhr-Universität Bochum. Within the scope of this thesis numerous instances of both sensors and electronics have been calibrated to obtain an accurate readout chain. The hysteresis effect of the temperature sensors is taken into account by fitting the corresponding subsamples separately. The RMS of the differences between these fits and the data typically yields 0.01°C . The typical hysteresis at -25°C amounts to 0.03°C . Several dedicated measurements have been performed to characterize the hysteresis effect. Furthermore, measures are taken to increase the production rate of accurate and reliable sensors and to obtain a high calibration throughput. The readout electronics, called THMP $\overline{\text{P}}$, is designed modularly so that it can read out several kinds of sensors, in particular resistance temperature sensors. Evaluating the calibrations of 10 devices with 64 readout channels each, a typical resistance uncertainty of $4\text{m}\Omega$ is determined, which is by a factor of two better than the design requirement. The reproducibility of the THMP $\overline{\text{P}}$ calibrations is in the order of the requirement.

Contents

1	Introduction	1
2	The Standard Model of Particle Physics	3
2.1	Quantum Field Theory and Global Symmetries	3
2.2	Elementary Fermions	4
2.2.1	Leptons	4
2.2.2	Quarks	4
2.3	Gauge Bosons and Fundamental Interactions	8
2.3.1	Quantum Electrodynamics	8
2.3.2	Electroweak Interaction	8
2.3.3	Quantum Chromodynamics	9
2.4	Open Questions	12
2.5	Mesons in the Quark Model	13
2.6	Exotic Mesons	14
I	Partial Wave Analysis of the Decay $J/\psi \rightarrow \phi\eta\eta$ at BESIII	17
3	Introduction to the Analysis of the Decay of $J/\psi \rightarrow \phi\eta\eta$	19
4	Experimental Setup	21
4.1	The BEPCII Accelerator	21
4.2	The BESIII Detector	23
4.2.1	Multilayer Drift Chamber	24
4.2.2	Time-of-Flight System	25
4.2.3	Performance of the PID-Systems	26
4.2.4	Electromagnetic Calorimeter	27
4.2.5	Muon Counter	29
4.2.6	Trigger System and Online Data Acquisition	29
4.2.7	BES Offline Software System	30
5	Event Selection	31
5.1	Data Sets	31
5.2	Selection of $\phi\eta\eta$ Candidates	31
5.2.1	Track Selection and Particle Identification	31
5.2.2	Photon Candidate Selection	31
5.2.3	ϕ and η Candidate Selection and Combinatorics	32
5.2.4	Kinematic Fits	32
5.2.5	Detector Acceptance, Selection Efficiency and the Selected Sample	35

5.3	Background Studies	37
5.3.1	Analysis of a Generic Monte Carlo Sample	37
5.3.2	$\pi^0\pi^0$ Background	39
5.3.3	Miscombination	41
5.3.4	Signal and Sideband Regions	42
6	Partial Wave Analysis Fundamentals	53
6.1	Isobar Model and Quantum Numbers	54
6.2	The Helicity Formalism	55
6.2.1	Quantum Mechanical States	55
6.2.2	Transition Amplitudes in the Helicity Formalism	58
6.3	Weight Function and Free Parameters	60
6.4	Dynamical Part of the Amplitude	62
6.4.1	Barrier Factors	63
6.4.2	K -Matrix Formalism	64
6.4.3	Chew-Mandelstam Function	65
6.4.4	Production of Resonances with the P -Vector Approach	66
6.4.5	Breit-Wigner Parametrization	67
6.4.6	Extraction of Pole Parameters from the T -Matrix	67
6.4.7	The $(\pi\pi)_S$ wave	68
6.5	Maximum Likelihood Method	69
6.6	Selection of Hypotheses	71
6.7	Analysis Software Package PAWIAN	72
7	Partial Wave Analysis Results	73
7.1	Systematic Survey for Contributing Resonances	75
7.2	K -Matrix Description for 2^{++} Contributions	82
7.3	Continuation of the Systematic Survey for Contributions	84
7.4	Determination of Branching Fractions	91
7.4.1	Multidimensional Efficiency Determination and Correction	92
7.4.2	Systematic Uncertainties	96
7.4.3	Results of the Determination of Branching Fractions	97
8	Conclusion and Discussion	99
II	Calibration of the Temperature Monitoring System for the Electro-	
	magnetic Calorimeter of the $\overline{\text{PANDA}}$ Target Spectrometer	101
9	Introduction to the Temperature Monitoring System for the $\overline{\text{PANDA}}$ EMC	103
10	The $\overline{\text{PANDA}}$ Experiment	105
10.1	Physics Program	105
10.2	The Antiproton Beam from HESR at FAIR	107
10.3	The $\overline{\text{PANDA}}$ Detector	110
10.3.1	Target Spectrometer	110
10.3.2	Forward Spectrometer	115
10.3.3	Detector Control System and Data Acquisition	117

11 The Electromagnetic Calorimeter of the Target Spectrometer	119
11.1 Physics Relevant for Calorimetry	119
11.1.1 Interaction with Matter	119
11.1.2 Electromagnetic Cascades	119
11.1.3 Scintillation	120
11.2 Layout of the $\bar{\text{P}}\text{ANDA}$ TS EMC	120
11.2.1 Requirements on the Energy Measurement	120
11.2.2 Hit Rate and Radiation Hardness Requirements	122
11.2.3 Properties of the Scintillator Material PWO	122
11.2.4 Geometric Layout	123
11.2.5 Photosensors	125
11.2.6 Thermal Requirements	127
12 The Forward Endcap of the TS EMC	129
12.1 Mechanics, Cooling and Insulation	129
12.2 Electronics	131
12.2.1 Readout-Chain	131
12.2.2 Light Pulser System	131
12.3 Assembly of Submodules	133
12.4 Mounting of Submodules	138
13 Ultrathin Platinum Resistance Temperature Sensors for $\bar{\text{P}}\text{ANDA}$	143
13.1 Requirements for $\bar{\text{P}}\text{ANDA}$ TS EMC Temperature Sensors	143
13.2 Platinum Resistance Temperature Sensors	143
13.3 Design of Ultrathin Platinum Resistance Temperature Sensors	144
13.4 Production Procedure	146
13.5 Required Amount of Temperature Sensors	149
13.6 Calibration of the Ultrathin Platinum Resistance Temperature Sensors	150
13.6.1 Calibration Setup	150
13.6.2 Calibration Procedure	151
13.6.3 Data Taking and Treatment	151
13.7 Quality Assessment	155
13.7.1 Reproducibility	156
13.8 Dedicated Studies	159
13.8.1 Hysteresis Effect	159
13.8.2 Longterm Stability	163
13.9 Supply Status and Outlook	167
13.9.1 Testing Contacting Methods	169
13.9.2 Improved Calibration Setup	170
14 Temperature and Humidity Monitoring Board for $\bar{\text{P}}\text{ANDA}$	173
14.1 Requirements for the THMP	173
14.2 Layout of the THMP	174
14.2.1 Mainboard	174
14.2.2 Piggyback Boards	176
14.3 Required Amount and Supply Status	177
14.4 Calibration of PBBs Dedicated for Temperature Sensors	178
14.4.1 Calibration Boards	178

14.4.2	Calibration Procedure	179
14.4.3	Data Treatment	179
14.4.4	Fitting Procedure	184
14.5	Estimation of Uncertainties	188
14.6	Quality Assessment	191
14.7	Reproducibility	194
14.8	Temperature Measurements at the Submodule Test Station	195
15	Conclusion and Discussion	201
A	Results of the Partial Wave Analysis	I
A.1	First Results of the Iterative Approach	I
A.2	Results of K -Matrix Description for 2^{++} Contributions	VI
A.3	Results of the Continued Systematic Survey for Contributions	VII
B	Results of the THMP Calibrations	XIII
	List of Acronyms	XXVII
	Bibliography	XXXI

1 Introduction

Gaining knowledge in particle physics requires typically large-scale experiments consisting of accelerators as well as particle detectors, which provide the process of interest with high luminosity and measure all available properties precisely. Once the data is available and all properties are retrieved from the detector responses, sophisticated analysis methods are employed to gain new insights into the fundamental interactions.

This thesis deals with both ends of this procedure. In the first part a huge data set consisting of 1.31 billion J/ψ events recorded by the the third generation of the Beijing Electron Spectrometer (BESIII) experiment is analyzed. In the BEPCII collider J/ψ mesons, bound states consisting of a charm and an anticharm quark, are produced from electron-positron annihilations at a center of mass energy of 3.096 GeV. The method of partial wave analysis is used to investigate intermediate resonances of the J/ψ decay into the final state consisting of the three mesons $\phi\eta\eta$. Regarding the ϕ meson as a recoil to the $\eta\eta$ system, the scalar and tensor resonances with isospin zero can be studied. Some of the scalar resonances are suspected to contain glueball admixtures, which is yet to be confirmed. The tensor resonances are a notoriously difficult field with seemingly contradictory results for different production and decay processes. Analyzing the $\phi\eta$ system the second η mesons as recoil particle, might reveal yet undiscovered tetraquark states which contain strangeonium in analogy to the puzzling Z_c states discovered in the charmonium sector in the past ten years. Learning more about so-called exotic states such as glueballs and tetraquarks would lead to a deeper understanding of the strong interaction, which determines how hadrons are composed of quarks and gluons.

In the second part of this thesis detector developments for the electromagnetic calorimeter of the \bar{P} ANDA target spectrometer are presented. The anti-Proton Annihilation at Darmstadt (\bar{P} ANDA) detector is currently under construction and will start operation in 2025 at the high energy storage ring (HESR) of the Facility for Antiproton and Ion Research (FAIR) near Darmstadt. Annihilations of an antiproton beam with momenta from 1.5 GeV/ c up to 15 GeV/ c and a fixed target will then be investigated. The detector is composed of two spectrometers, one surrounding the target pipe enclosed by a solenoid magnet, the other one in forward direction equipped with a dipole magnet. The homogeneous electromagnetic calorimeter of the \bar{P} ANDA target spectrometer is composed of lead tungstate crystals, which provide very fast scintillation light pulses. The temperature dependence of the scintillation light intensity requires a precise and stable temperature control. The calibration and assessment of the ultrathin temperature sensors used for monitoring the temperature of the electromagnetic calorimeter of the \bar{P} ANDA target spectrometer and the calibration and assessment of the customized electronics dedicated for their readout is the topic of the second part of this thesis.

Before going further into details within the two different parts, the standard model of particle physics is introduced in chapter 2.

2 The Standard Model of Particle Physics

The standard model of particle physics describes the elementary particles and the fundamental interactions among them, following the paradigm of a quantum field theory. The electromagnetic, the weak and the strong interaction are incorporated in the standard model, whereas the gravitation could not yet be included. The elementary particles are classified according to different properties. The most fundamental classification is according to their spin, an intrinsic property similar to an angular momentum. Particles with integer spin are called bosons and obey the Bose-Einstein statistics, whereas particles with half-integer spin are called fermions and obey the Fermi-Dirac statistics. In particular fermions are subject the Pauli exclusion principle, which states that two or more identical fermions cannot occupy the same quantum state. Each fermion has a corresponding antiparticle with the same mass but opposite charge. The fermions are then further classified into leptons and quarks.

2.1 Quantum Field Theory and Global Symmetries

Some general features of the standard model of particle physics follow directly from quantum field theory. Quantum field theory is a theoretical framework which relies on the Lagrangian formalism from classical field theory and combines quantum mechanics, which has been developed to describe the realm of very small objects, with special relativity, which has been developed to describe the realm of very fast objects.

In quantum mechanics a physical process is described as a transition from one state to another. These transitions are not deterministic but occur with a certain probability, so that the same initial state can transition in different final states.

Special relativity is based on two postulates: The laws of physics are invariant in all inertial systems and the speed of light in vacuum is the same for all systems. Hence the laws of physics are invariant under transformations, which map one inertial system to another. These transformations form a continuous group called Lorentz group in honor of Hendrik Antoon Lorentz. Elements of the homogeneous Lorentz group are rotations and boosts, linear coordinate transformations between two coordinate frames that move at constant velocity relative to each other, and concatenations thereof.

Continuous symmetries which hold at all points in space-time are called global symmetries. According to Emmy Noether's first theorem such global symmetries correspond to conservation laws: The invariance of physics's laws with respect to spatial translation corresponds to the conservation of (linear) momentum, invariance with respect to rotation corresponds to the conservation of angular momentum, and invariance with respect to time translation corresponds to the conservation of energy. In special relativity (in contrast to classical mechanics) not the rest mass, but the invariant mass $m = \sqrt{E^2 - p^2}$ is conserved in addition to energy, momentum and angular momentum, and particles with a rest mass of zero are allowed.

The space inversion, a point-reflection at the origin of the coordinate system, corresponding to a sign flip of all three Cartesian coordinates, is called parity transformation \hat{P} and forms a discrete subgroup of the Lorentz group. Systems which are invariant under parity transformation, are eigenstates of the operator and have eigenvalues $P = -1$ or $P = +1$. Depending on their behavior under rotations, geometrical objects can be classified into scalars, vectors and tensors of higher rank. Adding parity, the classification scheme can be extended to scalars with $P = 1$, pseudoscalars with $P = -1$, vectors with $P = -1$ and pseudovectors with $P = +1$. Almost all scalar physical quantities have positive parity, whereas almost all vector quantities have negative parity, except for the angular momentum L , since $\vec{L} = \vec{r} \times \vec{p} \rightarrow -\vec{r} \times -\vec{p} = \vec{L}$. Quantum systems which consist of several subsystems have a total parity which corresponds to the product of the individual parities of the subsystems, parity is a multiplicative quantum number. For a system A consisting of subsystems B and C, also the angular momentum L_{BC} between the subsystems has to be taken into account, thus $P_A = (-1)^{L_{BC}} P^B P^C$.

Another important discrete subgroup of the Lorentz group is generated by the time reversal transformation \hat{T} , which flips the sign of the time coordinate.

The charge conjugation \hat{C} changes the sign of each charge and thus maps each particle to its antiparticle. Only systems for which all charges are zero, i.e. photons and particle-antiparticle bound states, are eigenstates of charge conjugation. Similar to the parity, also eigenstates of the charge conjugation operator have eigenvalues $C = -1$ or $C = +1$ and the C -parity is a multiplicative quantum number.

With methods from quantum field theory it was possible to prove the CPT theorem, which states that all physical phenomena are invariant under the product of all three transformations.

2.2 Elementary Fermions

2.2.1 Leptons

The group of leptons consists of the three charged leptons the electron e^- , muon μ^- and tauon τ^- and their electrically neutral associates, the electron neutrino ν_e , the muon neutrino ν_μ and tauon neutrino ν_τ . The charged leptons have quite different masses, whereas the neutrinos are considered to be massless in the standard model. Taking into account the very different masses, the leptons are grouped into three generations.

Table 2.1 shows rounded values for the masses, besides the quantum numbers. Since they are elementary particles with no internal structure, only an upper limit for the radius is determined. The elementary fermions are assumed to be point-like, but for the sake of graphic demonstration the masses of the charged leptons, all quarks and the proton are depicted as spheres with corresponding volume in figure 2.1.

2.2.2 Quarks

There are six different quark types, which are distinguished through their so-called flavor: up (u), down (d), strange (s), charm (c), bottom (b) and top (t). Depending on their flavor, quarks carry an electric charge of $-\frac{1}{3}$ or $+\frac{2}{3}$ of the elementary charge e , while their antiparticles carry the opposite charge. Like the leptons the quarks are grouped into three generations, each of them containing one positively and one negatively charged quark.

	Generation	Name	Electric Charge $Q [e]$	Weak Isospin T_3	Color Charge	Flavor Quantum Number	Mass $m [\text{MeV}/c^2]$
Leptons	1 st	e	-1	$-\frac{1}{2}$	—	$L_e = +1$	0.511
		ν_e	0	$+\frac{1}{2}$	—		
	2 st	μ	-1	$-\frac{1}{2}$	—	$L_\mu = +1$	105.7
		ν_μ	0	$+\frac{1}{2}$	—		
	3 st	τ	-1	$-\frac{1}{2}$	—	$L_\tau = +1$	1777
		ν_τ	0	$+\frac{1}{2}$	—		
Quarks	1 st	u	$+\frac{2}{3}$	$+\frac{1}{2}$	r,g,b	$I_3 = +\frac{1}{2}$	2.2
		d	$-\frac{1}{3}$	$-\frac{1}{2}$	r,g,b	$I_3 = -\frac{1}{2}$	4.7
	2 st	c	$+\frac{2}{3}$	$+\frac{1}{2}$	r,g,b	$C = +1$	$1.27 \cdot 10^3$
		s	$-\frac{1}{3}$	$-\frac{1}{2}$	r,g,b	$S = -1$	96
	3 st	b	$-\frac{1}{3}$	$+\frac{1}{2}$	r,g,b	$B = +1$	$4.18 \cdot 10^3$
		t	$+\frac{2}{3}$	$-\frac{1}{2}$	r,g,b	$T = -1$	$160 \cdot 10^3$

Table 2.1: Quantum numbers and masses [1] of the twelve (left-handed) fermions

Historically it was far from obvious that there exist quarks at all, since only hadrons can be observed directly, which were in the beginning considered to be elementary particles. The most familiar hadrons are proton and neutron, which constitute the atomic nuclei and are therefore called nucleons.

In order to explain the symmetry between neutron and proton, which have almost the same mass and almost the same behavior in terms of the strong interaction, a non-scalar quantum number called isospin has been introduced. As a non-scalar quantum number it has similar properties as the spin, although they are totally unrelated otherwise: The spin of a fermion can be oriented either parallel or antiparallel with regard to the axis defined by e.g. an external magnetic field. Hence the projection of the spin to that axis is either $S_3 = +\frac{1}{2}$ or $S_3 = -\frac{1}{2}$. In an analogous manner proton and neutron are associated with the isospin projections $I_3 = +\frac{1}{2}$ and $I_3 = -\frac{1}{2}$, respectively.

Many new particles were discovered in the 1940s and 1950s. Some of these particles were heavier than the nucleons and in all observed decay processes a proton or neutron was

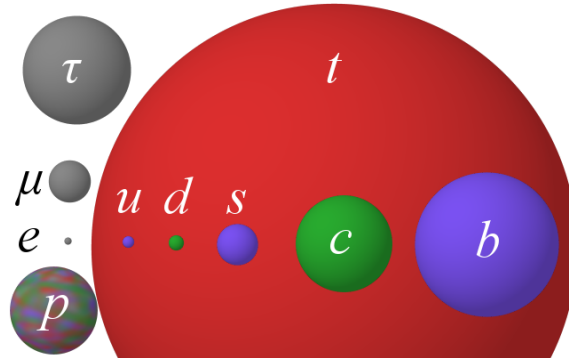


Figure 2.1: Charged lepton masses, current quark masses and the proton mass depicted as spheres of corresponding volume

$I_3 =$	-1	$-\frac{1}{2}$	0	$+\frac{1}{2}$	+1
$S = +1$		K^0		K^+	
$S = 0$	π^-		π^0, η, η'		π^+
$S = -1$		K^-		\bar{K}^0	

Table 2.2: Lightest spin 0 mesons sorted according to isospin projection and strangeness

$I_3 =$	-1	$-\frac{1}{2}$	0	$+\frac{1}{2}$	+1
$S = 0$		n		p	
$S = -1$	Σ^-		Σ^0, Λ		Σ^+
$S = -2$		Ξ^-		Ξ^0	

Table 2.3: Lightest spin $\frac{1}{2}$ baryons sorted according to isospin projection and strangeness

one of the daughter particles. This group of particles is called baryons, referring to their comparably high mass, and the baryon number \mathcal{B} is a conserved quantum number [2]. Other particles were found to have masses in the range between those of the electrons and nucleons, these are called mesons. Most of the newly found particles had a very short lifetime of around 10^{-24} s, while some had an astonishingly long lifetime of 10^{-10} s. It turned out, that there is a relation between the baryon number \mathcal{B} , charge Q , isospin projection I_3 and the occurrence of these strange comparably long-lived particles [3]. Thus, introducing strangeness S as another quantum number yielding $Q = I_3 + \frac{1}{2}Y$ with the hypercharge $Y = \mathcal{B} + S$ was reasonable.

The insight that the grouping of mesons and baryons known at that time according to strangeness and isospin projection matches the simplest generalization of the isospin symmetry to an approximate $SU(3)$ symmetry, lead to the postulation of up, down and strange quarks as constituents of hadrons. The schemes for the lightest mesons and baryons are shown in tables 2.2, 2.3 and 2.4. The baryons can be described as a composition of three quarks and the mesons as a composition of a quark and an antiquark, where any quark has baryon number $\mathcal{B} = \frac{1}{3}$, the up and down quark have isospin projections $I_3 = +\frac{1}{2}$ and $I_3 = -\frac{1}{2}$, respectively, but strangeness $S = 0$ and the strange quark has a strangeness of $S = -1$ but isospin projection $I_3 = 0$.

Considering the spin $\frac{3}{2}$ baryons Δ^{++} , Δ^- and Ω^- (table 2.4), which consists of three quarks with the same flavor, that all have the spin oriented in the same direction, the Pauli principle seems to be violated, unless there is yet another quantum number. This property is called color charge in analogy to red, green and blue light combining to neutral white light in additive mixture. Every quark carries one of the color charges red, green, or blue,

$I_3 =$	$-\frac{3}{2}$	-1	$-\frac{1}{2}$	0	$+\frac{1}{2}$	$+1$	$+\frac{3}{2}$
$S = 0$	Δ^-		Δ^0		Δ^+		Δ^{++}
$S = -1$		Σ^{*-}		Σ^{*0}		Σ^{*+}	
$S = -2$			Ξ^{*-}		Ξ^{*0}		
$S = -3$				Ω^-			

Table 2.4: Lightest spin $\frac{3}{2}$ baryons sorted according to isospin projection and strangeness

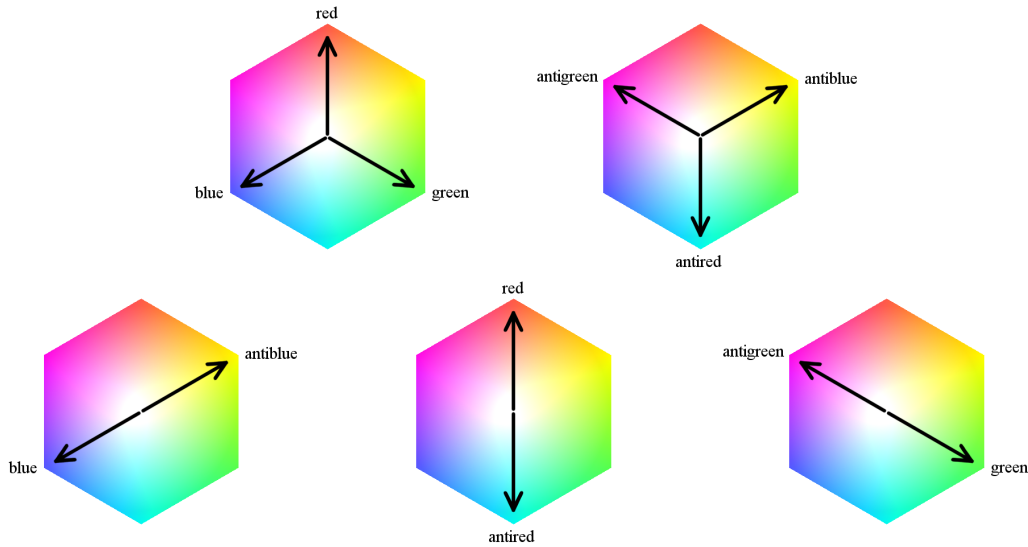


Figure 2.2: Simplest combinations composing a color neutral system

while every antiquark carries one of the anticolor charges antired, antigreen, or antiblue. Figure 2.2 depicts the simplest combinations to compose a color neutral system.

The existence of a fourth and fifth quark flavor has been proven by the discovery of the J/ψ , a meson composed of a charm quark and a charm antiquark (generally called charmonium), and the Υ , a meson composed of a bottom quark and a bottom antiquark (generally called bottomonium). Several years later also the top quark has been discovered, but its lifetime is too short to actually form a toponium meson, instead the top quark changes flavor to the forty times lighter bottom quark by emitting a W boson. The occurrence of these quarks in a hadron is reflected by the corresponding quantum numbers charmness C , bottomness B and topness T . Extending the hypercharge to $Y = B + S + C + B + T$ keeps the relation $Q = I_3 + \frac{1}{2}Y$ valid.

The determination of quark masses turns out to be quite difficult, since no pure quarks but only hadrons are directly observable. The constituent quark masses can be estimated by comparing the masses of hadrons with different quark content. Actually, not only the masses of the quarks but also their kinetic energy and the kinetic energy of the gluons

exchanged between them contribute to the mass of hadrons. In addition the gluons create virtual quark-antiquark pairs, which immediately annihilate again but also contribute to the total mass of the hadron. These virtual quarks and antiquarks are called sea quarks and the non-virtual quarks bound in the hadron are called current quarks. The determination of current quark masses at a fundamental level based on the quantum field theory of the strong interaction is described in [1]. Table 2.1 shows the quantum numbers of the quarks and current quark masses, apart from the quantum numbers and masses of leptons. The up, down and strange quark are regarded as light quarks, whereas the charm, bottom and top quarks are regarded as heavy quarks. Figure 2.1 does not only show the masses of the elementary fermions depicted as spheres of corresponding volume, but also the proton mass, showing impressively that the mass of the proton is much larger than the sum of its three constituting quarks' current quark masses.

2.3 Gauge Bosons and Fundamental Interactions

In a quantum field theory the fundamental interactions are mediated by gauge bosons, i.e. the electromagnetic interaction is mediated by the photon γ , the weak force by the charged W^\pm bosons and the neutral Z^0 boson and the strong interaction by gluons g . The Higgs boson is no gauge boson, it does not mediate an interaction, but it is a consequence of the Higgs mechanism, which could successfully be incorporated into the electroweak model to explain the generation of the elementary particles masses, for fermions as well as for the W^\pm and Z^0 bosons. The discovery of the Higgs boson with a mass of $m_H \approx 125 \text{ GeV}/c^2$ by the ATLAS [4] and CMS [5] experiments in July 2012 has been the most recent major confirmation of the standard model.

2.3.1 Quantum Electrodynamics

The massless photon couples to all particles with an electric charge, even the W bosons. Thus quantum electrodynamics (QED) basically describes the interaction of light with matter. Many physicists contributed to achieve fully covariant and gauge invariant formulations of QED, that were finite at any order in a perturbation series. One of the most famous among these is probably Richard Feynman, who based the calculus on diagrams, which also provide a nice way to depict different QED processes.

The QED coupling strength is closely related to the so-called fine-structure constant, a dimensionless quantity related to fundamental physical constants as

$$\alpha = \frac{1}{4\pi\epsilon_0} \frac{e^2}{\hbar c} \approx \frac{1}{137},$$

where e is the elementary charge, $\hbar = \frac{h}{2\pi}$ is the reduced Planck constant, c is the speed of light in vacuum and ϵ_0 is the permittivity of vacuum. The coupling strength may be assumed to be constant for most applications, but it actually slightly increases as two charges get closer together. The vacuum polarization partially screens charges at larger distances but gets reduced when the charges get closer.

2.3.2 Electroweak Interaction

The massive gauge bosons of the weak interaction couple to all elementary fermions. Describing the weak interaction requires the so-called weak isospin T and chirality as

additional quantum numbers. Fermions with negative chirality are called left-handed and have the weak isospin $T = \frac{1}{2}$. They can be grouped into doublets with $T_3 = \pm\frac{1}{2}$. Two quarks or two leptons, which are in the same generation, form such a doublet. Both chirality and weak isospin change signs for antiparticles. The W^\pm bosons have weak isospin $T_3 = \pm 1$ and thus mediate transformations between fermions with half-integer weak isospin of opposite sign.

The weak interaction can thus change the flavor of quarks, as for example the change of a down quark into an up quark, which transforms a neutron to a proton in the β -decay. Fermions with positive chirality and anti-fermions with negative chirality carry $T = 0$ and do not interact with the W^\pm bosons. The Z^0 boson has weak isospin $T = 0$ and interacts with all left- and right-handed fermions and antifermions, e.g. when two neutrinos scatter.

Due to the mass of the weak gauge bosons, the range of the weak interaction is very small, whereas the range of the electromagnetic interaction is infinite. Compared to the electromagnetic interaction the strength of the weak interaction is several orders of magnitude lower. The electromagnetic and the weak interaction were unified in the electroweak model.

Quantum field theories are characterized by their corresponding local gauge symmetries. The electroweak interaction is based on the $SU(2) \times U(1)$ group. The symmetry associated with weak isospin is represented by the $SU(2)$ group and the $U(1)$ group represents the symmetry associated with the weak hypercharge, which relates electric charge and weak isospin by $Q = T_3 - \frac{1}{2}Y_W$. The weak interaction violates parity conservation, whereas the electromagnetic interaction respects parity conservation. Also C -parity is violated by the weak interaction in such a way, that the product CP symmetry is almost conserved. According to the CPT theorem the product symmetry CPT must be conserved by the weak interaction, thus also the T symmetry must be violated slightly.

2.3.3 Quantum Chromodynamics

Gluons, which mediate the strong interaction, couple to all particles which carry color charge, i.e. to all quarks but not to leptons or any of the other gauge bosons. Referring to the color charge, the theory of the strong interaction is called quantum chromodynamics (QCD). The color charge symmetry of QCD is represented by the $SU(3)$ group, which means that exchanging any pair of the three different color charges has no effect on the physics. Thus the standard model is often referred to as $SU(3) \times SU(2) \times U(1)$. QCD preserves the global C , P and T symmetries.

In contrast to the electroweak gauge theory QCD is a non-Abelian gauge theory, so that gluons have the very special property, that they do not only mediate the strong interaction, but also participate in it, because they themselves carry color charge.

Experimentally the strong force appears to be of very short-range [6], namely at the scale of the atomic nuclei. At this scale the strong force is by more than two orders of magnitudes stronger than the electromagnetic force.

At first glance, there seems to be a contradiction between the short range of the strong interaction and the fact, that gluons are massless. The range of the strong force is not limited due to energy conservation but by inherent properties of the strong interaction. Whereas the electric field between electrically charged particles decreases rapidly with increasing distance, the gluon field forms a narrow flux tube, so that the strong force stays

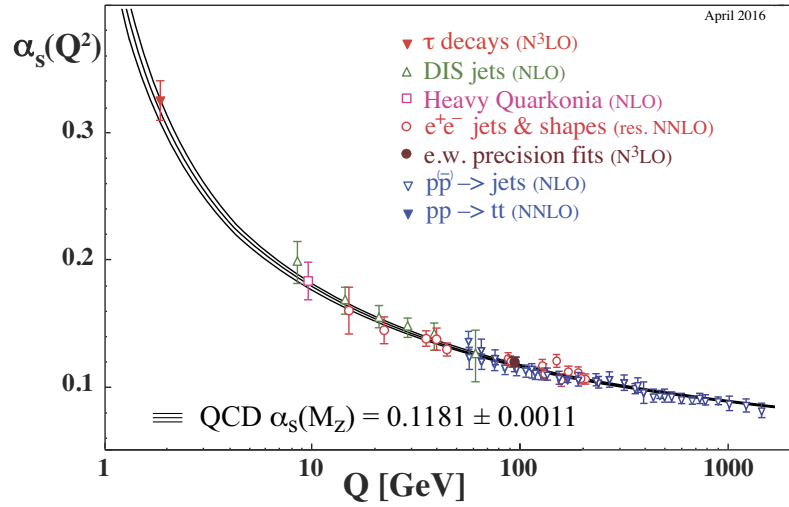


Figure 2.3: Summary of determinations of α_s based on perturbative approaches as a function of the energy scale Q [8]

almost constant beyond a certain distance and accordingly the energy increases linearly with the distance.

At large enough distances a quark-antiquark pair is spontaneously created from the vacuum, so that new hadrons are formed by hadronization. In high energy experiments tight cones of hadrons are created, so called jets, when a quark or gluon is knocked out of a proton. Qualitatively this is understood to be caused by the self-interaction of gluons, but an analytical proof is still missing and actually was announced as Millennium Prize Problem by the Clay Mathematics Institute in 2000 [7].

In QCD quark-antiquark vacuum polarization also leads to screening of the color charge, but besides these also gluon-gluon vacuum polarization occurs, which has the opposite effect called antiscreening. The effect of the vacuum polarization is reflected in the dependence of the strong coupling constant

$$\alpha_s(|q^2|) = \frac{12\pi}{(11n - 2f) \ln\left(\frac{|q^2|}{\Lambda^2}\right)}$$

on the momentum transfer q , where Λ is a constant scale parameter, n is the number of colors and f is the number of flavors, which amount to three and six in the Standard Model, respectively [6]. Since quark-antiquark vacuum polarization and gluon-gluon vacuum polarization have opposite effects, it depends on the number of different quarks (i.e. flavors) and the number of different gluons (i.e. color) which effect dominates. For theories with $11n > 2f$ the coupling constant decreases with increasing $|q^2|$ and hence antiscreening dominates, so that at short distances the strong force becomes relatively weak. Figure 2.3 shows determinations of the strong coupling constant in dependence of the momentum transfer based on perturbation theory. Accordingly quarks and gluons can be treated as free particles, which is the basis of asymptotic freedom.

The Cornell parametrization of the QCD potential

$$V(r) = -\frac{\alpha_s}{r} \left(1 - \left(\frac{r}{b}\right)^2\right) = -\frac{\alpha_s}{r} + \frac{\alpha_s}{b^2} r$$

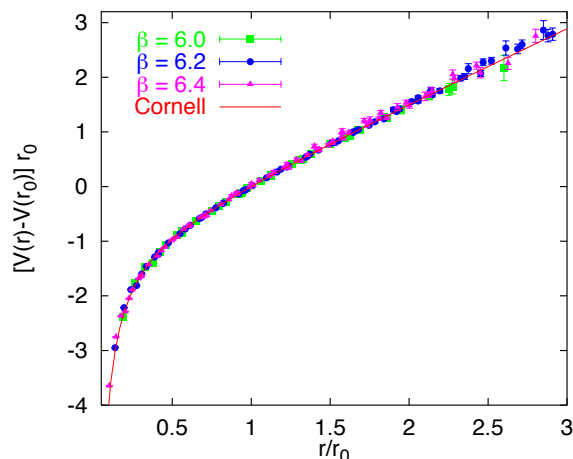


Figure 2.4: QCD potential obtained from quenched lattice calculations for $r_0 \approx 0.5$ fm, the different β values correspond to lattice spacings $a \approx 0.094$ fm, 0.069 fm and 0.051 fm, respectively and the red curve represents the Cornell parametrization with $b^2 = 0.295$ [10]

with a Coulomb-like term and a confinement term was proposed to describe the charmonium spectrum shortly after the discovery of the first charmonium resonances [9]. Figure 2.4 shows a comparison between the Cornell potential and results from lattice QCD.

Analyzing the properties of quantum chromodynamics is very complicated and various techniques have been developed to tackle different challenges:

Since asymptotic freedom implies that the coupling constant is small for high values of the momentum transfer, perturbation theory can be used under these conditions, so that not an infinite number of contributing terms must be calculated, but a finite number of terms is sufficient to yield quite accurate approximate results.

For processes with small momentum transfer and larger distances, the coupling constant is close to one, so that terms of higher orders cannot be neglected anymore and thus non-perturbative approaches are needed. One example for a non-perturbative approach is lattice QCD, formulated on a lattice of points in space-time. A lattice spacing a results in a momentum cut-off at the order $\frac{1}{a}$, so that integrals can be calculated numerically instead of analytically. When the size of the lattice is infinitely large and the spacing a is infinitesimally small, the approximations approach continuum QCD, but with decreasing lattice spacing the numerical calculations get computationally so costly, that large supercomputers are needed. To decrease computational effort the so-called quenched approximation can be used, in which the quark fields are treated as non-dynamic variables.

Another example for a non-perturbative approach is chiral perturbation theory, an effective field theory based on a Lagrangian with a chiral symmetry in addition to the QCD symmetries. The chiral symmetry is both spontaneously broken by dynamical symmetry breaking and explicitly broken by the non-zero quark masses.

There are several suitable quantities to experimentally test the perturbative regime of QCD such as the running of the QCD coupling, scaling violation in deep inelastic scattering, vector boson production at hadron colliders, jet cross sections, heavy-quark production and so forth. In the non-perturbative regime quantitative tests are more difficult both

experimentally and theoretically. Measuring masses and form factors of hadrons and their decay branching fractions still remains to be fully exploited, which might also result in a definitive observation of bound states solely consisting of gluons, so-called glueballs, which are predicted by QCD in an experimentally accessible energy range, but turn out to be very difficult to identify.

2.4 Open Questions

Besides numerous confirmations, there is also a number of questions left open by the standard model and even some contradictions.

First of all gravitation as a fundamental interaction is not yet included. Secondly the assumption that neutrinos are massless is contradicted and the conservation of the lepton family number is violated by the observation of neutrino oscillations, which can be explained by mass eigenstates different from the weak eigenstates. Since no evidence for an accumulation of antimatter in the universe has been found by now, the question arises why there is such a huge asymmetry between baryonic matter and antimatter, although both the electromagnetic and strong interactions preserve the baryon number and the CP violation of the weak interaction cannot fully account for the effect. Some physicists think that the number of 19 free parameters in the standard model is too large and that there should be a more general theory which predicts these parameters [11].

The experimental efforts are not at their end with the discovery of a new particle, but all accessible quantities are measured as precisely possible. If experimental results differ from theoretical predictions it might be due to experimental errors or statistical fluctuations, but with more data preferably from different experiments doubts should be cleared: The experimentally measured value of the magnetic dipole moment of the muon significantly differs from the Standard Model predictions [12]. Although the Standard Model predictions for ordinary hydrogen fit well to the experimental measurements, the measured radius of so called muonic hydrogen, a muon-proton system, differs significantly from the precise Standard Model predictions [13]. Already data from the BaBar experiment indicated an excess of a certain B meson decay ($\bar{B} \rightarrow D^{(*)} \tau^- \bar{\nu}_\tau$) compared to Standard Model predictions [14], which is validated by results from LHCb [15] as well as results from the Belle experiment [16].

Even though all elementary particles predicted by the Standard Model have been observed, the situation for composite states, namely hadrons, is somewhat more complicated and will be discussed below.

There are several concepts under investigation, which intend to complete the Standard Model. Supersymmetry adds another class of symmetries to the Standard Model predicting a fermionic partner particle for each boson and a bosonic partner particle for each fermion, respectively. This supersymmetry must be broken, because these partner particles have different masses. Actually, they must be quite heavy, since none of them has been observed yet. Supersymmetry would provide an elegant solution to many problems of the Standard Model. An approach to add masses to the neutrinos is the so-called seesaw mechanism. There exists also a number of models assuming that quarks and leptons are not elementary but composite of so-called preons, in order to explain why there are three generations of quarks and leptons. String theory and loop quantum gravity are approaches towards an inclusion of gravitation into the Standard Model.

$n^{2S+L}L_J$	J^{PC}	$I = 1$	$I = \frac{1}{2}$	$I = 0$	
1^1S_0	0^{-+}	π	K	η	η'
1^3S_1	1^{--}	$\rho(770)$	$K^*(892)$	$\omega(782)$	$\phi(1020)$
1^1P_1	1^{+-}	$b_1(1235)$	$K_1(1400)$	$h_1(1170)$	$h_1(1380)$
1^3P_0	0^{++}	$a_0(1450)$	$K_0^*(1430)$	$f_0(1370)$	$f_0(1710)$
1^3P_1	1^{++}	$a_1(1260)$	$K_1(1270)$	$f_1(1285)$	$f_1(1420)$
1^3P_2	2^{++}	$a_2(1320)$	$K_2^*(1430)$	$f_2(1270)$	$f_2'(1525)$
1^1D_2	2^{-+}	$\pi_1(1235)$	$K_2(1770)$	$h_1(1170)$	$h_1(1380)$
1^3D_0	1^{--}	$\rho(1700)$	$K^*(1680)$	$\omega(1650)$	————
1^3D_1	2^{--}	————	$K_2(1820)$	————	————
1^3D_2	3^{--}	$\rho_3(1690)$	$K_3^*(1780)$	$\omega_3(1670)$	$\phi_3(1850)$
1^1F_1	3^{+-}	————	————	————	————
1^3F_2	2^{++}	————	————	$f_2(1910)$	$f_2(2010)$
1^3F_3	3^{++}	————	$K_3(2320)$	————	————
1^3F_4	4^{++}	$a_4(2040)$	$K_4^*(2045)$	————	$f_4(2050)$
2^1S_0	0^{-+}	$\pi(1300)$	$K(1460)$	$\eta(1295)$	$\eta(1475)$
2^3S_1	1^{--}	$\rho(1450)$	$K^*(1410)$	$\omega(1420)$	$\phi(1680)$

Table 2.5: A possible classification of mesons into nonets [1, 17]

2.5 Mesons in the Quark Model

The description of hadronic properties by the minimum-quark-content part of the wave function (neglecting the influence of gluons and sea quarks) is called the quark model. The term meson refers then to the bound state of a quark and an antiquark, which may have a different flavor than the quark.

The spins of the quark and the antiquark can couple to the total intrinsic spin $S = 0$ or $S = 1$, depending on whether they are aligned parallel or antiparallel. The total spin \vec{J} is the sum of the intrinsic spin \vec{S} and the angular momentum \vec{L} between the quark and the antiquark, so that these quantum number fulfill the triangle inequality $|L - S| \leq J \leq |L + S|$. The angular momentum also determines the parity of the meson as $P = (-1)^L$. The C -parity is only defined for mesons, which consist of a quark and an antiquark of the same flavor. In that case the C -parity is determined by the intrinsic spin and the angular momentum as $C = (-1)^{L+S}$. The C -parity can be generalized to the G -parity for states with isospin $I = 1$ and is in that case determined as $G = (-1)^{I+L+S}$.

The mesons are classified in multiplets according to their J^{PC} quantum number.

Table 2.5 shows a possible assignment to multiplets for many of the known mesons, which are composed of light quarks. The first column provides the spectroscopic notation, where the radial excitation is denoted by n and the orbital excitation is decoded by the letters S for $L = 0$, P for $L = 1$, D for $L = 2$ and so on, whereas the intrinsic spin S and the total spin J are given as superscript and subscript, respectively. Checking the different L, S combinations it becomes obvious, that not all combinations of J^{PC} can be reached using the relations listed above. The quantum numbers $0^{--}, 0^{+-}, 1^{-+}, 2^{+-}, 3^{-+}, \dots$ are forbidden for bound quark-antiquark pairs.

Classifying the mesons according to their flavor, the $SU(3)$ symmetry yields an octet and a singlet. The isoscalar ($I = 0$) octet state can mix with the singlet state of the same J^{PC} multiplet, so that mass eigenstates different from the $SU(3)$ eigenstates $\frac{1}{\sqrt{6}}|u\bar{u} + d\bar{d} - 2s\bar{s}\rangle$ and $\frac{1}{\sqrt{3}}|u\bar{u} + d\bar{d} + s\bar{s}\rangle$ are observed. In case of the vector mesons the mixing is almost ideal, meaning that the $\phi(1020)$ is almost pure $|s\bar{s}\rangle$, whereas the $\omega(782)$ contains almost no $|s\bar{s}\rangle$ component but is almost a pure $\frac{1}{\sqrt{2}}|u\bar{u} + d\bar{d}\rangle$ state. For the pseudoscalar mesons η and η' the mixing is very small, so that the η is basically equal to the octet state and η' is the singlet state.

Furthermore for states with isospin $I = \frac{1}{2}$ neither C -parity nor G -parity are defined so that the mesons, which are assigned to the $1^{+\pm}, 2^{-\pm}, \dots$ multiplets each mix. Since J , P and C are conserved under QCD, but L and S are not, also mesons assigned to 1^3S_1 and 1^3D_0 might actually be mixtures of these excited states.

2.6 Exotic Mesons

Besides pairs of a quark and an antiquark there are some more possibilities how a hadron with baryon number $\mathcal{B} = 0$ can be composed: Combining any number of quarks with the same number of antiquarks yields a color-singlet state. Apart from a quark-antiquark pair the next simplest combination consists of two quarks and two antiquarks.

Depending on their inner structure these states are named tetraquarks, meson-meson molecules or diquarkonia. Tetraquarks are compact states with small distances between all four particles. For meson-meson molecules each of the quarks has a small distance to one of the antiquarks, basically forming two mesons which are bound loosely together. In diquarkonia the distance between the two quarks as well as the distance between the two antiquarks is very small, forming a diquark and a diantiquark with a slightly larger distance between them.

Qualitatively, the mass order of the four-quark states is expected to be inversed compared to the pseudoscalar nonet, so that the singlet state would be lighter than the octet states. Actually, this is the case for the scalar states $f_0(500), f_0(980), a_0(980)$ and $K^*(980)$, which is why these are not contained in the meson list in table 2.5.

QCD also allows for states which do not contain any quarks or antiquarks but solely consist of gluons. Such glueballs may also carry exotic quantum numbers, which are forbidden for quark-antiquark pairs. Figure 2.5 shows a glueball mass spectrum obtained from lattice QCD calculations in the quenched approximation. The 0^{++} ground state is predicted at a mass of $1710 \text{ MeV}/c^2$ with an uncertainty of about $100 \text{ MeV}/c^2$.

Since glueballs can mix with nearby $q\bar{q}$ states with the same quantum numbers, the three observed physical states $f_0(1370), f_0(1500)$ and $f_0(1710)$ are considered to be mixtures of a glueball and the two isoscalar $q\bar{q}$ states of the 0^{++} nonet with masses around $1500 \text{ MeV}/c^2$. Different mixing schemes have been proposed [18, 19]. Often the $f_0(1500)$ is considered to contain the largest fraction of the pure glueball, which is why it is not contained in the meson list in table 2.5, but other schemes favor the $f_0(1710)$ as glueball candidate.

Besides states with more or less quarks and antiquarks, also the existence of quark-antiquark pairs which are bound by an excited gluon, so-called hybrids, are conceivable. According to predictions from gluon flux tube models these are expected in the $1.9 \text{ GeV}/c^2$ region. The predictions from lattice QCD yield slightly lower masses. There are actually two candidates, the $\pi_1(1400)$ and $\pi_1(1600)$ with exotic quantum numbers 1^{-+} , which could be hybrids or four-quark states.

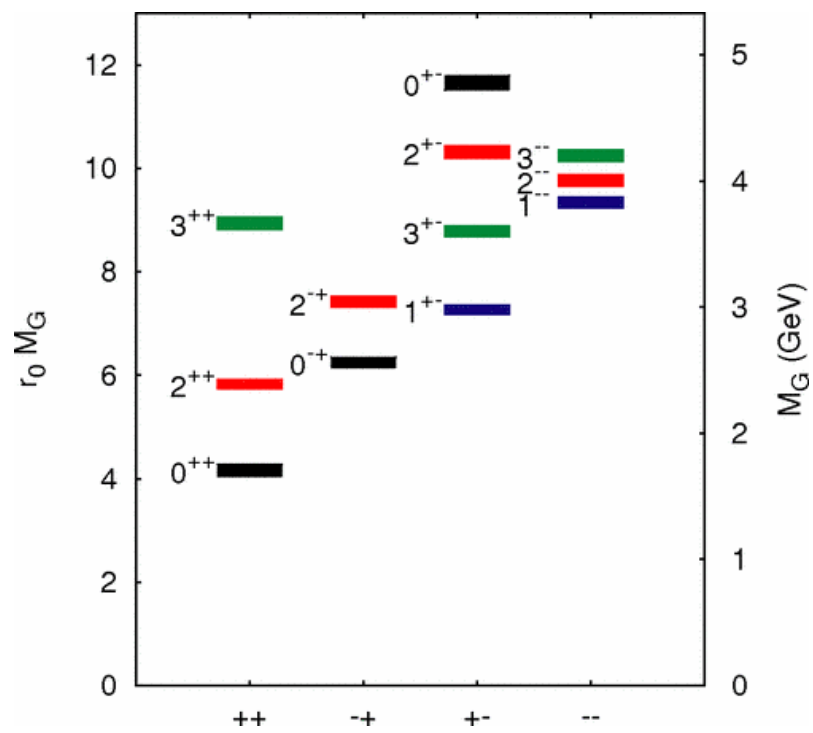


Figure 2.5: Predicted glueball mass spectrum from lattice QCD in the quenched approximation [20]

Part I

Partial Wave Analysis of the Decay $J/\psi \rightarrow \phi\eta\eta$ at BESIII

3 Introduction to the Analysis of the Decay of $J/\psi \rightarrow \phi\eta\eta$

The decay $J/\psi \rightarrow \phi\eta\eta$ is well suited to examine different topics in the field of hadron spectroscopy. On the one hand the $\eta\eta$ system provides the means to inspect the isoscalar f_0 and f_2 resonances. On the other hand investigations of the $\phi\eta$ system assist the search for strangeonium like states analogously to the Z_c states. In combination with the analysis of similar decay processes as $J/\psi \rightarrow \phi\pi\pi$, $J/\psi \rightarrow \phi K\bar{K}$, $J/\psi \rightarrow \omega\pi\pi$ [21], $J/\psi \rightarrow \omega K\bar{K}$, $J/\psi \rightarrow \gamma\eta\eta$ [22] and $J/\psi \rightarrow \gamma\pi^0\pi^0$ [23, 24] conclusive insights can be obtained concerning both topics.

The spectrum of light isoscalar mesons with spin zero (f_0) is being investigated since many years, but despite all efforts remains relatively poorly understood due to broad overlapping resonances. The importance of understanding the scalar meson spectrum is underlined by the expectation for the lightest glueball to have scalar quantum numbers (cf. figure 2.5, [20]). Since glueballs can mix with nearby conventional mesons with the same quantum numbers, their identification is challenging. Contradicting mixing schemes [18, 19] could be confirmed or excluded with further experimental input.

The system of two pseudoscalar mesons in J/ψ decays with a vector meson as recoil or radiative J/ψ decays have the advantage to be comparably simple. Due to parity conservation and angular momentum conservation contributions necessarily have an even angular momentum and positive parity as well as C -parity, yielding the quantum numbers $J^{PC} \in \{0^{++}, 2^{++}, 4^{++} \dots\}$. For a pair of η mesons the isospin of intermediate resonances must be $I = 0$. The recoil meson should provide further constraints on the quark content. Figure 3.1 shows the two lowest order diagrams for the J/ψ decay into a resonance X with a ϕ meson as recoil particle. In case of the connected diagram the quark content of the resonance X is determined to be $s\bar{s}$. In case of the disconnected diagram besides $s\bar{s}$ also any other quark-antiquark pair of the same flavor is possible. Since the coupling constant of the strong interaction depends on the momentum transfer, simple vertex counting is not sufficient to estimate the probability ratio between these two diagrams.

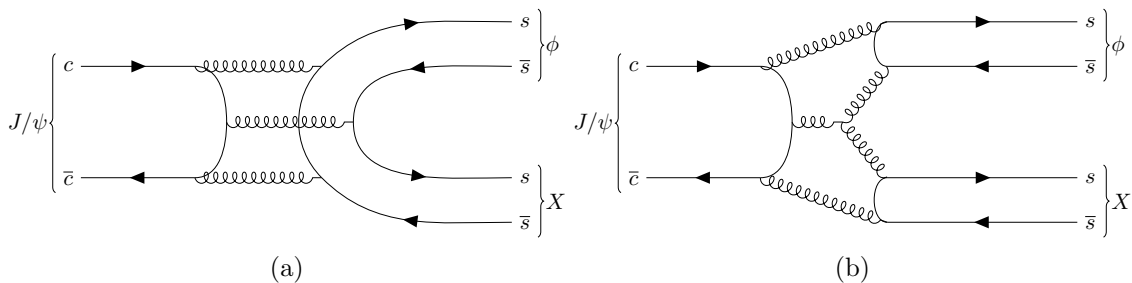


Figure 3.1: Lowest order diagrams for the decay of a J/ψ meson into a ϕ meson and a resonance X , which are distinguished by the quark lines connecting the two decay products (a) or being disconnected (b)

In 2010 the $Z_c(4430)$, a resonance-like structure in the $\psi(2S)\pi^\pm$ system, has been observed by the Belle experiment. The $Z_c(3900)$ discovered in the $J/\psi\pi^\pm$ system in 2013 by the BESIII experiment was the first of several further of these states to be found. Because both the $\psi(2S)$ and the J/ψ are very compact states, the Z_c states must already contain $c\bar{c}$, but due to their charge they must also contain at least an additional quark and antiquark so that the Z_c are considered to be tetraquark states. Intermediate resonances occurring in the J/ψ decay with an η meson as recoil particle, which decay into a ϕ and an η meson, are necessarily electrically neutral and isoscalar. Since the s quark is much lighter than the c quark and the ϕ meson is additionally not as compact as the $\psi(2S)$ or J/ψ mesons, it is not a priori clear if a resonance in the $\phi\eta$ system contains $s\bar{s}$. Compared to the charged charmonium-like Z_c states it is not possible to clearly identify tetraquarks, because the quark and antiquark of the η meson can also be generated in the decay process. Since there is not much known about resonances decaying into $\phi\eta$, also finding conventional mesons would deliver valuable information.

No analysis of the decay $J/\psi \rightarrow \phi\eta\eta$ has been reported yet. The decay probability for this process is rather small, so that for former experiments the statistics have probably been too low to obtain significant results. For the presented analysis the sample of $1.31 \cdot 10^9$ J/ψ events recorded by the BESIII experiment in 2009 and 2012 is used, which is larger than any other sample of directly produced J/ψ events recorded before. The BESIII experiment located at the Institute of High Energy Physics of the Chinese Academy of Sciences in Beijing measures the products of electron-positron collisions at center of mass energies from 2 GeV to 4.6 GeV.

Before the decay $J/\psi \rightarrow \phi\eta\eta$ can be analyzed, the corresponding events have to be selected from the J/ψ data sample, which contains also all other kinds of J/ψ decay processes. The detector acceptance and selection efficiency are determined by using a phase space distributed Monte Carlo data sample for which the detector response is simulated and the same selection criteria are applied. It must be ensured that the remaining backgrounds from J/ψ decays with other topologies are small, before a partial wave analysis of the selected data sample can be performed. The partial wave analysis is a technique in which the data is described by probability amplitudes decomposed in interfering individual components for different quantum numbers.

In the presented analysis the helicity formalism is used to describe the angular dependence of the process. For the description of the energy dependence both the Breit-Wigner distribution as well as the K -matrix formalism are used. The latter ensures the conservation of unitarity and in the case of a single resonance in a single decay channel reduces to a Breit-Wigner distribution.

The determination of which contributions are present in the analyzed spectrum, depends on the selection of the best hypothesis. Information criteria from model selection theory are used to guideline the systematic approach of iteratively adding resonances, which yield the most significant improvement of the fit quality.

4 Experimental Setup

The data sets this analysis is based on have been recorded by BESIII at the second generation of the Beijing electron-positron collider (BEPCII).

The predecessor experiments BES and BESII were operated at BEPC by the Institute of High Energy Physics of the Chinese Academy of Sciences from 1989 to 2004. Since March 2009 BESIII is taking data. The collider is designed to operate in the tau-charm mass region and thus covers the energy range $\sqrt{s} = (2 - 4.6)$ GeV. The BESIII collaboration, consisting of 59 institutes from 13 nations, publishes results in the fields of electroweak interactions, light hadron spectroscopy, charmonium spectroscopy, tau physics, charm physics, precision measurements of QCD and CKM parameters and search for new physics. [25]

Both the BEPCII collider and the BESIII detector will be presented in more detail in the following.

4.1 The BEPCII Accelerator

BEPC was a single ring electron-positron storage ring operated in single bunch mode. Several measures were taken to improve its luminosity by two orders of magnitude through an upgrade. The most important update is the installation of two separate beam pipes, one for the electron and the other for the positron beam. The key technologies to increase the luminosity were the injector upgrade, the low impedance kickers, the vacuum system and the superconducting insertion magnets. Electron and positron bunches are injected into the storage ring by the linear accelerator (LINAC) with energies of (1.89-2.5) GeV. The beams collide under a crossing angle of ± 11 mrad as shown in figure 4.1 and thus define the interaction point. A pair of superconducting quadrupoles is inserted into the detector as close as possible to the interaction point to squeeze the transverse size of the beams and direct them on the collision point. The layout of the accelerator facility is shown in figure 4.2. The layout has been optimized to reach the design luminosity of $10^{33} \text{ cm}^{-2}\text{s}^{-1}$ with 93 bunches spaced by 8 ns adding up to a beam current of 910 mA at 1.89 GeV beam energy, since the physics was focussed on the study of decays of the J/ψ , $\psi(3686)$, $\psi(3770)$ and nearby resonances. [26]

A comparison of the design parameters of BEPC and BEPCII is given in table 4.1.

The design luminosity has been achieved with beam currents of 849 mA and 852 mA and 119 bunches on April 5th, 2016 [27].

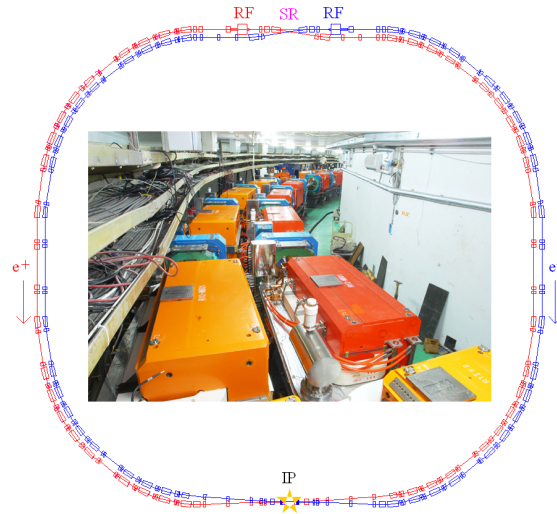


Figure 4.1: Layout of the BEPCII rings [27]

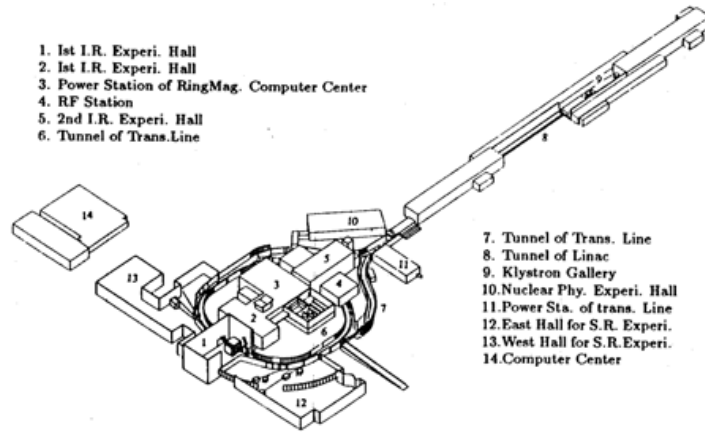


Figure 4.2: Overview of the BEPC facility [26]

Parameter	BEPC	BEPCII
Center of Mass Energy (GeV)	2 – 5	2 – 4.6
Circumference (m)	240.4	237.5
Peak Luminosity at $2 \times 1.89 \text{ GeV (cm}^2\text{s}^{-1}\text{)}$	$\approx 10^{31}$	$\approx 10^{33}$
Number of Bunches	2×1	2×93
Beam Current (A)	2×0.035	2×0.91
Bunch Spacing (m/ns)	—	2.4/8
Bunch Length (σ_z) (cm)	≈ 5	1.5
Bunch Size ($\sigma_x \times \sigma_y$) ($\mu\text{m} \times \mu\text{m}$)	$\approx 840 \times 37$	$\approx 380 \times 5.7$
Relative Energy Spread	$5 \cdot 10^{-4}$	$5 \cdot 10^{-4}$
Crossing Angle (mrad)	—	± 11

Table 4.1: BEPCII design parameters compared to those of BEPC [25]

4.2 The BESIII Detector

In order to precisely determine the momenta, masses and energies of the decay products generated by the high luminosity collisions of the BEPCII, also the BES detector has been subject to a major upgrade from BESII to BESIII. The layered, cylindrically symmetric configuration of the BESIII detector is shown in figure 4.3 with the different subsystems indicated. The 1 T superconducting solenoid magnet forces charged particles onto curved track. These tracks are measured by the multilayer drift chamber (MDC), which directly surrounds the beryllium beam pipe and incorporates the superconducting quadrupole (SCQ) magnets. The time-of-flight (TOF) system consists of two layers of plastic scintillators and surrounds the MDC and is itself surrounded by the CsI(Tl) electromagnetic calorimeter (EMC). All these subdetectors are enclosed by the superconducting coil (SC coil) of the solenoid. The flux return yoke of the solenoid incorporates the muon counter systems (MUCs) which are based on resistive plate chambers (RPCs). The most important parameters of the different subsystems are presented in more detail in the following.

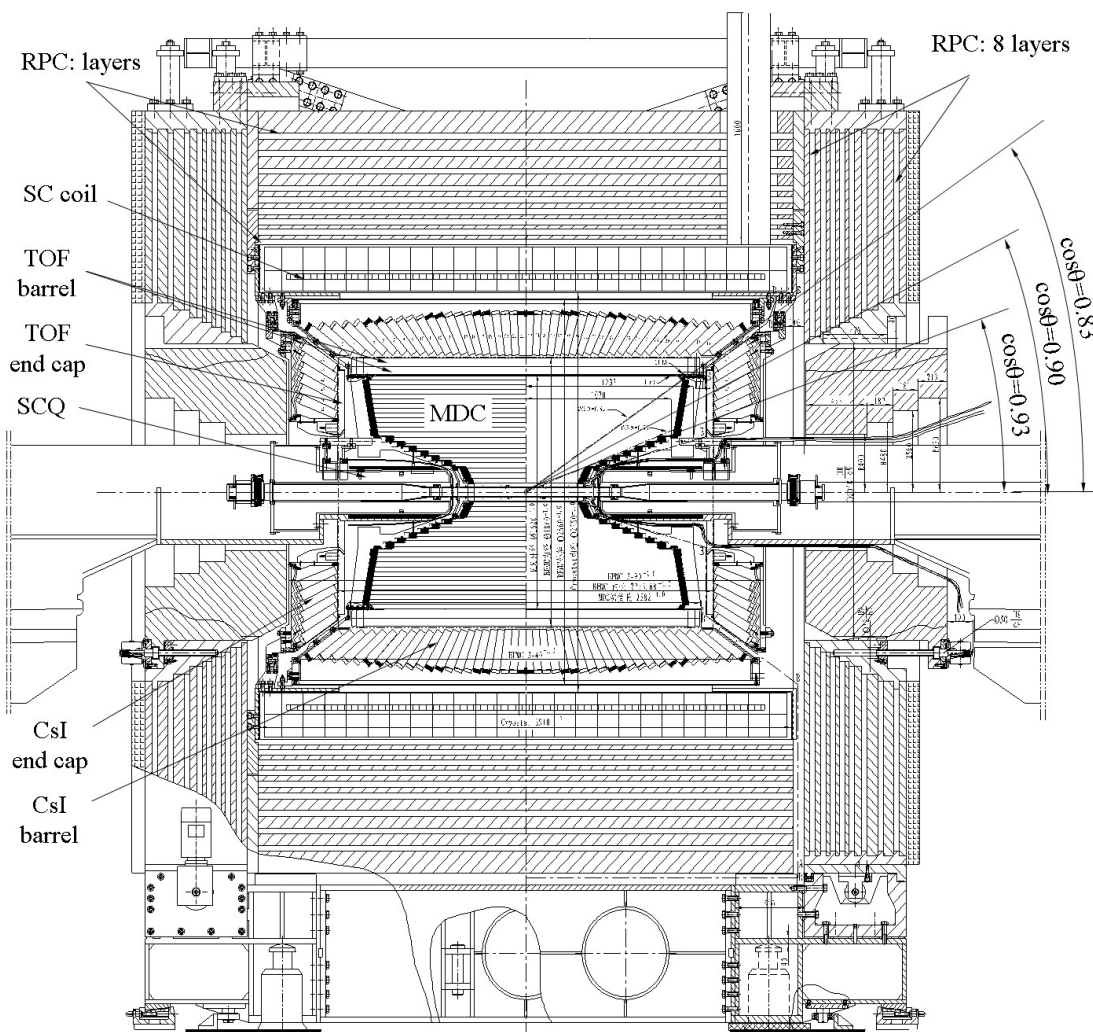


Figure 4.3: Configuration of the BESIII detector [25]

4.2.1 Multilayer Drift Chamber

The MDC is used to measure the three-dimensional tracks of charged particles. The curvature of these tracks in the magnetic field is correlated to their momentum. Besides determining the momentum by measuring the track, the amplitude drop of the signals along the track corresponds to the energy loss per distance dE/dx . Since the energy loss is a function of the velocity β , the combination of momentum and energy loss allows for particle identification. In order to determine the momentum as precisely as possible, the MDC is placed close to the interaction point.

Drift chambers are basically an array of wires at high voltage (anodes) running through a chamber with conducting walls at a ground potential (cathode), which is filled with gas. When a charged particle passes through the gas, it will ionize molecules of the gas along its track. The ions and electrons are accelerated by the uniform electric field and themselves can ionize other molecules, causing a localized cascade.

The MDC has a cylindrically symmetric shape with an outer radius of 810 mm and an inner radius of 59 mm, leaving only 2 mm of space to the beryllium beam pipe. It consists of an inner and an outer chamber with individual aluminum end plates, but sharing the same gas volume. The 25 mm thick end plates of the inner chamber, which accommodates the quadrupoles, have a stepped shape, whereas the 18 mm thick end plates of the outer chamber have a slightly conical shape. This modular design enables the replacement of the inner chamber in case of radiation damage. The inner shell of the inner chamber consists of a 1.2 mm thick carbon fiber composite. The outer shell of the outer chamber is made of 11.5 mm carbon fiber composite in order to provide the mechanical support, which is necessary to bear the load of the detector. In total the MDC is 2582 mm long. Small drift cells consisting of one sense wire surrounded by eight field wires are arranged in 43 layers, the field wires being shared by neighboring cells. In total the MDC contains 6796 sense wires and 21844 field wires. As shown in figure 4.3, the innermost and outermost layers cover polar angles with $|\cos\theta| \leq 0.93$ and $|\cos\theta| \leq 0.83$, respectively. The sense wires consist of gold-plated tungsten with 3% rhenium and have a diameter of 25 μm , whereas the field wires consist of gold-plated aluminum and have a diameter of 110 μm to reduce the material budget. In order to determine positions of tracks along the sense wires, the wires of some layers have small stereo angles, whereas for most layers the wires are aligned axially. In order to compensate field variations along the stereo wires, additional field wires are added between axial and stereo layers. Besides the detector geometry the momentum measurement precision is also affected by the interaction of the charged tracks with the materials inside the drift chamber volume. Most of the secondary charged particles generated by the e^+e^- collisions are expected to have a momentum of less than 1 GeV, so that multiple Coulomb scattering is critical for the momentum resolution. So on the one hand the radiation length should be as long as possible to avoid disturbance of the track, on the other hand the ionization probability should be high enough to guarantee for a good dE/dx resolution. For the MDC a gas mixture of 60% helium and 40% propane is kept under a pressure of 3 bar above the ambient atmospheric pressure. [25]

A comparison of achieved values and design values for the key performance parameters is shown in table 4.2. Nonetheless, the inner chamber had to be exchanged due to aging effects which are caused by the huge beam related background. In 2012 the gains of the inner chamber showed an obvious decrease of up to 26% for the innermost layer. In addition, the innermost four layers appeared to be discharging, which turned out to be caused by the Malter effect [28], a typical aging for wires due to a thin insulating film

	Achieved Value	Design Value
Spatial Resolution σ_{xy}	115 μ m	130 μ m
Momentum Resolution σ_p/p	0.47%@1 GeV	0.5%@1 GeV
Energy Loss Resolution dE/dx	5.2%	6-7%
Hit Efficiency ε	$\geq 95\%$	98%

Table 4.2: Summary of MDC performance values [29]

formed on the surface of cathode wires. Hence the high voltages had to be decreased in order to protect the detector, which worsened the performance. The short-term upgrade plan envisages building a new inner drift chamber to replace the previous one. The long-term upgrade plan foresees building a 3-layer central gaseous electron multiplier (CGEM) inner tracker. [29]

The new inner drift chamber has almost the same dimensions as the previous one. In order to reduce the background rate, the wire lengths had to be shortened. The azimuthal angle coverage is still the same, just the ineffective area beyond this angle has been minimized. Hence the new end plates are elongated with eight steps towards the interaction point, while the inner shell has been shortened. The performance of the new inner chamber has been tested with cosmic rays. A spatial resolution of 127 μ m and a dE/dx resolution of 6.4% have been achieved, which meets the requirements. [30]

Both planar chambers and the cylindrical gaseous electron multiplier (GEM) prototype have been tested on the H4 beam line of the super proton synchrotron (SPS) (CERN). Efficiencies and resolutions of the planar GEM chambers have been evaluated for several settings and have proven to be stable. The complete CGEM is under construction and is expected to be completed in 2018. [31]

4.2.2 Time-of-Flight System

While the energy loss dE/dx indirectly gives information about β , the TOF provides a direct measurement of the velocity βc . With the measured time of flight t_{meas} determined by the TOF and the length of the flight path L determined by the reconstructed track, the velocity can be calculated by $\beta c = \frac{L}{t_{\text{meas}}}$. Knowing the momentum from MDC measurements and the velocity, the mass can be determined using

$$p = \gamma m v = \frac{m \beta c}{1 - \beta^2} \Rightarrow m^2 = p^2 \frac{1 - \beta^2}{\beta^2}.$$

The TOF is based on plastic scintillation counters and is composed of a double layer barrel of the time-of-flight system (BTOF) and two single layer end cap of the time-of-flight system (ETOF). Each barrel layer consists of 88 scintillator bars, which are 2.3 m long, 50 mm thick and have a trapezoidal cross section. The two layers are mounted on the outer surface of the carbon fiber shell of the MDC in a staggered arrangement to avoid gaps. Thus the inner radius of the barrel is 0.81 m. Compared to a single layer the availability of two layers improves the system reliability and two independent measurements of the particle flight time improve the time resolution. Hamamatsu fine mesh photomultiplier tubes (PMTs) are directly attached to both ends of the scintillator bars. Each end cap is comprised of 48 scintillation counters with a trapezoidal shape, which are 50 mm thick and 480 mm long. On the outside surface of each bar a PMT is attached. The end caps

are mounted behind the MDC end plates and thus 1.4 m apart from the interaction point. These dimensions result in a polar angle coverage of $|\cos\theta| < 0.82$ for the barrel and $0.85 < |\cos\theta| < 0.95$ for the end caps. [25]

The experimentally determined time resolution for the BTOF is even better than 70 ps. Whereas the ETOF performance is more affected by noise and background, thus the time resolution for Bhabha events varies from 100 ps to 200 ps for different positions. The ETOF time resolution is determined to 110 ps for muons, 148 ps for electrons and 138 ps for pions, respectively. The π/K separation power is 2σ up to 1.0 GeV. For a more advanced physics program the 2σ π/K separation power is needed up to momenta of 1.4 GeV/c. An aging effect has been observed for the attenuation length and the light yield. The average decreasing rate for the attenuation length has been determined to be 4.3% per year. The efficiency is correlated with the attenuation length and decreases as the attenuation length decreases. The light yield decreased with an average rate of 4.9% per year. Thus an upgrade of the ETOF system with multigap resistive plate chamber (MRPC) technology has been foreseen. The new ETOF design should be less affected by scattering and more readout pads could be used for tracking, so that with an intrinsic MRPC resolution of 50 ps the total resolution could be less than 80 ps. [29]

The new design of the ETOF system including MRPC modules has been tested and successfully installed in October 2015. The average intrinsic resolution of the MRPC modules and the average efficiency have been determined to approximately 60 ps and more than 96%, respectively. [32]

4.2.3 Performance of the PID-Systems

As figure 4.4 (a) shows, the dE/dx resolution is not good enough to separate electrons, muons and pions from each other for momenta around 0.2 GeV/c. Similarly the separation of electrons and kaons fails around (0.5–0.6) GeV/c. A good kaon-pion separation with a significance of 3σ can be achieved up to 0.6 GeV/c and a good electron-pion separation can be obtained above 0.4 GeV/c. With the expected time resolution of 100 ps to 110 ps for the TOF a kaon-pion separation with 2σ significance can be achieved up to 0.9 GeV, as can be deduced from the typical squared mass distributions of electron, kaon, and proton versus their momentum, which are shown in figure 4.4 (b). [33]

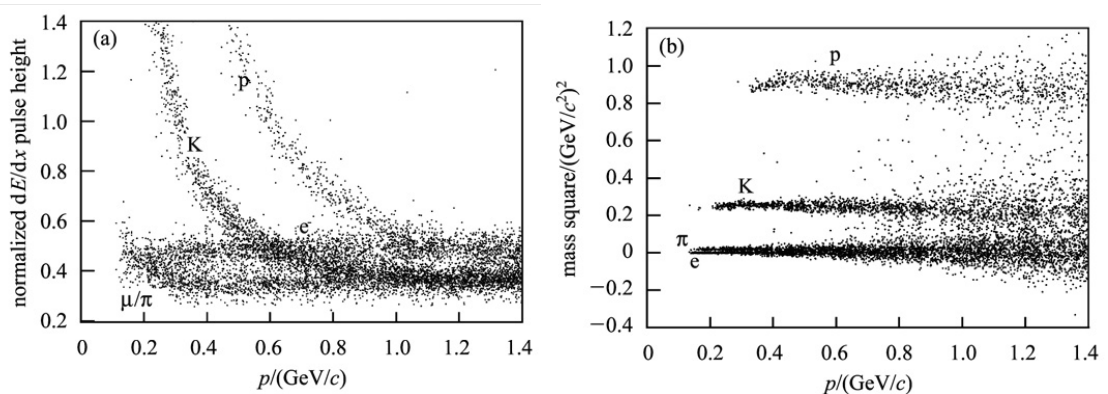


Figure 4.4: (a) Normalized pulse heights vs. momentum of charged particles [33]

(b) Mass square distribution from TOF measurements [33]

4.2.4 Electromagnetic Calorimeter

The EMC is the only subdetector which provides information on the energy and flight direction of photons. Moreover, energy and flight direction of electrons and positrons are measured with the EMC, thus it is an important tool to distinguish electrons and positrons from other charged particles as for example pions.

The highest energy to be expected from photons of the process $e^+e^- \rightarrow \gamma\gamma$ is defined by the beam energy of up to 2.3 GeV. In order to distinguish photons directly produced in radiative decays from close by pairs of photons originating from the decay of neutral pions or η mesons, the photon energy threshold is as low as 25 MeV in the barrel and 50 MeV in the two end caps. A high light yield is necessary to cover the range of (0.02 – 2.1) GeV with an energy resolution of at least $\frac{\sigma_E}{E} = 2.5\%/\sqrt{E}$. A fine segmentation of the calorimeter is not only important to accurately measure the hit coordinates of photons and identify even highly energetic neutral pions with a small angle between the two photons, but also in order to distinguish particles by their different energy deposition patterns. At low energies the patterns of pions and electrons can be quite similar, so that an excellent energy resolution is needed to distinguish electrons from pions by requiring a good agreement between the measured momentum and the measured energy. Besides high light yield and a fine segmentation, further requirements are put on the EMC due to its location within the solenoid. The photosensors must be functional in the magnetic field and the full detector layout needs to be compact. [25]

The EMC of the BESIII detector is comprised of thallium doped cesium iodide crystals arranged in a barrel and two end caps, which are each read out by two large area photodiodes. CsI(Tl) has a high light yield and a short radiation length of 1.85 cm. The crystals are 28 cm long, which corresponds to 15.1 radiation lengths. The front and rear faces measure typically $5.2 \times 5.2 \text{ cm}^2$ and $6.4 \times 6.4 \text{ cm}^2$, respectively. Thus, by using appropriate algorithms for the recognition of the energy deposition pattern, a spatial resolution of $\sigma_{x,y} \leq 6 \text{ mm}/\sqrt{E}$ should be achievable. The light collection efficiency has been optimized by wrapping each crystal in two layers of 130 μm Tyvek paper and one layer of 25 μm Mylar covered with 25 μm aluminum, which also provides radio frequency shielding, electric isolation between crystals and mechanical protection. [25]

The barrel consists of 44 rings, each comprised of 120 crystals, which adds up to 5280 crystals. All crystals point to the collision point with a small tilt of $1^\circ - 3^\circ$ in θ and 1.5° in the ϕ direction, to avoid leakage of photons through the chinks between neighboring crystals. The barrel has an inner radius of 94 cm and an inner length of 276 cm, which results in a polar angle coverage of $|\cos\theta| < 0.83$. The end cap crystals have 33 different shapes, but their dimensions are similar to the barrel crystals. Each end cap consists of 6 rings and vertically splits into two halves, so that they can open horizontally in order to give access to the MDC. In total the end caps consist of $(64+64+80+80+96+96) \cdot 2 = 960$ crystals. The end caps are placed at a distance of 138 cm from the collision point, they have an inner radius of 88 cm and an outer radius of 110 cm. Thus the end caps cover polar angles in the range of $0.84 < |\cos\theta| < 0.95$. A small gap between the end caps and the barrel is needed to allow for mechanical support structures and service lines of the inner detectors to pass through. [25]

A drawback of CsI(Tl) is the temperature coefficient of $0.3\%/^\circ\text{C}$ and its slight hygroscopic nature. Hence a flow of dry nitrogen is used to maintain a dry atmosphere and prevent degradation of the crystal surfaces. The Hamamatsu S2744-08 photodiodes have a size of $1 \times 2 \text{ cm}^2$ and are directly connected to a preamplifier. In order to remove the heat

produced by the preamplifiers and keep the temperature of the CsI(Tl) crystals stable at ambient temperature, active water cooling is required. Approximately 200 humidity sensors with an accuracy of $\pm 3\%$ and 600 semiconductor temperature sensors with an accuracy of $\pm 0.5^\circ\text{C}$ are distributed throughout the EMC. [25]

Radiation damage causes a light yield reduction by about 10% per rad of the received radiation dose. Two positive intrinsic negative (PIN) diode radiation sensors are installed on the inner surface of each EMC end cap, in order to monitor the radiation level. Additionally 72 radiation sensitive field effect transistors (RadFET) radiation sensors are installed on the front faces of crystals at representative locations. Since the crystals can have different degradation rates due to radiation and also photodiode responses and electronics gains undergo variations, a light pulsing system has been installed to monitor the changes in the response of the readout chain. The light pulsing system consists of a pulse generator, LED light sources, light mixers, optical fiber bundles and a reference system to check the system's stability. The optical fiber bundles distribute the light pulses to 88 crystals in the barrel and 60 crystals in the end caps. The Quartz fibers have a diameter of $300\ \mu\text{m}$ and the non-uniformity of light delivery is less than 10%. The light pulses are similar to the light pulses of the CsI(Tl) crystals concerning spectrum, rise-time and shape. The reference system, which monitors the stability peak by peak, consists of two photodiodes and a ^{241}Am radioactive source. The system stability is 0.5% and can be improved to 0.3% after an offline correction which compensates for the temperature dependency. [25]

The offline high precision EMC calibration of BESIII uses Bhabha scattering events to compensate for effects such as non-linearity of the crystal light yields, temperature dependence of the light yield, back and side leakages, dead material between crystals, crystal non-uniformities, and radiation damages [25]. Figure 4.5 shows the resolution obtained from Monte Carlo (MC) simulations and data taking in 2009 and 2012 at a center of mass energy of $3.097\ \text{GeV}$. The results are in good agreement with each other. The energy resolution is about 2.3% and 4.1% in the barrel and end caps, respectively. The two cusps correspond to the gaps between barrel and end caps. [34]

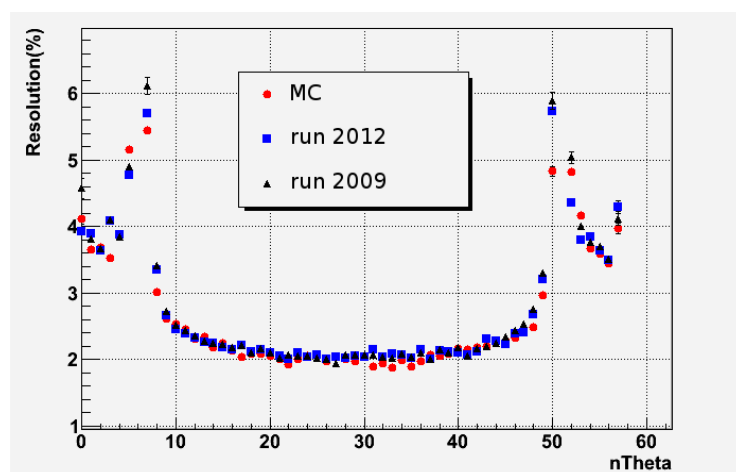


Figure 4.5: Energy resolution for Bhabha scattering at $E_{\text{CMS}} = m_{J/\psi}$ [34]

4.2.5 Muon Counter

The outermost part of the BESIII detector is the iron return yoke, which surrounds the solenoid coil and contains the muon counter system (MUC). The main purpose of the MUC is to distinguish muons from hadrons, especially pions which have the most similar mass.

The MUC consists of resistive plate chamber (RPC) interspersed with the steel plates of the magnetic flux return yoke of the solenoid. The RPCs are filled with a gas mixture of Ar/C₂F₄H₂/C₄H₁₀ in the ratios 50:42:8. [25]

Both the barrel and the end caps of the return yoke are divided into nine layers of varying thickness. Nine detection layers are installed in the barrel, but due to space limitations only eight detection layers are installed in the end caps. Each detection layer consists of two RPC layers and one pickup strip layer arranged as a sandwich. The barrel detection layers have a length of 3.94 m and the radius of the innermost detection layer is 1.700 m, so that the polar angle coverage is $|\cos\theta| < 0.75$. The innermost end cap detection layers have a distance of 2.050 m to the interaction point and cover a polar angle of $0.75 < |\cos\theta| < 0.89$. In total 89% of the solid angle are covered. [25]

The high voltage of the MUC was decreased from 7.7 kV to 7.5 kV, in order to protect the chambers and the electronics in 2013. Regardless of the decrease in high voltage the efficiency is still 95% and the spatial resolution is still 26 mm. The noise level is below 0.01 Hz/cm² and has no influence on the tracking. [29]

In 2016 the muon identification has been improved by aligning the MUC with the MDC based on cosmic ray events taken without a magnetic field and di-muon events selected from data taken at $\sqrt{s} = 3.686$ GeV with the magnetic field turned on. The di-muon events were also used to determine the magnetic field strength in the MUC by comparison with MC simulations. [35]

4.2.6 Trigger System and Online Data Acquisition

The BESIII trigger system consists of two trigger levels, a hardware trigger (L1) and a software trigger (L3). When BEPCII runs in the multi-bunch mode with 93 bunches, these have a distance of only 8 ns. The hardware trigger system is synchronized with the accelerator radio frequency and thus operates at 41.65 MHz. The trigger clock is distributed to the readout electronics of the TOF, MDC and EMC sub-trigger systems, and synchronizes the operation of the entire data acquisition. The data obtained from the different subsystems is stored in pipeline buffers as long as one trigger latency of 6.4 μ s, so that the trigger system does not cause any dead time. Optical fibers are used to transmit the data at high speed from the front-end electronics to the trigger system and to avoid ground loops. The trigger logic PCBs utilize FPGAs to generate the trigger primitives and conditions, which are then passed to the Global Trigger Logic for making final trigger decisions. [25]

The L1 trigger is supposed to reduce cosmic ray and beam related background to a level below the physics event rate of 2 kHz expected at the J/ψ peak at the peak luminosity, so that the maximum L1 trigger rate would be 4 kHz. When an L1 trigger signal is received, the data acquisition system reads the event data stored in the buffers and transfers it to an online computing farm (L3), which runs event building and filtering software. The L3 trigger reduces the data rate to a level of approximately 40 Mb/s, which is acceptable for permanent storage. [25]

4.2.7 BES Offline Software System

The object-oriented C++ framework bes offline software system (BOSS) is used for offline data analysis and MC simulation. The data processing and analysis is based on the Gaudi package. The geometry of the BESIII detector is described in the geometry design markup language (GDML). Persistent raw data can thus be reconstructed and converted to ROOT files for further analysis by the data summary tape (DST) Service.

5 Event Selection

5.1 Data Sets

The BESIII data set of $(1.310 \pm 0.007) \cdot 10^9$ J/ψ events, which includes $(0.2237 \pm 0.0014) \cdot 10^9$ events recorded in 2009 and $(1.087 \pm 0.006) \cdot 10^9$ events recorded in 2012, is used for this study. Corresponding to the recorded data samples two MC samples comprising in total of $1.225 \cdot 10^9$ J/ψ events have been generated for the collaboration, which include all the J/ψ decays according to the branching ratios listed in [36]. This sample will be referred to as the generic MC sample in the following. A MC sample of $1 \cdot 10^6$ phase space distributed $J/\psi \rightarrow \phi\eta\eta$ events is generated for this analysis and used to determine the efficiency of the applied selection criteria as well as for the partial wave analysis fits presented in chapter 7.

This analysis is based on BOSS 6.6.4.p03.

5.2 Selection of $\phi\eta\eta$ Candidates

In this analysis the ϕ meson is reconstructed from its decay into two charged kaons. The η meson is reconstructed from its decay into two photons. The final state consists therefore of the two charged kaons and four photons, and only events with tracks of two oppositely charged kaons and at least four photons are retained for further analysis.

5.2.1 Track Selection and Particle Identification

Since no intermediate resonances with long lifetimes are expected, the two tracks should originate from a point close to the interaction point. Events with tracks, which are more than 10 cm apart from the interaction point along the beamline or lie on a radius of more than 1 cm apart from the beam are discarded. Only tracks which are fully contained in the MDC volume can be measured precisely, so the azimuthal angle of the momenta reconstructed by the tracks must hold $|\cos\theta| < 0.92$. Based on the specific energy loss dE/dx determined with the MDC and the time of flight determined by the TOF detector, the probability that the track in question originates from an electron, a pion, a kaon, a muon, or a proton can be calculated. Only if the probability for the kaon hypothesis is the largest for both tracks, the event will be accepted.

5.2.2 Photon Candidate Selection

The only detector which measures photons is the EMC. When a photon hits the EMC, the generated electromagnetic shower will cause signals in several crystals, hence a photon is reconstructed by summing the information of neighboring crystals, which form a so-called cluster. The photon energy is reconstructed by summing the energy of all cluster crystals and the momentum can be extracted by determining the point of impact of the photon by computing an average over the positions of the cluster crystals, which is logarithmically

weighted with the signal amplitude. According to the different noise levels of barrel and end cap, a minimal energy deposit of 25 MeV for the barrel ($|\cos\theta| < 0.8$) and 50 MeV for the end caps ($0.86 < |\cos\theta| < 0.92$) is required to ensure the signal has not been generated by electronics noise or background radiation. Another means to reject fake hits is the requirement that the corresponding time of flight should be less than 700 ns. In order to eliminate signals from charged particles, only signals with no charged track in a cone with an opening angle of 10° around the corresponding cluster are considered as photons.

5.2.3 ϕ and η Candidate Selection and Combinatorics

Due to electromagnetic split-off and beam background, additional photons occur, thus the number of photons has only a lower limit. Even if an event contains only four photons, there are still three possibilities to combine the four photons to two pairs. Of all possible two photon combinations, only those are considered as η -candidates which fulfill $0.4 \text{ GeV} < m_{\gamma\gamma} < 0.7 \text{ GeV}$. The mass window is chosen to be rather broad so that a background estimation with sidebands is still possible.

Kaon pairs within the invariant mass window $|1020 \text{ MeV}/c^2 - m_{KK}| < 8 \text{ MeV}/c^2$ are considered as ϕ candidates.

5.2.4 Kinematic Fits

Due to energy and momentum conservation, the sum of the four-momenta of all final state particles must be equal to the initial four-momentum of the J/ψ . A kinematic fit with these four constraints (4C) is applied to the $J/\psi \rightarrow KK\gamma\gamma\gamma\gamma$ candidate events, which means that the four-momenta of all final state particles are varied until the constraints are met. A χ_{4C}^2 value is determined and combinations with $\chi_{4C}^2 < 35$ are considered as signal events, combinations with $\chi_{4C}^2 < 200$ are kept for background studies, and combinations with $\chi_{4C}^2 > 200$ are discarded from further consideration.

Since the natural width of the η resonance is much smaller than the detector resolution, another kinematic fit is performed under the $J/\psi \rightarrow KK\eta\eta$ hypothesis (H0), with additionally constraining the invariant mass of both photon pairs to the nominal η mass according to the particle data group (PDG), resulting in six constraints in total. Only events for which the combination with the least χ_{H0}^2 value fulfills $\chi_{H0}^2 < 35$ are considered as signal events.

In order to avoid ambiguities, events with more than one considered combination are required to have a difference of less than 10 between the least and the second least χ_{H0}^2 value and thus fulfill $\chi_{H0,2\text{nd}}^2 - \chi_{H0,1\text{st}}^2 < 10$.

Due to a large background contribution from events of the topology $J/\psi \rightarrow \phi X$, $X \rightarrow \pi^0\pi^0$ with X being an f_0 or f_2 meson, one more kinematic fit is performed under the $J/\psi \rightarrow KK\pi^0\pi^0$ hypothesis (H1), with additional constraints to the invariant mass of both photon pairs to the nominal π^0 mass according to the PDG resulting as well in six constraints in total. Events for which at least one combination leads to a $\chi_{H1}^2 < 200$ are considered as background events.

The χ_{H0}^2 distribution for the selected recorded events and signal MC events, which passed all selection criteria except for the χ_{4C}^2 and the χ_{H0}^2 criterion, is shown in figure 5.1a, a red arrow indicates the χ_{H0}^2 limit. In order to compare their shapes, the distribution for the signal MC sample is scaled by a factor of 0.05 so that it does not exceed the distribution

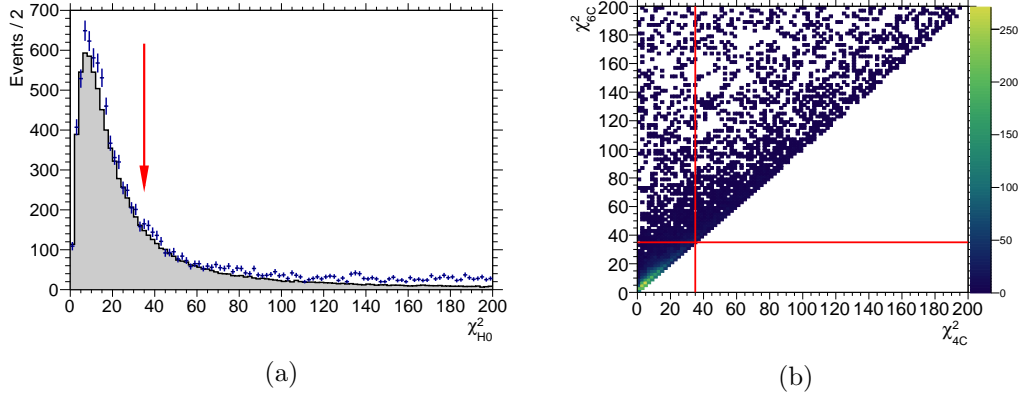


Figure 5.1: (a) Distribution of χ_{H0}^2 for the recorded events (blue) and signal MC events (black), which passed all selection criteria except for the χ_{H0}^2 and $\chi_{4\text{C}}^2$ criteria, the red arrow indicates the selection criterion $\chi_{\text{H0}}^2 < 35$; the distribution of the signal MC sample is scaled so that it does not exceed the distribution of the recorded sample
 (b) Distribution of $\chi_{4\text{C}}^2$ vs. χ_{H0}^2 for recorded events, which passed all selection criteria except for the χ_{H0}^2 and $\chi_{4\text{C}}^2$ criteria, the red lines indicate the selection criteria $\chi_{4\text{C}}^2 < 35$ and $\chi_{\text{H0}}^2 < 35$

for the recorded sample, because it is to be expected that the data sample also contains background events. Often a χ^2 limit is optimized according to the significance $\frac{S}{\sqrt{S+B}}$ but in order to perform a partial wave analysis it is more important to obtain a very clean data sample than to obtain a high significance. Figure 5.1b shows the $\chi_{4\text{C}}^2$ vs. χ_{H0}^2 distribution, to make the correlation between these parameters obvious. The $\chi_{4\text{C}}^2$ value is always smaller than the χ_{H0}^2 value, so that the selection criterion $\chi_{4\text{C}}^2$ has no effect if the selection criterion χ_{H0}^2 is also applied. The $\chi_{4\text{C}}^2$ selection criterion serves the purpose to allow for a realistic background estimation, where one or both photon pairs do not originate from an η meson. For this kind of background estimation the χ_{H0}^2 selection criterion should not be applied because it will favor combinations for which the invariant mass of both photon pairs is close to the η mass. Choosing the best combination according to the least χ_{H0}^2 value could thus result in a bias, so that background events rather show up in the $\eta\eta$ peak region instead of next to it. Estimating the background by looking into sideband regions would thus lead to a systematic underestimation.

Figure 5.2a shows the χ_{H1}^2 distribution for the recorded events, which passed all selection criteria except for the χ_{H1}^2 criterion. All the events shown in this figure will be considered as background, the right edge of the histogram corresponds to the χ_{H1}^2 limit.

It has been considered to also perform a kinematic fit to the $J/\psi \rightarrow KK\pi^0\eta$ hypothesis (H2), but since a criterion based on the according χ_{H2}^2 has turned out to be rather ineffective it has been dropped. The χ_{H2}^2 distribution of the recorded events, which passed all selection criteria except the one for the χ_{H2}^2 is shown in figure 5.2b. Compared to the χ_{H1}^2 distribution one conspicuous difference is the missing enhancement for low χ^2 values. In contrast to the χ_{H1}^2 criterion, which discards almost all $J/\psi \rightarrow \phi\pi^0\pi^0$ events, the χ_{H2}^2 criterion has no significant rejection power. Comparing the number of background events,

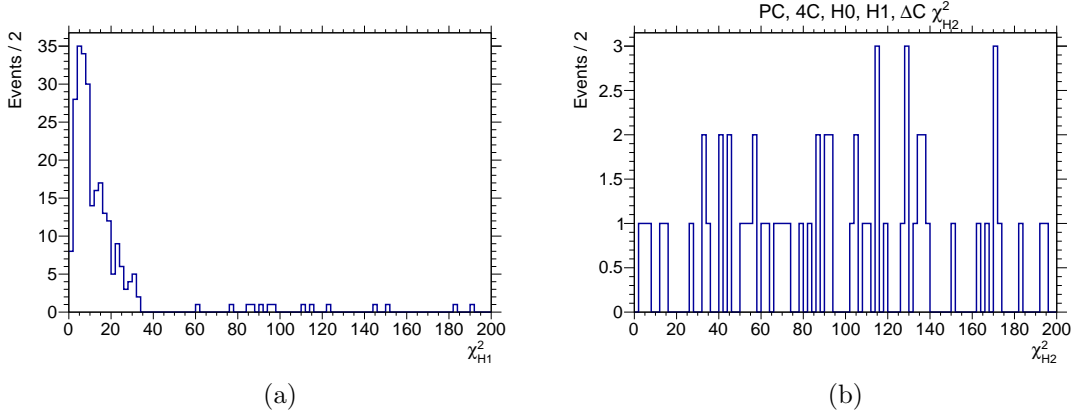


Figure 5.2: Distribution of χ_{H1}^2 (a) and χ_{H2}^2 (b) for recorded events, which passed all selection criteria except for the χ_{H1}^2 criterion and the χ_{H2}^2 criterion, respectively

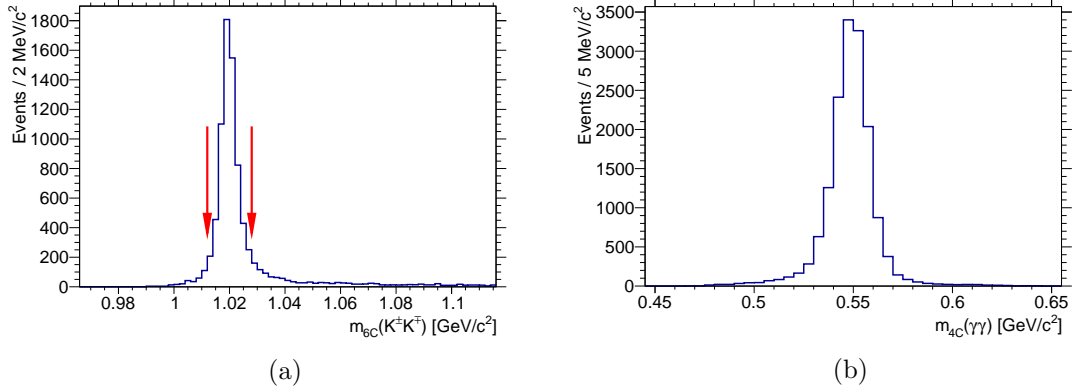


Figure 5.3: (a) Invariant K^+K^- mass distribution for recorded events, which passed all selection criteria except for the ϕ mass window, indicated by the red arrows (b) Invariant $\gamma\gamma$ mass distribution for recorded events, which passed all selection criteria except for the χ_{H0}^2 criterion

which still pass the selection criteria according to the generic MC sample only two events less pass if the χ_{H2}^2 is applied, but XX signal events are rejected in that case.

Figure 5.3a shows the invariant K^+K^- mass distribution after the 6C fit for recorded events, which passed all selection criteria except for the ϕ mass window. Besides the clear peak at the ϕ mass the rest of the phase space contains only few events, so that the $K^+K^-\eta\eta$ background contribution is small. The invariant $\gamma\gamma$ mass distribution after the 4C fit for recorded events, which passed all selection criteria except for the χ_{4C}^2 and χ_{H0}^2 criteria, is shown in figure 5.3b. There are two entries per event, one per η candidate. The peak at the η mass is slightly asymmetric due to the energy dependent detection efficiency of the EMC. Besides the peak there are only very few events, so that the $\phi\eta\gamma\gamma$ and $\phi\gamma\gamma\gamma$ background distribution is small, too. However the application of the χ_{H0}^2 criterion will even further reduce this kind of background. A more sophisticated background study by means of sidebands follows in section 5.3.4.

5.2.5 Detector Acceptance, Selection Efficiency and the Selected Sample

To be able to find meaningful interpretations of the obtained distributions, it is crucial to know the detector acceptance and selection efficiency, because these could lead to structures in the distributions which have no physical meaning. For this purpose a phase space distributed MC sample of $10^6 J/\psi \rightarrow \phi\eta\eta$ events has been generated. The detector response is simulated with a geometry and tracking (Geant4) model of the BESIII detector and the events are reconstructed from the detector response just the same as the recorded beam data. In total 123917 reconstructed signal MC events pass all selection criteria, so that the average efficiency over the full phase space amounts to 12.39%. Figure 5.4 shows the invariant $\eta\eta$ and $\phi\eta$ mass distributions for the ratio between the selected reconstructed events and the generated events. At low invariant $\eta\eta$ masses the efficiency actually amounts more than 16%, but for increasing invariant $\eta\eta$ masses the efficiency drops more and more until it reaches zero at the end of the phase space. The efficiency drop at higher invariant $\eta\eta$ masses leads to lower statistics in this region of the phase space. The efficiency over the invariant $\phi\eta$ mass is comparably flat, but a slight increase for higher invariant masses is visible.

The efficiency for the squared invariant $\eta\eta$ versus $\phi\eta$ and $\phi\eta$ versus $\eta\eta$ mass distributions is shown in figure 5.5. In this distributions it becomes obvious, that the efficiency behavior for the invariant $\phi\eta$ mass is actually caused by the drop for high invariant $\eta\eta$ masses. If the $\eta\eta$ system has a high invariant mass, the ϕ has only very little kinetic energy and thus the kaons, which originate from the decay of the ϕ , are more likely to have low momenta. This efficiency drop is caused by a low detection acceptance for low momentum kaons. The efficiency should be considered, when interpreting the intensities visible in the mass distributions for the selected recorded data are shown in figure 5.6. In the invariant $\eta\eta$ mass distribution a clear peak is visible at about $1.5 \text{ GeV}/c^2$ and a knee shaped structure at about $1.7 \text{ GeV}/c^2$, above $1.8 \text{ GeV}/c^2$ the distribution levels off. Since the efficiency shows no structures at $1.5 \text{ GeV}/c^2$ or $1.7 \text{ GeV}/c^2$, there must be a physical reason for these structures. Above $1.8 \text{ GeV}/c^2$ there might be structures, which are just not obvious due to the strongly decreased efficiency.

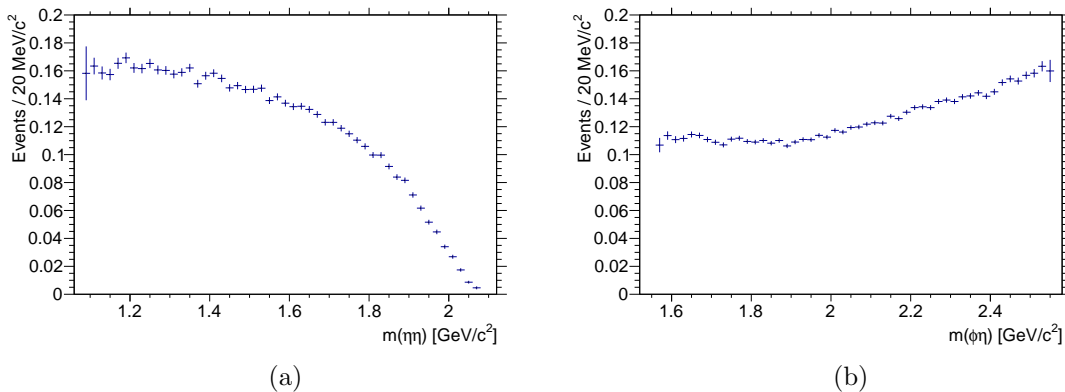


Figure 5.4: Invariant $\eta\eta$ (a) and $\phi\eta$ (b) mass distributions for the reconstructed signal MC events which passed all selection criteria, divided by the distribution of all generated events

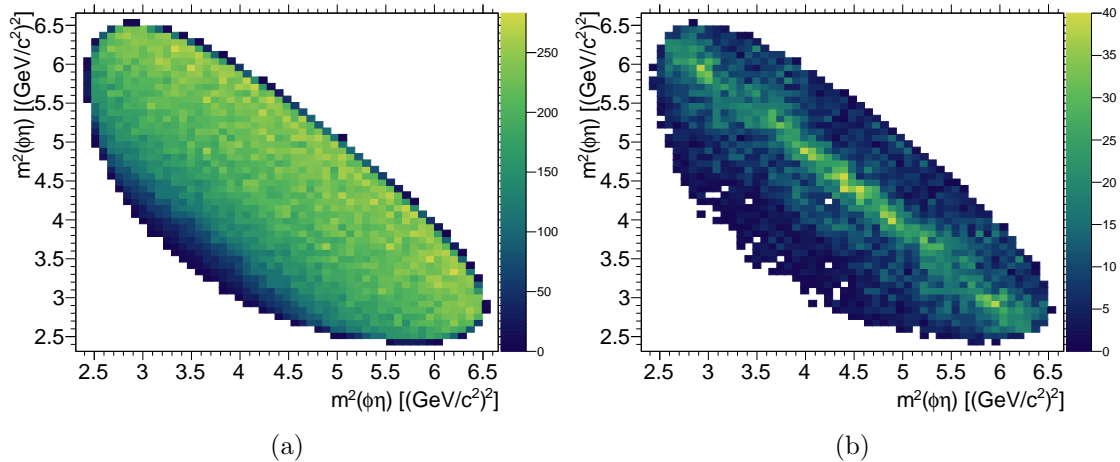


Figure 5.5: Squared invariant $\phi\eta$ vs. $\phi\eta$ mass distributions for the reconstructed signal MC events which passed all selection criteria divided, by the distribution of all generated events (a) and for the selected recorded data sample (b)

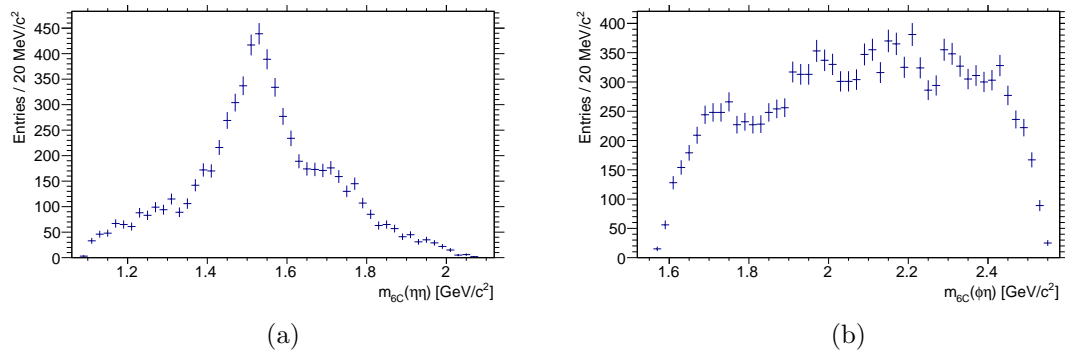


Figure 5.6: Invariant $\eta\eta$ (a) and $\phi\eta$ (b) mass distributions for the recorded events which passed all selection criteria

The invariant $\phi\eta$ mass distribution shows two bumps at about $1.7 \text{ GeV}/c^2$ and just below $2 \text{ GeV}/c^2$. Above $2 \text{ GeV}/c^2$ the content of neighboring bins varies so that it is not obvious if there are additional structures in that region, too. The squared invariant $\phi\eta$ versus $\phi\eta$ mass distribution of the recorded data shown in figure 5.5 yields the same conclusions. In such a Dalitz plot resonances result in horizontal, vertical or slanted bands, depending on the system in which they occur. The clear slanted band corresponds to the peak at $1.5 \text{ GeV}/c^2$ in the invariant $\eta\eta$ mass distribution. The bumps visible in the invariant $\phi\eta$ mass distribution correspond to the faintly visible vertical and horizontal bands at about $2.9 (\text{GeV}/c^2)^2$ and slightly below $4 (\text{GeV}/c^2)^2$, respectively.

Since it is impossible to tell for a single event if there was an intermediate resonance involved in the decay process at all and especially in which system of the final state particles, always both possible $\phi\eta$ combinations are taken into account. Thus, the Dalitz plots shown in figure 5.5 are necessarily perfectly symmetric.

5.3 Background Studies

A first look at the invariant K^+K^- and $\gamma\gamma$ mass spectra revealed only very little background pollution for the selected recorded data sample. In order to achieve meaningful Partial Wave Analysis results, it is very important to reduce the background as much as possible.

In this chapter different data and MC driven background studies are presented.

5.3.1 Analysis of a Generic Monte Carlo Sample

The generic MC sample introduced in section 5.1 has been studied to identify possible background sources. Since the truth information of each event is accessible, the generated decay chain can be deduced for each event. In total 11994 events of the generic MC data sample passed all selection criteria. The different contributions are listed according to their frequency in table 5.1. Only 73 events are from background contributions, which corresponds to 0.6%.

Decay Chain $J/\psi \rightarrow \dots$	Final State	Category	Number of Events
$\phi f_0(1710), f_0(1710) \rightarrow \eta\eta$	$\phi\eta\eta$	signal	5531
$\phi\eta\eta$	$\phi\eta\eta$	signal	4882
$\phi f_2'(1525), f_2'(1525) \rightarrow \eta\eta$	$\phi\eta\eta$	signal	1041
$\phi f_0(1500), f_0(1500) \rightarrow \eta\eta$	$\phi\eta\eta$	signal	493
$\phi f_0(1370), f_0(1370) \rightarrow \eta\eta$	$\phi\eta\eta$	signal	52
$\phi f_2(1270), f_2(1270) \rightarrow \eta\eta$	$\phi\eta\eta$	signal	27
$\gamma\phi\phi, \phi \rightarrow \gamma\eta$	$\phi\gamma\eta$	1	15
$K^- K^+ f_2'(1525), f_2'(1525) \rightarrow \eta\eta$	$K^- K^+ \eta\eta$	2	10
$\gamma\eta(2225), \eta(2225) \rightarrow \phi\phi, \phi \rightarrow \gamma\eta$	$\phi\gamma\eta$	1	7
$\eta h_1(1380), h_1(1380) \rightarrow K^{*-}(892)K^+,$ $K^{*-}(892) \rightarrow K^- \pi^0$	$K^- K^+ \pi^0 \eta$	3	7
$K^- K^+ f_0(1710), f_0(1710) \rightarrow \eta\eta$	$K^- K^+ \eta\eta$	2	6
$\phi f_0(1710), f_0(1710) \rightarrow \pi^0 \pi^0$	$\phi \pi^0 \pi^0$	4	5
$\eta h_1(1380), h_1(1380) \rightarrow K^- K^{*+}(892),$ $K^{*+}(892) \rightarrow \pi^0 K^+$	$K^- K^+ \pi^0 \eta$	3	5
$\phi\eta\eta', \eta' \rightarrow \gamma\gamma$	$\phi\eta\eta'$	5	2
$\phi f_2(1270), f_2(1270) \rightarrow \pi^0 \pi^0$	$\phi \pi^0 \pi^0$	4	2
$\phi f_0(1500), f_0(1500) \rightarrow \pi^0 \pi^0$	$\phi \pi^0 \pi^0$	4	1
$K^- \eta K^{*+}(892), K^{*+}(892) \rightarrow \pi^0 K^+$	$K^- K^+ \pi^0 \eta$	3	1
$K^- f_2(1270)K^+, f_2(1270) \rightarrow \eta\eta$	$K^- K^+ \eta\eta$	2	1
$\eta' h_1(1380), \eta' \rightarrow \gamma\gamma, h_1(1380) \rightarrow K^{*-}(892)K^+,$ $K^{*-}(892) \rightarrow K^- \pi^0$	$K^- K^+ \pi^0 \eta'$	6	1
$\phi \pi^0 \pi^0$	$\phi \pi^0 \pi^0$	4	1
$\gamma\eta_c, \eta_c \rightarrow \eta h_1(1380), h_1(1380) \rightarrow K^- K^{*+}(892),$ $K^{*+}(892) \rightarrow \pi^0 K^+$	$\gamma K^- K^+ \pi^0 \eta$	6	1
$\gamma\eta_c, \eta_c \rightarrow \phi f_0(1710), f_0(1710) \rightarrow \eta\eta$	$\gamma\phi\eta\eta$	6	1
$\gamma\eta_c, \eta_c \rightarrow \phi f_0(1710), f_0(1710) \rightarrow \pi^0 \pi^0$	$\gamma\phi \pi^0 \pi^0$	6	1
$\phi f_0(1710), f_0(1710) \rightarrow \eta\eta, \eta \rightarrow e^+ e^- \gamma$	$\phi\eta\eta$	6	1
$\phi f_0(1370), f_0(1370) \rightarrow \pi^0 \pi^0$	$\phi \pi^0 \pi^0$	4	1
$\phi f_1(1285), f_1(1285) \rightarrow \pi^0 a_0^0(980), a_0^0(980) \rightarrow \pi^0 \eta$	$\phi \pi^0 \pi^0 \eta$	6	1
$K^{*-}(892)\omega K^+, \omega \rightarrow \gamma\pi^0, K^{*-}(892) \rightarrow K^- \pi^0$	$K^- K^+ \pi^0 \pi^0$	6	1
$\gamma\eta_c, \eta_c \rightarrow \phi\phi, \phi \rightarrow \gamma\eta$	$\gamma\phi\gamma\eta$	6	1
$K_2^{*-}(1430)\eta K^+, K_2^{*-}(1430) \rightarrow K^- \pi^0$	$K^- K^+ \pi^0 \eta$	3	1

Table 5.1: Decay chains of generic MC events, which pass all selection criteria

Category of Decay Chain	Final State	Number of Events
1 $J/\psi \rightarrow \gamma(\eta(2225) \rightarrow)\phi\phi, \phi \rightarrow \gamma\eta$	$\phi\gamma\eta$	22
2 $J/\psi \rightarrow K^+K^-(f_0/f_2 \rightarrow)\eta\eta$	$K^-K^+\eta\eta$	17
3 $J/\psi \rightarrow \eta(h_1(1380) \rightarrow)KK^*, K^*_{(2)} \rightarrow K\pi^0$	$K^-K^+\pi^0\eta$	14
4 $J/\psi \rightarrow \phi(f_0/f_2 \rightarrow)\pi^0\pi^0$	$\phi\pi^0\pi^0$	10
5 $J/\psi \rightarrow \phi\eta\eta'$	$\phi\eta\eta'$	2
6 Other		8
Total		73

Table 5.2: Categories of decay chain topologies for background events of the generic MC sample, which pass all selection criteria

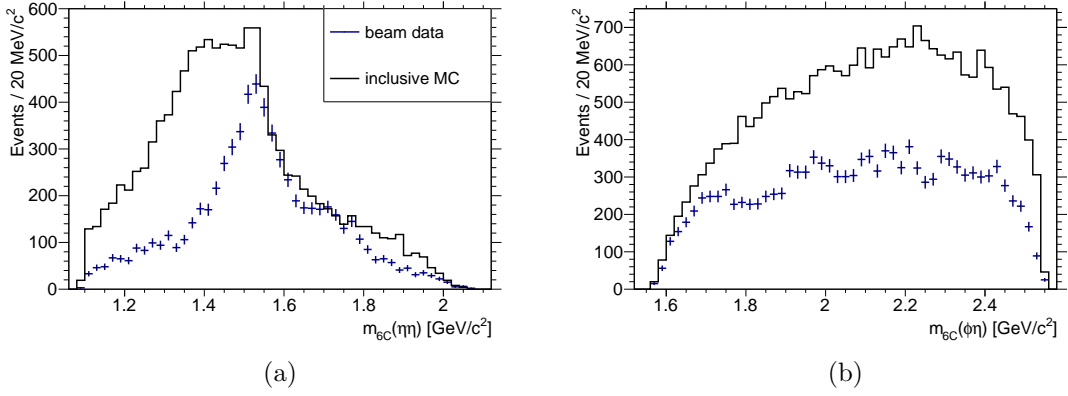


Figure 5.7: Distribution of the invariant $\eta\eta$ mass (a) and $\phi\eta$ mass (b) for generic MC and recorded events, which pass all selection criteria

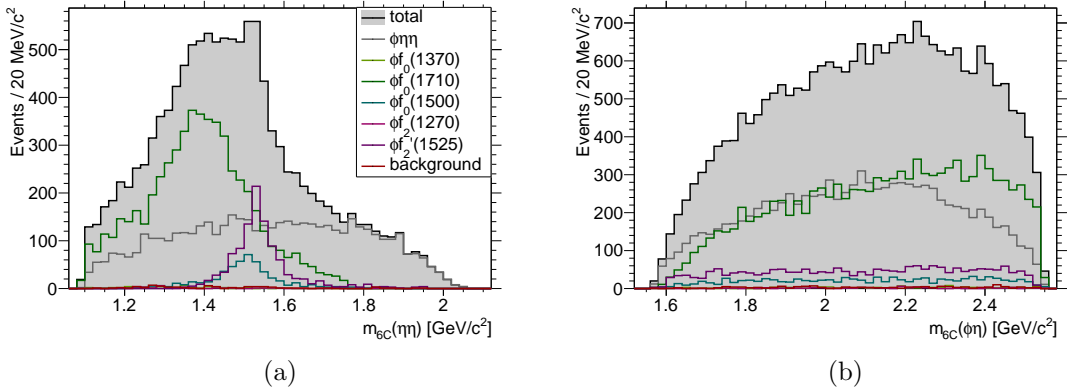


Figure 5.8: Distribution of the invariant $\eta\eta$ mass (a) and $\phi\eta$ mass (b) for generic MC events, which pass all selection criteria; the individual contributions are shown as colored lines

Background channels with a similar topology are grouped in table 5.2. Since the $J/\psi \rightarrow \phi\pi^0\pi^0$ background is efficiently discarded by the χ_{H1}^2 criterion as discussed in section 5.3.2, the largest remaining background contribution is from $J/\psi \rightarrow \gamma\phi\phi$ events with one ϕ decaying to $\gamma\eta$. The two next largest contributions originate from $J/\psi \rightarrow K^+K^-\eta\eta$ events, where the invariant mass of the two kaons matches the ϕ mass but they actually do not originate from a ϕ resonance, as well as from J/ψ decays involving K^* resonances.

Figure 5.7 shows a comparison of the invariant $\eta\eta$ and $\phi\eta$ mass for the generic MC sample and the recorded beam data sample. The generic MC sample contains almost twice as many events as the recorded data sample. The most striking difference is located below 1.5 GeV.

Figure 5.8 shows the invariant $\eta\eta$ and $\phi\eta$ mass for the generic MC sample in total as well as individually for the signal contributions and the background contribution. As expected, the distinct peak in the $\eta\eta$ spectrum originates from the $f'_2(1525)$ resonance. The major difference to the recorded beam data is caused by a contribution identified as the $f_0(1710)$ resonance. This is very astonishing, since the position of the structure is rather below 1.5 GeV/ c^2 .

It is to be expected, that the generic MC sample does not perfectly describe the data, since it is based on the information available at the time the generic MC sample was generated. Nevertheless, this sample is a useful tool to indicate which background channels contaminate the selected recorded data sample.

5.3.2 $\pi^0\pi^0$ Background

Most of the events containing two neutral pions are rejected by the χ_{H1}^2 criterion. In the generic MC sample 10 of those events remain, but the generic MC sample does not describe the recorded data very well. In order to properly check how many of these events are expected to remain in the recorded data sample despite the χ_{H1}^2 criterion, a phase space distributed $J/\psi \rightarrow \phi\pi^0\pi^0$ MC sample containing 10^6 events has been generated. The number of reconstructed events which pass all selection criteria corresponds to the combined detector acceptance and selection efficiency for this decay channel $\epsilon_{\phi\pi^0\pi^0}$, so that the number of background events in the selected recorded sample can be estimated by

$$N_{\phi\pi^0\pi^0} = N_{J/\psi} \cdot B(J/\psi \rightarrow \phi\pi^0\pi^0) \cdot B(\phi \rightarrow K^+K^-) \cdot B^2(\pi^0 \rightarrow \gamma\gamma) \cdot \epsilon_{\phi\pi^0\pi^0}.$$

The branching fractions of all involved decays $B(J/\psi \rightarrow \phi\pi^0\pi^0) = (5.0 \pm 1.0) \cdot 10^{-4}$, $B(\phi \rightarrow K^+K^-) = (48.9 \pm 0.5)\%$ and $B(\pi^0 \rightarrow \gamma\gamma) = (98.823 \pm 0.034)\%$ are obtained from [1]. The number of J/ψ events $N_{J/\psi}$ amounts to $1.39 \cdot 10^9$ events. The number of remaining $\phi\pi^0\pi^0$ events of the $J/\psi \rightarrow \phi\pi^0\pi^0$ MC sample after all selection criteria have been applied, must thus be scaled by 0.313 to obtain the number of $\phi\pi^0\pi^0$ events to be expected in the recorded sample. Indeed only one single event of the $\phi\pi^0\pi^0$ MC sample passes all selection criteria, which means that no remaining event is to be expected for the recorded sample.

The rejection power of the χ_{H1}^2 criterion becomes obvious when looking at the 860 events of the $\phi\pi^0\pi^0$ MC sample which pass all selection criteria except for the χ_{H1}^2 criterion. This corresponds to 269 events, which are to be expected additionally in the recorded data sample if not applying the χ_{H1}^2 criterion. The squared invariant $\eta\eta$ vs. $\phi\eta$ mass distribution of these events is shown in figure 5.9b. Most of these events show up at low invariant $\eta\eta$ masses.

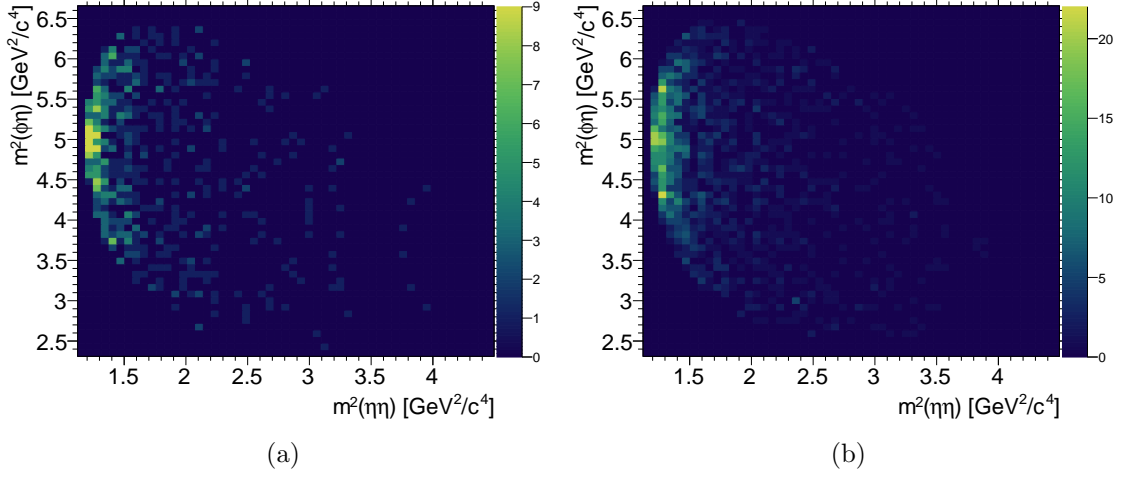


Figure 5.9: Distribution of the squared invariant $\eta\eta$ vs. $\phi\eta$ mass of events, which passed all selection criteria except for the χ_{H1}^2 criterion
 (a) for $J/\psi \rightarrow \phi\eta\eta$ MC
 (b) for $J/\psi \rightarrow \phi\pi^0\pi^0$ MC

	Generic MC		Phase Space MC		Expectation			Data
	$\phi\eta\eta$	$\phi\pi^0\pi^0$	$\phi\eta\eta$	$\phi\pi^0\pi^0$	$\phi\eta\eta$	$\phi\pi^0\pi^0$	Sum	
Without $\pi^0\pi^0$ Veto	12068	1032	124259	860	6640	269	6909	6877
With $\pi^0\pi^0$ Veto	12026	10	123917	1	6622	0	6622	6622
Difference	44	1022	342	859	18	269	288	255

Table 5.3: Comparison of number of selected generic MC events, efficiency, number of expected events, and number of selected recorded events when applying or not applying the χ_{H1}^2 criterion, which vetoes $\pi^0\pi^0$ events

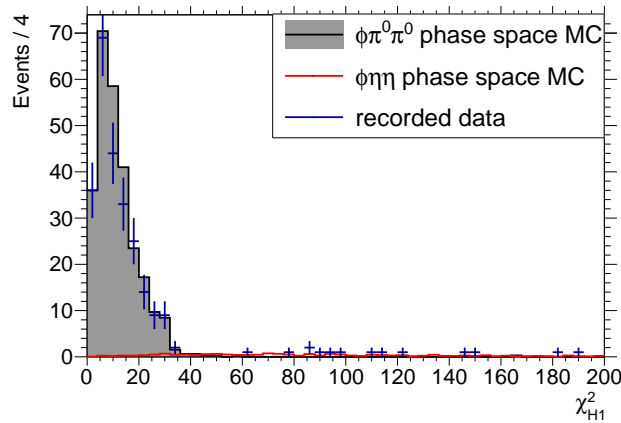


Figure 5.10: Distribution of χ_{H1}^2 for recorded events (blue), $J/\psi \rightarrow \phi\eta\eta$ MC events scaled by 0.05 as in figure 5.1a (red) and $J/\psi \rightarrow \phi\pi^0\pi^0$ MC events scaled according to branching fractions and sample sizes by 0.313 (black, gray shaded area), which passed all other selection criteria except for the χ_{H1}^2 criterion

Not only the $\phi\pi^0\pi^0$ background contribution, but also the signal yield is effected by the χ_{H1}^2 criterion. The effect can be studied with the phase space distributed signal MC sample. In total 342 $J/\psi \rightarrow \phi\eta\eta$ MC events of this sample are discarded due to the χ_{H1}^2 criterion. The squared invariant $\eta\eta$ vs. $\phi\eta$ mass distribution of these events is shown in figure 5.9a. The distribution of these events is very similar to the distribution for the $J/\psi \rightarrow \phi\pi^0\pi^0$ MC events. Thus it is very difficult to keep these signal events when rejecting the $\pi^0\pi^0$ background.

Assuming all 6622 selected events of the recorded data sample are signal events, the number of signal events discarded due to the $\pi^0\pi^0$ veto can be estimated to 18 events by the yields of the signal MC sample obtained with and without the veto. Since the signal MC is phase space distributed and does not contain any resonant structures, the correct distribution of the signal is not respected. Indeed there are fewer entries for low invariant $\eta\eta$ masses, so that the actual influence of the χ_{H1}^2 criterion is probably even weaker. In agreement with these considerations, instead of $6622 + 269 + 18 = 6909$ only 6877 events of the recorded sample are selected when dropping the χ_{H1}^2 criterion. Figure 5.10 shows the χ_{H1}^2 distribution for recorded events compared to scaled $J/\psi \rightarrow \phi\eta\eta$ and $J/\psi \rightarrow \phi\pi^0\pi^0$ MC events. All numbers relevant for the evaluation of the $\pi^0\pi^0$ veto are shown in table 5.3.

5.3.3 Miscombination

Even if an event actually is a signal event, it still might be reconstructed wrongly. The difficulty is caused by combinatorics: For four photons, there are three possibilities to combine them to two pairs. If there are more than four photons, this number must be multiplied by the number of possibilities to select four of n photons, which is given by the binomial coefficient. For most events, only for one of the combinations both $\gamma\gamma$ pairs have an invariant mass within the η mass window, and for even more events only one combination yields a good χ_{H0}^2 value.

The ratio of miscombined events among the signal events is determined by studying the truth-matched sample of 10^6 phase space distributed $J/\psi \rightarrow \phi\eta\eta$ MC events. Of the 123917 signal MC events which pass all selection criteria, 583 events are wrongly combined, corresponding to a miscombination fraction of 0.47%.

If the requirement, that the difference between the least and the second least χ_{H0}^2 values should be greater than 10 (ambiguity veto), is dropped, the yield of signal MC events increases from 123917 to 124397 and the miscombination fraction increases from 0.47% to 0.60% as shown in table 5.4. The choice of the limit value to be 10 is motivated by the distribution of the least versus second least χ_{H0}^2 value for miscombined signal MC events shown in figure 5.11.

	Phase Space MC	Miscombination Events	Miscombination Fraction [%]	Recorded Data	Expectation
Without Ambiguity Veto	124397	741	0.60	6650	40
With Ambiguity Veto	123917	583	0.47	6622	31
Difference	480	158	0.13	28	9

Table 5.4: Comparison of efficiency, miscombination fraction, number of reconstructed recorded events and number of miscombined events to be expected in the data sample with and without applying the ambiguity veto

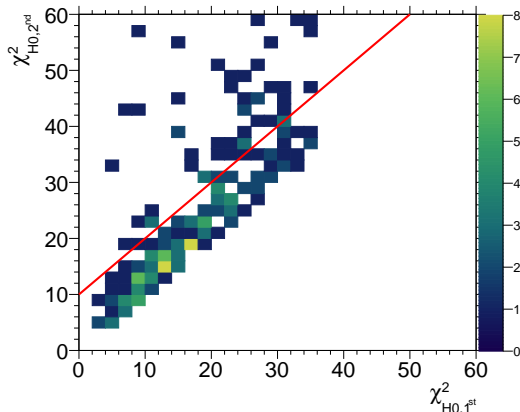


Figure 5.11: Distribution of least vs. second least χ^2_{H0} for miscombined signal MC events

For the recorded data sample, the number of selected events increases by 28 from 6622 to 6650 if the ambiguity veto is dropped. In agreement with that, an increase to 6648 events is to be expected according to the yields of signal MC events with and without the veto. The tiny difference might on the one hand, be explained by the fact that the recorded data sample is not phase space distributed, or, on the other hand, the ambiguity veto might also reduce background. Assuming the miscombination fraction is the same for the recorded data sample as for the signal MC sample, there are still 31 miscombined events, which pass all selection criteria. Compared to the different categories of background contributions listed in table 5.2, the miscombination actually is the dominating source of background.

5.3.4 Signal and Sideband Regions

In addition to the background studies based on the MC samples, a background study based on the recorded data sample has been performed. The approach of considering sideband regions in order to get some insight on the background below a peak is based on the assumption that the background events are distributed comparably below the signal peak and next to it. For the $J/\psi \rightarrow \phi\eta\eta$ decay, there is the ϕ peak in the spectrum of the invariant K^+K^- mass spectrum and there are the η peaks in the invariant $\gamma\gamma$ mass spectra.

It should be carefully considered if the applied selection criteria cause a distortion of the background which leads to more background below the peak and less background in the sideband region. This would lead to a systematic underestimation of the background contribution. Actually, the χ^2_{H0} criterion introduces such a bias, since combinations which have an invariant $\gamma\gamma$ mass close to the nominal η mass for both $\gamma\gamma$ pairs are favored. Thus, for the sideband studies presented in this chapter, the χ^2_{H0} criterion is not applied, which on the other hand results in a higher background level.

A good portion of the background which is usually suppressed due to the χ^2_{H0} criterion can be removed by the χ^2_{4C} criterion as indicated in figure 5.1b. Additionally a criterion on the invariant $\gamma\gamma$ mass is performed. In order to optimally mimic the usual data selection with the χ^2_{H0} criterion, the signal region is defined by a circle with a radius of 20 MeV

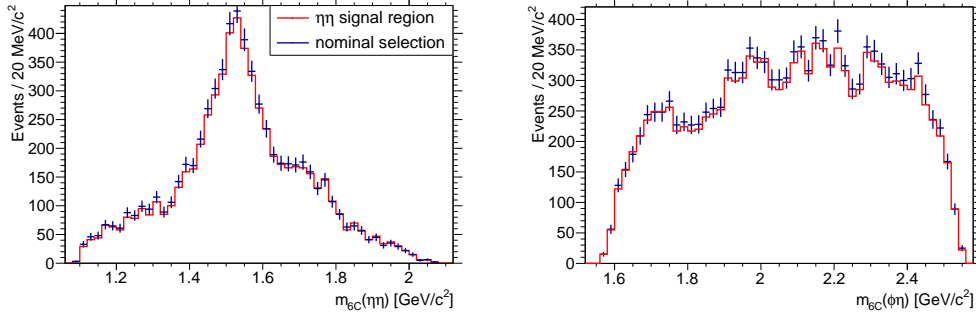


Figure 5.12: Comparison of the invariant $\eta\eta$ mass distribution (left) and invariant $\phi\eta$ mass distribution (right) for all 6622 selected recorded events and for the 6418 recorded events in the signal region

around $m_\eta \approx 0.55 \text{ GeV}/c^2$ in the plane of the invariant mass of both $\gamma\gamma$ pairs which are considered as η candidates, so that

$$\sqrt{(m_{\gamma_1\gamma_2} - m_\eta)^2 + (m_{\gamma_3\gamma_4} - m_\eta)^2} < 20 \text{ MeV}/c^2.$$

Applying this criterion additionally to the nominal selection criteria yields 6119 events, which is 92.40% of the originally 6622 selected events. Dropping the χ_{H0}^2 criterion and only applying the χ_{4C}^2 and the circular mass criterion yields 6418 events, which is 96.92% compared to the originally 6622 selected events. Figure 5.12 shows a comparison of the invariant $\eta\eta$ and $\phi\eta$ mass spectra for these two data sets, which are in good agreement.

In case of a one-dimensional distribution, two regions below and above the nominal mass can be considered as sideband regions. The regions should be chosen so that the range corresponds to the data selection or they should be weighted to be comparable. If all ranges are equal, the yield in the two sideband regions should be added with a weight of 0.5, to estimate the background yield below the peak. With this method reasonable results are obtained in case of constant or linear background.

Already in the case of two resonances, a plane is spanned and eight neighboring regions can be defined. For example, in case of an $\eta\eta$ signal, background contributions of the kind $\eta\gamma\gamma$, $\gamma\gamma\eta$ and $\gamma\gamma\gamma\gamma$ are possible, where the invariant mass of the $\gamma\gamma$ pair can be below or above the nominal η mass. The vertically and horizontally neighboring regions are comparable to the sideband regions of a one-dimensional distribution. Using a weight of 0.5 results in an averaging the $\eta\gamma\gamma$ and $\gamma\gamma\eta$ kinds of background. In contrast to the one-dimensional case, there is additionally the $\gamma\gamma\gamma\gamma$ kind of background, which is this way accounted for twice, since it appears in all four of these sideband regions. Countermeasures can be taken by also considering the four diagonally neighboring sideband regions which only contain the $\gamma\gamma\gamma\gamma$ kind of background, weighting them with -0.25 will compensate for the double counting.

Indeed together with the ϕ peak in the invariant K^+K^- spectrum three dimensions are to be considered. Unfortunately the ϕ resonance is so close to the K^+K^- threshold, that only a region above the nominal ϕ mass can be considered. The sideband regions are circles with a radius of $20 \text{ MeV}/c^2$ around $m_{\gamma\gamma} = 50 \text{ MeV}/c^2$ and $m_{\gamma\gamma} = 60 \text{ MeV}/c^2$ in the

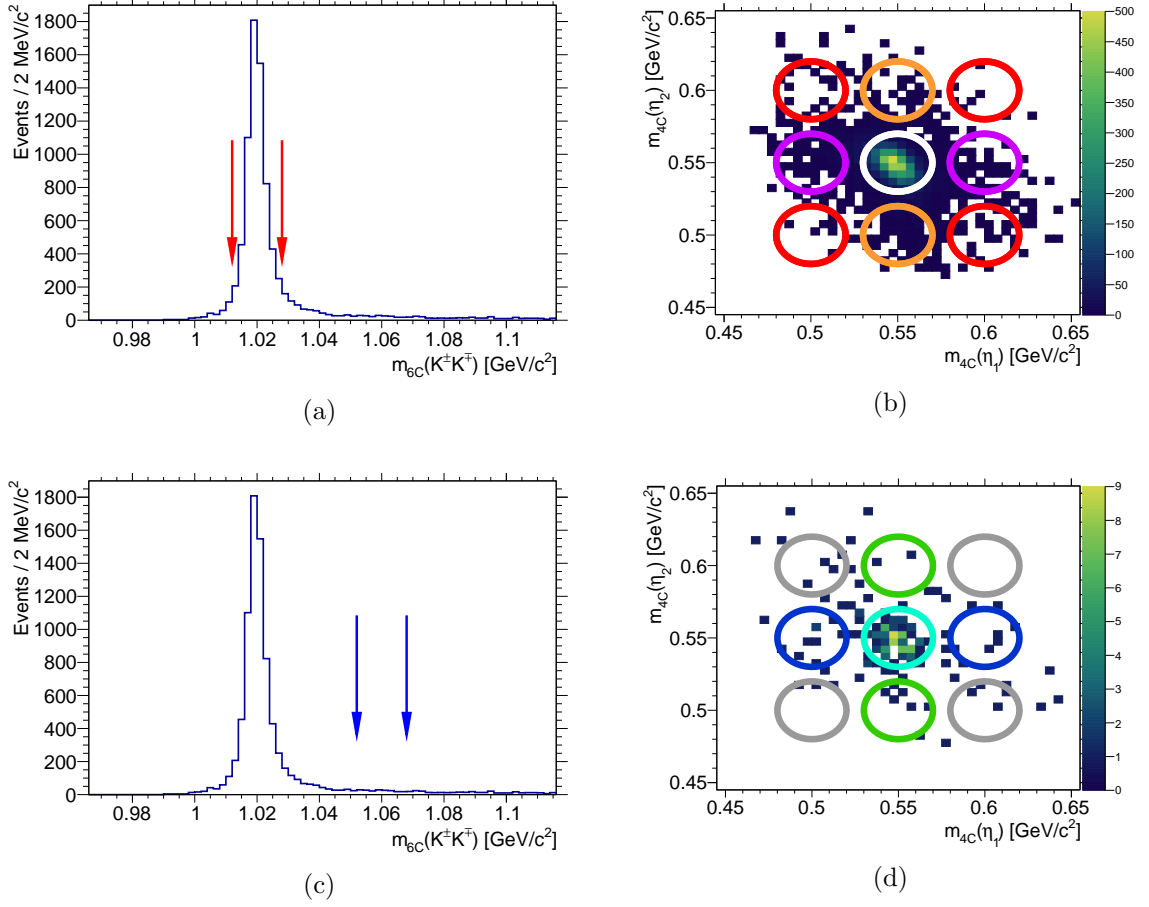


Figure 5.13: Invariant K^+K^- mass distribution for recorded events, which passed all selection criteria except for the ϕ mass window, the red arrows indicate the limits of the ϕ signal region (a) and the blue arrows indicate the limits of the ϕ sideband region (c) and invariant η vs. η mass distribution for recorded events, which passed all selection criteria except for the χ_{H0}^2 criterion (b) and the ϕ mass window, but instead the ϕ sideband window (d)

m_η versus m_η plane, and cover either the range from 1012 MeV/c² to 1028 MeV/c² or the range from 1052 MeV/c² to 1068 MeV/c² in the m_{KK} spectrum.

Figure 5.13 depicts the different sideband regions and shows the corresponding distributions for the recorded data sample, obtained without the application of the χ_{H0}^2 criterion. The corresponding distributions for the signal MC sample are shown in figure 5.14. Obviously also signal events occur in the sideband regions. Table 5.5 shows how often the different kinds of background occur in the different sideband regions and the weights which should be applied, so that each kind of background is only considered once.

The weighted sidebands are examined for the phase space distributed signal MC sample, for the recorded data sample and for the generic MC sample, for which can be distinguished between signal events and background events. Table 5.6 shows the observed number of events in the individual sideband regions for the phase space distributed signal MC sample,

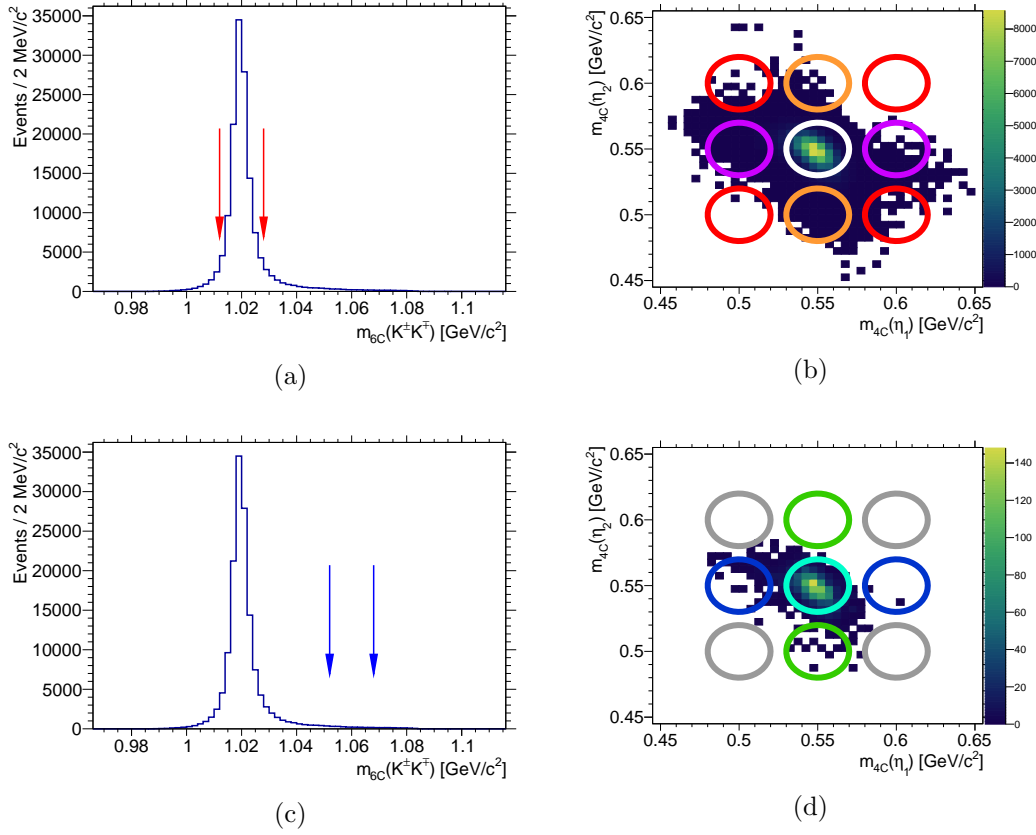


Figure 5.14: Invariant K^+K^- mass distribution for signal MC events, which passed all selection criteria except for the ϕ mass window, the red arrows indicate the limits of the ϕ signal region (a) and the blue arrows indicate the limits of the ϕ sideband region (c) and invariant η vs. η mass distribution for signal MC events, which passed all selection criteria except for the χ_{H0}^2 criterion (b) and the ϕ mass window, instead the ϕ sideband window (d)

Background	Orange	Violet	Red	Teal	Green	Azure	Grey	Total
$\phi\eta\gamma\gamma$	2	0	0	0	0	0	0	1
$\phi\gamma\gamma\eta$	0	2	0	0	0	0	0	1
$\phi\gamma\gamma\gamma\gamma$	2	2	4	0	0	0	0	1
$K^+K^-\eta\eta$	0	0	0	1	0	0	0	1
$K^+K^-\eta\gamma\gamma$	2	0	0	1	2	0	0	1
$K^+K^-\gamma\gamma\eta$	0	2	0	1	0	2	0	1
$K^+K^-\gamma\gamma\gamma\gamma$	2	2	4	1	2	2	4	1
Weight	0.5	0.5	-0.25	1	-0.5	-0.5	0.25	1

Table 5.5: Number of sideband regions in which the different background contributions occur and corresponding weights for the sideband region categories

	Weight	Signal MC	Data	Total	Generic MC Background	Signal
Signal		1192959	6418	11502	54	11448
Orange	0.50	1133	87	101	21	80
	0.50	66	35	23	16	7
Violet	0.50	1664	123	197	37	160
	0.50	142	44	35	23	12
Red	-0.25	3	7	6	6	0
	-0.25	34	16	22	17	5
	-0.25	49	21	23	19	4
	-0.25	0	7	0	0	0
Teal	1.00	1785	182	66	42	24
Green	-0.50	17	11	8	8	0
	-0.50	0	3	9	9	0
Azure	-0.50	31	10	9	9	0
	-0.50	2	7	8	8	0
Grey	0.25	0	3	2	2	0
	0.25	0	4	3	3	0
	0.25	0	5	10	10	0
	0.25	0	0	0	0	0
Total	1.00	3241	301.25	218	66.75	151.25
Ratio	—	2.72%	4.69%	1.90%	—	1.32%

Table 5.6: Number of events found in the different sideband regions for signal MC events, recorded events, total, background, and signal events of generic the MC sample

the recorded beam data, the full generic MC sample, the background contribution from the generic MC sample and the signal contribution from the MC sample.

Figure 5.15 shows the invariant $\eta\eta$ and $\phi\eta$ mass distributions for recorded events from the signal region and the weighted sideband regions. With 4.69% the fraction is relatively low and the distribution is rather flat, only below the $f'_2(1525)$ a slight enhancement can be seen. Figure 5.17 shows the symmetrized $\phi\eta$ versus $\phi\eta$ Dalitz plots for data and signal MC events from the weighted sideband regions. Resonances in $\eta\eta$ or $\phi\eta$ show up as horizontal, vertical or diagonal stripes in these kinds of plots. Since the distribution of the signal MC events is quite smooth, no structures seem to be introduced by the selection of the sideband regions. However, the existence of signal MC events in the sideband regions questions how many of the events of the recorded sample observed in the sideband are really background and how many are actually signal events. The recorded events show a structure corresponding to the $f'_2(1525)$, which could correspond to a $J/\psi \rightarrow \phi f'_2(1525), f'_2(1525) \rightarrow \pi^0 \pi^0$ background contribution, but could also correspond to leakage of signal events in the sideband regions.

Figure 5.18 shows the invariant $\eta\eta$ and $\phi\eta$ mass distributions for generic MC events from the signal region and the weighted sideband regions, as well as the background contribu-

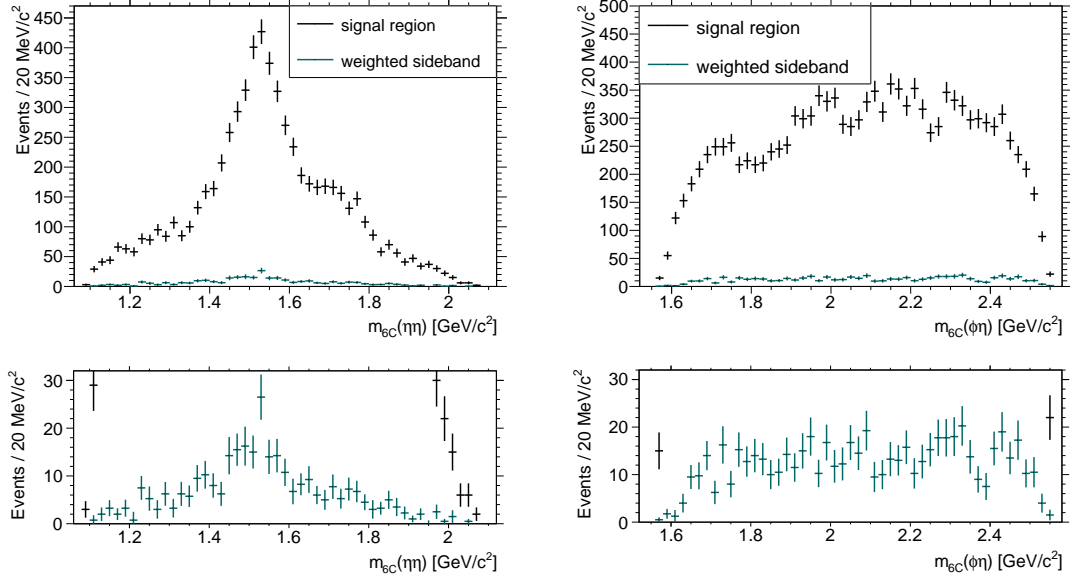


Figure 5.15: Comparison of the invariant $\eta\eta$ mass distribution (left) and invariant $\phi\eta$ mass distribution (right) for recorded events in the signal (black) and the weighted sideband regions (dark teal) on full scale (top) and zoomed (bottom)

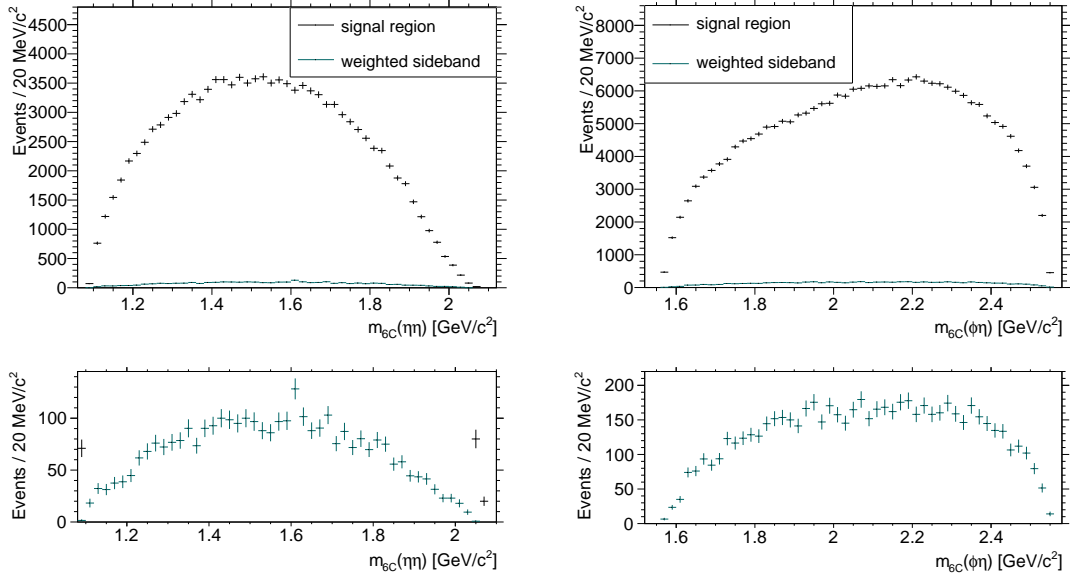


Figure 5.16: Comparison of the invariant $\eta\eta$ mass distribution (left) and invariant $\phi\eta$ mass distribution (right) for signal MC events in the signal (black) and the weighted sideband regions (dark teal) on full scale (top) and zoomed (bottom)

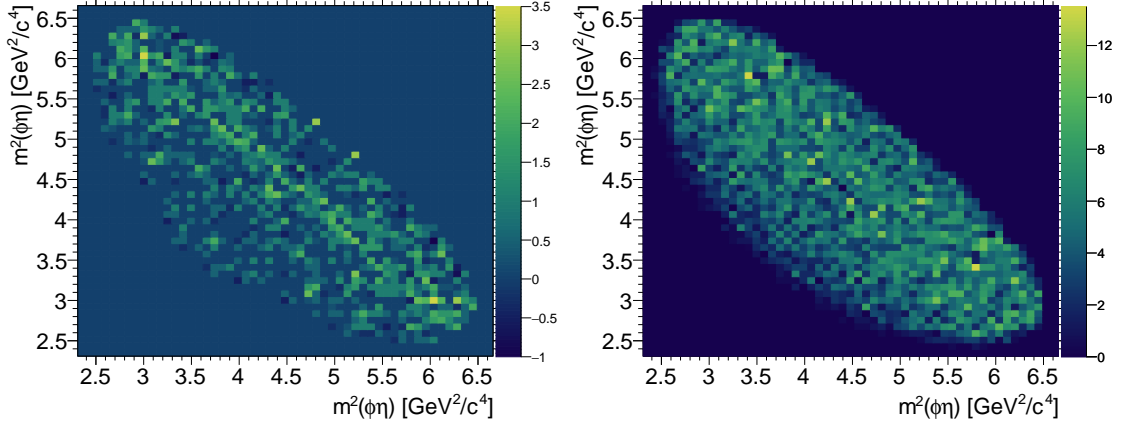


Figure 5.17: Squared invariant $\phi\eta$ vs. $\phi\eta$ mass distribution for recorded data (left) and signal MC (right) events in the weighted sideband regions

tion of the generic MC sample from the weighted sideband regions. Indeed the $f'_2(1525)$ structure is less clear for the background contributions than for all events in the sideband region, indicating that a good part of this structure in the recorded sample is actually generated by signal events, too. For the generic MC sample, the background fraction in the signal region is known to be $\frac{54}{11502} = 0.47\%$. Using the weighted yield in the sideband regions, the background ratio is slightly overestimated to $\frac{66.75}{11502} = 0.58\%$.

Figure 5.19 shows the symmetrized $\phi\eta$ versus $\phi\eta$ Dalitz plots for all signal MC events and for the background contribution of the generic MC sample from the weighted sideband regions.

Knowing the distribution of signal events from a MC sample, it is possible to estimate how many of the recorded events observed in the sideband regions are actually background events. However, just subtracting the fraction of signal MC events in the sideband from the fraction of events from the recorded data sample in the sideband is systematically wrong. Assuming the number of background events b contained in the signal region, and in a sideband region is the same, and additionally p and s signal events are contained in the signal (**peak**) and **sideband** region, respectively. One can expect to find a total of $N_{\text{pk}}^{\text{dat}} = p + b$ recorded events in the signal region and $N_{\text{sb}}^{\text{dat}} = s + b$ recorded events in the sideband region. The total of number of signal events in the selected recorded data sample is not known a priori. Assuming the MC sample correctly describes the distribution of signal events in data, there is an unknown scaling factor α between the signal MC sample and the signal yield in the recorded data sample, so that $N_{\text{pk}}^{\text{MC}} = \alpha \cdot p$ signal events of the MC sample are in the signal region and $N_{\text{sb}}^{\text{MC}} = \alpha \cdot s$ signal events of the MC sample are in the sideband region. The simple subtraction would yield

$$\begin{aligned} \frac{N_{\text{sb}}^{\text{dat}}}{N_{\text{pk}}^{\text{dat}}} - \frac{N_{\text{sb}}^{\text{MC}}}{N_{\text{sb}}^{\text{MC}} = \alpha \cdot s} &= \frac{s + b}{p + b} - \frac{\alpha \cdot s}{\alpha \cdot p} = \frac{s + b}{p + b} - \frac{s \left(1 + \frac{b}{p}\right)}{p \left(1 + \frac{b}{p}\right)} = \frac{s + b - s \left(1 + \frac{b}{p}\right)}{p + b} \\ &= \frac{b}{p + b} - \frac{s \frac{b}{p}}{p + b} = \frac{b}{p + b} \left(1 - \frac{s}{p}\right), \end{aligned}$$

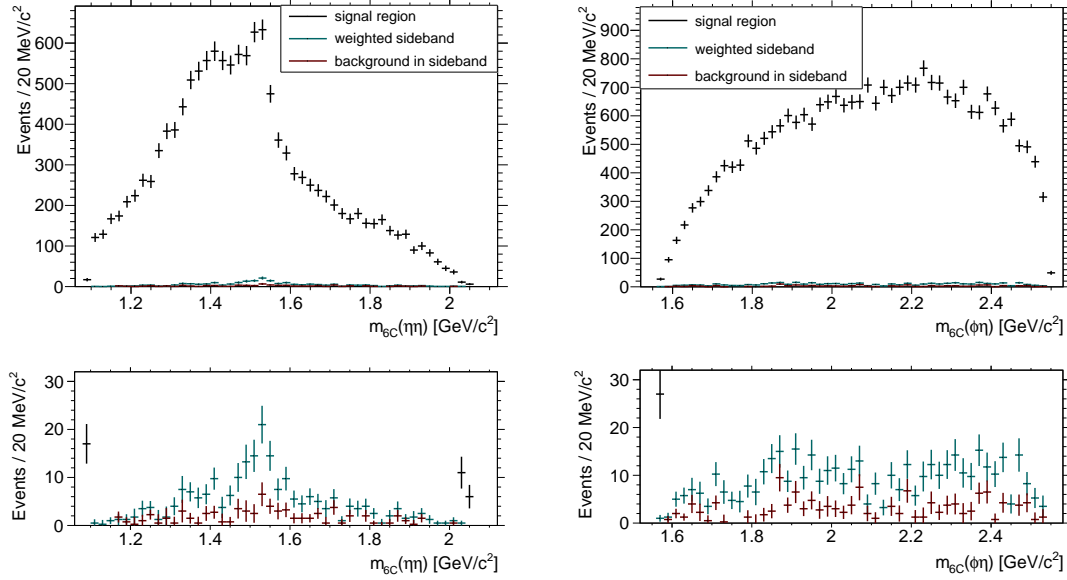


Figure 5.18: Comparison of the invariant $\eta\eta$ mass distribution (left) and the invariant $\phi\eta$ mass distribution (right) for generic MC events in the signal (black) and the weighted sideband regions (dark teal) and the background contributions in the weighted sideband regions (dark red) on full scale (top) and zoomed (bottom)

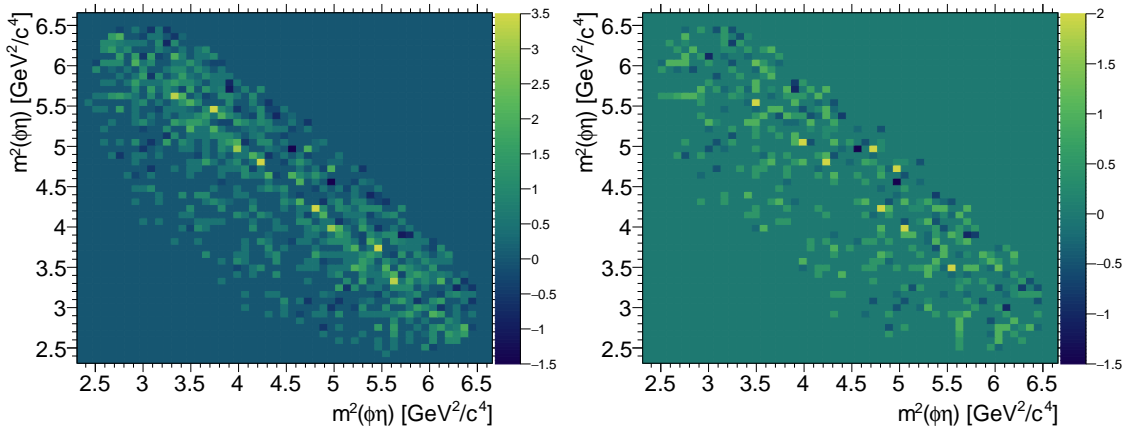


Figure 5.19: Squared invariant $\phi\eta$ vs. $\phi\eta$ mass distribution for all events of the generic MC sample in the weighted sideband regions (left) and the background of the generic MC sample in the weighted sideband regions (bottom)

Correction Sample	Data	Generic MC
Signal MC	2.03%	-0.84%
Generic MC	3.42%	0.58%

Table 5.7: Corrected background fraction estimations using the weighted sideband of the recorded data and the generic MC sample and corrections according to the yield of signal events in the signal and sideband regions of the signal MC sample and the signal yield of the generic MC sample

which has a systematic error as large as the signal leakage to the sidebands. The fraction of background events in the signal region can be estimated correctly by

$$\begin{aligned}
\frac{\frac{N_{\text{pk}}^{\text{MC}}}{N_{\text{sb}}^{\text{MC}}} N_{\text{sb}}^{\text{dat}} - N_{\text{pk}}^{\text{dat}}}{\frac{N_{\text{pk}}^{\text{MC}}}{N_{\text{sb}}^{\text{MC}}} N_{\text{pk}}^{\text{dat}} - N_{\text{pk}}^{\text{dat}}} &= \frac{\frac{\alpha \cdot p}{\alpha \cdot s} (s + b) - (p + b)}{\frac{\alpha \cdot p}{\alpha \cdot s} (p + b) - (p + b)} = \frac{\frac{p}{s} s + \frac{p}{s} b - p - b}{\left(\frac{p}{s} - 1\right)(p + b)} \\
&= \frac{\left(\frac{p}{s} - 1\right)b}{\left(\frac{p}{s} - 1\right)(p + b)} = \frac{b}{p + b}.
\end{aligned} \tag{5.1}$$

Applying equation (5.1) on the generic MC sample instead of recorded data, for in total $N_{\text{pk}}^{\text{dat}} = 11502$ events in the signal region, in total $N_{\text{sb}}^{\text{dat}} = 218$ events in the sideband region, $N_{\text{sb}}^{\text{MC}} = 11448$ signal events in the signal region, and $N_{\text{sb}}^{\text{MC}} = 151.25$ signal events in the sideband region, a background fraction of 0.58% is obtained compared to the originally estimated 1.32%. This value equals the fraction of background events in the weighted sideband region, instead of the fraction of background events in the signal region. However, the assumption of having the same amount of background events in the weighted sideband region as in the signal region is not fulfilled for the generic MC sample. Nonetheless, it is a prove of the principle.

Both the signal yield of the generic MC sample and the phase space distributed signal MC sample provide the means for a correction of the background estimation in the signal region. The background ratios obtained for recorded events and generic MC events based on corrections according to the signal MC sample and the generic MC sample are shown in table 5.7.

Surprisingly, the background ratio for the generic MC sample obtained by correcting according to the phase space distributed signal MC sample is negative, so that a discrepancy between the distribution of signal events in the phase space distributed MC sample and the generic MC sample becomes obvious. The reason for this discrepancy might just be the circumstance that the resonances are not accounted for. For the data sample, background ratios of 2.03% and 3.42% are obtained when correcting with the phase space distributed MC sample and the signal events of the generic MC sample, respectively.

Influence of the χ_{H0}^2 Criterion

In order to study the influence of the χ_{H0}^2 criterion on the estimation of the background fraction, the phase space distributed signal MC sample and the signal events of the generic MC sample should be scaled reasonably so that the fraction of events removed in data and

Correction Sample	Data	Generic MC
Signal MC	18.973	1.847
Generic MC	10.285	1.001

Table 5.8: Scaling factors between to match the signal yield of the different samples determined by equation (5.2)

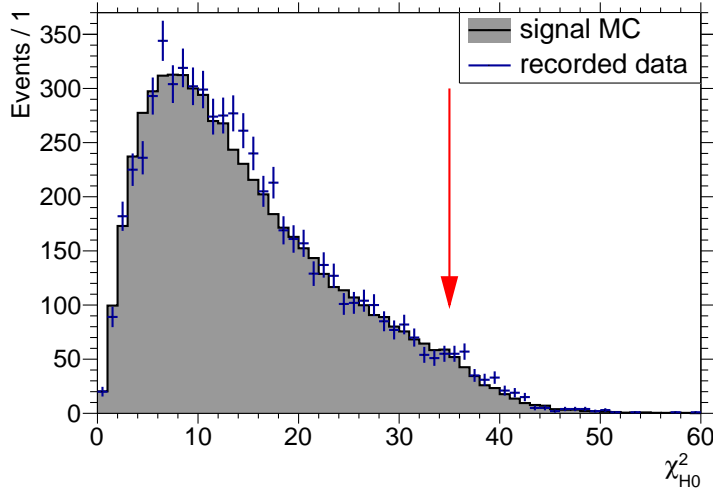


Figure 5.20: Distribution of χ_{H0}^2 for recorded and signal MC events scaled by $\frac{1}{\alpha} = 0.0527$ from the signal region (left) and for data and generic MC events scaled by $\frac{1}{\alpha} =$ from the signal region (right), the $\chi_{H0}^2 < 35$ criterion is indicated by the red arrow

the two MC samples can be compared. Using the same assumptions as above, the scaling factor α can be determined by

$$\frac{N_{pk}^{MC} - N_{sb}^{MC}}{N_{pk}^{dat} - N_{sb}^{dat}} = \frac{\alpha \cdot p - \alpha \cdot s}{(p + b) - (s + b)} = \frac{\alpha(p - s)}{p - s} = \alpha \quad (5.2)$$

The obtained scaling factors α are shown in table 5.8. The scaling factor obtained for the generic MC sample when using equation 5.2 with the distribution of the signal events of the generic MC sample is not exactly 1.000 because the assumption that the same number of events is in the signal region as in the weighted sum of the sideband region is not fulfilled.

Figure 5.20 shows that the χ_{H0}^2 for recorded events and scaled signal MC events matches quite well even beyond the limit. The estimation of the background level to about 2% can thus be considered reliable.

6 Partial Wave Analysis Fundamentals

In order to understand the structures visible in the mass spectra of the selected data different measures can be taken. In case of a clear individual peak the signal is very likely caused by a resonance, its peak position and width can easily be determined and the angular distribution of its daughter particles can help to determine its spin-parity quantum numbers. Usually the situation is more complicated with kinematically overlapping resonances and quantum mechanical interference between the contributions, which cannot be separated easily. In that case, the deduction of quantum numbers becomes quite difficult and also the peak positions and widths can be distorted from their physical meaning. Very broad or weakly contributing resonances might even not be recognized at all. In the special case of a spin-zero initial state and three spin-zero final state particles actually the Dalitz plot contains already all information and a Dalitz plot analysis can be applied.

In general, the best approach is to fit all phase space dimensions at once. Partial wave analysis means that the used model is capable to describe different possibly contributing intermediate resonances and the interferences between them. At best, the fitting model also ensures the conservation of unitarity, like the K -matrix.

The concept of partial waves has been introduced first in scattering theory and refers to the decomposition of a scattered plane wave on a spherically symmetric potential according to the angular momentum. For the description of decaying resonances this concept is generalized and also the spin is used for a decomposition of the transition amplitudes. The intensity distribution over the phase space observed by an experiment corresponds to the differential cross section and can be compared with the absolute square of the coherent sum of partial wave amplitudes for different contributions.

After clarifying which intermediate resonances are to be expected for the decay $J/\psi \rightarrow \phi\eta\eta$ in section 6.1, the helicity formalism is introduced in section 6.2. In section 6.3 the helicity formalism is applied to the process $J/\psi \rightarrow \phi\eta\eta$ and a weight function is derived, which is used to weight the phase space distributed MC sample to fit the selected data. Section 6.4 presents the K -matrix approach to parameterize the energy dependence of contribution, which in the limit case corresponds to a Breit-Wigner function. In the presented analysis a K -matrix is used to parameterize the dynamics of scalar and tensor contributions in the $\eta\eta$ system. For the scalar contributions the pole positions and coupling strengths are fixed to values obtained by coupled channel fit with data from different experiments for several different decay channels 6.4.7. The pole positions and coupling strengths of the K -matrix which describes the tensor contributions are released. To constrain the parameters to reasonable values, a coupled fit with scattering data describing the channels $\pi\pi$, $\eta\eta$, and $K\bar{K}$ has been performed. In section 6.5 the maximum likelihood method for optimizing parameters of a fit is introduced and the likelihood function used is presented. Section 6.6 is dedicated to answer the question on how to decide which intermediate resonances are describing the data the best. The analysis software PAWIAN, which provides tools to apply all the methods mentioned above and which has been used for the presented analysis, is introduced in section 6.7. Finally in chapter 7 the results of numerous different fits to the selected data are presented and evaluated.

6.1 Isobar Model and Quantum Numbers

The amplitude model used for the analysis presented here is based on the isobar model, where the complete reaction is described as a chain of two-body decays. Thus, for the decay $J/\psi \rightarrow \phi\eta\eta$ there are two subsystems in which intermediate resonances can occur: resonances X with the ϕ meson as a recoil particle decaying into two η mesons, thus the reaction can be written as

$$J/\psi \rightarrow \phi X, \quad X \rightarrow \eta\eta$$

and resonances Y with an η meson as a recoil particle decaying into a ϕ and an η meson, hence giving

$$J/\psi \rightarrow \eta Y, \quad Y \rightarrow \phi\eta.$$

Before starting to fit any hypothesis to the data, it should be checked which quantum numbers possibly contributing resonances might have, provided that the quantum numbers for the initial and final state particles are

$$\begin{array}{rcccl} & J/\psi & \rightarrow & \phi & \eta & \eta. \\ J^{PC} : & 1^{--} & \rightarrow & 1^{--} & 0^{-+} & 0^{-+} \\ I^G : & 0^- & \rightarrow & 0^- & 0^+ & 0^+ \end{array}$$

For both kinds of resonances the production as well as the decay processes are driven by the strong interaction. Thus the conservation of isospin I , parity P , C -parity and G -parity can be expected in addition to the conservation of spin, which holds for all kinds of interactions. This means that for a resonance α decaying into the two particles a and b the equations

$$P_\alpha = (-1)^{L_{ab}} P_a P_b, \quad C_\alpha = C_a C_b \quad \text{and} \quad G_\alpha = G_a G_b \quad (6.1)$$

and the triangle inequalities

$$\begin{aligned} |I_a - I_b| &\leq I_\alpha \leq |I_a + I_b|, \\ |j_a - j_b| &\leq S_{ab} \leq |j_a + j_b| \quad \text{and} \quad |S_{ab} - L_{ab}| \leq J_\alpha \leq |S_{ab} + L_{ab}| \end{aligned} \quad (6.2)$$

must hold, where L_{ab} denotes the angular momentum between the particles a and b . Thus for both kinds of possibly contributing resonances the isospin I is obviously 0, since the initial state and all final state particles have isospin 0.

The C -parity and G -parity are easily checked to be both positive for a resonance X decaying into $\eta\eta$ and both negative for a resonance Y decaying into $\phi\eta$, respectively.

For the resonances decaying into two η mesons the quantum numbers are rather constrained, since both are spin $j_\eta = 0$ particles, so their coupled spin is $S_{\eta\eta} = 0$ and the spin J_X of the X resonance must be equal to the angular momentum $L_{\eta\eta}$ between the two η mesons. The parity of the resonance X just depends on the angular momentum $L_{\eta\eta}$ between the two η mesons as $P_X = (-1)^{L_{\eta\eta}}$, because both have the same parity. The production process $J/\psi \rightarrow \phi X$ does not provide any further constraints. Another constraint arises due to the symmetry of having two identical daughter particles, so that $C_X = (-1)^{L_{\eta\eta}}$ must hold. Since the C_X parity is positive, that means that only even angular momenta $L_{\eta\eta}$ between the η mesons are possible, so that the parity P_X is positive, too. Thus the spin parity quantum numbers allowed for the resonance X are

$$I_X^{G_X} (J_X^{P_X C_X}) = 0^+ (J_X^{++})$$

where J_X must be even. According to the nomenclature for hadrons these resonances are called f_{J_X} .

For resonances Y decaying into a ϕ and an η meson the case is a bit more complicated. Since the ϕ meson has a spin of $j_\phi = 1$, whereas the η meson has a spin of $j_\eta = 0$, the coupled spin of the two daughter particles is unambiguously fixed to be $S_{\phi\eta} = 1$. The angular momentum $L_{\phi\eta}$ between the daughter particles ϕ and η then couples with this spin, so that $J_Y = L_{\phi\eta} - 1$, $J_Y = L_{\phi\eta}$ and $J_Y = L_{\phi\eta} + 1$ are all possible. The parity P_Y must fulfill $P_Y = (-1)^{L_{\phi\eta}+1}$, since the ϕ and the η meson have opposite parity signs, but even for a known spin J_Y still both parity assignments are possible. Looking at the production process $J/\psi \rightarrow \eta Y$ yields the same result

$$I_Y^{G_Y}(J_Y^{P_Y C_Y}) = 0^-(J_Y^{\pm-})$$

For $P_Y = -1$ these resonances are called ϕ_{J_Y} or ω_{J_Y} , for $P_Y = +1$ an even spin J_Y would yield an exotic set of quantum numbers, whereas an odd spin J_Y corresponds to an h_{J_Y} resonance.

6.2 The Helicity Formalism

The spatial distribution of decay products depends characteristically on the spin of the decaying particle. For spin-zero particles the decay products are uniformly distributed over all directions in the center of mass frame, but for higher spins the angular distributions of the decay products are in general not uniform. The angular distribution of the decay contains not only information on the absolute value of the spin but also on the spin orientation of the decaying particle and thus also on its production process. For that reason the ϕ meson's decay into a pair of oppositely charged kaons is taken into account in the analysis presented in this thesis, while the η mesons are considered to be final state particles.

Since angles are not Lorentz invariant, the shape of an angular distribution depends on the coordinate system. Several so-called spin formalisms are applicable, in this thesis the helicity formalism is used. The spin-orbit formalism from non-relativistic quantum mechanics is not applicable for relativistic systems, because the angular momentum is defined in the center of mass frame, but the spins of the decay products are defined in their own rest frames. The helicity is invariant under rotations and boosts along the momentum-axis of a particle [37], as long as the boost is small enough so that the direction of the momentum does not flip. The Rarita-Schwinger formalism is also implemented in the PAWIAN software, but even though it is considered to be the physically superior, it has the disadvantage of considerably higher computational effort.

6.2.1 Quantum Mechanical States

The quantum mechanical state of a single free particle at rest can be fully and unambiguously described by its total spin j and its projection m to an arbitrarily defined quantization axis denoted as $|j, m\rangle$. Mathematically, the unambiguousness, i.e. linear independence or orthogonality, and completeness of this description are expressed as

$$\langle j', m' | j, m \rangle = \delta_{j'j} \delta_{m'm} \quad \text{and} \quad \sum_{j, m} |j, m\rangle \langle j, m| = I,$$

where I denotes the identity operator. Dealing with a decay chain with several stages it is mandatory to describe particles not only non-relativistically at rest but also relativistically with a certain momentum \vec{p} . Such a description in the canonical reference system can basically be achieved by applying a Lorentz boost to the quantum mechanical state $|j,m\rangle$ in the center of mass system with the velocity $\vec{\beta} = \frac{1}{mc}\vec{p}$ corresponding to the momentum \vec{p} . Since a Lorentz boost can easily be defined along an axis of the chosen coordinate system, e.g. the z -axis, it is useful to first rotate the coordinate system so that the z -axis is aligned with $\vec{\beta}$, then boost along this new axis z_c of the canonical reference frame with the absolute value of the velocity $\beta = |\vec{\beta}| = |\frac{1}{mc}\vec{p}| = \frac{p}{mc}$ and rotate back, which can be written as

$$|\vec{p},j,m\rangle = |p,\phi,\theta,j,m\rangle = R^{-1}(\phi,\theta,0)L_z\left(\frac{p}{mc}\right)R(\phi,\theta,0)|j,m\rangle,$$

where ϕ and θ are the Euler angles for which $\hat{\beta} = R(\phi,\theta,0)\hat{z}$. A rotation $R(\alpha,\beta,\gamma)$ by the Euler angles α , β and γ transforms the quantum mechanical state as

$$R(\alpha,\beta,\gamma)|j,m\rangle = \sum_{m'} D_{mm'}^j(\alpha,\beta,\gamma)|j,m'\rangle.$$

The complex unitary Wigner- D -matrices are hence defined by

$$\begin{aligned} \langle j,m'|R(\alpha,\beta,\gamma)|j,m\rangle &= \sum_{m'} D_{m,m'}^j(\alpha,\beta,\gamma)\langle j,m|j,m'\rangle \\ &= D_{m,m'}^j(\alpha,\beta,\gamma) = e^{-im'\alpha}d_{m,m'}^j(\beta)e^{-im\gamma}, \end{aligned} \quad (6.3)$$

and can also be expressed by real Wigner- d -matrices. These are presented explicitly for example in the Review of Particle Physics [1]. The Wigner- D -matrices are unitary matrices of dimension $2j+1$ and satisfy the group property

$$\sum_k D_{m'k}^j(R)D_{mk}^{j*}(R) = \delta_{m'm}$$

where the subscripts denote the row and column of the respective matrix element and the asterisk denotes the complex conjugate. Note that the subscripts of the matrix multiplication are swapped compared to usual matrix multiplication, since the adjoint matrix is not only complex conjugated but also transposed.

Defining the quantization axis along the direction of the momentum \vec{p} results in a special projection of the spin, called helicity, which is denoted by

$$\lambda = \vec{j} \cdot \hat{p} = \vec{j} \cdot \frac{\vec{p}}{|\vec{p}|}.$$

By definition the helicity is invariant under rotations, because the quantization axis rotates with the system. Thus omitting the rotation back to the original orientation of the coordinate axes leads to the description of the quantum mechanical state in the helicity frame

$$|\vec{p},j,\lambda\rangle = L_z\left(\frac{p}{mc}\right)R(\phi,\theta,0)|j,\lambda\rangle,$$

where the new z -axis z_h points along the momentum vector \vec{p} and the new y -axis y_h points perpendicular to the former z -axis as well as the momentum $\hat{y}_h = \hat{z} \times \hat{p}$. Figure 6.1 illustrates the two kinds of coordinate transformations. Typically, these quantum mechanical

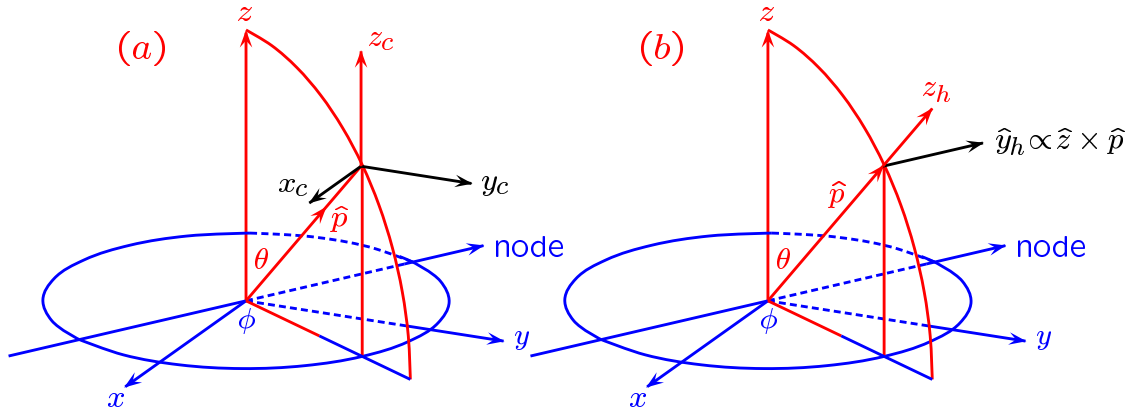


Figure 6.1: Coordinate transformation to the canonical system (left) and the helicity system (right) [38]

states are normalized as

$$\langle \vec{p}', j', \lambda' | \vec{p}, j, \lambda \rangle = (2\pi)^3 (2E) \delta^{(3)}(\vec{p}' - \vec{p}) \delta_{j', j} \delta_{\lambda', \lambda}, \quad (6.4)$$

so that they are Lorentz-invariant and the completeness relation can be written as

$$\sum_{jm} \int |\vec{p}, j, m\rangle \langle \vec{p}, j, m| \tilde{d}p = I$$

with $\tilde{d}p = \frac{d^3\vec{p}}{(2\pi)^3(2E)}$ [38].

Consider now a system of two particles a and b with masses m_a and m_b , momenta \vec{p}_a and \vec{p}_b , spins J_a and J_b and helicities λ_a and λ_b . The quantum mechanical two particle state is just the direct product

$$|\vec{p}_a, \lambda_a; \vec{p}_b, \lambda_b\rangle = |\vec{p}_a, j_a, \lambda_a\rangle \otimes |\vec{p}_b, j_b, \lambda_b\rangle$$

of the two quantum mechanical one particle states. The spins of the two particles are considered to be fixed and are thus suppressed.

In the center of mass frame the two particles have opposite momenta, so that $\vec{p}_a = -\vec{p}_b = \vec{q}$. The total energy of the system is given by $m = E_a + E_b$. From the relativistic energy-momentum relation $E_{a/b}^2 = \vec{p}_{a/b}^2 + m_{a/b}^2$ follows that the individual particle energies can be expressed in terms of the masses as $E_a = \frac{m^2 - m_b^2 + m_a^2}{2m}$ and analogously $E_b = \frac{m^2 - m_a^2 + m_b^2}{2m}$. The absolute value of the momentum \vec{q} can be expressed in terms of the masses as

$$q = \sqrt{\vec{p}_a^2} = \sqrt{\vec{p}_b^2} = \frac{\sqrt{(m^2 - (m_a + m_b)^2)(m^2 - (m_a - m_b)^2)}}{2m}. \quad (6.5)$$

The direction of the momentum \vec{q} can be defined by its spherical angles ϕ and θ . The state vector can thus be expressed in the spherical coordinates $q = |\vec{q}|$, ϕ , and θ as $|q, \phi, \theta, \lambda_a, \lambda_b\rangle$. It can be shown that the normalization is then given by

$$\langle q', \phi', \theta', \lambda'_a, \lambda'_b | q, \phi, \theta, \lambda_a, \lambda_b \rangle = (2\pi)^6 \frac{4\sqrt{s}}{q} \delta^4(P' - P) \delta(\cos \theta' - \cos \theta) \delta_{\lambda'_a \lambda_a} \delta_{\lambda'_b \lambda_b}$$

in spherical coordinates [37]. Being defined in the center of mass system the quantum mechanical two particle states have momentum $\vec{P} = 0$ and are thus eigenstates of the total four-momentum with eigenvalue $P = (m, 0, 0, 0)$. The eigenstate $|P\rangle$ can be factored out as

$$|q, \phi, \theta, \lambda_a, \lambda_b\rangle = (2\pi)^3 \left(\frac{4\sqrt{s}}{q} \right)^{\frac{1}{2}} |q, \phi, \eta, \lambda_a, \lambda_b\rangle |P\rangle$$

as follows from the normalization given above [37].

In order to respect not only the conservation of energy and momentum but also of angular momentum, the quantum mechanical two particle states should be expressed in a basis of total angular momentum eigenstates $|J, M, \lambda_a, \lambda_b\rangle$. A quantum mechanical two particle state $|q, \phi, \theta, \lambda_a, \lambda_b\rangle$ does not have a defined total spin J and projection M . Considering first the special case of \vec{q} pointing in the direction of the quantization axis, so that $\phi = 0$ and $\theta = 0$ and then rotating the system to obtain the general case for \vec{q} pointing in any direction, the coefficients

$$\langle J, M, \lambda'_a, \lambda'_b | \phi, \theta, \lambda_a, \lambda_b \rangle = \sqrt{\frac{2J+1}{4\pi}} D_{M, \lambda_{ab}}^J(\phi, \theta, 0) \delta_{\lambda_a, \lambda'_a} \delta_{\lambda_b, \lambda'_b} \quad (6.6)$$

are obtained for the basis of total angular momentum eigenstates [37, 38], where $\lambda_{ab} = \lambda_a - \lambda_b$.

To respect angular momentum dependent phenomena as the one described in subsection 6.4.1, another base change to the LS scheme is necessary. The inner product between the two bases is given by

$$\begin{aligned} \langle J', M', L_{ab}, S_{ab} | J, M, \lambda_a, \lambda_b \rangle &= \sqrt{\frac{2L_{ab}+1}{2J+1}} \langle L_{ab}, 0, S_{ab}, \lambda_{ab} | J, \lambda_{ab} \rangle \cdot \dots \\ &\dots \langle J_a, \lambda_a, J_b, -\lambda_{ab} | S_{ab}, \lambda_{ab} \rangle \delta_{J, J'} \delta_{M, M'}, \end{aligned} \quad (6.7)$$

where $\langle J_a, \lambda_a, J_b, -\lambda_{ab} | S_{ab}, \lambda_{ab} \rangle$ and $\langle L_{ab}, 0, S_{ab}, \lambda_{ab} | J, \lambda_{ab} \rangle$ are the Clebsch-Gordan coefficients, which describe the coupling of the two particle spins j_a, λ_a and j_b, λ_b to the total spin S_{ab}, λ_{ab} and the coupling of that total spin with the angular momentum L_{ab} to the total angular momentum J, λ_{ab} . Both bases are complete, so that

$$\sum_{J, M, \lambda_a, \lambda_b} |J, M, \lambda_a, \lambda_b\rangle \langle J, M, \lambda_a, \lambda_b| = I \quad \text{and} \quad \sum_{J, M, l, s} |J, M, l, s\rangle \langle J, M, l, s| = I. \quad (6.8)$$

6.2.2 Transition Amplitudes in the Helicity Formalism

Consider a two-body reaction $a + b \rightarrow c + d$ with the momentum \vec{p}_a , the total spin S_a , the parity P_a and the helicity λ_a of particle a and analogously for particles b, c and d . In the center of mass system the transition from the initial state $a + b$ to the final state $c + d$ can be described by a transition matrix S as

$$\langle \vec{p}_c, \lambda_c, \vec{p}_d, \lambda_d | S | \vec{p}_a, \lambda_a, \vec{p}_b, \lambda_b \rangle = (4\pi)^2 \frac{s}{\sqrt{p_c p_a}} \langle \phi, \theta, \lambda_c, \lambda_d | S | 0, 0, \lambda_a, \lambda_b \rangle.$$

Because of the Lorentz invariant normalization of the single particle states given in equation (6.4) also the absolute square of this transition amplitude summed over the helicities is

Lorentz invariant [38]. For simplification it is common to factor out the energy-momentum conservation

$$\langle \phi, \theta, \lambda_c, \lambda_d | S | 0, 0, \lambda_a, \lambda_b \rangle = (2\pi)^4 \delta^{(4)}(P_c + P_d - P_a - P_b) \langle \phi, \theta, \lambda_c, \lambda_d | S(s) | 0, 0, \lambda_a, \lambda_b \rangle$$

where the S -matrix then depends on the invariant center of mass energy s [38]. Splitting the part off, which describes an interaction, as $S = 1 + iT$ the invariant transition amplitude \mathcal{M} can be defined via the T -matrix as

$$\mathcal{M} = (4\pi)^2 \frac{s}{\sqrt{p_c p_a}} \langle \phi, \theta, \lambda_c, \lambda_d | T(s) | 0, 0, \lambda_a, \lambda_b \rangle.$$

Consider now a resonance α with total spin J_α and spin projection M_α along an arbitrarily defined z -axis. The amplitude describing the decay of this resonance into two particles a and b with helicities λ_a and λ_b can be expanded by inserting the completeness relation (6.8) and using equation (6.6) as

$$\begin{aligned} \mathcal{A}_{\lambda_a, \lambda_b}^{J_\alpha, M_\alpha} &= 4\pi \sqrt{\frac{s}{q}} \langle \phi, \theta, \lambda_a, \lambda_b | \mathcal{M} | J_\alpha, M_\alpha \rangle \\ &= 4\pi \sqrt{\frac{s}{q}} \sum_{J', M', \lambda'_a, \lambda'_b} \langle \phi, \theta, \lambda_a, \lambda_b | J', M', \lambda'_a, \lambda'_b \rangle \langle J', M', \lambda'_a, \lambda'_b | \mathcal{M} | J_\alpha, M_\alpha \rangle \\ &= 4\pi \sqrt{\frac{s}{q}} \sqrt{\frac{2J_\alpha + 1}{4\pi}} D_{M', \lambda_{ab}(\phi, \theta, 0)}^{J_\alpha*} \delta_{\lambda_a, \lambda'_a} \delta_{\lambda_b, \lambda'_b} \delta_{J_\alpha, J'} \delta_{M_\alpha, M'} \langle J', M', \lambda_a, \lambda_b | \mathcal{M} | J_\alpha, M_\alpha \rangle \\ &= \sqrt{\frac{2J_\alpha + 1}{4\pi}} D_{M_\alpha, \lambda_{ab}(\phi, \theta, 0)}^{J_\alpha*} F_{\lambda_a, \lambda_b}^\alpha, \end{aligned} \quad (6.9)$$

where the helicity decay amplitude F is defined as

$$F_{\lambda_a, \lambda_b}^\alpha = 4\pi \sqrt{\frac{s}{q}} \langle J_\alpha, M_\alpha, \lambda_a, \lambda_b | \mathcal{M} | J_\alpha, M_\alpha \rangle.$$

The dependence on \mathcal{M} is fully contained in the Wigner- D -matrix [38]. The helicity amplitude F does not depend on \mathcal{M} but only on the rotational invariant properties J , λ_a and λ_b , since the Lorentz invariant transition amplitude \mathcal{M} is in particular rotational invariant [38].

Using equation (6.7) the helicity amplitude can be expanded to the LS -scheme by

$$\begin{aligned} \langle J, M, \lambda_a, \lambda_b | \mathcal{M} | J, M \rangle &= \sum_{J', M', L_{ab}, S_{ab}} \langle J, M, \lambda_a, \lambda_b | J', M', L_{ab}, S_{ab} \rangle \langle J', M', L_{ab}, S_{ab} | \mathcal{M} | J, M \rangle \\ &= \sum_{J', M', L_{ab}, S_{ab}} \sqrt{\frac{2L_{ab} + 1}{2J + 1}} \langle L_{ab}, 0, S_{ab}, \lambda_{ab} | J, \lambda_{ab} \rangle \dots \\ &\quad \dots \langle S_a, \lambda_a, S_b, -\lambda_{ab} | S_{ab}, \lambda_{ab} \rangle \delta_{J, J'} \delta_{M, M'} \dots \\ &\quad \dots \langle J', M', L_{ab}, S_{ab} | \mathcal{M} | J, M \rangle, \end{aligned}$$

and defining the partial-wave amplitude

$$f_{L_{ab}, S_{ab}}^\alpha = 4\pi \sqrt{\frac{s}{q}} \langle J, M, L_{ab}, S_{ab} | \mathcal{M} | J, M \rangle,$$

so that F can be expressed as

$$F_{\lambda_a, \lambda_b}^\alpha = \sum_{L_{ab}, S_{ab}} \sqrt{\frac{2L_{ab} + 1}{2J_\alpha + 1}} f_{L_{ab}, S_{ab}}^\alpha \langle L_{ab}, 0, S_{ab}, \lambda_{ab} | J_\alpha, \lambda_{ab} \rangle \langle J_a, \lambda_a, J_b, -\lambda_{ab} | S_{ab}, \lambda_{ab} \rangle. \quad (6.10)$$

For strong and electromagnetic interactions parity is conserved. It can be shown, that this conservation results in the symmetry relation

$$F_{\lambda_a, \lambda_b}^\alpha = P_\alpha \cdot P_a \cdot P_b \cdot (-1)^{-J_\alpha + J_a + J_b} F_{-\lambda_a, -\lambda_b}^\alpha$$

of the decay amplitudes [38]. If the two daughter particles a and b are identical, this additional symmetry results in the symmetry relation

$$F_{\lambda_a, \lambda_b}^\alpha = (-1)^{J_\alpha} F_{\lambda_b, \lambda_a}^\alpha$$

by looking at the symmetrized helicity state and in the LS scheme it can be shown that symmetrized states vanish, if $L + S$ is not even [38].

Since the helicity amplitudes $F_{\lambda_a, \lambda_b}^\alpha$ correspond to fit parameters, that means that the number of free parameters is reduced due to the symmetry relation.

6.3 Weight Function and Free Parameters

Only the differential cross section $\frac{d\sigma}{d\Omega}$ is experimentally accessible, which can be interpreted as a normalized probability density function on the phase space. In the presented analysis the detector acceptance and reconstruction efficiency are taken into account by using phase space distributed reconstructed MC events in the likelihood function, so that the phase space factor and other constant factors can be omitted in the actually minimized weight function [37].

The different possible spins and spin projections for intermediate resonances are summed coherently, so that the relative phase of the complex amplitudes has an influence on the total amplitude corresponding to potential interference between different contributions. All initial and final state spin projections, which are not fixed or determined by the experiment must be summed incoherently.

As there are the two different possible decay chains $J/\psi \rightarrow \phi X$ with $\phi \rightarrow K^+ K^-$ and $X \rightarrow \eta \eta$ as well as $J/\psi \rightarrow \eta Y$ with $Y \rightarrow \phi \eta$ and $\phi \rightarrow K^+ K^-$, the weight function is

$$\begin{aligned} \frac{d\sigma}{d\Omega} \propto w = & \sum_{M_{J/\psi}} \sum_{\substack{\lambda_{K^+}, \lambda_{K^-} \\ \lambda_{\eta_1}, \lambda_{\eta_2}}} \left| \left(\sum_X \left[\sum_{\lambda_\phi, \lambda_X} \mathcal{A}_{\lambda_\phi, \lambda_X}^{J_{J/\psi}, M_{J/\psi}} \left(\sum_{\lambda_{\eta_1}, \lambda_{\eta_2}} \mathcal{A}_{\lambda_{\eta_1}, \lambda_{\eta_2}}^{J_X, \lambda_X} \right) \right] + \dots \right. \right. \\ & \dots + \sum_Y \left[\sum_{\lambda_{\eta_1}, \lambda_Y} \mathcal{A}_{\lambda_{\eta_1}, \lambda_Y}^{J_{J/\psi}, M_{J/\psi}} \left(\sum_{\lambda_\phi, \lambda_{\eta_2}} \mathcal{A}_{\lambda_\phi, \lambda_{\eta_2}}^{J_Y, \lambda_Y} \right) + \dots \right. \\ & \left. \left. \dots + \sum_{\lambda_{\eta_2}, \lambda_Y} \mathcal{A}_{\lambda_{\eta_2}, \lambda_Y}^{J_{J/\psi}, M_{J/\psi}} \left(\sum_{\lambda_\phi, \lambda_{\eta_1}} \mathcal{A}_{\lambda_\phi, \lambda_{\eta_1}}^{J_Y, \lambda_Y} \right) \right] \right) \dots \\ & \left. \dots \mathcal{A}_{\lambda_{K^+}, \lambda_{K^-}}^{J_\phi, \lambda_\phi} \right|^2. \end{aligned}$$

The two η mesons cannot be distinguished experimentally in terms of their production process, but they have different momenta. In order to respect that symmetry, the according amplitudes are added twice, once for each possible assignment.

For the first decay process, the decay of the J/ψ into either ϕX or ηY the ϕ angle is not well-defined. One axis is defined by the beam direction of the colliding e^+e^- pair, that gives the z -axis, but with unpolarized beams, the dependence on the ϕ angle vanishes. Thus compared to equation (6.9) the Wigner- D -matrices in the amplitudes

$$\begin{aligned} \mathcal{A}_{\lambda_\phi, \lambda_X}^{J/\psi, M_{J/\psi}} &= \sqrt{\frac{2J_{J/\psi} + 1}{4\pi}} d_{M_{J/\psi}, \lambda_{\phi X}}^{J_{J/\psi}}(\theta_\phi^{\phi\eta\eta}) F_{\lambda_\phi, \lambda_X}^{J/\psi} \quad \text{and} \\ \mathcal{A}_{\lambda_\eta, \lambda_Y}^{J/\psi, M_{J/\psi}} &= \sqrt{\frac{2J_{J/\psi} + 1}{4\pi}} d_{M_{J/\psi}, \lambda_{\eta Y}}^{J_{J/\psi}}(\theta_\eta^{\phi\eta\eta}) F_{\lambda_\eta, \lambda_Y}^{J/\psi} \end{aligned}$$

reduced to the Wigner- d -Matrices according to equation (6.3). The notation $\lambda_{\phi X} = \lambda_\phi - \lambda_X$ is used for abbreviation as introduced in the context of equation (6.6).

Due to the production of the J/ψ in an electromagnetic process only spin projections $M = \pm 1$ are possible, because the e^+e^- annihilation results in a virtual photon which can only have helicities $\lambda = \pm 1$ and produces the charm anticharm pair, which forms the J/ψ meson. Since all four final state particles have spin zero also their helicities must be zero.

Carrying out the transformation to the total angular momentum basis of the amplitude as given in equation (6.9) yields then

$$\begin{aligned} w = \frac{3}{(4\pi)^3} \sum_{M_{J/\psi} = -1, 1} & \left| \left(\sum_X \sqrt{2J_X + 1} \left[\sum_{\lambda_\phi, \lambda_X} d_{M_{J/\psi}, \lambda_{\phi X}}^1(\theta_\phi^{\phi\eta_1\eta_2}) \dots \right. \right. \right. \\ & \left. \left. \left. \dots \cdot D_{\lambda_X, 0}^{J_X^*}(\phi_{\eta_1}^{\eta_1\eta_2}, \theta_{\eta_1}^{\eta_1\eta_2}, 0) \cdot F_{\lambda_\phi, \lambda_X}^{J/\psi} \cdot F_{0,0}^X \right] + \dots \right. \right. \\ & \left. \left. \dots + \sum_Y \sqrt{2J_Y + 1} \left[\sum_{\lambda_Y, \lambda_\phi} \left(d_{M_{J/\psi}, -\lambda_Y}^1(\theta_{\eta_1}^{\phi\eta_1\eta_2}) \dots \right. \right. \right. \right. \\ & \left. \left. \left. \dots \cdot D_{\lambda_Y, \lambda_\phi}^{J_Y^*}(\phi_\phi^{\phi\eta_2}, \theta_\phi^{\phi\eta_2}, 0) \cdot d_{M_{J/\psi}, -\lambda_Y}^1(\theta_{\eta_2}^{\phi\eta_1\eta_2}) \dots \right. \right. \right. \\ & \left. \left. \left. \left. \dots \cdot D_{\lambda_Y, \lambda_\phi}^{J_Y^*}(\phi_{\eta_1}^{\phi\eta_1}, \theta_{\eta_1}^{\phi\eta_1}, 0) \right) \cdot F_{0, \lambda_Y}^{J/\psi} \cdot F_{\lambda_\phi, 0}^Y \right] \right) \dots \right. \\ & \left. \left. \left. \dots \cdot D_{\lambda_\phi, 0}^{1^*}(\phi_{K^+}^\phi, \theta_{K^+}^\phi, 0) \cdot F_{0,0}^\phi \right| \right|^2. \end{aligned}$$

The angles are defined for the particle denoted by the subscript in the helicity frame of the system denoted in superscript pointing in the direction. After the extension to the LS -scheme of the helicity decay amplitudes given in equation (6.10) only the amplitudes $f_{L_{\phi, X}, S_{\phi, X}}^{J/\psi}$, $f_{L_{\eta, \eta}, 0}^X$, $f_{L_{\eta, Y}, J_Y}^{J/\psi}$, $f_{L_{\phi, \eta}, 1}^Y$, $f_{L_{K^+, K^-}, 0}^\phi$ remain as free parameters, besides those parameters which describe the energy dependence. Since the amplitudes are complex numbers, that yields two real parameters per amplitude, which one might choose to be the real and imaginary part or the magnitude and the phase. Magnitude and phase are in this case closer related to the physical meaning.

Resonance	J^{PC}	Possible (L,S) Combinations		n	n_{free}
		Production	Decay		
X	0^{++}	(0,1),(2,1)	(0,0)	6	4
	2^{++}	(0,1),(2,1),(2,2),(2,3),(4,3)	(2,0)	12	10
	4^{++}	(2,3),(4,3),(4,4),(4,5),(6,5)	(4,0)	12	10
Y	1^{--}	(1,1)	(1,1)	4	2
	2^{--}	(1,2),(3,2)	(1,1),(3,1)	8	6
	3^{--}	(3,3)	(3,1)	4	2
	4^{--}	(3,4),(5,4)	(3,1),(5,1)	8	6
	5^{--}	(5,5)	(5,1)	4	2
	1^{+-}	(0,1),(2,1)	(0,1),(2,1)	8	6
	3^{+-}	(2,3),(4,3)	(2,1),(4,1)	8	6

Table 6.1: Possible (L,S) combinations for different accessible J^{PC} quantum numbers of resonances X decaying into two η mesons and resonances Y decaying into a ϕ and an η meson, corresponding number of parameters n and free parameters n_{free}

The number of amplitudes depends on how many (L,S) combinations are actually possible for the respective decay process and of course on which resonances are included in the fit hypothesis. The possible (L,S) combinations for resonances with different J^{PC} quantum numbers, which can appear as intermediate resonances in the decay $J/\psi \rightarrow \phi\eta\eta$, according to the rules (6.1) and (6.2) introduced in subsection 6.1 are listed in table 6.1.

The product of two complex numbers is itself a complex number and can thus be fully described by two real parameters, so that for each resonance the magnitude and phase of either one production or decay amplitude can be fixed without loss of generality. The phase between the different summands and their different magnitudes are of importance, so only for one of the possible (L,S) combinations magnitude and phase may be fixed.

Since the weight function is the square of the absolute of the summed amplitudes, the overall phase has no meaning and thus one phase can be fixed additionally without loss of generality.

The description of the mass dependence introduces further parameters, this is discussed in the following section.

6.4 Dynamical Part of the Amplitude

Besides the angular distributions which contain information on the spins of intermediate states the invariant mass distributions of different final state particle combinations is of high interest. Resonances might show up as peaks at the corresponding mass in the invariant mass distribution, but the respective line shape depends also on the available phase space, nearby thresholds, and other nearby resonances. Furthermore not all bumps originate directly from resonances, but also interference and phase space reflections influence the invariant mass distributions.

The centrifugal barrier factors take the suppression of high angular momenta close to thresholds into account and are thus useful independent of the parameterization of the dynamics. Compared to other parameterizations, a great advantage of the K -matrix

formalism is that it ensures the conservation of probability by retaining the unitarity of the scattering operator. It can be shown, that in the simplest case of only one resonance and one possible decay channel a K -matrix equals a relativistic Breit-Wigner function, but the sum of Breit-Wigner functions does usually not respect probability conservation and should not be used for the description of overlapping resonances. Especially for the $(\pi\pi)_S$ wave, where not only resonances but also other dynamical effects occur a description with the K -matrix formalism is mandatory.

6.4.1 Barrier Factors

If the mass m of a decaying particle is close to the sum of the daughter particle's masses $m_a + m_b$, also the breakup momentum q as given in equation (6.5) is small and a decay with a higher angular momentum becomes very unlikely. This suppression of higher angular momenta is called the centrifugal barrier effect. The semiclassical impact parameter $\frac{\sqrt{L(L+1)}}{q}$ has been introduced to take the centrifugal barrier effect into account. Later on, the impact parameter has been refined to

$$F_L(q) = \sqrt{\frac{|h_L^{(1)}(1)|^2}{x^2 |h_L^{(1)}(x)|^2}}$$

based on the assumption that two-particle interactions are negligible outside an interaction radius R [39], where $x = \frac{q}{q_R}$ and h_l are the spherical Hankel functions of the first kind. The momentum q_R corresponds to the interaction radius $R = \frac{\hbar}{q_R}$ and is usually chosen to be $q_R \approx 200 \text{ MeV}/c$ for light mesons, corresponding to $R \approx 1 \text{ fm}$, and by definition $F_l(q_R) = 1$.

The spherical Hankel functions are solutions of Bessel's differential equation

$$x^2 \frac{d^2 y}{dx^2} + x \frac{dy}{dx} (x^2 - L^2) = 0,$$

which arises when searching for separable solutions for the Helmholtz equation in cylindrical or spherical coordinates and therefore important for problems of wave propagation and static potentials. They fulfill the recursion relation

$$\frac{2L+1}{x} h_L^{(1)}(x) = h_{L-1}^{(1)}(x) + h_{L+1}^{(1)}(x).$$

Substituting with $z = x^2$ [40], the first four barrier factors are

$$\begin{aligned} F_0(q) &= 1 \\ F_1(q) &= \sqrt{\frac{2z}{z+1}} \\ F_2(q) &= \sqrt{\frac{13z^2}{(z-3)^2 + 9z}} \\ F_3(q) &= \sqrt{\frac{277z^3}{z(z-15)^2 + 9(2z-5)}} \\ F_4(q) &= \sqrt{\frac{12746z^4}{(z^2 - 45z + 105)^2 + 25z(2z-21)^2}}. \end{aligned}$$

When normalized to the breakup momentum q_α of a resonance with mass m_α , these factors read as

$$B^L(q, q_\alpha) = \frac{F_L(q)}{F_L(q_\alpha)}$$

and are called Blatt-Weisskopf barrier factors.

The centrifugal barrier effect is not only distorting the line shape of resonances with low invariant masses close to the threshold, but also the line shape of resonances with high invariant masses close to the opposite edge of the phase space, since their production proceeds with a small breakup momentum. In order to properly test if contributions with masses close to threshold are present in the $\phi\eta$ or $\eta\eta$ spectrum, the Blatt-Weisskopf barrier factors are important for a correct description of their shapes.

6.4.2 K -Matrix Formalism

In general the energy dependent part of the transition amplitude of a two-body scattering process $a + b \rightarrow c + d$ can be described by a scattering operator S , which transfers an initial state $|i\rangle$ into a final state $|f\rangle$, so that

$$|f\rangle = S|i\rangle.$$

Conservation of probability then corresponds to the unitarity of S , i.e. $SS^\dagger = S^\dagger S = I$, where S^\dagger denotes the adjoint operator S , that is the complex conjugated and transposed operator S , and I denotes the unity operator. It is desirable to separate the part of the scattering operator which describes that the initial state does not undergo any interaction and thus the final state is just the same as the initial state, from the part which describes interactions, by defining an operator T such that

$$S = I + 2iT.$$

As shown in [41] it directly follows from the unitarity of S , that the operator K defined by

$$K^{-1} = T^{-1} + iI$$

must be Hermitian, i.e. $K^\dagger = K$. From time reversal invariance additionally follows, that K must be symmetric [41], from which follows that it must be real.

The dimensions of S , T and K depend on the number of available channels, so for e.g. a two-channel problem these can be expressed by 2×2 matrices.

From the unitarity of the S -matrix follows, that the amplitudes corresponding to diagonal entries of the T -matrix can be expressed as

$$T_{jj} = \frac{1}{2i}(\eta \exp(2i\delta_j) - 1),$$

where δ_j denotes the phase shift and η denotes the elasticity for the scattering from channel j to channel j [1]. For purely elastic scattering the elasticity η equals one, in general it fulfills $0 \leq \eta \leq 1$. The energy evolution of such an amplitude traces a counterclockwise circle tangential to the real axis at 0 and a phase of 2δ from its center at $\frac{i}{2}$, but the amplitude leaves the so called unitary circle where inelasticity arises so that $\eta < 1$ [1].

In order to obtain Lorentz-invariant transition operators denoted by \hat{T} and \hat{K} , their dependence on the phase space factors must be canceled out by

$$T = \rho^{\frac{1}{2}} \hat{T} \rho^{\frac{1}{2}} \quad \text{and} \quad K = \rho^{\frac{1}{2}} \hat{K} \rho^{\frac{1}{2}}, \quad (6.11)$$

respectively [41]. The phase space matrix ρ is a diagonal matrix, so that one index suffices for unambiguous identification of the diagonal elements

$$\rho_i = \frac{2q^{(i)}}{m} = \sqrt{\frac{(m^2 - (m_c + m_d)^2)(m^2 - (m_c - m_d)^2)}{m^2}}, \quad (6.12)$$

where $q^{(i)}$ denotes the breakup momentum of channel i with final state particle masses m_c and m_d as defined in equation (6.5) and m denotes the invariant mass of the corresponding two-body system. In case of final state particles with identical masses the second factor in equation (6.12) vanishes. Plugging 6.11 into the definition of the K -matrix gives

$$\begin{aligned} \hat{K}^{-1} &= \hat{T}^{-1} + i\rho I \\ \Rightarrow \hat{T} &= \hat{K} + i\hat{K}\rho\hat{T} = \hat{K} + i\hat{T}\rho\hat{K} \end{aligned}$$

when multiplying with \hat{K} and \hat{T} from left and right, respectively, and vice versa. This equation can be solved for \hat{T} to

$$\hat{T} = \hat{K}(I - i\rho\hat{K})^{-1} = (I - i\hat{K}\rho)^{-1}\hat{K}. \quad (6.13)$$

Intermediate resonances α occur in the \hat{K} -matrix coefficients

$$\hat{K}_{ij} = \sum_{\alpha} \frac{g_{\alpha i}^0 B_{\alpha i}^L(m) g_{\alpha j}^0 B_{\alpha j}^L(m)}{m_{\alpha}^2 - m^2} + C_{ij}(m) \quad (6.14)$$

as poles, where $g_{\alpha i}^0$ describes the coupling strength of the resonance α to the channel i and $B_{\alpha i}^L(m) = B^L(q^{(i)}, q_{\alpha}^{(i)})$ denotes the centrifugal Blatt-Weisskopf barrier factors introduced in subsection 6.4.1, with the breakup momentum q^i (6.5) already inserted to emphasize the dependence on m .

The polynomials $C_{ij}(m)$ describe non-resonant ‘background’ contributions [42].

The factors $g_{\alpha i}^0$ are related to the phase space factor, the K -matrix width $\Gamma_{\alpha i}$ for channel i and the mass m_{α} of the resonance α by

$$g_{\alpha i}^0 = \sqrt{\frac{m_{\alpha} \Gamma_{\alpha i}}{\rho_i(m_{\alpha})}},$$

where the K -matrix width is in general neither identical with the width observed in an experimental mass distribution nor with the width of the corresponding T -matrix pole α in the complex energy plane [41] described in the following subsection.

6.4.3 Chew-Mandelstam Function

The \hat{K} -matrix approach with the phase space matrix ρ as described above usually delivers a proper fit of physical amplitudes, but it has an important shortcoming because it violates analyticity. First of all it is ill-defined at $m = 0$, additionally for unequal masses $m_c \neq m_d$

an unphysical cut is introduced, because ρ first becomes imaginary for $m < m_c + m_d$ which introduces a physical cut, but then becomes real again for $m < |m_c - m_d|$.

For none of the decay channels considered in this analysis the masses of the two final state particles are unequal. Nonetheless, the analyticity at $m = 0$ should be ensured.

A common Ansatz to bypass these issues is the replacement of the phase space factor $i\rho$ in equation (6.12) by an analytic function that produces the identical imaginary part on the right-hand cut [1].

A diagonal matrix $C(s)$ with $C(0) = 0$ and elements of the form $C_{ij} = C_i(s)\delta_{ij}$ can be introduced by

$$C_i(s) = C_i(s; m_a, m_b) = -\frac{2}{\pi} \left(-\frac{\sqrt{((m_a + m_b)^2 - s)((m_a - m_b)^2 - s)}}{s} \dots \right. \\ \dots \ln \left(\frac{\sqrt{((m_a + m_b)^2 - s)} + \sqrt{(m_a - m_b)^2 - s}}{2\sqrt{m_a m_b}} \right) + \dots \\ \dots \left. + \left(\frac{m_a^2 - m_b^2}{2s} - \frac{m_a^2 + m_b^2}{2(m_a^2 - m_b^2)} \right) \ln \left(\frac{m_a}{m_b} \right) - \frac{1}{2} \right),$$

which is called Chew-Mandelstam function. These elements are analytic in s except for the right-hand cuts across which the discontinuities are provided by $\text{Im } C(s) = \rho(s)$ [43]. For a function $K(s)$, which is complex differentiable on all points of its domain except for a discrete set of isolated points (its poles), the T -matrix defined by

$$T(s) = (I - K(s)C(s))^{-1}K(s)$$

in analogy to equation (6.13) is unitary and analytic [43].

6.4.4 Production of Resonances with the P Vector Approach

The K -matrix formalism is naturally used for scattering processes $a + b \rightarrow c + d$, but it can also be generalized for a parameterized production of resonances. Replacing the \hat{K} -matrix in the numerator in equation (6.13) by a corresponding production amplitude vector \hat{P} as suggested by Aitchison [44], results to the vector

$$\hat{F} = (I - i\hat{K}\rho)^{-1}\hat{P} = \hat{T}\hat{K}^{-1}\hat{P}, \quad (6.15)$$

which then corresponds to the \hat{T} -matrix. The coefficients of the \hat{P} -vector are defined by

$$\hat{P}_i = \sum_{\alpha} \frac{\beta_{\alpha}^0 g_{\alpha i}^0 B_{\alpha i}^L(m)}{m_{\alpha}^2 - m^2} + C'_i(m), \quad (6.16)$$

where $g_{\alpha i}^0$ and m_{α} are the same parameters as in the \hat{K} -matrix defined in equation (6.14) so that the \hat{P} -vector has exactly the same poles as the \hat{K} -matrix and β_{α}^0 describes the production strength of the resonance α . It might be convenient to rescale the β^0 's by

$$\beta_{\alpha}^0 = \beta_{\alpha} \sqrt{\frac{m_{\alpha} \Gamma_{\alpha}}{\rho(m_{\alpha})}},$$

so that the β parameters become dimensionless.

6.4.5 Breit-Wigner Parametrization

For a single resonance α and a single channel the \hat{K} -matrix becomes just a real number

$$\hat{K} = \frac{(g_\alpha^0)^2 (B_\alpha^L(m))^2}{m_\alpha^2 - m^2} = \frac{m_\alpha \Gamma_\alpha (B_\alpha^L(m))^2}{\rho(m_\alpha) (m_\alpha^2 - m^2)}$$

and also ρ is just a number, so that $\rho^{\frac{1}{2}}$ commutes with \hat{K} and thus

$$K = \hat{K} \rho = \frac{m_\alpha \Gamma_\alpha}{m_\alpha^2 - m^2} \frac{\rho(m)}{\rho(m_\alpha)} (B_\alpha^L(m))^2. \quad (6.17)$$

By inserting (6.17) and the one dimensional version of (6.16) in the definition of the \hat{F} -vector (6.15) it is reduced to

$$\begin{aligned} \hat{F} &= (1 - i\rho\hat{K})^{-1} \hat{P} = \left(1 - i \frac{m_\alpha \Gamma_\alpha}{m_\alpha^2 - m^2} \frac{\rho(m)}{\rho(m_\alpha)} (B_\alpha^L(m))^2 \right)^{-1} \frac{\beta_\alpha^0 g_\alpha^0 B_\alpha^L(q, q_\alpha)}{m_\alpha^2 - m^2} \\ &= \frac{m_\alpha^2 - m^2}{m_\alpha^2 - m^2 - i m_\alpha \Gamma_\alpha \frac{\rho(m)}{\rho(m_\alpha)} (B_\alpha^L(m))^2} \frac{\beta_\alpha \frac{m_\alpha \Gamma_\alpha}{\rho(m_\alpha)} B_\alpha^L(q, q_\alpha)}{m_\alpha^2 - m^2} \\ &= \beta_\alpha \frac{m_\alpha \Gamma_\alpha B_\alpha^L(q, q_\alpha)}{m_\alpha^2 - m^2 - i \frac{\rho(m)}{\rho(m_\alpha)} m_\alpha \Gamma_\alpha (B_\alpha^L(m))^2}, \end{aligned}$$

which is a relativistic Breit-Wigner function multiplied by the constant factor β_α .

The widely used approach to describe several resonances by sums of Breit-Wigner functions results in unphysical line shapes, if the resonances are overlapping or close to a threshold.

6.4.6 Extraction of Pole Parameters from the T -Matrix

Even though the \hat{K} -matrix is unambiguously related to the \hat{T} -matrix, the \hat{T} -matrix pole parameters, which carry the physical meaning, cannot easily be determined from the K -matrix pole parameters. With equation (6.13) the \hat{K} -matrix for a certain set of parameters can be transformed into the corresponding \hat{T} -matrix.

By evaluating the \hat{T} -matrix for different complex values of the center of mass energy $\sqrt{s} = m$ the pole positions can be determined numerically. The real part corresponds to the invariant mass of the pole m_α , whereas its negative imaginary part corresponds to $\Gamma_\alpha/2$, so that $m = m_\alpha - i\frac{\Gamma}{2}$. [45] The two dimensional real plane of corresponding to expectable complex values of m is called energy plane.

Since there are two solutions for the square root, which defines the breakup momentum in equation (6.5), the energy plane is a Riemann surface with sheets connected along the real axis. The number of Riemann sheets doubles with each considered channel. Usually the same pole occurs on several Riemann sheets, but only the pole parameters obtained from the sheet next to the physical sheet are physically meaningful [1].

Another important pole parameter is the residue of a pole that quantifies its coupling to the various channels. That is technically quite challenging and the implementation in partial wave interactive analysis (PAWIAN) has not been ready in time for determinations in the scope of this thesis.

6.4.7 The $(\pi\pi)_S$ wave

For the $\eta\eta$ system studied in the scope of this thesis the contribution of the f_0 mesons with quantum numbers $I^G J^{PC} = 0^+ 0^{++}$ is expected to be large. There are several overlapping resonances with significant coupling to several decay channels in the relevant mass range. A \hat{K} -matrix parameterization with five poles appearing in the channels $\pi\pi$ ($i = 1$), $\bar{K}K$ ($i = 2$), $\eta\eta$ ($i = 3$), $\eta\eta'$ ($i = 4$) and 4π ($i = 5$) has been fitted to nine data sets from different experiments, namely

1. GAMS data on the S -wave two/meson production in the reactions $\pi p \rightarrow \pi^0 \pi^0 n, \eta\eta n$ and $\eta\eta' n$ at small transferred nucleon momenta, $|t| < 0.2 (\text{GeV}/c)^2$
2. GAMS data on the $\pi\pi$ S -wave production in the reaction $\pi p \rightarrow \pi^0 \pi^0 n$ at large transferred momenta, $0.30 (\text{GeV}/c)^2 < |t| < 1.0 (\text{GeV}/c)^2$
3. BNL data on $\pi^- p \rightarrow K \bar{K} n$
4. CERN-Munich data on $\pi^+ \pi^- \rightarrow \pi^+ \pi^-$
5. Crystal Barrel data on $p\bar{p} \rightarrow \pi^0 \pi^0 \pi^0, \pi^0 \pi^0 \eta, \pi^0 \eta\eta$ (at rest from annihilation in liquid H_2)
6. Crystal Barrel data on $p\bar{p} \rightarrow \pi^0 \pi^0 \pi^0, \pi^0 \pi^0 \eta, \pi^0 \eta\eta$ (at rest from annihilation in gaseous H_2)
7. Crystal Barrel data on $p\bar{p} \rightarrow \pi^+ \pi^- \pi^0, K^+ K^- \pi^0, K_S K_S \pi^0, K^+ K_S \pi^-$ (at rest from annihilation in liquid H_2)
8. Crystal Barrel data on $n\bar{p} \rightarrow \pi^0 \pi^0 \pi^-, \pi^- \pi^- \pi^+, K^S K^- \pi^0, K_S K_S \pi^-$ (at rest from annihilation in liquid D_2)
9. E852 Collaboration data on the $\pi\pi$ S -wave production in the reaction $\pi^- p \rightarrow \pi^0 \pi^0 n$ at squared transferred nucleon momenta of $0 (\text{GeV}/c)^2 < |t| < 1.5 (\text{GeV}/c)^2$

and is provided in reference [46].

Explicitly the parameterization

$$\hat{K}_{ij}(s) = \left(\sum_{\alpha} \frac{g_i^{\alpha} g_j^{\alpha}}{m_{\alpha}^2 - s} + f_{ij}^{\text{scatt}} \frac{1 \text{ GeV}^2 - s_0^{\text{scatt}}}{s - s_0^{\text{scatt}}} \right) f_{A0}(s)$$

has been used, where f_{ij}^{scatt} and s_0^{scatt} are parameters to describe a slowly changing background contribution. The so-called Adler-Zero term [47]

$$f_{0A}(s) = \frac{1 \text{ GeV}^2 - s_{A0}}{s - s_{A0}} \cdot \left(s - s_A \frac{m_{\pi}^2}{2 \text{ GeV}^2} \right)$$

suppresses the false kinematic singularity at $s = 0$ in the physical region near the $\pi\pi$ threshold. The \hat{P} vector corresponding to this K -matrix is parameterized as

$$\hat{P}_i(s) = \sum_{\alpha} \frac{\beta_{\alpha} g_i^{\alpha}}{m_{\alpha}^2 - s} + f_{1i}^{\text{prod}} \frac{1 \text{ GeV}^2 - s_0^{\text{prod}}}{s - s_0^{\text{prod}}}.$$

Besides β_{α} also f_{1i}^{prod} and s_0^{prod} are free parameters of the fit. [48]

m_α [GeV/ c^2]	$g_{\pi\pi}^\alpha$ [GeV/ c^2]	$g_{\bar{K}K}^\alpha$ [GeV/ c^2]	$g_{4\pi}^\alpha$ [GeV/ c^2]	$g_{\eta\eta}^\alpha$ [GeV/ c^2]	$g_{\eta\eta'}^\alpha$ [GeV/ c^2]
0.65100	0.22889	-0.55377	0.00000	-0.39899	-0.34639
1.20360	0.94128	0.55095	0.00000	0.39065	0.31503
1.55817	0.36856	0.23888	0.55639	0.18340	0.18681
1.21000	0.33650	0.40907	0.85679	0.19906	-0.00984
1.82206	0.18171	-0.17558	-0.79658	-0.00355	0.22358
s_0^{scatt}	f_{11}^{scatt}	f_{12}^{scatt}	f_{13}^{scatt}	f_{14}^{scatt}	f_{15}^{scatt}
-3.92637	0.23399	0.15044	-0.20545	0.32825	0.35412
$s_{A0} = -0.15$	$s_A = 1$				

Table 6.2: K-matrix parameters from a global analysis [46] of the available $\pi\pi$ scattering data from threshold up to 1900 MeV/ c^2 [48]

In contrast to the phase space factor defined in equation (6.12), the phase space factor

$$\rho_i(s) = \sqrt{\frac{(s - (m_c + m_d)^2)}{s}},$$

has been used for the decay channels $\pi\pi$, $\bar{K}K$, $\eta\eta$ and $\eta\eta'$ to avoid the false singularity in the physical region. For equal masses of the decay products, as it is the case for the first three of these channels, that is actually the same, because the second factor in equation (6.12) vanishes. For the 4π channel the case is more complicated, details are given in [46].

The resulting parameters are displayed in table 6.2.

There are several other partial wave analyses, which use [49, 50, 51, 48, 52, 53, 54, 55] or confirm [56] these parameters, which probably demonstrates best that this is one of the best parameterizations of the $(\pi\pi)_S$ wave available at the time.

6.5 Maximum Likelihood Method

The probably most well-known fitting method is the method of least squares. When dealing with distributions instead of measured values at known points, the parameter space must be segmented into bins in order to obtain two values, one for the data and one for the fitted parameterization, of which the squared difference can be determined. Especially for multidimensional parameter spaces these bins might have very little or even no content. The maximum likelihood method allows for event based, unbinned fitting.

The likelihood $\mathcal{L}(\theta)$ of a hypothesis for which the underlying probabilistic model is characterized by a set of parameters θ is the probability $P(y|\theta)$ to measure data values y regarded as a function of θ . If the data consists of independent and identically distributed values $y = (y_1, \dots, y_N)$ with the probability distribution function $f(y, \theta)$, the joint probability distribution function factorizes and the likelihood function is given as

$$\mathcal{L}(\theta) = \prod_{i=1}^N f(y_i, \theta),$$

where the number of observations N is regarded to be fixed.

In the presented analysis the likelihood function

$$\mathcal{L}(\theta) \propto N! \cdot \exp\left(-\frac{N - \bar{N}}{2N}\right) \prod_{i=1}^N \frac{w(\vec{\Omega}_i, \vec{\theta})}{\int w(\vec{\Omega}, \vec{\theta}) \epsilon(\vec{\Omega}) d\Omega}$$

is used, where $\vec{\Omega}$ denotes the phase space coordinates, $\vec{\theta}$ denote the parameters of the probability density function w , and ϵ describes the detector acceptance and reconstruction and selection efficiency. The exponential term is introduced to obtain mean weights of approximately one for the maximal likelihood, where \bar{N} is defined as

$$\bar{N} = N \cdot \frac{\int w(\vec{\Omega}, \vec{\theta}) \epsilon(\vec{\Omega}) d\Omega}{\int \epsilon(\vec{\Omega}) d\Omega}.$$

Instead of actually determining the function ϵ , a sample of M homogeneously distributed MC events is generated, propagated through a detector response simulation, reconstructed and selected for estimation, so that

$$\int w(\vec{\Omega}, \vec{\theta}) \epsilon(\vec{\Omega}) d\Omega = \sum_{j=1}^M w(\vec{\Omega}_j, \vec{\theta}) \Rightarrow \int \epsilon(\vec{\Omega}) d\Omega = M. \Rightarrow \bar{N} = N \cdot \frac{\sum_{j=1}^M w(\vec{\Omega}_j, \vec{\theta})}{M}$$

Because the logarithm is strictly monotonic increasing, maxima in the likelihood function correspond to maxima in the logarithmized likelihood function $\ln(\mathcal{L})$, which transforms the product into a sum and thereby reduces the computational complexity drastically. The maximum likelihood estimators can thus be found by solving the so-called likelihood equation

$$\frac{\partial \ln \mathcal{L}}{\partial \theta} = 0.$$

From this equation it is also obvious, that a constant factor in the likelihood function, which does not depend on the parameters θ , will not have any influence on the maximum of $\ln(\mathcal{L})$ or \mathcal{L} and may therefore be added or dropped as desired. For technical reasons a negative sign is introduced, so that the maximizing problem can be transformed into a minimizing problem, yielding finally the negative log-likelihood (NLL) function

$$-\ln(\mathcal{L}(\vec{\theta})) = -\sum_{i=1}^N \ln(w(\vec{\Omega}_i, \vec{\theta})) + N \ln\left(\frac{\sum_{j=1}^M w(\vec{\Omega}_j, \vec{\theta})}{M}\right) + \frac{N}{2} \left(\frac{\sum_{j=1}^M w(\vec{\Omega}_j, \vec{\theta})}{M} - 1\right)^2,$$

where the first summand corresponds to the numerator of the product in the likelihood function, the second term corresponds to the denominator and the last summand corresponds to the exponential term. Since the number of events is constant, the factor $N!$ in the likelihood function has been dropped. Due to the third term for the minimal NLL the weight function fulfills $w(\vec{\Omega}_j, \vec{\theta}) \approx M$, so that the second and the third term will vanish upon successful minimization.

6.6 Selection of Hypotheses

Usually there is a number of alternative models available and in order to make valid inference from data, the crucial question is which is the best model to describe the data. Following the principle of parsimony, the model which describes the data best with the least number of parameters should be favored. The question of the best model can thus be pinned down to the question on how to weigh the fit quality against the number of fitted parameters.

In particle physics the likelihood ratio test is quite popular. The ratio of the maximized likelihoods is the test statistic, so if its distribution is known for the null hypothesis, the p value for the obtained ratio can be determined. Luckily the elaborate determination of that distribution can be skipped, since two times the negative logarithm of the ratio corresponds approximately to a χ^2 distribution according to Wilks theorem [57]. It should only be used for nested hypotheses, that is if the null hypothesis is a special case of the other one by fixing some parameters e.g. to zero. The different considered hypotheses must then be tested with strictly increasing or decreasing complexity.

Akaike proposed to base model selection on the Kullback-Leibler information. The Kullback-Leibler information

$$I(f,g) = \int f(x) \log \left(\frac{f(x)}{g(x|\theta)} \right) dx$$

denotes the information that is lost, when model g is used to approximate model f . It can also be interpreted as the distance between the two models. To calculate the Kullback-Leibler distance between two models actually these models and their parameters must be known. Akaike showed that the distance of a chosen model to the underlying true model, which generated the data, can be estimated based on the empirical log-likelihood function at its maximum point. [57]

After figuring out that the maximized log-likelihood is biased upward as an estimator of the true underlying model approximately as much as the amount k of estimated parameters for the according model, he proposed the information criterion

$$\text{AIC} = -2 \ln(\mathcal{L}(\theta|y)) + 2k, \quad (6.18)$$

where the factor of -2 is chosen, because of its meaning for the likelihood ratio tests [57]. Since not the akaike information criterion (AIC) value itself, but rather the difference between the AIC values of two models is pertinent, any other constant global factor or offset would not change the outcome. A smaller AIC value means, that a model is closer to the underlying reality that generated the data. In contrast to model tests, AIC can also be used to compare different kind of models, which do not need to be nested. [57]

All statements made about properties of the AIC are based on the assumption, that the data set is fixed. Models that are fitted to different data, and if it is just a subset, should not be compared by the AIC or any other information criterion [57].

The Bayesian Information Criterion is defined as

$$\text{BIC} = -2 \ln(\mathcal{L}(\vec{\theta}|\vec{y})) + k \ln(N), \quad (6.19)$$

where N denotes the size of the considered data sample. Even though it looks quite similar to AIC, bayesian information criterion (BIC) is no estimator of the Kullback-Leibler

distance. It has been derived by Schwarz in a Bayesian context, assuming equal prior probability for each model and very vague priors on the parameters, given the model [57]. As a dimension consistent criterion it provides that the probability to choose the true model with increasing sample size approaches 1. Obviously this property is based on the assumption, that there does not only exist a true model with fixed low k , which generates the data, but that it actually is contained in the set of tested models.

In short AIC chooses the best hypothesis, which might differ with the sample size, whereas BIC chooses the true hypothesis, if the sample size is large enough. Where for the AIC the term $+2K$ has the purpose to obtain a good estimator for the relative Kullback-Leibler distance, the $+k \cdot \ln(N)$ term of BIC fulfills merely the purpose of a penalty term for too complex hypotheses. Consequently the trade off between a simple model and a good description of the data is answered differently: BIC favors rather hypotheses with fewer parameters compared to AIC. In the cases where AIC and BIC favor different hypotheses as a compromise between overfitting and underfitting the difference in the sum $BIC+AIC$ is used to select a hypothesis in the presented analysis.

6.7 Analysis Software Package PAWIAN

The software package PAWIAN is developed at the Institut für Experimentalphysik I of Ruhr-Universität Bochum to provide a generic software package, which supports all the physics that can be studied in proton-antiproton annihilations with the PANDA experiment but also reactions of other hadron physics experiments [52].

PAWIAN is programmed object oriented in C++ and has only few dependencies, namely the C++ Boost libraries for different functionalities as serialization and network communication, the package qft++ for the evaluation of e.g. Clebsch-Gordan coefficients and Wigner-D-matrices, the minimizer Minuit2 [58], the package log4cpp for thread secure output during runtime, and the analysis framework ROOT for the generation of plots.

The operation is controlled user friendly by means of a configuration file, so that no programming knowledge is needed. Different spin formalisms like the canonical formalism, the helicity formalism or the Rarita-Schwinger tensor formalism are available and can be selected by key words in the configuration file. Also different dynamical parameterizations as Breit-Wigner, Flatté and K -matrix can be chosen individually for each contribution. In case of coupled channel analyses one configuration file per channel and a global configuration file are used. The details of a K -matrix are also put in an individual file. PAWIAN can generate a file with start parameters from the configuration files and saves the parameters obtained by the minimization of the unbinned negative log-likelihood periodically. Based on these results further steps as the generation of plots or a scan of the complex energy plane can be taken.

Numerous partial wave analyses have already been performed with PAWIAN, many of which in the scope of Ph.D. theses at the Institut für Experimentalphysik I based on BESIII data [59, 60, 24, 61, 62, 21, 63] or Crystal Barrel at low energy antiproton ring (LEAR) data [42], but an increasing number of external users utilize PAWIAN for partial wave analysis, too. Besides the production of resonances in electron-positron annihilations also proton-antiproton annihilation and two-photon fusion are supported by PAWIAN.

7 Partial Wave Analysis Results

The analysis results presented in this section are obtained from a partial wave analysis utilizing an iterative approach for hypothesis testing. Starting with a base hypothesis in each iteration step new hypotheses are formed by extending the base hypothesis by each considered contribution. In each iteration step the hypothesis, for which the sum of AIC and BIC value decreased most significantly compared to the current base hypothesis, is chosen as the new base hypothesis of the next step of the iteration.

In this analysis the initial base hypothesis consists of the $(\pi\pi)_S$ wave contribution parameterized by a K -matrix with 5 poles and 5 channels and the corresponding P -vector as described in subsection 6.4.7, as well as the $f'_2(1525)$ contribution parameterized with relativistic Breit-Wigner function including Blatt-Weisskopf barrier factors. All parameters of the K -matrix except for the coupling strength of the individual poles are fixed to the values given in reference [46] and also the mass and width parameters of the $f'_2(1525)$ are fixed to the values given in table 7.1.

Especially in the first steps of the iteration, when no comprehensive description of the data is available yet, one cannot just add a resonance with certain quantum numbers with free parameters for mass and width and expect the fit to provide reasonable results. Typically, unphysically broad contributions are obtained, since this way the description can be improved almost everywhere. At first it should thus be tested, if known resonances can significantly improve the data description with resonance parameters corresponding to the world average.

All 33 resonances listed in the Review of Particle Physics [1] with appropriate quantum numbers were considered, including those listed as “further states”. Table 7.1 and 7.2 list all these resonances with their mass and width values and the known branching fractions. For the $f_2(1270)$ and the $f'_2(1525)$ resonances the branching fractions which are relevant for this analysis are known so that the fractional yield to be expected can be roughly estimated as 0.2% and 15% of the selected events, respectively. The dynamics of all these listed resonances are parameterized by relativistic Breit-Wigner functions including Blatt-Weisskopf barrier factors. Furthermore also a contribution without dynamics is considered, which is in the following referred to as phase space distributed contribution. For the first iteration steps the mass and width values of all resonances are fixed to the values given in table 7.1 and 7.2, later on the mass and width parameters are released in the fit, also for the $f'_2(1525)$.

Eventually, a K -matrix parameterization is utilized for the f_2 contributions and fitted to the data selected for this analysis in a coupled channel approach together with various data sets from other experiments giving access to relevant properties of two-body scattering processes.

As motivated in section 6.6, the sum of the information criteria BIC+AIC is used to evaluate, whether a hypothesis is significantly better than another one. A detailed overview of the number of free parameters, NLL, BIC, AIC, BIC+AIC and $\Delta\text{BIC}+\Delta\text{AIC}$ values for all tested hypotheses can be found in the appendix A for each iteration.

J^{PC}	Name	Mass [MeV]	Width [MeV]	PDG Mass [MeV]	PDG Width [MeV]	$\mathcal{B}(J/\psi \rightarrow \phi X)$	$\mathcal{B}(X \rightarrow \eta\eta)$
2^{++}	$f_2(1270)$	1275	185	1275.5 ± 0.8	$186.7^{+2.2}_{-2.5}$	$(3.2 \pm 0.6) \cdot 10^{-4}$	$(4.0 \pm 0.8) \cdot 10^{-3}$
	$f_2(1430)$	1430	300	1430	13-150	—	—
	$f_2'(1525)$	1525	76	$1521.9^{+1.8}_{-1.5}$	$81.4^{+2.4}_{-2.0}$	$(8 \pm 4) \cdot 10^{-4}$	$(10.4 \pm 2.2)\%$
	$f_2(1565)$	1565	134	1562 ± 13	134 ± 8	—	seen
	$f_2(1640)$	1639	99	1639 ± 6	99^{+60}_{-40}	—	—
	$f_2(1810)$	1810	300	1815 ± 12	197 ± 22	—	seen
	$f_2(1910)$	1941	170	1934 ± 16	141 ± 40	—	seen
	$f_2(1950)$	1944	472	1944 ± 12	472 ± 18	—	seen
	$f_2'(2010)$	2011	202	2011^{+60}_{-80}	202 ± 60	—	—
4^{++}	$f_4(2050)$	2044	208	2018 ± 11	237 ± 18	—	$(2.1 \pm 0.8) \cdot 10^{-3}$

Table 7.1: Intermediate resonances considered for the decay $J/\psi \rightarrow \phi X, X \rightarrow \eta\eta$ with quantum numbers other than 0^{++} with the mass and width values used for fitting, the mass and width values and the branching fractions as stated by the PDG [1]

J^{PC}	Name	Mass [MeV]	Width [MeV]	PDG Mass [MeV]	PDG Width [MeV]	$\mathcal{B}(J/\psi \rightarrow \eta Y)$	$\mathcal{B}(Y \rightarrow \phi\eta)$
1^{--}	$X(1575)$	*	1576	818	1576^{+49+98}_{-55-91}	$818^{+22+64}_{-23-133}$	—
	$\phi(1680)$		1680	150	1680 ± 20	150 ± 50	—
	$\omega(1650)$		1670	315	1670 ± 30	315 ± 35	—
	$X(1750)$	*	1753	122	$1753.5 \pm 1.5 \pm 2.3$	$122.2 \pm 6.2 \pm 8.0$	—
	$\omega(1960)$	*	1960	195	1960 ± 25	195 ± 60	—
	$\phi(2170)$		2189	79	2188 ± 10	83 ± 12	—
	$\omega(2205)$	*	2205	350	2205 ± 30	350 ± 90	—
	$\omega(2290)$	*	2290	275	2290 ± 20	275 ± 35	—
	$\omega(2330)$	*	2330	435	2330 ± 30	435 ± 75	—
2^{--}	$\omega_2(1975)$	*	1975	175	1975 ± 20	175 ± 25	—
	$\omega_2(2195)$	*	2195	225	2195 ± 30	225 ± 40	—
3^{--}	$\omega_3(1670)$		1668	173	1667 ± 4	168 ± 10	—
	$\phi_3(1850)$		1854	87	1854 ± 7	87^{+28}_{-23}	—
	$\omega_3(1945)$	*	1945	115	1945 ± 20	115 ± 22	—
	$\omega_3(2255)$	*	2255	175	2255 ± 15	175 ± 30	—
	$\omega_3(2285)$	*	2285	230	2285 ± 60	230 ± 40	—
4^{--}	$\omega_4(2250)$	*	2250	150	2250 ± 30	150 ± 50	—
5^{--}	$\omega_5(2250)$	*	2250	320	2250 ± 70	320 ± 95	—
1^{+-}	$h_1(1595)$		1594	384	1594^{+18}_{-60}	384^{+90}_{-120}	—
	$h_1(1965)$	*	1965	345	1965 ± 45	345 ± 75	—
	$h_1(2215)$	*	2215	325	2215 ± 40	325 ± 55	—
3^{+-}	$h_3(2025)$	*	2025	145	2025 ± 20	145 ± 30	—
	$h_3(2275)$	*	2275	190	2275 ± 25	190 ± 45	—

Table 7.2: Intermediate resonances considered for the decay $J/\psi \rightarrow \eta Y, Y \rightarrow \phi\eta$ with the mass and width values used for fitting, the mass and width values and the branching fractions as stated by the PDG [1]; resonances listed as “further states” [64] are marked with *

7.1 Systematic Survey for Contributing Resonances

Following an iterative approach, the best hypothesis of the previous iteration step is the base hypothesis of the next iteration step to which all other hypotheses are compared to. Table 7.3 shows the difference between the BIC+AIC value of the respective base hypothesis and the best as well as second best hypotheses

$$\Delta\text{BIC} + \Delta\text{AIC} = \left(\text{BIC}^{\text{base}} - \text{BIC}\right) + \left(\text{AIC}^{\text{base}} - \text{AIC}\right)$$

for each iteration step, since absolute values of BIC or AIC are irrelevant, but only the difference between the values need to be compared. Positive $\Delta\text{BIC}+\Delta\text{AIC}$ values correspond to an improved description compared to the base hypothesis.

For the first two iteration steps one hypothesis yields the best results for all criteria (cf. tables A.1 and A.2). In the first step all hypotheses with additional f_2 resonances at higher masses yield similarly good results, all using 43 free parameters to describe the data. The hypothesis with an additional $f_2(1810)$ contribution yields the best result, closely followed by the hypothesis with an additional $f_2(1950)$ resonance. In the next iteration step the hypothesis with an additional $\omega_2(1975)$ resonance yields by far the most significantly improved values for all information criteria. The second best hypothesis with an additional $\omega_2(2195)$ has the same quantum numbers and thus describes the data also with 49 free parameters, but provides a more than 200 counts lower $\Delta\text{BIC}+\Delta\text{AIC}$ value.

In the third iteration step, on the one hand the hypothesis with an additional $f_4(2050)$ resonance yields the most negative NLL value, but on the other hand the hypothesis with an additional $\phi(1680)$ resonance yields the best values for all other criteria (cf. table A.3). The reason for the worse significance is that the hypothesis with the additional $f_4(2050)$ has eight free parameters more. The $\phi(1680)$ resonance is therefore considered to yield the most significant improvement and is added to the base hypothesis for the next iteration step. The hypothesis with an additional $X(1750)$, which has also the same quantum numbers as the $\phi(1680)$ resonance, provides the second largest but significantly lower $\Delta\text{BIC}+\Delta\text{AIC}$ value.

In the fourth iteration step the evaluation gets more complicated as shown in table A.4. Again the hypothesis with the additional $f_4(2050)$ yields the most negative NLL value

Iteration	Best Hypothesis of Iteration	n_{free}	$\Delta\text{BIC}+\Delta\text{AIC}$	2 nd Best Hypothesis	n_{free}	$\Delta\text{BIC}+\Delta\text{AIC}$
0	$(\pi\pi)_S + f_2'(1525)$	33	—	—	—	—
1	$\dots + f_2(1810)$	43	670.66	$\dots + f_2(1950)$	43	664.44
2	$\dots + \omega_2(1975)$	49	319.81	$\dots + \omega_2(2195)$	49	112.79
3	$\dots + \phi(1680)$	51	190.11	$\dots + X(1750)$	51	159.23
(a)	optimized mass+width	51	73.22	—	—	—
(b)	$\dots + h_1(2215)$	57	42.73	phase space	52	25.24

Table 7.3: Fit results of base hypothesis and the best hypotheses of each of the first three iteration steps with mass and width values of all resonances fixed according to tables 7.1 and 7.2 as well as of the iteration steps with optimized mass and width values according to tables 7.4 and 7.5

Contribution	Mass [MeV]	Deviation from PDG [σ]	Width [MeV]	Deviation from PDG [σ]
$f'_2(1525)$	1528 ± 2	2.3	88 ± 4	1.4
$\omega_2(1975)$	1945 ± 9	-1.4	184 ± 20	0.3
$\phi(1680)$	1709 ± 6	1.4	133 ± 17	-0.3

Table 7.4: Fit results of free mass and width values with statistical uncertainties for the hypothesis $(\pi\pi)_S$ -wave, $f'_2(1525)$, $f_2(1810)$, $\omega_2(1975)$, and $\phi(1680)$

and also the most negative AIC value, but just adding phase space distributed background yields the most negative BIC value and also the most negative value for the sum BIC+AIC. Besides the hypothesis with additional phase space distributed contribution, the five hypotheses with an additional $f_4(2050)$, $h_1(2215)$, $\phi_3(1850)$, $\omega_3(2255)$ or $\omega_3(2285)$, respectively, yield a positive $\Delta\text{BIC}+\Delta\text{AIC}$ value.

Taking the ambiguity as a sign, that a quite comprehensive description of the data has already been achieved, the mass and width parameters of the resonances parameterized with a relativistic Breit-Wigner function, namely $f'_2(1525)$, $\omega_2(1975)$ and $\phi(1680)$, except for the $f_2(1810)$, were released. The $f_2(1810)$ does not correspond to a clearly visible peak, but to a rather broad structure so that releasing its mass and width parameters would just result into an unphysically broad resonance. The resulting mass and width values are shown with their respective statistical uncertainty in table 7.4.

For a comparison with the mass and width values from the PDG [1] listed in table 7.1 and table 7.2, the difference of the values is normalized to multiples of σ , which is estimated by the squared sum of the respective uncertainties yielding the deviation definitions

$$\delta_{\text{PDG}}m = \frac{m^{\text{fit}} - m^{\text{PDG}}}{\sqrt{(\Delta m^{\text{fit}})^2 + (\Delta m^{\text{PDG}})^2}} \quad \text{and} \quad \delta_{\text{PDG}}\Gamma = \frac{\Gamma^{\text{fit}} - \Gamma^{\text{PDG}}}{\sqrt{(\Delta \Gamma^{\text{fit}})^2 + (\Delta \Gamma^{\text{PDG}})^2}},$$

respectively. For a Gaussian distribution with a standard deviation of σ , about 68% of the area is contained within a 1σ range of the mean, about 95% in a 2σ range, and about 99.7% in a 3σ range, which demonstrates how likely it is to observe a certain extent of deviation. The PDG determines averages and uncertainties for all reliable measurements of a quantity, which might be precise but contradictory so that a huge error is obtained. Since the obtained mass and width values are just intermediate results, only the statistical but not the systematical uncertainties are determined, the deviations should thus not be taken too seriously.

All mass and width values listed in table 7.4 agree well with the values provided by the PDG. The mass and width values of the $f'_2(1535)$ show the largest relative deviations, but these are also determined with the highest precision.

The hypothesis is used as a new base hypothesis and all hypotheses with an additional contribution, which yield a decreased sum of BIC and AIC value in the fourth iteration, are tested. Table A.5 shows the results for all tested hypotheses. Again the hypothesis with an additional $f_4(2050)$ provides the best NLL and AIC values, respectively, whereas the hypothesis with phase space distributed background yields the most negative BIC and BIC+AIC values and thus the largest difference to the base hypothesis.

For the resonances, which yielded a positive $\Delta\text{BIC}+\Delta\text{AIC}$ value in the fourth iteration step, it is also tested if the fit result can be improved by letting mass and width parameters

Contribution	Mass [MeV]	Deviation from PDG [σ]	Width [MeV]	Deviation from PDG [σ]
$f_2'(1525)$	1528 ± 2	2.3	83 ± 4	0.3
$\omega_2(1975)$	1956 ± 8	-0.9	172 ± 18	-0.1
$\phi(1680)$	1706 ± 7	1.2	112 ± 17	-0.7
$h_1(2215)$	2117 ± 11	-2.4	116 ± 18	-3.6

Table 7.5: Fit results of free mass and width values with statistical uncertainties for the hypothesis $(\pi\pi)_S$ -wave, $f_2'(1525)$, $f_2(1810)$, $\omega_2(1975)$, $\phi(1680)$, and $h_1(2215)$

of the respective additional contribution free, but keeping the mass and width parameters for the other contributions fixed to the values given in table 7.4. The mass and width values for all additional contributions are shown in table A.7 and the corresponding fit results are shown in table A.6. For most of these resonances the width value just increased until it reached the boundary set in the fit, only for the $h_1(2215)$ resonance and the $\phi_3(1850)$ reasonable mass and width values could be obtained. Thus for the hypothesis consisting of the contributions $(\pi\pi)_S$, $f_2'(1525)$, $f_2(1810)$, $\omega_2(1975)$, $\phi(1680)$, and $h_1(2215)$ the mass and width parameters of all resonances except for the $f_2(1810)$ were released simultaneously. The obtained mass and width values of this fit are shown in table 7.5 and the fit results are shown in table 7.3 in comparison to the hypotheses without the $h_1(2215)$. Compared to the mass and width values obtained without the $h_1(2215)$ contribution all width values are decreased and the mass values are changed slightly. The agreement with the values given by the PDG [1] is improved for most values. For the $h_1(2215)$ resonance the obtained mass is about $100 \text{ MeV}/c^2$ lower than the value provided by the PDG and also the width is even more significantly smaller.

Figures 7.1 and 7.2 show the invariant mass distributions of the individual contributions of the best hypothesis for each iteration step. Correspondingly figure 7.3 shows the Dalitz plots obtained from fits of the base hypothesis and the best hypotheses of iterations 4 and (b) and of the selected recorded data for comparison. Already the base hypothesis provides a quite good description of the data.

It might be helpful for the interpretation to also know the Dalitz plot distributions for the individual contributions, these are shown in figure 7.4. Due to the symmetry induced by two identical η mesons in the final state, an intermediate resonance decaying to a ϕ and an η meson shows up as a horizontal and a vertical band in the $m_{\phi\eta}^2$ vs. $m_{\phi\eta}^2$ Dalitz plot. Consequently, two bumps appear in the invariant $\phi\eta$ mass distribution for each such resonance, a narrow one and a broad one. An intermediate resonance decaying to a pair of η mesons results in a slanted band in the $m_{\phi\eta}^2$ vs. $m_{\phi\eta}^2$ Dalitz plot. Structures along the band are caused by the spin properties of the respective intermediate resonance.

Table 7.6 summarizes the fit fractions of the individual contributions for each hypothesis. Since the $(\pi\pi)_S$ wave contribution spans over the full $\eta\eta$ invariant mass range, it is to be expected, that its fit fraction decreases with any added resonance. For narrow resonances like the $f_2'(1525)$, the fit fraction is not expected to change significantly due to a resonance added in another region of the phase space. For most of the hypotheses the fit fraction of the $f_2'(1525)$ resonance is about 27%, but for the iteration steps 2 and (b) it amounts to only about 21%. For some hypothesis the fit might have converged in a local minimum instead of the global minimum. In the invariant $\eta\eta$ mass distribution of the iteration

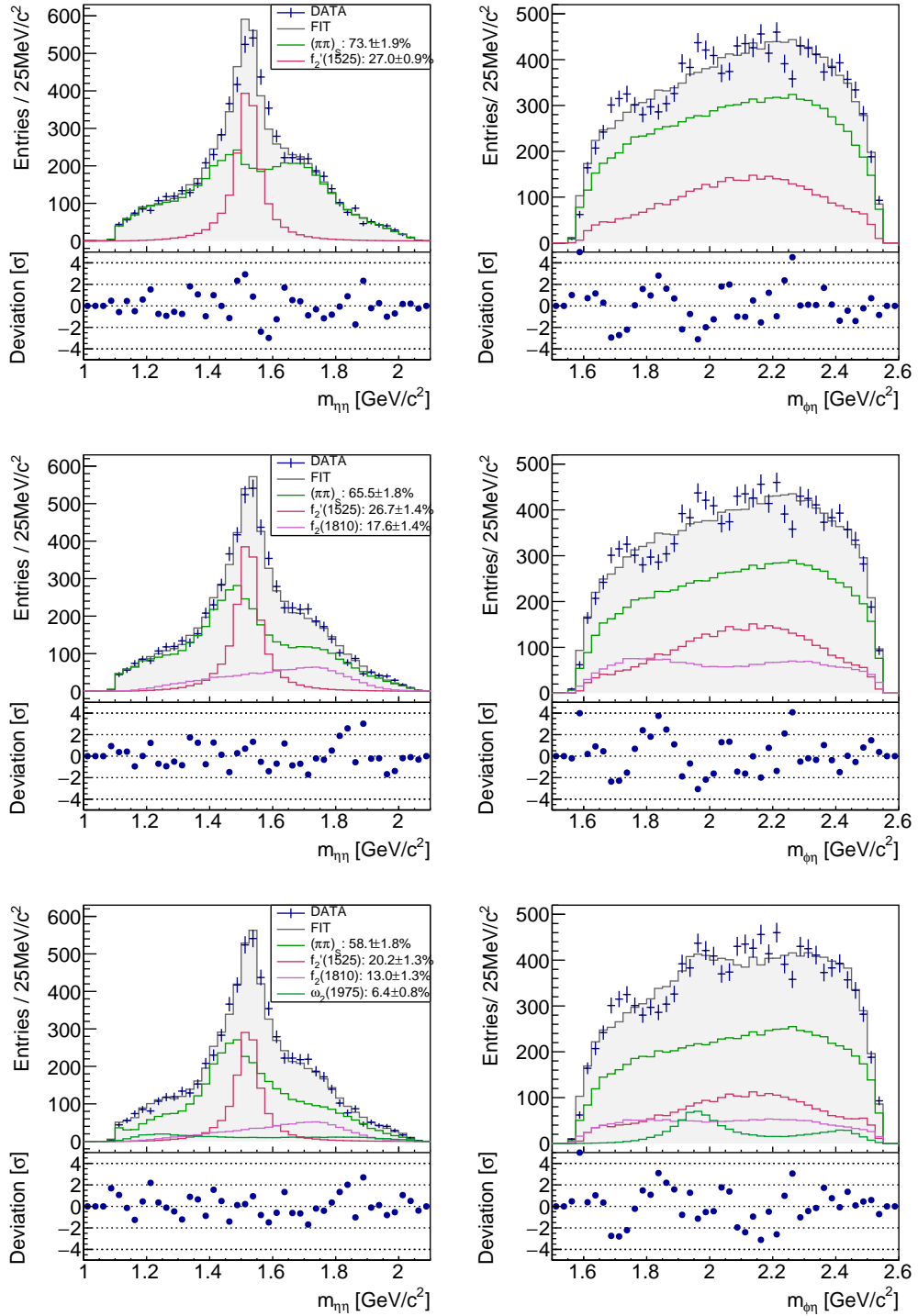


Figure 7.1: Invariant $\eta\eta$ and $\phi\eta$ mass distributions with the individual contributions of the initial base hypothesis (top row) with an additional $f_2(1810)$ (mid row) and an additional $\omega_2(1975)$ resonance (bottom row)

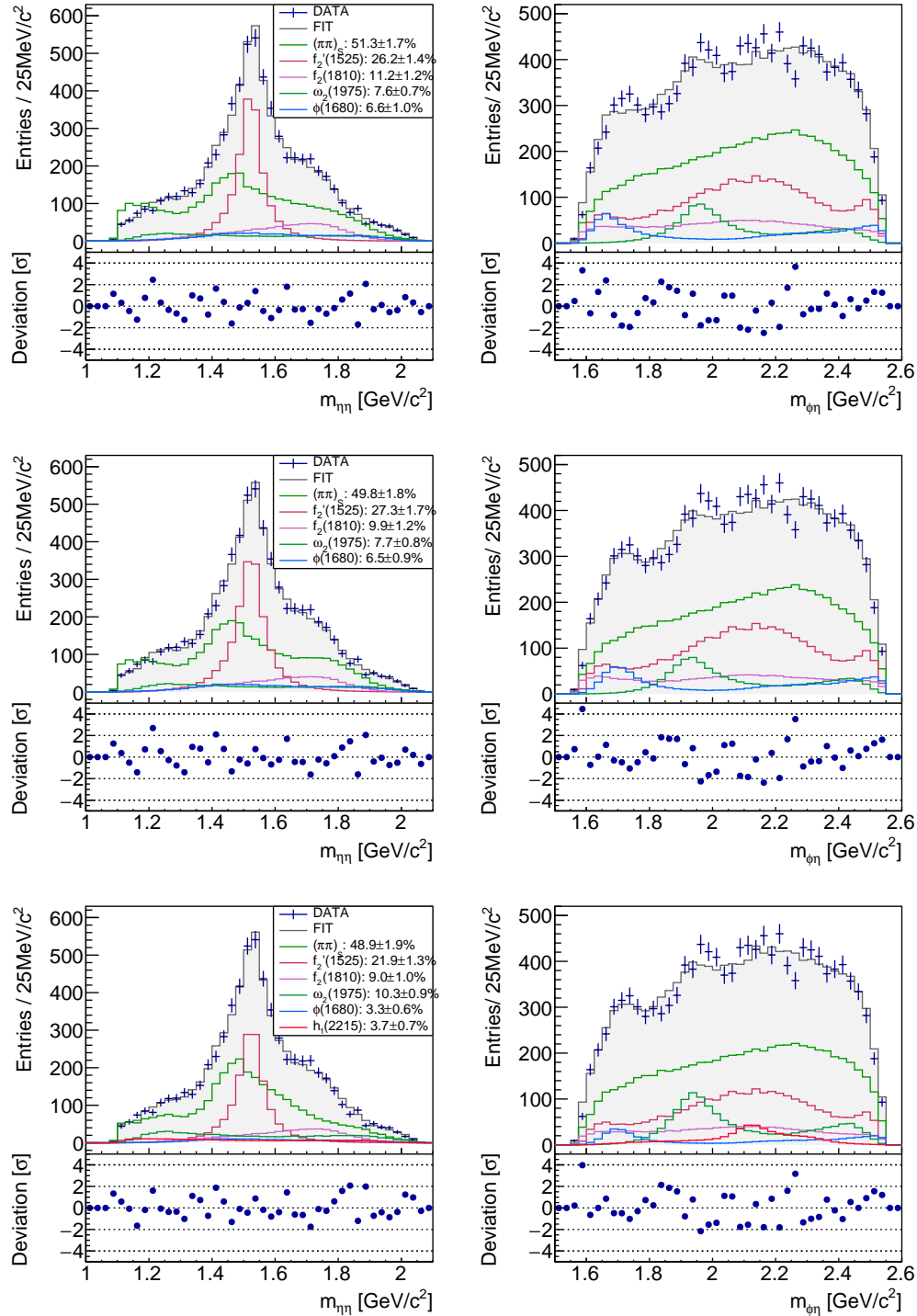


Figure 7.2: Invariant $\eta\eta$ and $\phi\eta$ mass distributions with the individual contributions of the hypothesis $(\pi\pi)_S$, $f_2'(1525)$, $f_2(1810)$, $\omega_2(1975)$ and $\phi(1680)$ with masses and widths as given in tables 7.1 and 7.2 (top row) and masses and widths optimized as given in table 7.4 (mid row) and an additional $h_1(2215)$ resonance and masses and widths optimized as given in table 7.5 (bottom row)

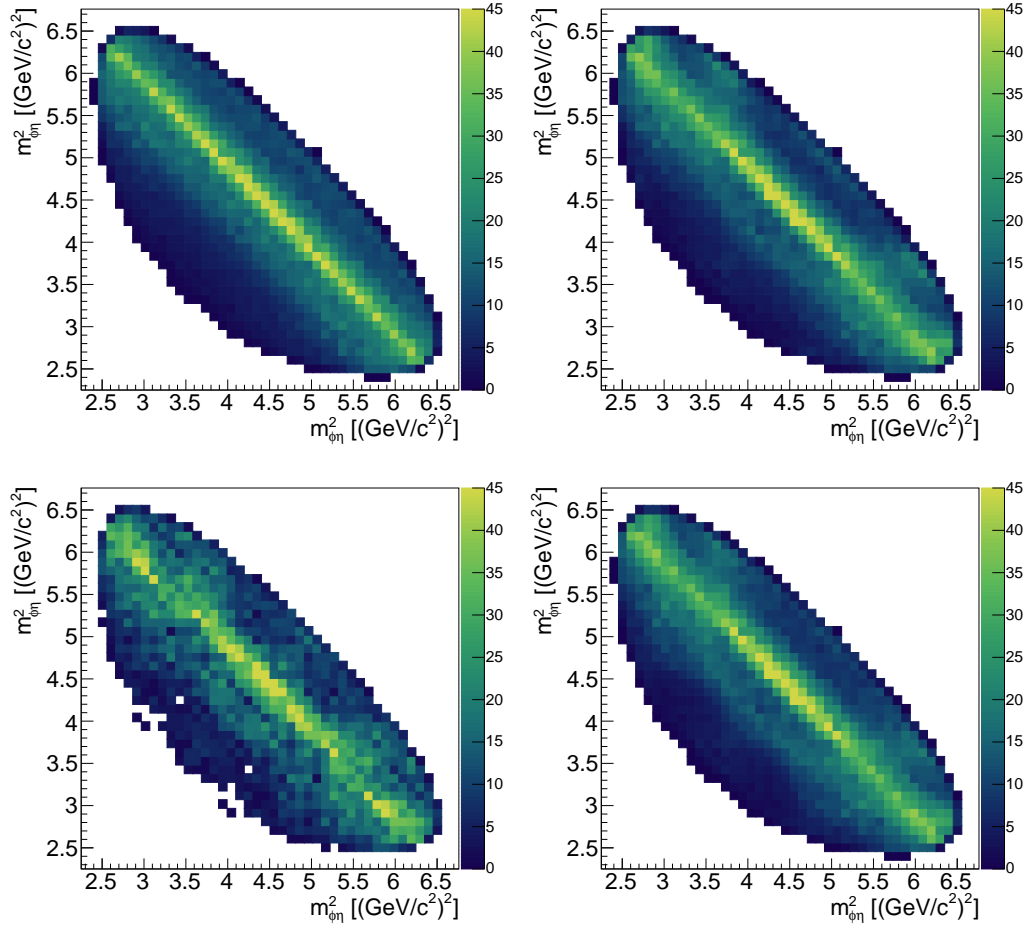


Figure 7.3: Dalitz plots of the recorded data sample (bottom left) and obtained by fits of the initial base hypothesis (0: top left) with additional $f_2(1810)$, $\omega_2(1975)$, and $\phi(1680)$ resonances with mass and width values as given in tables 7.1 and 7.2 (3: top right) and an additional $h_1(2215)$ resonance with mass and width parameters of all resonances optimized to the values given in table 7.5 (b: bottom right)

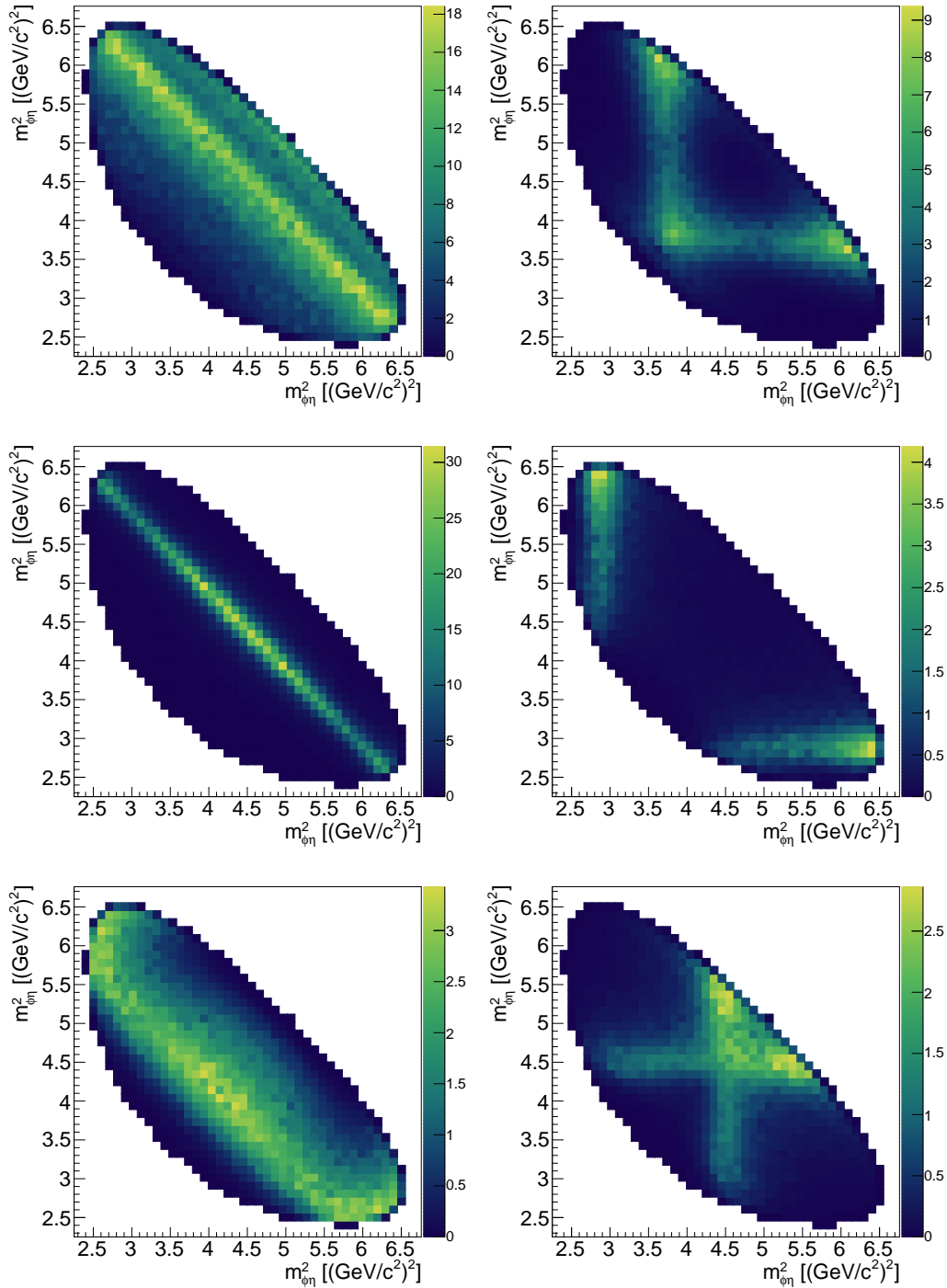


Figure 7.4: Dalitz plots of the $(\pi\pi)_S$ (top, left), $f_2'(1525)$ (center, left) and $f_2(1810)$ (bottom, left), $\omega_2(1975)$ (top, right), $\phi(1680)$ (center, right) and $h_1(2215)$ (bottom, right) contributions of the hypothesis containing $(\pi\pi)_S$ -wave, $f_2'(1525)$, $2_2(1810)$, $\omega_2(1975)$, $\phi(1680)$ and $h_1(2215)$ contributions with mass and width values as given in table 7.5

Iteration	Fit Fraction [%]						Sum
	$(\pi\pi)_S$	$f'_2(1525)$	$f_2(1810)$	$\omega_2(1975)$	$\phi(1680)$	$h_1(2215)$	
0	73.1 ± 1.9	27.0 ± 0.9	————	————	————	————	100.1 ± 2.3
1	65.5 ± 1.8	26.7 ± 1.4	17.6 ± 1.4	————	————	————	109.8 ± 3.3
2	58.1 ± 1.8	20.2 ± 1.3	13.0 ± 1.3	6.4 ± 0.8	————	————	97.7 ± 3.3
3	51.3 ± 1.7	26.2 ± 1.4	11.2 ± 1.2	7.6 ± 0.7	6.6 ± 1.0	————	102.9 ± 3.3
(a)	49.8 ± 1.8	27.3 ± 1.7	9.9 ± 1.2	7.7 ± 0.8	6.5 ± 0.9	————	101.3 ± 3.7
(b)	48.9 ± 1.9	21.9 ± 1.3	9.0 ± 1.0	10.3 ± 0.9	3.3 ± 0.6	3.7 ± 0.7	97.1 ± 3.3

Table 7.6: Fit fractions of the individual contributions and their sum with statistical uncertainties

steps 3 and (a) the contribution of the $(\pi\pi)_S$ wave exceeds the total fit yield, which is a clear indication for destructive interference, most probably with the $\phi(1680)$ resonance. Adding the $h_1(2215)$ resonance in the last iteration step significantly increases the fit fraction of the $\omega_2(1975)$ resonance, whereas the fit fraction of the $\phi(1680)$ resonance is decreased to 3.3%, so that the fraction of the $h_1(2215)$ resonance is actually larger with 3.7%. The destructive interference between the $(\pi\pi)_S$ wave and the $\phi(1680)$ resonance thereby vanishes.

Since there is still a visible discrepancy between fit and data in the region around 2.1 GeV in the invariant $\phi\eta$ mass distribution, as a next step contributions with all allowed quantum numbers and with a mass of 2.1 GeV have been tested. At first, fits with fixed mass and a width of just 0.1 GeV were performed, then successively mass and width were released. It turned out that different contributions are favored depending on the width of the $f_2(1810)$, so that no reliable conclusion can be drawn. Thus a better description of the 2^{++} contributions is needed before it is reasonable to test further contributions.

7.2 K -Matrix Description for 2^{++} Contributions

In order to take threshold effects and unitarity properly into account a K -matrix description for the dynamics of the f_2 contributions is used. Ideally, all possible decay channels to which the resonances couple significantly should be parameterized. In order to obtain physically meaningful results, properties for the $\pi\pi$ channel [65], the $\eta\eta$ [66, 67] and the $K\bar{K}$ [68] channel extracted from scattering data have been utilized to introduce additional constraints. Besides these four channels additionally an effective 4π channel is included in the K -matrix so that there are enough parameters available for compensation to ensure unitarity.

Using $\pi\pi$ scattering data the $f_2(1270)$ resonance must be included in the K -matrix, even though it does not seem to significantly contribute in the $J/\psi \rightarrow \phi X, X \rightarrow \eta\eta$ decay. The resonances $f'_2(1525)$ and $f_2(1810)$ should of course also be included, but it might be necessary to include even more resonances. Thus it was tested whether hypotheses with three, four or five poles yield the best results. In order to achieve fast convergence and reasonable results, the $(\pi\pi)_S$ -wave, $\omega_2(1975)$ and $\phi(1680)$ were included in all three hypotheses with all parameters fixed to the values obtained for the best fit of iteration step (a) (cf. table 7.3) with Breit-Wigner descriptions for the f_2 resonances at first.

In a second step the parameters of the $(\pi\pi)_S$ -wave and the Breit-Wigner resonances were released.

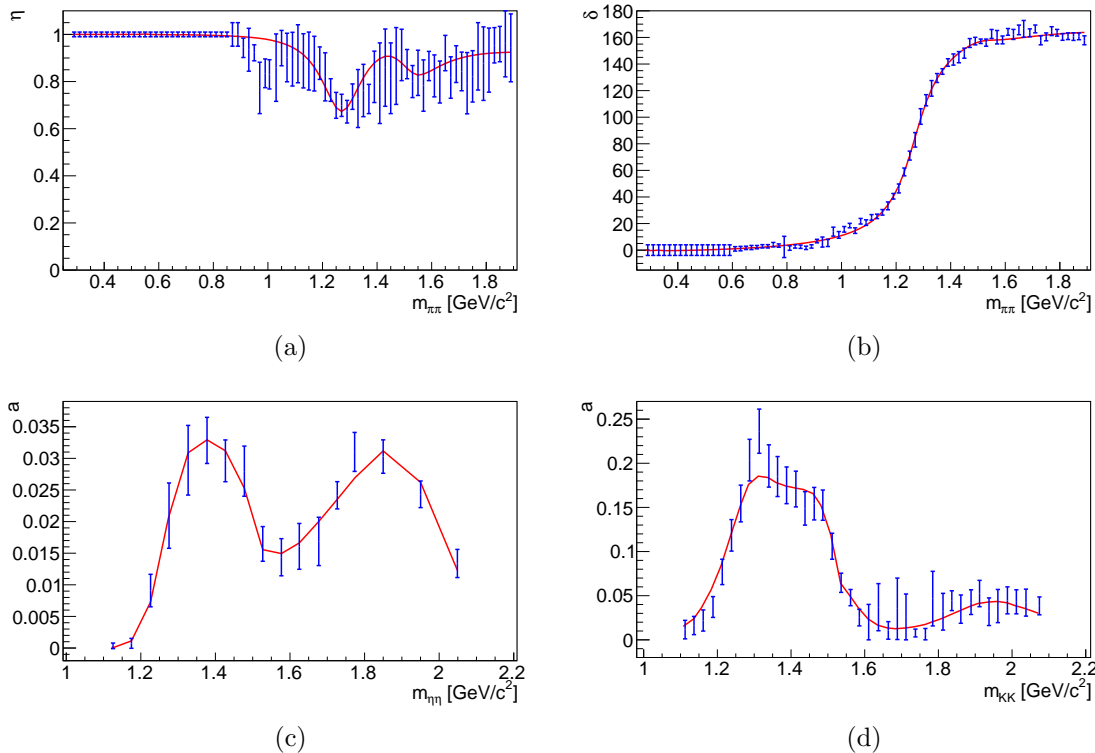


Figure 7.5: Elasticity (a) and phase shift (b) for the $\pi\pi$ channel [65] and amplitude related properties for the $\eta\eta$ [67] (c) and the $K\bar{K}$ [68] channel (d) obtained from scattering data (blue) and fit result of a 4-pole K -matrix with L and S dependent production amplitudes (red)

Considering the mass range from $2m_\eta \approx 1 \text{ GeV}/c^2$ to $m_{J/\psi} - m_\phi \approx 2 \text{ GeV}/c^2$, an individual P -vector for each LS -combination of the resonance production might be necessary, but that also leads to numerous additional free parameters. Thus for each considered number of poles it has also been tested, whether or not the available data provides sensitivity to the parameters of individual P -vectors for each possible angular momentum L or even for each possible LS combination of the resonance production.

The most negative BIC+AIC value is obtained by the fit with four poles and independent production amplitudes for both, L and S . Figure 7.5 shows a comparison between this fit result and the additionally used data.

Since the considered data set has changed by additionally using results from analysis of scattering data, the BIC and AIC values are no longer comparable with the values obtained from the fits to the J/ψ data set alone.

In tables A.8, A.9 and A.10 the results of all tested hypotheses are listed. For the K -matrices with three or five poles the best result is obtained when only L dependent production amplitudes are used.

After a reasonable K -matrix parameterization of the f_2 -contributions is found, meaningful testing of hypotheses with further contributions is now possible.

7.3 Continuation of the Systematic Survey for Contributions

Starting with the hypothesis consisting of $(\pi\pi)_S$ -wave, $\omega_2(1975)$, $\phi(1680)$, and the f_2 -matrix described above the iterative approach is continued. Since the f_2 contribution is already described by the K -matrix no further f_2 resonances are tested, but the $f_4(2050)$ and the remaining 22 intermediate resonances decaying to a ϕ and an η meson listed in table 7.2 are considered in each iteration step.

Before discussing additional contributions, it is interesting to compare the new base hypothesis to the results obtained, when using a Breit-Wigner function describe the dynamics of the f_2 resonances. Table 7.7 lists the obtained mass and width values for the poles of the f_2 -matrix as well as for resonances described by a Breit-Wigner function obtained for the new base hypothesis.

For both resonances described with Breit-Wigner dynamics mass values are increased compared to the values obtained for the best hypothesis of iteration step (a) (cf. table 7.4). The width value for the $\omega_2(1975)$ is decreased such that its distance from the value provided by the PDG is increased.

The pole parameters of the T -matrix corresponding to the K -matrix obtained by the fit are determined as described in subsection 6.4.6. As already indicated in subsection 6.4.2 the mass and width obtained for a pole of the T -matrix is not necessarily identical with the mass and width observable in a certain mass distribution.

The parameters obtained for the first pole of the f_2 -matrix, however, coincide nicely with the world average of the mass and width values of the $f_2(1270)$ determined in [1] and listed in table 7.1.

For the second and third pole with a mass slightly above $1500 \text{ MeV}/c^2$ the two resonances $f_2'(1525)$ and $f_2(1565)$ should both be considered. The mass value determined for the second pole matches well with the precisely known mass of the $f_2'(1525)$ resonance. The mass value determined for the third pole is somewhat smaller than the mass of the $f_2(1565)$ resonance, but still in good agreement considering the uncertainty is $\Delta m^{\text{PDG}} = 13 \text{ MeV}/c^2$ and thus one order of magnitude larger than for the $f_2'(1525)$ resonance.

Contribution	Mass [MeV]	Deviation from PDG [σ]	Width [MeV]	Deviation from PDG [σ]	Compared to
1 st f_2 pole	1268 ± 2	-3.5	185 ± 3	-0.4	$f_2(1270)$
2 nd f_2 pole	1519 ± 5	-0.6 -3.1	180 ± 8	11.8 4.1	$f_2'(1525)$ $f_2(1565)$
3 rd f_2 pole	1544 ± 5	4.2 -1.3	34 ± 16	-5.6 -2.9	$f_2'(1525)$ $f_2(1565)$
4 th f_2 pole	1904 ± 11	5.5 -1.5 -2.5	383 ± 14	7.1 5.7 -3.9	$f_2(1810)$ $f_2(1910)$ $f_2(1950)$
$\omega_2(1975)$	1961 ± 7	-0.7	155 ± 15	-0.7	$\omega_2(1975)$
$\phi(1680)$	1724 ± 7	2.1	135 ± 20	-0.3	$\phi(1680)$

Table 7.7: Fit results of free mass and width values with statistical uncertainties for the hypothesis $(\pi\pi)_S$ -wave, f_2 -matrix, $\omega_2(1975)$, and $\phi(1680)$

Iteration	Best Hypothesis of Iteration	n_{free}	$\Delta\text{BIC}+$ ΔAIC	2 nd Best Hypothesis	n_{free}	$\Delta\text{BIC}+$ ΔAIC
I	new base hypothesis	102	—	—	—	—
II	$\dots + h_1(195)$	110	4.57	$\dots + X(1575)$	106	-1.87

Table 7.8: Fit results of the new base hypothesis consisting of $(\pi\pi)_S$, $\omega_2(1975)$, $\phi(1680)$ contributions and an f_2 -matrix with 4 poles and LS dependent production amplitudes and the best hypotheses of the next iteration step with a K -matrix description of the f_2 contributions

The widths of the second and third pole on the other hand do not at all match with the respective resonances, they actually seem to be swapped. The width value for the second pole is even larger than the width of the $f_2(1565)$ and the width of the third pole even smaller than the width of the $f'_2(1525)$.

For the fourth pole it is difficult to decide which f_2 resonance it should be compared to, as $f_2(1810)$, $f_2(1910)$, and $f_2(1950)$ are all close by. The mass determined for the fourth pole fits best to the $f_2(1910)$, but the width of the $f_2(1910)$ is the smallest of these three resonances and the width determined for the fourth pole is more than twice as large, larger than the width of the $f_2(1810)$, but not as large as the width of the $f_2(1950)$.

In the next iteration step, the mass and width values of the additional resonances are fixed at first. Similar as in the fourth iteration step the hypothesis with the additional $f_4(2050)$ resonance yields the most negative NLL value and also the most negative AIC value. On the other hand the $\phi_3(1850)$ resonance is more significant according to the other information criteria. Table A.11 shows the fit result values for all tested hypotheses. Actually the hypothesis with the additional $h_1(2215)$ resonance yields a more negative NLL value compared to the hypothesis with the additional $\phi_3(1850)$ resonance, but with four free parameters more it cannot compete in terms of the BIC or AIC value.

The picture changes significantly, when mass and width values of the additional resonances are released. For most hypotheses the NLL increases by 2 or 3, but for the hypothesis with an additional $h_1(1965)$ resonance it increases by more than 17, so that the NLL, BIC, AIC, and consequently also the AIC+BIC value are each the most negative ones compared to all other hypotheses. Actually it is the only hypothesis, which yields a positive $\Delta\text{BIC}+\Delta\text{AIC}$ value, the second best hypothesis with an additional $X(1575)$ provides an $\Delta\text{BIC}+\Delta\text{AIC}$ value of -1.87 . Table 7.8 summarizes the obtained results of the first iteration step compared to the base hypothesis. The fit result values for all tested hypotheses are listed in table A.12.

Most of the 1^{--} resonances yield almost the same fit result values starting from the $\phi(2170)$ with the lowest mass up to the $\omega(2330)$ with the highest mass. In table A.13 the obtained mass and width values for the additional resonances are listed and indeed all those 1^{--} resonances with the same fit results reached the same values.

The mass obtained for the $h_1(1965)$ is larger than the value from the PDG [1] listed in table 7.2, but still in very good agreement due to the comparably large uncertainty of $\Delta m^{\text{PDG}} = 45 \text{ MeV}/c^2$. Even though the width value provided by the PDG for the $h_1(1965)$ resonance has a huge uncertainty, the width obtained by the fit is significantly smaller. The mass and width obtained for the $h_1(2215)$ resonance in best hypothesis of iteration step (b) is smaller than the nominal mass value. Nonetheless, there is still a

Contribution	Mass [MeV]	Deviation from PDG [σ]	Width [MeV]	Deviation from PDG [σ]	Compared to
1 st f_2 pole	1268 ± 2	-3.5	185 ± 3	-0.4	$f_2(1270)$
2 nd f_2 pole	1519 ± 4	-0.7 -3.2	184 ± 7	13.9 4.7	$f'_2(1525)$ $f_2(1565)$
3 rd f_2 pole	1542 ± 4	-1.3 4.8	37 ± 2	-5.6 -15.7	$f'_2(1525)$ $f_2(1565)$
4 th f_2 pole	1903 ± 11	5.4 -1.6 -2.5	385 ± 13	7.4 5.8 -3.9	$f_2(1810)$ $f_2(1910)$ $f_2(1950)$
$\omega_2(1975)$	1960 ± 7	-0.7	158 ± 16	-0.6	$\omega_2(1975)$
$\phi(1680)$	1726 ± 7	2.2	150 ± 21	0.0	$\phi(1680)$
$h_1(1965)$	1979 ± 8	0.3	59 ± 15	-3.7	$h_1(1965)$

Table 7.9: Fit results for free mass and width values with statistical uncertainties for the hypothesis $(\pi\pi)_S$ -wave, f_2 -matrix, $\omega_2(1975)$, $\phi(1680)$, and $h_1(1965)$

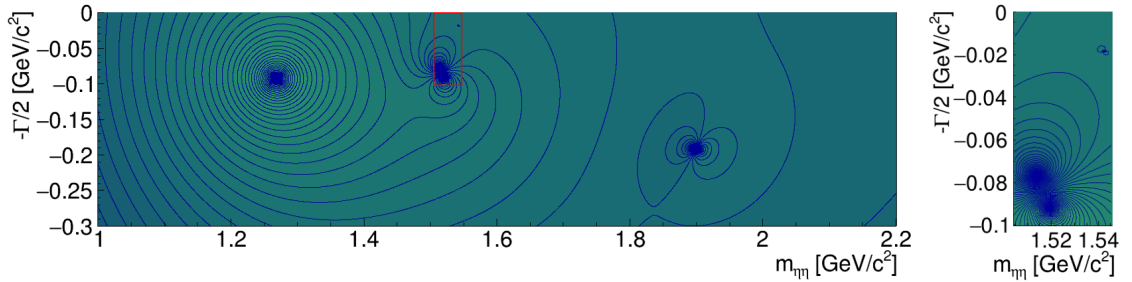


Figure 7.6: Complex energy plane with f_2 -matrix poles for the hypothesis $(\pi\pi)_S$, f_2 -matrix, $\omega_2(1975)$, $\phi(1680)$, and $h_1(1965)$ and zoomed section containing the second and third pole

discrepancy of almost $140 \text{ MeV}/c^2$ between the obtained mass value for that hypothesis and the mass obtained for the $h_1(1965)$. Besides that, also the width values differ by a factor of two. Compared to the current base hypothesis the mass and width values remain almost unchanged as shown in tables 7.7 and 7.9.

Figure 7.6 shows the poles of the f_2 -matrix in the complex energy plane. The third pole is hard to see, it appears just as a small dot above the second pole, so that a zoomed section is shown, too.

Expanding the base hypothesis by the $h_1(1965)$, all hypotheses with an additional contribution from table 7.2 and the $f_4(2050)$ are tested once more. The results of all these fits are displayed in table A.14. The mass and width of the resonances were released and the obtained values are shown in table A.15. Even two hypotheses with additional resonances with exotic quantum numbers were tested, but these do not yield a positive $\Delta\text{BIC}+\Delta\text{AIC}$ value. Of all tested hypotheses the one with an additional $\omega_5(2250)$ resonance is the only one, which significantly improves the description of the data. Again the hypothesis with the additional $f_4(2050)$ yields the most negative NLL, but for both hypotheses either the

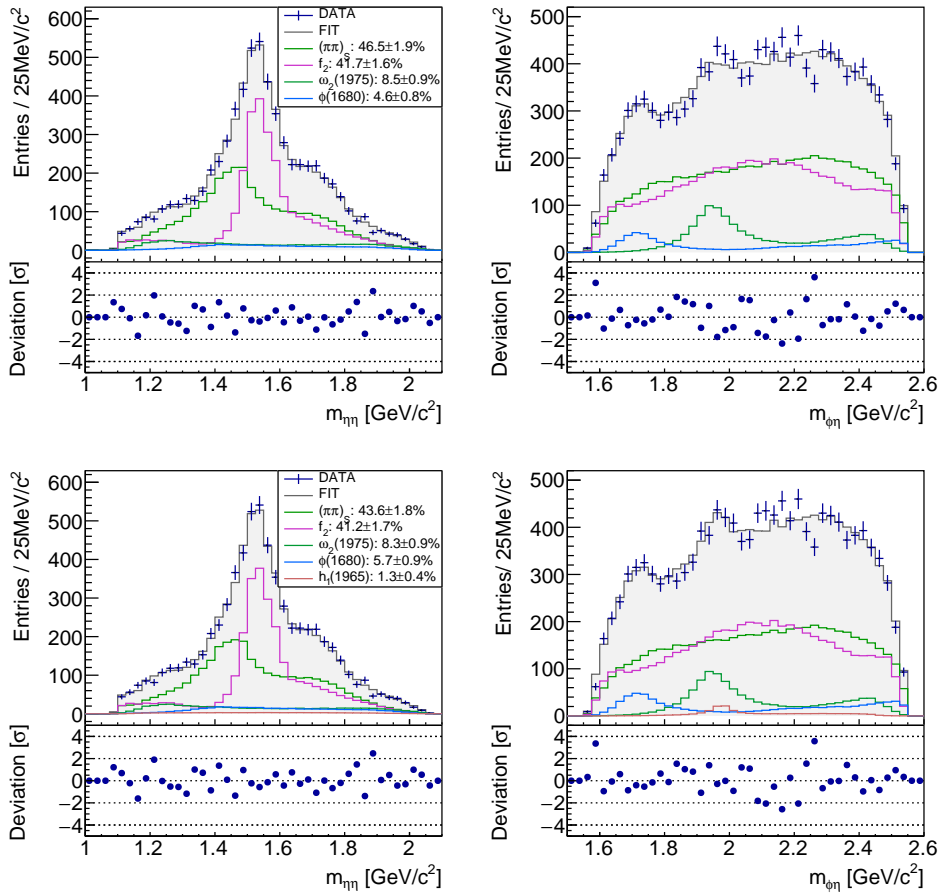


Figure 7.7: Invariant $\eta\eta$ and $\phi\eta$ mass distributions with the individual contributions of the hypothesis $(\pi\pi)_S$, f_2 -matrix, $\omega_2(1975)$ and $\phi(1680)$ with free masses and widths (top row), and with an additional $h_1(1965)$ (bottom row)

mass or the width value of the additional resonance reached the upper limit and is thus not considered to be reasonable.

As already stated for the previous iteration step, most of the hypotheses with additional 1^{--} resonances yield the same fit result, now even for the $\omega(1960)$, that means for start parameters in a range of over almost $400 \text{ MeV}/c^2$ the same mass of $2138 \text{ MeV}/c^2$ and width of $72 \text{ MeV}/c^2$ are obtained. Maybe the analysis of a sample with increased statistics would yield further insight into possible contributions, but for the selected data sample further contributions do not lead to a significant improvement, so the hypothesis consisting of $(\pi\pi)_S$, f_2 -matrix, $\omega_2(1975)$, $\phi(1680)$ and $h_1(2215)$ is the finally best hypothesis.

Figure 7.7 shows the invariant $\eta\eta$ and $\phi\eta$ mass distributions for the best hypotheses of the last two iteration steps.

As shown in table 7.10 the fraction of the $(\pi\pi)_S$ is decreased for the best hypothesis of iteration step I with a K -matrix description of the f_2 contributions compared to the best hypothesis obtained in iteration step (a) with a Breit-Wigner description of the f_2 resonances. The fraction of the $\omega_2(1975)$ resonance is increased, whereas the fraction of the $\phi(1680)$ resonance is decreased. Since it is technically quite challenging to extract the yield for individual poles, only the fit fraction of the combined yield of the f_2 contribution

Iteration	Fit Fraction [%]					
	$(\pi\pi)_S$	f_2 -Matrix	$\omega_2(1975)$	$\phi(1680)$	$h_1(1965)$	Sum
(a)	49.8 ± 1.8	37.2 ± 2.1	7.7 ± 0.8	6.5 ± 0.9	—————	101.2 ± 3.7
I	46.5 ± 1.9	41.7 ± 1.6	8.5 ± 0.9	4.6 ± 0.8	—————	101.3 ± 2.8
II	43.6 ± 1.8	41.2 ± 1.7	8.3 ± 0.9	5.7 ± 0.9	1.3 ± 0.4	100.1 ± 2.8

Table 7.10: Fit fractions of the individual contributions and their sum with statistical uncertainties

is determined [1]. The fraction of the f_2 -matrix is higher than the sum of the fractions of the $f'_2(1525)$ and $f_2(1810)$ resonances, as to be expected for an improved description of the f_2 contributions, which includes also non-resonant ‘background’ terms. In the invariant $\eta\eta$ mass distribution displayed in figure 7.7, an f_2 contribution is also visible at about $1.2 \text{ GeV}/c^2$. On the other hand the hypotheses containing an $f_2(1270)$ resonance of iteration steps 0-3 based on Breit-Wigner descriptions did not provide a significantly better description of the data. Compared to the expected fit fraction of 0.2% for the $f_2(1270)$ the yield of that contribution is also too large, it might be caused by the non-resonant ‘background’ terms instead.

The fit fractions of the f_2 contribution and the $\omega_2(1975)$ decrease only very slightly due to the $h_1(1965)$ resonance added to the base hypothesis in iteration step II, whereas the fit fraction of the $\phi(1680)$ resonance is significantly increased. The $h_1(1965)$ resonance itself has a fit fraction of 1.3%. The fit fraction of the $(\pi\pi)_S$ wave is increased significantly, so that the sum of the individual fit fractions is actually 100% and there does not seem to be much interference.

Figure 7.8 shows the Dalitz plots for the selected recorded data and the fit result of the finally best hypothesis. The corresponding production and decay angular distributions are shown in figures 7.9 and 7.10. The fit describes the data quite well, most deviations seem to be just statistical fluctuations. The only exception is the distribution of the $\cos(\theta_\eta^{\eta\eta})$, the azimuthal angle of one of the η mesons in the helicity frame of the $\eta\eta$ system: Around zero in six bins in a row the total fit yield is lower than the data and at ± 1 in three neighboring bins the total fit yield is larger than the data. The symmetry of the distribution is no coincidence, for each event two entries are made, one for each η , because from the physics point of view they are indistinguishable. Except for the angular distributions of the ϕ in the helicity frame of the $\phi\eta\eta$ system all angular distributions are similarly symmetrized.

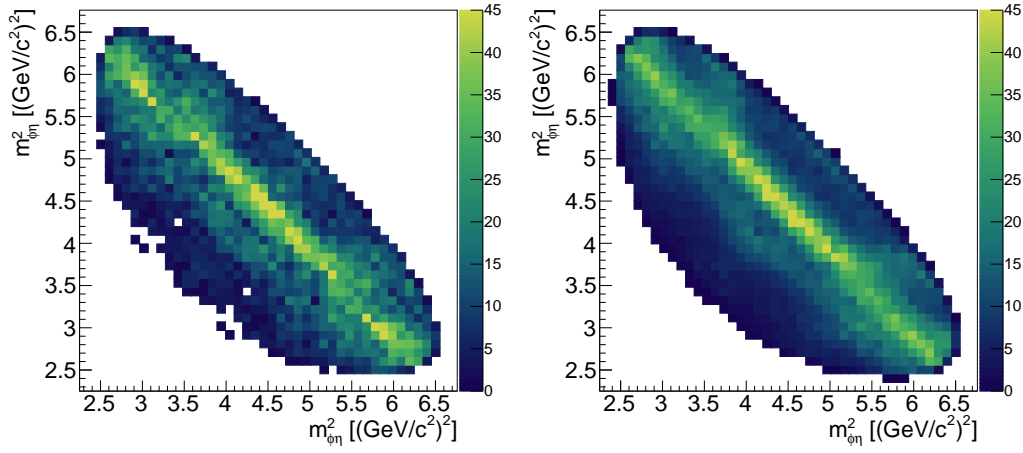


Figure 7.8: Dalitz plots of recorded data and the hypothesis $(\pi\pi)_S$, f_2 -matrix, $\omega_2(1975)$, $\phi(1680)$, and $h_1(1965)$ resonance with free masses and widths

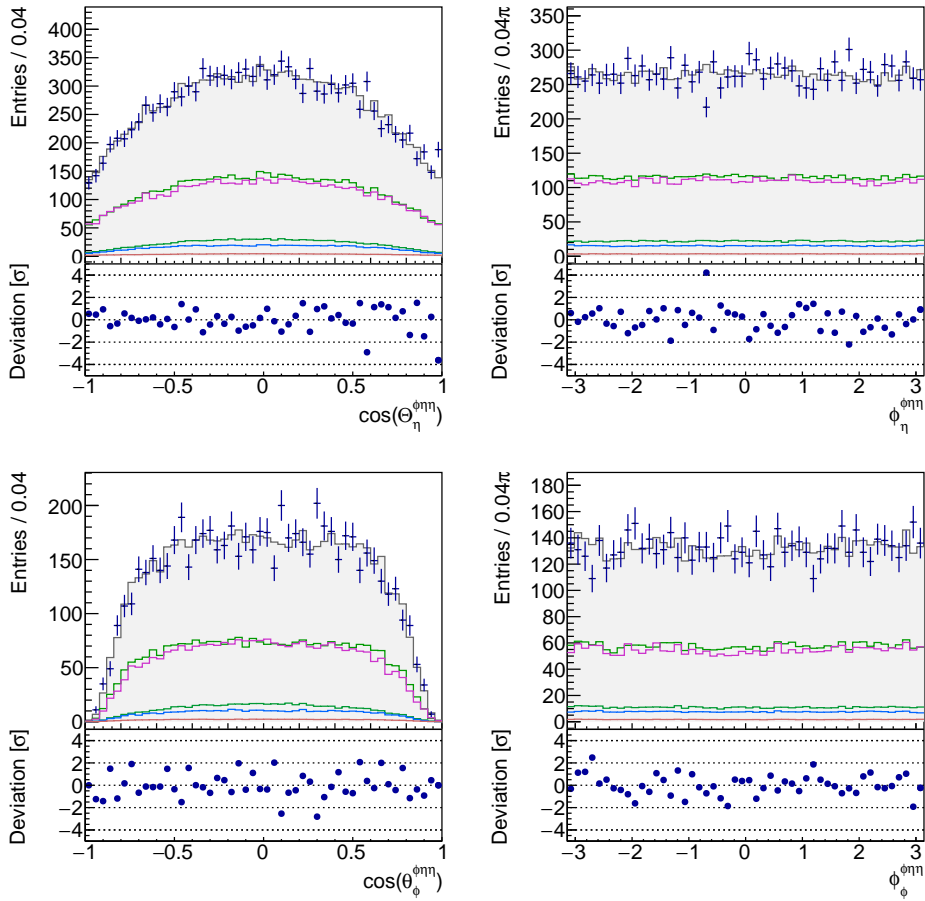


Figure 7.9: Production angular distributions of the best hypothesis and the individual contributions

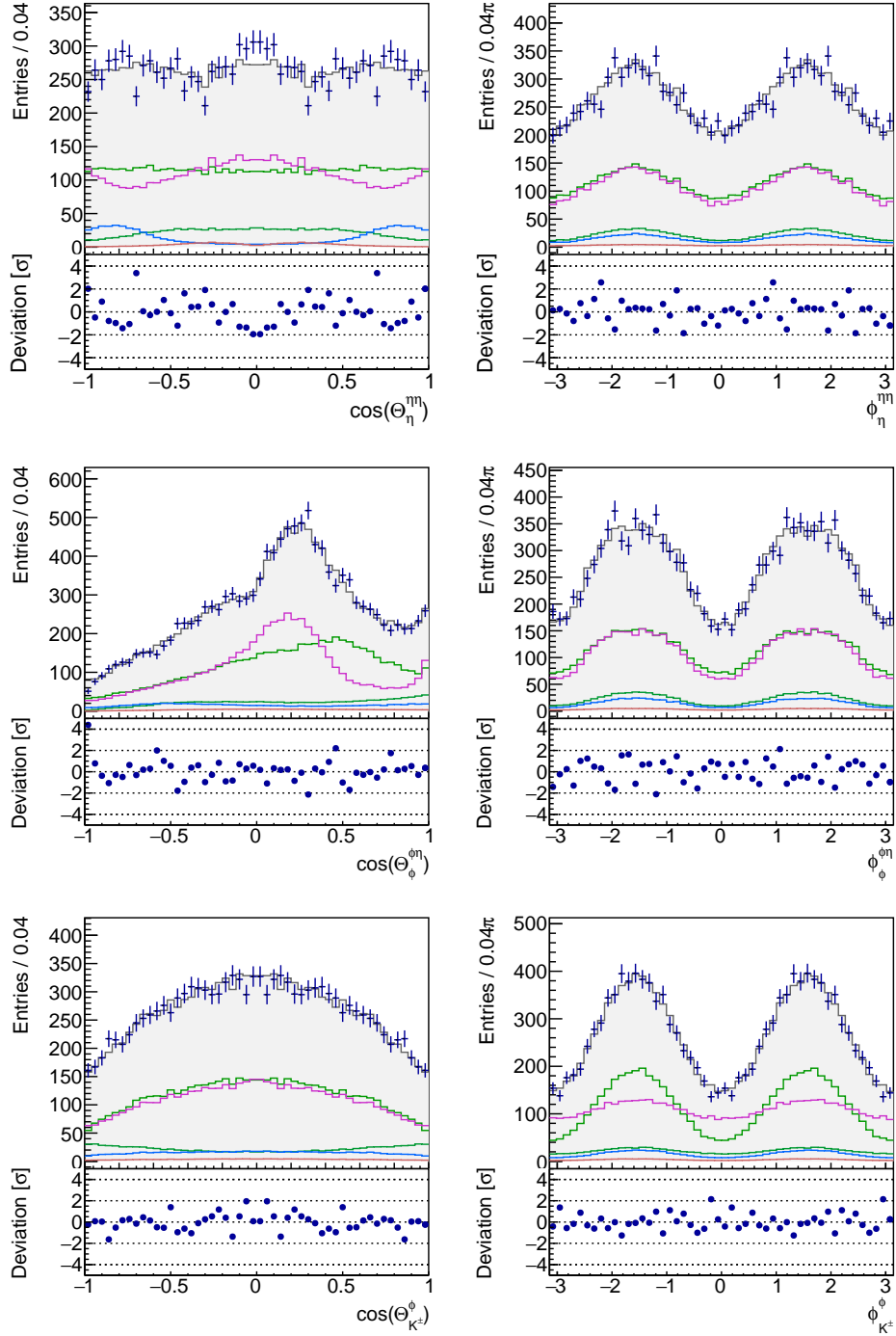


Figure 7.10: Decay angular distributions of the best hypothesis and the individual contributions

7.4 Determination of Branching Fractions

The number of in total selected events N_{tot} for the decay $J/\psi \rightarrow \phi\eta\eta$ equals the number of recorded J/ψ events $N_{J/\psi}$ reduced by the probabilities that the desired decay process of the J/ψ and its daughter particles also by the detector acceptance and reconstruction efficiency for the complete reaction ϵ_{tot}

$$N_{\text{tot}} = N_{J/\psi} \cdot \mathfrak{B}(J/\psi \rightarrow \phi\eta\eta) \cdot \mathfrak{B}(\phi \rightarrow K^+K^-) \mathfrak{B}(\eta \rightarrow \gamma\gamma)^2 \cdot \epsilon_{\text{tot}},$$

under the assumption, that the selection is so pure that no background events are contained. Regarding the different possible decays of a particle as branches this probability is called branching fraction. Vice versa the branching fraction of the decay can be determined by

$$\mathfrak{B}(J/\psi \rightarrow \phi\eta\eta) = \frac{N_{\text{tot}}}{N_{J/\psi} \cdot \mathfrak{B}(\phi \rightarrow K^+K^-) \mathfrak{B}(\eta \rightarrow \gamma\gamma)^2 \cdot \epsilon_{\text{tot}}}.$$

In this section also the branching fractions for the decay processes of the contributions identified in the previous chapter are determined from the yield of the according contribution given by the fit.

For each contribution the branching fraction of its production in the decay of the J/ψ and the branching fraction of its own decay into the considered final state particles have to be taken into account additionally, so that

$$\begin{aligned} N_X &= N_{J/\psi} \cdot \mathfrak{B}(J/\psi \rightarrow \phi X) \cdot \mathfrak{B}(X \rightarrow \eta\eta) \cdot \mathfrak{B}(\phi \rightarrow K^+K^-) \mathfrak{B}(\eta \rightarrow \gamma\gamma)^2 \cdot \epsilon_X \quad \text{or} \\ N_Y &= N_{J/\psi} \cdot \mathfrak{B}(J/\psi \rightarrow \eta Y) \cdot \mathfrak{B}(Y \rightarrow \phi\eta) \cdot \mathfrak{B}(\phi \rightarrow K^+K^-) \mathfrak{B}(\eta \rightarrow \gamma\gamma)^2 \cdot \epsilon_Y, \end{aligned}$$

where N_X and N_Y denote the yield of the fit for the corresponding contribution. By setting the production amplitudes of all other contributions to zero, the efficiency can be determined for each contribution individually by the ratio between weighted reconstructed and generated MC events as described in the following subsection. This way all phase space dimensions and thus the non-uniformity in the efficiency distribution are properly accounted for.

If either the branching fraction of the production or the decay is known before, the other one can be determined from the obtained fit results. If neither the production nor the decay of the resonance is known yet, the product branching fraction can be determined as

$$\begin{aligned} \mathfrak{B}(J/\psi \rightarrow \phi X) \cdot \mathfrak{B}(X \rightarrow \eta\eta) &= \frac{N_X}{N_{J/\psi} \cdot \mathfrak{B}(\phi \rightarrow K^+K^-) \mathfrak{B}(\eta \rightarrow \gamma\gamma)^2 \cdot \epsilon_X} \quad \text{or} \\ \mathfrak{B}(J/\psi \rightarrow \eta Y) \cdot \mathfrak{B}(Y \rightarrow \phi\eta) &= \frac{N_X}{N_{J/\psi} \cdot \mathfrak{B}(\phi \rightarrow K^+K^-) \mathfrak{B}(\eta \rightarrow \gamma\gamma)^2 \cdot \epsilon_Y}. \end{aligned}$$

As shown in tables 7.1 and 7.2 in most cases neither production nor decay branching fraction are known, so that only the product branching fraction can be determined here. The two exceptions are the $f_2(1270)$ and the $f_2'(1525)$. The $f_2(1270)$ is not included in the best hypothesis with the Breit-Wigner description and cannot be individually extracted for the K -matrix description of the f_2 contribution. Hence only for the $f_2'(1525)$ an individual branching fraction can be determined. The relative uncertainty of the production branching fraction amounts to 50% and is thus much larger than the uncertainty for the

decay branching fraction, which amounts to approximately 20%. Thus the latter is used to obtain a more precise value for the production branching fraction.

Table 7.12 contains the values needed for the determination of branching fractions, which are independent of the hypotheses.

In the following subsections the efficiency is determined by means of the partial wave analysis result and the considered systematic uncertainties are estimated, so that in subsection 7.4.3 the results can be given with statistical and systematic uncertainties.

7.4.1 Multidimensional Efficiency Determination and Correction

As it has already been stated in subsections 5.2.5 and 6.3 the obtained distributions are all influenced by the detector acceptance and the selection efficiency. A first simple estimation is presented in subsection 5.2.5. Usually, when performing a one dimensional fit the efficiency is parameterized, but for a fit considering the full phase space that would be quite difficult. In this analysis the efficiency and detector acceptance are accounted for by using phase space distributed MC events for which the detector response is simulated and the same reconstruction and selection algorithms are applied as for the recorded data. Now, that a good description of the data is obtained, a more sophisticated efficiency determination can be performed: Both the N_{gen} phase space distributed generated MC events as well as the N_{rec} reconstructed and selected MC events are weighted by the weight function w (cf. subsection 6.3) with the amplitudes θ determined by the best fit according to their phase space position $\vec{\tau}_j$, summed and the latter divided through the former that yields

$$\epsilon_{J/\psi} = \frac{\sum_{j=1}^{N_{\text{rec}}} w(\vec{\tau}_j, \theta)}{\sum_{j=1}^{N_{\text{gen}}} w(\vec{\tau}_j, \theta)} = 12.41\%.$$

This way the probability distribution over the complete phase space is correctly accounted for.

The experimentally unavoidable influence of the detector on the different distributions can be canceled out by performing a multidimensional efficiency correction. Figure 7.11 shows the Dalitz plot distributions of recorded data and reconstructed MC events obtained by means of this efficiency correction. The efficiency corrected one-dimensional invariant mass distributions are shown in figure 7.12 and the efficiency corrected angular distributions are shown in figures 7.13 and 7.14.

In agreement with the efficiency curve determined in subsection 5.2.5 the efficiency corrected yield is increased for higher invariant $\eta\eta$ mass values, whereas the invariant $\phi\eta$ mass distribution is basically unchanged. Correspondingly the yield for low azimuthal ϕ angles in the $\phi\eta$ helicity frame is increased. Besides that the distribution of the azimuthal production angles as well as the distribution of the polar decay angles of the $\phi\eta$ and $\eta\eta$ system are flat after the efficiency correction.

Table 7.11a and table 7.11b contain the number of reconstructed events and the according efficiency for the individual contributions of the best hypothesis with the Breit-Wigner description and the best hypothesis with the K -matrix description of the f_2 contributions, respectively. With the efficiency determined by means of the partial wave analysis it is now possible to determine meaningful branching fractions for the different contributions.

Contribution	Efficiency ϵ [%]	Yield N	Contribution	Efficiency ϵ [%]	Yield N
Total	12.50	6622 ± 81	Total	12.41	6622 ± 80
$(\pi\pi)_S$	12.67	3086 ± 125	$(\pi\pi)_S$	12.67	2886 ± 115
$f'_2(1525)$	13.39	1564 ± 98	f_2	12.85	2728 ± 106
$f_2(1810)$	12.21	524 ± 67	$\omega_2(1975)$	12.41	551 ± 59
$\omega_2(1975)$	12.13	619 ± 64	$\phi(1680)$	10.93	380 ± 63
$\phi(1680)$	10.70	224 ± 47	$h_1(1965)$	11.61	86 ± 24
$h_1(1965)$	13.68	209 ± 43			

(a) (b)

Table 7.11: Number of events of the different contributions with statistical uncertainties and their individual efficiencies determined from the best fit with the Breit-Wigner description (a) and the K -matrix description (b) for the f_2 contributions

Quantity	Value	Source
$N_{J/\psi}$	$(1310.6 \pm 7.0) \cdot 10^6$	[36]
$\mathfrak{B}(\phi \rightarrow K^+K^-)$	$(48.9 \pm 0.5)\%$	[1]
$\mathfrak{B}(\eta \rightarrow \gamma\gamma)$	$(39.41 \pm 0.20)\%$	[1]

Table 7.12: Fit independent values needed for the determination of branching fractions

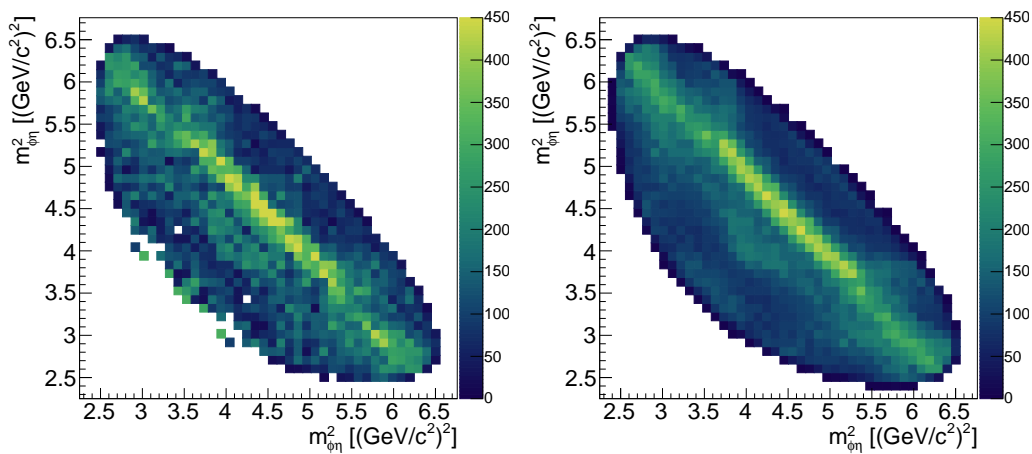


Figure 7.11: Efficiency corrected Dalitz plots of recorded data (left) and weighted reconstructed MC events (right) by means of the fitted hypothesis $(\pi\pi)_S$, f_2 -matrix, $\omega_2(1975)$, $\phi(1680)$, and $h_1(1965)$ with free masses and widths

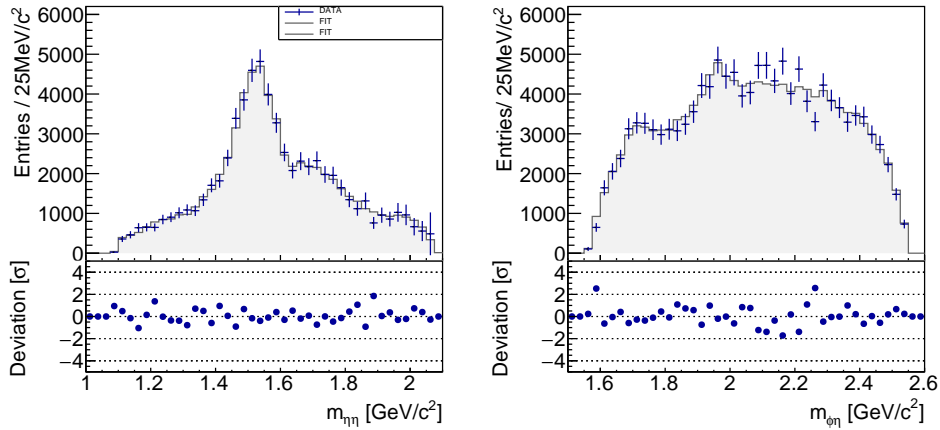


Figure 7.12: Efficiency corrected invariant $\eta\eta$ and $\phi\eta$ mass distributions of the hypothesis $(\pi\pi)_S$, f_2 -matrix, $\omega_2(1975)$, $\phi(1680)$ and $h_1(1965)$ with free masses and widths

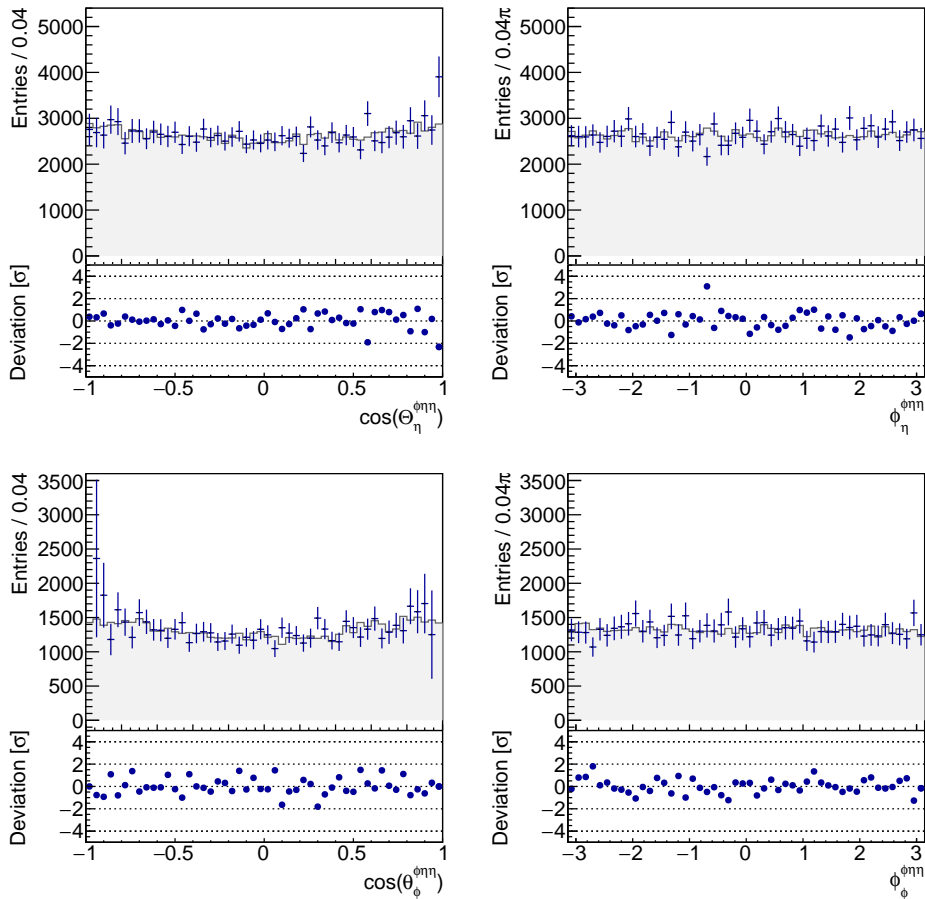


Figure 7.13: Efficiency corrected production angle contributions of the hypothesis $(\pi\pi)_S$, f_2 -matrix, $\omega_2(1975)$, $\phi(1680)$ and $h_1(1965)$ with free masses and widths

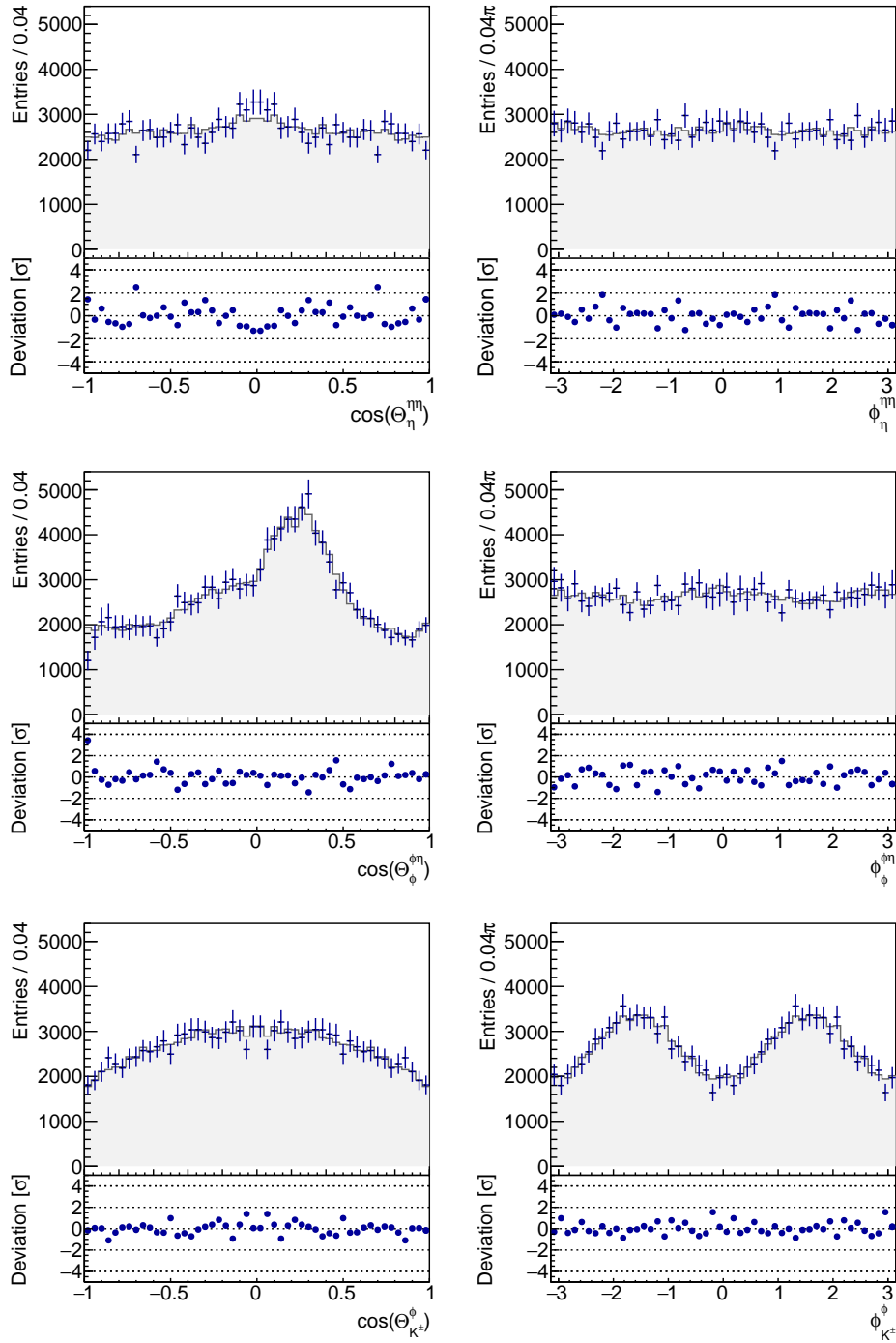


Figure 7.14: Efficiency corrected decay angular distributions of the hypothesis $(\pi\pi)_S$, f_2 -matrix, $\omega_2(1975)$, $\phi(1680)$ and $h_1(1965)$ with free masses and widths

7.4.2 Systematic Uncertainties

Many of the systematic uncertainties arise due to the experimental conditions, these have already been evaluated for other analyses by the BESIII collaboration and are presented here briefly.

Total number of events in the J/ψ sample

The large J/ψ data sample of $1.31 \cdot 10^9$ events recorded by BESIII consists actually of two subsamples. A first data set of $(223.7 \pm 1.4) \cdot 10^6$ was recorded already in 2009. In 2012 a second much larger subsample of $(1086.9 \pm 6.0) \cdot 10^6$ has been recorded. In total that results in $(1310.6 \pm 7.0) \cdot 10^6$ recorded J/ψ events. The relative uncertainty of the number of J/ψ events is hence 0.5%. [36]

Photon Detection

The photon detection efficiency is studied with a control sample of the initial state radiation process $e^+e^- \rightarrow \gamma\mu^+\mu^-$ at center-of-mass energies corresponding to the J/ψ and $\psi(3770)$ resonances. The photon detection efficiency is determined to be 1% by checking the success rate of matching the predicted photon position obtained by a kinematic fit to the two muon tracks with the photon detected in the EMC [69]. Since there are four photons to be detected for the two η mesons in this analysis that results in a total uncertainty of 4%.

Tracking Efficiency and Identification Uncertainty for Charged Kaons

The kaon tracking efficiency is determined with a sample of $J/\psi \rightarrow K^*(892)^0 K^0 + c.c. \rightarrow K_S^0 K^+ \pi^- + c.c. \rightarrow K^+ \pi^- \pi^+ \pi^- + K^- \pi^+ \pi^- \pi^+$ events in the scope of the study of radiative χ_{cJ} decays into a vector meson [70]: The difference in the kaon tracking efficiency between recorded data and MC events is about 2% and considered as the uncertainty of the kaon tracking efficiency. In the same analysis [70] the efficiency of the kaon particle identification (PID) is obtained by studying the control sample $J/\psi \rightarrow K^+ K^- \pi^0$. Again the difference between the determined kaon PID efficiency for recorded data and for MC events is 2% and considered as the systematic uncertainty of the PID. Since there are two kaons to be detected for the ϕ mesons in this analysis just as in that study, an uncertainty of 2% is used for both tracking and PID.

External branching fractions

For the determination of branching fractions for intermediate resonances the branching fraction of the decay of the ϕ into a pair of charged kaons and the branching fraction of the decay of an η into a pair of photons are used. The values are given with an uncertainty of 1% and 0.5% for the branching fraction $\mathfrak{B}(\phi \rightarrow K^+ K^-)$ and the branching fraction $\mathfrak{B}(\eta \rightarrow \gamma\gamma)$, respectively [1].

Choice of Hypothesis

The systematic uncertainty caused by choosing a certain hypothesis to describe the data is estimated by comparing two hypotheses, which describe the data similarly well. By choosing a hypothesis with one more contribution than the considered one it is possible

Source of Systematic Uncertainty	Relative Extent
Total number of J/ψ events	0.5 %
Photon detection (4 photons)	4 %
Tracking (2 kaons)	2 %
Particle identification (2 kaons)	2 %
$\mathfrak{B}(\phi \rightarrow K^+ K^-)$	1 %
$\mathfrak{B}(\eta \rightarrow \gamma\gamma)$	0.5 %
Quadratic sum	5.05%

Table 7.13: Systematic uncertainties independent of the hypothesis

Contribution	Uncertainty due to Choice of Hypothesis	Total Systematic Uncertainty	Contribution	Uncertainty due to Choice of Hypothesis	Total Systematic Uncertainty
Total	0.00%	5.05%	Total	0.00%	5.05%
$(\pi\pi)_S$	3.73%	6.28%	$(\pi\pi)_S$	1.12%	5.17%
$f'_2(1525)$	1.72%	5.34%	f_2	2.63%	5.70%
$f_2(1810)$	15.19%	16.01%	$\omega_2(1975)$	1.24%	5.20%
$\omega_2(1975)$	3.93%	6.40%	$\phi(1680)$	5.40%	7.40%
$\phi(1680)$	9.67%	10.91%	$h_1(1965)$	0.03%	5.05%
$h_1(1965)$	3.23%	5.99%			

(a)

(b)

Table 7.14: Total systematic uncertainties and systematic uncertainties caused by the choice of hypothesis for the number of events from the best fit with the Breit-Wigner description (a) and the K -matrix description (b) of the f_2 resonances

to obtain uncertainties for all contributions at once. For the best fit obtained with a Breit-Wigner parameterization for the f_2 resonances the hypothesis with an additional $f_2(1270)$ is chosen for that purpose. The $f_2(1270)$ is anyway contained when the K -matrix description for the f_2 resonances is used and it probably will have a larger influence on the parameters of the $f'_2(1525)$ contribution than a contribution with different quantum numbers. For the best fit obtained with the K -matrix description for the f_2 resonances the hypothesis with an additional $\phi(2170)$ is chosen.

Table 7.13 summarizes all considered systematic uncertainties independent of the performed fit, whereas tables 7.14a and 7.14b list the systematic uncertainties obtained by the comparison between the two similar hypothesis. The total systematic uncertainty is determined by the squared sum of the individual systematic uncertainties.

7.4.3 Results of the Determination of Branching Fractions

The total and product branching fractions with their individual statistical uncertainty retrieved from tables 7.11a and 7.11b and a systematic uncertainty of 5% determined for the best fit with the Breit-Wigner description for the f_2 resonances are shown in table 7.15 and the ones determined from the best fit with the K -matrix description are shown in table 7.16.

	Value	Statistical Error	Systematic Error
$\mathfrak{B}(J/\psi \rightarrow \phi\eta\eta)$	$5.32 \cdot 10^{-4}$	$0.64 \cdot 10^{-4}$	$0.27 \cdot 10^{-4}$
$\mathfrak{B}(J/\psi \rightarrow \phi(\pi\pi)_S) \cdot \mathfrak{B}((\pi\pi)_S \rightarrow \eta\eta)$	$2.57 \cdot 10^{-4}$	$0.10 \cdot 10^{-4}$	$0.17 \cdot 10^{-4}$
$\mathfrak{B}(J/\psi \rightarrow \phi f'_2(1525)) \cdot \mathfrak{B}(f'_2(1525) \rightarrow \eta\eta)$	$1.09 \cdot 10^{-4}$	$0.06 \cdot 10^{-4}$	$0.06 \cdot 10^{-4}$
$\mathfrak{B}(J/\psi \rightarrow \phi f_2(1810)) \cdot \mathfrak{B}(f_2(1810) \rightarrow \eta\eta)$	$4.90 \cdot 10^{-5}$	$0.53 \cdot 10^{-5}$	$0.78 \cdot 10^{-5}$
$\mathfrak{B}(J/\psi \rightarrow \eta\omega_2(1975)) \cdot \mathfrak{B}(\omega_2(1975) \rightarrow \phi\eta)$	$5.66 \cdot 10^{-5}$	$0.47 \cdot 10^{-5}$	$0.36 \cdot 10^{-5}$
$\mathfrak{B}(J/\psi \rightarrow \eta\phi(1680)) \cdot \mathfrak{B}(\phi(1680) \rightarrow \phi\eta)$	$2.07 \cdot 10^{-5}$	$0.39 \cdot 10^{-5}$	$0.23 \cdot 10^{-5}$
$\mathfrak{B}(J/\psi \rightarrow \eta h_1(2215)) \cdot \mathfrak{B}(\phi(1680) \rightarrow \phi\eta)$	$1.81 \cdot 10^{-5}$	$0.33 \cdot 10^{-5}$	$0.11 \cdot 10^{-5}$

Table 7.15: Determined product branching fractions for the different contributions of the best fit with the Breit-Wigner description of the f_2 resonances

	Value	Statistical Error	Systematic Error
$\mathfrak{B}(J/\psi \rightarrow \phi\eta\eta)$	$5.37 \cdot 10^{-4}$	$0.65 \cdot 10^{-4}$	$0.27 \cdot 10^{-4}$
$\mathfrak{B}(J/\psi \rightarrow \phi(\pi\pi)_S) \cdot \mathfrak{B}((\pi\pi)_S \rightarrow \eta\eta)$	$2.34 \cdot 10^{-4}$	$0.09 \cdot 10^{-4}$	$0.12 \cdot 10^{-4}$
$\mathfrak{B}(J/\psi \rightarrow \phi f_2) \cdot \mathfrak{B}(f_2 \rightarrow \eta\eta)$	$2.21 \cdot 10^{-5}$	$0.09 \cdot 10^{-5}$	$0.11 \cdot 10^{-5}$
$\mathfrak{B}(J/\psi \rightarrow \eta\omega_2(1975)) \cdot \mathfrak{B}(\omega_2(1975) \rightarrow \phi\eta)$	$4.46 \cdot 10^{-5}$	$0.48 \cdot 10^{-5}$	$0.23 \cdot 10^{-5}$
$\mathfrak{B}(J/\psi \rightarrow \eta\phi(1680)) \cdot \mathfrak{B}(\phi(1680) \rightarrow \phi\eta)$	$3.08 \cdot 10^{-5}$	$0.51 \cdot 10^{-5}$	$0.18 \cdot 10^{-5}$
$\mathfrak{B}(J/\psi \rightarrow \eta\phi h_1(1965)) \cdot \mathfrak{B}(\phi(1680) \rightarrow \phi\eta)$	$0.69 \cdot 10^{-5}$	$0.19 \cdot 10^{-5}$	$0.04 \cdot 10^{-5}$

Table 7.16: Determined product branching fractions for the different contributions of the best fit with the K -matrix description of the f_2 resonances

Only for the decay branching fraction of the $f'_2(1525)$ determined as

$$\mathfrak{B}(J/\psi \rightarrow \phi f'_2(1525)) = (10.5 \pm 0.6_{\text{stat}} \pm 2.3_{\text{sys}}) \cdot 10^{-4}$$

a comparison with the averaged branching fraction $(8 \pm 4) \cdot 10^{-4}$ listed in the PDG review [1] is possible. The branching fraction determined in the analysis presented here is in good agreement with this averaged branching fraction. Actually there are only two branching fraction determinations averaged: The result from the DM2 experiment [71] the branching fraction is determined to $(12.3 \pm 0.6 \pm 2.0) \cdot 10^{-4}$ in $J/\psi \rightarrow \text{hadrons}$ processes and by MARKII [72] it is determined to $(4.8 \pm 1.8) \cdot 10^{-4}$ in $J/\psi \rightarrow K^+K^-K^+K^-$. These two values do not agree and obviously the result determined in this analysis agrees much better with the former one.

8 Conclusion and Discussion

The decay $J/\psi \rightarrow \phi\eta\eta$ was studied based on a data sample corresponding to $1.31 \cdot 10^9$ J/ψ events recorded with the BESIII experiment in 2009 and 2012. Events with two oppositely charged kaons and at least four photons were selected corresponding to the subsequent decays $\phi \rightarrow K^+K^-$ and $\eta \rightarrow \gamma\gamma$. Besides criteria based on particle identification and particle multiplicities kinematic fits constraining the data to match the initial four-momentum and the η mass were performed. For further background reduction also a fit to match the pion mass with any possible two-photon combination was performed.

The remaining background has been investigated by means of a generic MC sample, a phase space distributed $J/\psi \rightarrow \phi\pi^0\pi^0$ data sample as well as event distributions in sideband regions of the recorded data sample, the generic MC sample and a phase space distributed signal MC sample. Taking into account signal contributions in the sideband regions the remaining background level is estimated to 2%.

The combination of detector acceptance and applied selection criteria yields 6622 selected events with an estimated efficiency of 12.5%. The efficiency drops to almost zero for high $\eta\eta$ masses, but is comparably flat over the $\phi\eta$ mass. A clear peak is obvious at about $1.5 \text{ GeV}/c^2$ accompanied by a knee shaped enhancement at about $1.7 \text{ GeV}/c^2$ in the $\eta\eta$ spectrum. The identification of the clear peak with the $f'_2(1525)$ resonance is confirmed by the generic MC sample. Two bumps at about $1.7 \text{ GeV}/c^2$ and just below $2 \text{ GeV}/c^2$ are visible in the $\phi\eta$ spectrum, for higher masses the fluctuation between neighboring peaks is too large to draw conclusions.

Partial wave amplitudes are fitted to the data to identify the quantum numbers, yield, mass and width of intermediate resonances. Starting with the initial base hypothesis consisting of the $(\pi\pi)_S$ wave described by a K -matrix and the $f'_2(1525)$ resonance described by a Breit-Wigner distribution. All known contributions with appropriate quantum numbers are added individually to form new hypotheses and in iterative steps the hypothesis which yielded the most significant improvement of the fit quality is used as new base hypothesis. The fit quality is here measured by the sum of the information criteria BIC and AIC.

In the first three iteration steps with fixed mass and width parameters the $f_2(1810)$, $\omega_2(1975)$ and $\phi(1689)$ contributions are identified as relevant contributions. For released mass and width parameters additionally the $h_1(2215)$ yields to a significant improvement of the fit quality.

In order to obtain a better description of the 2^{++} contribution, a K -matrix is used and the fit is coupled with measurements from scattering data to constrain three more channels in addition to the $\eta\eta$ channel. The description with a K -matrix with four poles and individual P -vectors for the different LS combinations is significantly better than with a K -matrix with three of five poles or neglecting the S or even LS dependency of the P -vector.

The K -matrix description is optimized for a hypothesis including the $\omega_2(1975)$ and $\phi(1680)$ contributions with released mass and width parameters. In a further iteration step the hypothesis with an additional $h_1(1975)$ contribution is the only contribution which improves the fit quality.

Product branching fractions are determined for all contributions. Of all determined contributions only for the $f_2'(1525)$ the branching fractions have already been determined previously by other experiments. The uncertainty of the product branching fraction is much larger than for the decay branching fraction. Thus the decay branching fraction is used to determine the product branching fraction from the obtained fit results to $\mathcal{B}(J/\psi \rightarrow \phi f_2'(1525)) = (10.5 \pm 0.6_{\text{stat}} \pm 2.3_{\text{sys}}) \cdot 10^{-4}$. The large uncertainty of the value given by the PDG [1] is caused by two disagreeing measurements from DM2 and MARKII. The branching fraction obtained with the presented analysis agrees well with the one obtained by DM2.

Part II

Calibration of the Temperature Monitoring System for the Electromagnetic Calorimeter of the PANDA Target Spectrometer

9 Introduction to the Temperature Monitoring System for the $\overline{\text{PANDA}}$ EMC

The anti-Proton Annihilation at Darmstadt ($\overline{\text{PANDA}}$) experiment is based on an antiproton beam with momenta ranging from $1.5 \text{ GeV}/c$ up to $15 \text{ GeV}/c$ impinging on a fixed target. The rich $\overline{\text{PANDA}}$ physics program aims for a better understanding of the strong interaction. The cooled antiproton beam with a relative momentum spread in the order of $10^{-5} - 4 \cdot 10^{-5}$ will be provided by the HESR of the Facility for Antiproton and Ion Research (FAIR) currently under construction near Darmstadt. In combination with the $\overline{\text{PANDA}}$ hydrogen target system luminosities up to $2 \cdot 10^{32} \text{ cm}^{-1}\text{s}^{-1}$ will be reached. In order to precisely measure also those particles, which are boosted in forward direction, the detector is composed of a target spectrometer and a forward spectrometer. Tracks of charged particles in the target spectrometer are bent by a superconducting solenoid magnet and particles in the acceptance of the forward spectrometer are additionally bent by a dipole magnet.

Within the solenoid magnet a homogeneous crystal calorimeter will be used to reconstruct electrons, positrons and photons by measuring their deposited energy and flight direction. Lead tungstate (PbWO_4 , PWO-II) is chosen as scintillator material due to its radiation hardness, fast response time and high density, which allows for a compact setup. In order to achieve a low energy threshold the light yield is increased by operating the EMC at -25°C .

The temperature dependence of the scintillation light yield requires a precise and stable temperature control. To keep a good energy resolution, the temperature variation should not exceed $\pm 0.1^\circ\text{C}$ and the temperature gradient along the crystals should not exceed $0.1^\circ\text{C}/\text{cm}$.

Ultrathin platinum resistance temperature sensors have been developed at the Institut für Experimentalphysik I at Ruhr-Universität Bochum because no commercially available temperature sensors fulfill the strict spatial limitations. In the tight geometry of the EMC only $150 \mu\text{m}$ gaps in between neighboring scintillator crystals are available for the temperature sensors and their cables. Furthermore the strong temperature precision requirement of 0.02°C to ensure appropriate temperature regulation is not even met by temperature sensors of the highest precision class defined in the industrial norm. In order to measure the resistance of the temperature sensors with the according precision of 0.08% , the Temperature and Humidity Monitoring board for $\overline{\text{PANDA}}$ (THMP) has been developed at the Institut für Experimentalphysik I.

The design of the temperature sensors is based on a four-wire resistance measurement of the resistance of a thin platinum wire with $25 \mu\text{m}$ diameter and a length of about 0.5 m , so that it matches the properties of common Pt100 sensors. To determine the individual characteristics of each ultrathin temperature sensor, these are calibrated in a dedicated calibration setup at temperatures between -30°C and $+30^\circ\text{C}$. Just as commercial Pt100 sensors, also the ultrathin sensors show a hysteresis effect, so that the calibration data is split into two samples with increasing and decreasing temperatures, respectively. A third

order polynomial is well suited to describe the temperature dependence of the measured resistance.

Only if the standard deviation of the data points from the fit functions is below $0.02\text{ }^{\circ}\text{C}$, the calibration measurement validates the suitability of the sensor. To ensure the reliability of the temperature sensors, the results obtained from several calibration measurements are compared. In dedicated measurements the hysteresis effect and the longterm behavior of the sensors are studied.

The THMP design is modular so that besides the resistance temperature sensors also humidity and pressure sensors can be read out. Key components are a mainboard with a microcontroller, a 14-bit ADC and connectors to mount piggyback boards with different designs to read out the different kinds of sensors. The required resistance resolution is determined by the requirements on the resolution of the temperature sensors to 0.08%. Even when using only high precision components the electronics cannot be produced with such a precision. In order to obtain the required resistance resolution, each readout channel of the electronics has to be calibrated. Therefore, the individual readout channels are connected to different temperature stable, precise resistors with known values. During the measurement the THMP is exposed to different environmental temperatures in a climate chamber, so that the temperature dependence of the electronics can be taken into account. The uncertainty for the connected resistors and the environmental temperature are determined from multiple calibration measurements, so that the propagated uncertainty provides a reliable estimation of the resistance measurement precision. Furthermore, the reproducibility of the calibration parameters is investigated.

10 The $\overline{\text{PANDA}}$ Experiment

The anti-Proton Annihilation at Darmstadt ($\overline{\text{PANDA}}$) experiment is one of the key experiments at the Facility for Antiproton and Ion Research (FAIR) currently under construction on the ground of the GSI in Darmstadt. The high energy storage ring (HESR) will provide a cooled antiproton beam with a momentum resolution of $\frac{\Delta p}{p} = 10^{-5} - 4 \cdot 10^{-5}$ at beam momenta between 1.5 GeV/ c and 15 GeV/ c . When these antiprotons impinge on the fixed target, luminosities up to $2 \cdot 10^{32} \text{cm}^{-2} \text{s}^{-1}$ can be reached. Studying the thereby accessible physics with the versatile $\overline{\text{PANDA}}$ detector will be enriching for various fields in hadron physics.

Major topics of the rich physics program of the $\overline{\text{PANDA}}$ experiment are presented shortly in the following section. A detailed discussion of these topics can be found in [73]. The generation of the antiproton beam and its properties are outlined in section 10.2 and the properties and features of the different subdetectors of the $\overline{\text{PANDA}}$ detector are portrayed in section 10.3

10.1 Physics Program

The $\overline{\text{PANDA}}$ experiment aims at a better understanding of the strong interaction. Perturbation theory has been employed successfully to describe physics phenomena at very small quark distances, where the coupling constant is small, but can not be used at larger quark distances. Some important questions concerning the strong interaction still remain open, for example it is not yet fully understood how hadrons obtain their mass or how confinement works. A great advancement in the understanding of the strong interaction is expected from the definitive identification of exotic matter such as multi-quark states, gluons and hybrids. There have actually been several observations at energies, where no $q\bar{q}$ states have been predicted, which are thus considered as candidates for exotic matter. In order to gain new insights, systematic studies with high statistic precision are needed to extract the features of these states.

Some candidates for exotic matter are known for a long time, as the $a_0(980)$ and $f_0(980)$, which are suspected to have admixtures of a $K\bar{K}$ molecule or the supernumerous $f_0(1370)$, $f_0(1500)$ and $f_0(1710)$, which might be caused by mixing with a glueball. But in the light meson sector there are many states with a rather broad width so that states with the same quantum numbers mix and assignments are ambiguous. The already observed charmonium states are rather narrow compared to their mass differences, so that they are well separated and a definitive identification is more likely. Especially in the past few years several candidates for exotic matter have been observed in the charmonium mass range above the $D\bar{D}$ threshold in different production processes at the B -factories, LHCb and BESIII, including for example the $X(3872)$, $Z_c(3900)$, $Y(4260)$, and $Y(4360)$. With the $\overline{\text{PANDA}}$ experiment these states can be produced in formation, which enables new possibilities of studies. In electron-positron collisions charmonia can be formed directly via a virtual photon, but then the quantum numbers are fixed to 1^{--} and charmonia

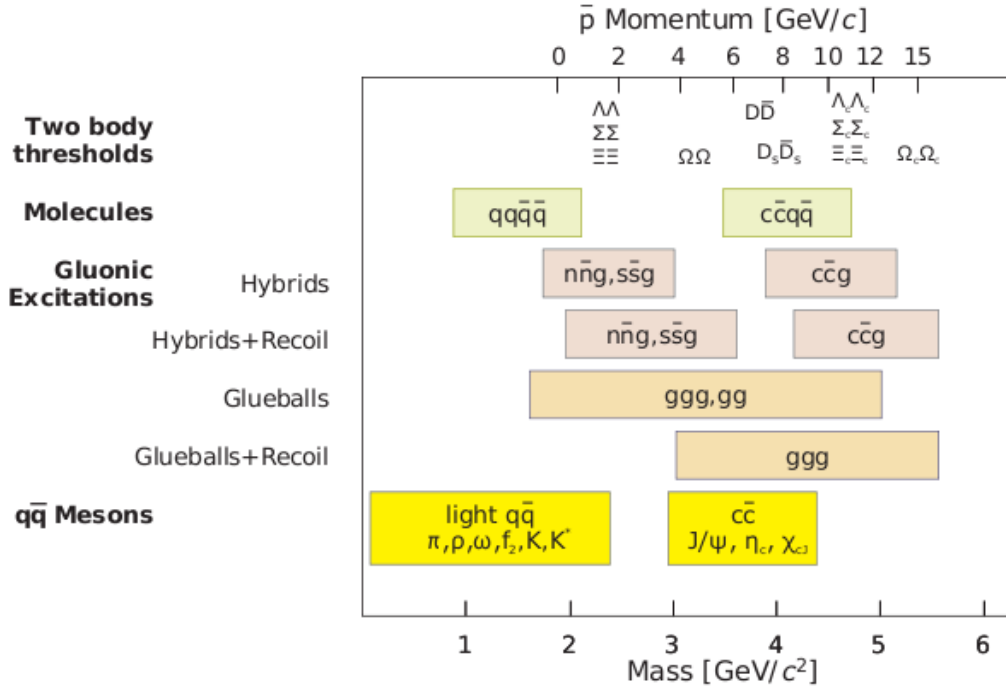


Figure 10.1: Beam momentum and center of mass range accessible for \bar{P} ANDA at the HESR [74]

with other quantum numbers have to be produced with a recoil. With a high precision antiproton beam on a hydrogen target states with any non-exotic quantum number can be accessed in formation, which provides several advantages. Compared to production with recoil particles the reconstruction ambiguities are reduced and also the production cross section is much higher, which results in high statistics. But most important is the possibility to scan resonances by tuning the beam momentum to different momenta, so that the obtained spectrum does not depend on the energy resolution of the detector but on the high precision of the beam. Knowing the exact mass and shape of very narrow charmonium states as e.g. the $X(3872)$, which lies directly at the $D\bar{D}^*$ threshold and is suspected to be a meson-molecule or a tetraquark, would clarify its nature. Furthermore antiproton-proton annihilations are a gluon-rich environment in which the production of glueballs and hybrids is assumed to be likely. Besides charmonium spectroscopy the \bar{P} ANDA experiment can also carry out a significant charmed meson spectroscopy program, where for example the $D_{s0}^*(2317)^\pm$ and the $D_{s1}(2460)^\pm$ are discussed as meson-molecule candidates. In the case of baryon spectroscopy even in the nucleon sector, where the most data is available, the agreement with quark model predictions is quite low and for strange baryons the situation is even worse. The \bar{P} ANDA experiment will expand the experimental knowledge especially in the regime of (multi-)strange and charm baryons. Figure 10.1 shows which kind of hadrons are accessible at which center of mass energy and antiproton momentum respectively.

Quite naturally antiproton-proton annihilations also enable investigations of the proton structure. The time-like electromagnetic form factor of the proton can be determined by the process $p\bar{p} \rightarrow e^+e^-$. Several experiments have measured the time-like form factor for low momentum transfer q^2 down to the threshold, but the \bar{P} ANDA experiment will

provide information on the high q^2 region, where knowledge is scarce and incomplete so far.

Replacing the hydrogen target by a target with heavier nuclei the $\bar{\text{P}}\text{ANDA}$ experiment can investigate the in-medium properties of hadrons and study hypernuclei. So far studies of in-medium properties were focussed on the light quark sector, with the $\bar{\text{P}}\text{ANDA}$ experiment it will be possible to extend the studies to the charm sector. Such investigations aim at understanding the origin of hadron masses in the context of spontaneous chiral symmetry breaking and its partial restoration in a hadronic environment [75]. Apart from that the J/ψ -nucleus dissociation cross section can be deduced from measurements of the J/ψ and D production cross sections in antiproton annihilations on different nuclear targets. This dissociation cross section is a fundamental parameter to understand J/ψ suppression in heavy ion collisions, which is interpreted as an indication of quark-gluon plasma.

Hypernuclei consist in contrast to conventional nuclei not only of protons and neutrons but contain at least one strange hadron. Strangeness thus adds a new dimension to the chart of nuclides. Although single and double Λ -hypernuclei have been discovered decades ago, only six double Λ hypernuclei are known by now. By means of an antiproton beam, hypernuclei with more than one strange hadron can be produced efficiently.

10.2 The Antiproton Beam from HESR at FAIR

The antiproton beam for the $\bar{\text{P}}\text{ANDA}$ experiment is provided by the high energy storage ring (HESR), which is part of FAIR. FAIR is currently under construction on the ground of the Gesellschaft für Schwerionenforschung and will upgrade the already existing universal linear accelerator (UNILAC) and synchrotron with a bending power of 18 Tm (SIS-18) with a new proton linear accelerator and use them as a preaccelerator and injector. [76]

The whole project with civil construction, accelerator construction and experimental is described in detail in the FAIR Baseline Technical Report [77]. The Green Paper [78] motivates and describes the modularized stepwise construction of FAIR, which takes cost estimates and firm funding commitments of the member states into account and enables a swift project start still providing outstanding research programs for all four experimental pillars with the modularized start version (MSV). Upgrades of the facility with further accelerators will follow later on, after further research and development and funding commitments have been achieved. [76]

The core accelerator of FAIR is the double-ring heavy ion synchrotron with a bending power of 100 Tm (SIS-100), a circumference of about 1100 meters, which will accelerate protons to energies up to 30 GeV or heavy ions as to energies up to 2.7 GeV. By using a system of different storage and cooler rings parallel operation of all four scientific programs can be realized [76]. Figure 10.2 displays the MSV of the FAIR accelerator complex.

For the production of antiprotons 5 ns bunches of protons with an energy of 30 GeV from the heavy ion synchrotron with a bending power of 100 Tm (SIS-100) will be directed on the antiproton production target every 10 seconds. The rate is limited by the capacity of the subsequent collector ring (CR) not by the capacity of the SIS-100, the remaining bunches can be used for other experiments, which run in parallel. When a proton hits a nucleon of the target material consisting of nickel the kinetic energy can be transformed to particle-antiparticle pairs, as protons and antiprotons. Besides antiprotons also a large variety of other secondary particles with a broad momentum and angular distribution is produced. A combination of a magnetic horn and a momentum separation station

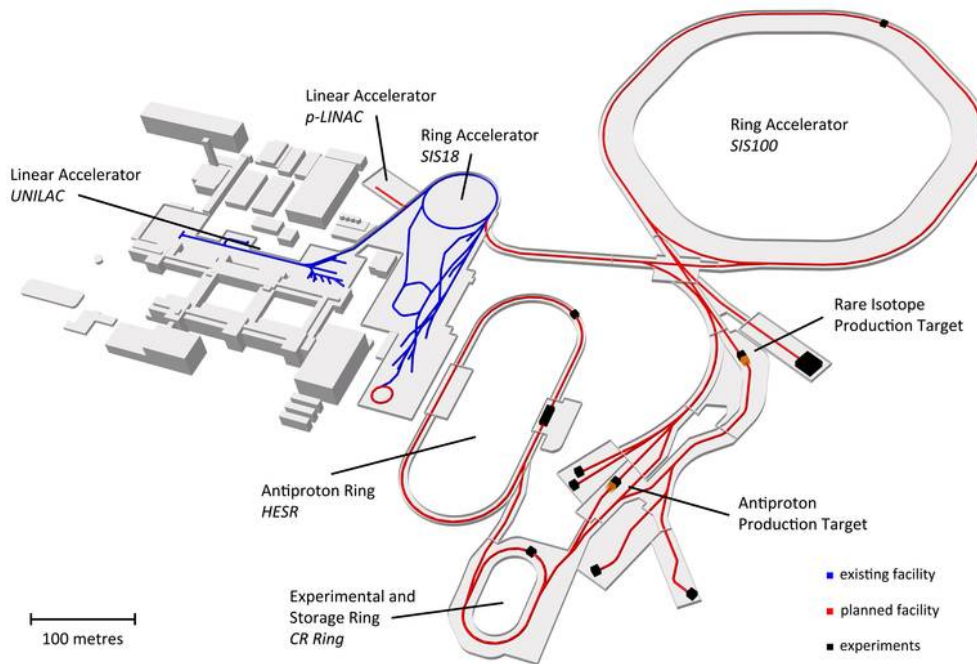


Figure 10.2: Overview of the FAIR complex [76]

is foreseen at the transfer path to the CR to enable an efficient antiproton collection. The accepted antiprotons will have a momentum of about $3.8 \text{ GeV}/c$ with a spread of 3%. [79, 80]

The CR collects the antiprotons, cools them stochastically and debunches them adiabatically. The debunching corresponds to an increased spatial spread along the direction of propagation and already decreases the momentum spread to 0.7%. The cooling does not effect the mean momentum, but reduces the spread further down to 0.1% and also reduces the transverse emittance by a factor of almost 50, which describes the spatial beam spread transverse to the direction of propagation, thereby the luminosity is increased. [79, 81]

In the MSV of FAIR the antiprotons will be directly injected into HESR, later the facility will be upgraded by the recuperated experimental storage ring (RESR), which is intended for accumulation of antiprotons and further stochastic beam cooling [79, 82]. The RESR will not only increase the intensity of the antiproton beam, but also enable parallel operation of nuclear structure, astrophysics and reactions (NUSTAR) and atomic, plasma physics and applications (APPA) with \bar{P} ANDA [78].

The HESR is specially designed for the needs of the \bar{P} ANDA experiment. The injected antiprotons can be both decelerated and accelerated to cover the beam momentum range from $1.5 \text{ GeV}/c$ up to $15 \text{ GeV}/c$. The combination of the antiproton beam with precise momentum and very small emittance with the dense internal proton target of the \bar{P} ANDA detector results in a high luminosity. To obtain optimal momentum precision and maximal luminosity two different operation modes are planned for the HESR. Table 10.1 gives an overview of the intended momentum precision and luminosity values and the available momentum range for the high luminosity (HL) and high resolution (HR) mode, respec-

	HL Mode	HR Mode
Momentum Range [GeV/c]	1.5 - 15	1.5 - 8.9
Momentum Spread σ_p/p	$\approx 10^{-4}$	$\leq 4 \cdot 10^{-5}$
Number of Stored Antiprotons	10^{11}	10^{10}
Peak Luminosity [$\text{cm}^{-2}\text{s}^{-1}$]	$2 \cdot 10^{32}$	$2 \cdot 10^{31}$

Table 10.1: Intended parameters for the HL and HR mode [79]

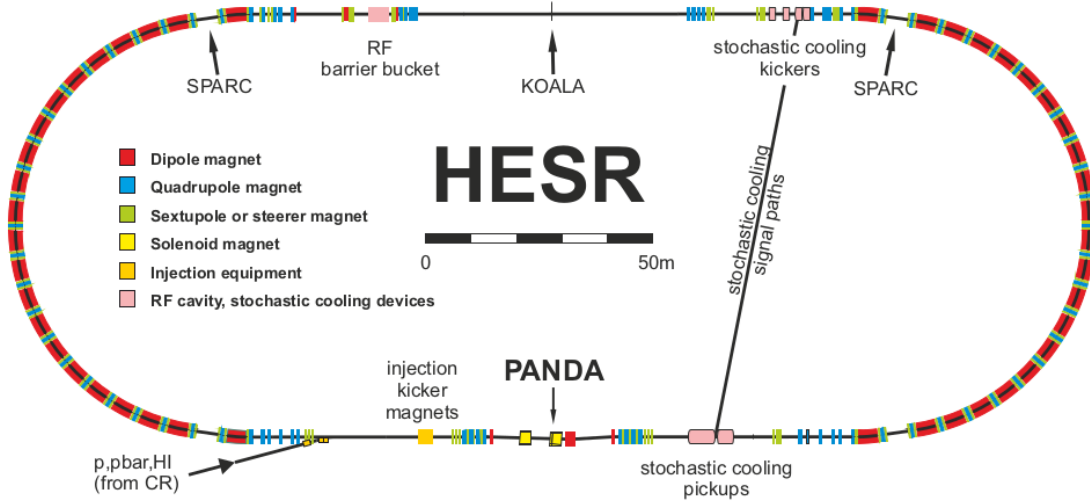


Figure 10.3: Scheme of the HESR [85]

tively. To achieve these values the increased luminosity and higher precision provided by the RESR as well as both electron and stochastic cooling are needed.

As shown in figure 10.3 the HESR is shaped like a race track with two arcs, which bend the beam by 180° , and two straight sections of 155 m length each. In total the circumference sums up to 575 m. The $\bar{\text{P}}\text{ANDA}$ detector will be placed on the same straight section, in which the antiprotons from the CR are injected. The 4.5 MV electron cooling system will be placed on the other straight section at a later stage, currently research and development are performed by means of a 2 MV electron cooling system at the cooler synchrotron (COSY) of Forschungszentrum Jülich [83, 84].

The HESR is composed of 44 dipoles for bending the beam, 84 quadrupoles for focusing the beam, multi-harmonic radio frequency cavities for acceleration and deceleration and cooling devices [79]. The fields of solenoid magnet and the dipole magnet contained in the $\bar{\text{P}}\text{ANDA}$ detector have to be compensated with two additional dipole magnets, one downstream and one upstream of the $\bar{\text{P}}\text{ANDA}$ detector, and a solenoid magnet upstream of the detector [86]. For two further experiments the interest to use the HESR as well has been expressed. The straight section, where the electron cooling system will be placed later on, has been proposed as location for the key experiment for $\bar{\text{P}}\text{ANDA}$ luminosity determination (KOALA) experiment [87]. Since the MSV does not include the new experimental storage ring (NESR), the HESR is considered as an alternative by the stored particles atomic research collaboration (SPARC), which is one of the collaborations under the umbrella of the experimental pillar APPA at FAIR [88].

10.3 The \bar{P} ANDA Detector

The \bar{P} ANDA experiment is based on an antiproton beam hitting a fixed proton target. Besides the proton target also other target materials like deuterium nitrogen or argon can be used in order to fully exploit the experimental potential. Independent of the particular process, the scattering products will be subject to a Lorentz boost downstream along the beam axis. Forward angles in the center of mass system are thus strongly decreased by the coordinate transformation to the laboratory system. Thus the \bar{P} ANDA detector consists of two spectrometers: The target spectrometer contains a superconducting solenoid magnet and surrounds the interaction point (IP), where the target system crosses the beam pipe. The forward spectrometer is located downstream of the target spectrometer and utilizes a dipole magnet so that a good resolution can be obtained for small forward angles in the lab system and a solid angle coverage of almost 4π is achieved. Both spectrometers consist of subdetectors, which cover the remits of charged particle tracking, particle identification and electromagnetic calorimetry so that the four-momenta of all kinds of final state particles can be determined. Figure 10.4 shows a labeled layout of the \bar{P} ANDA detector with the different subdetectors it is composed of. The purpose, functionality and envisaged performance parameters of the different subdetectors will be presented in the following two subsections.

10.3.1 Target Spectrometer

The target spectrometer is arranged in a barrel shape around the beam pipe and contains the target system. The crossing point of the antiproton beam and the proton target defines the IP. Particles emitted from the IP at polar angles below 5° vertically and below 10° horizontally are intentionally not measured in the target spectrometer, but traverse it unaffected to be measured with a higher angular precision in the forward spectrometer.

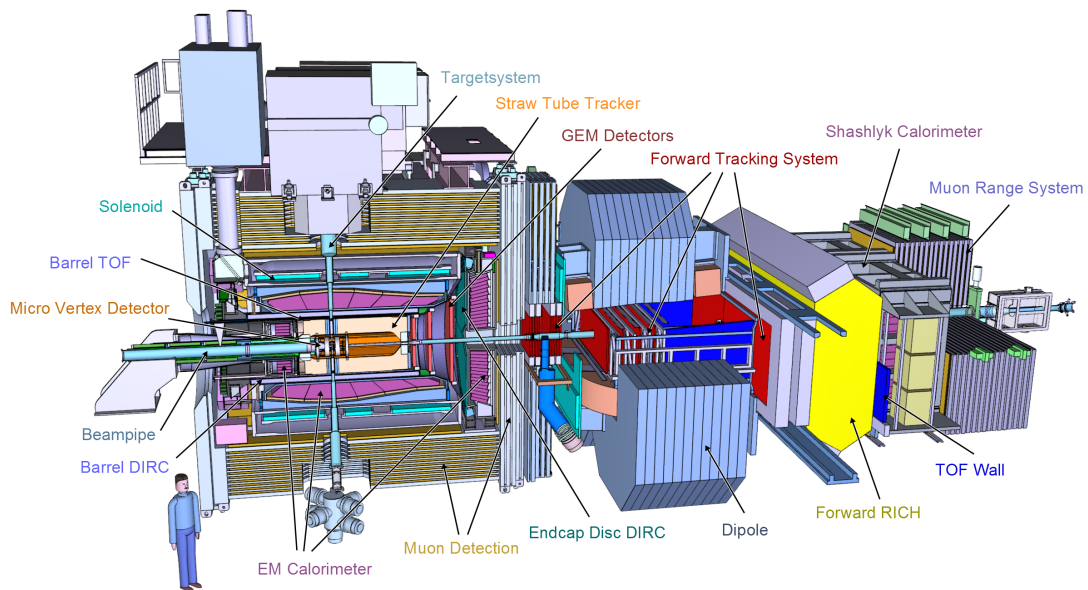


Figure 10.4: Layout of the \bar{P} ANDA detector

	Cluster Target	Pellet Target
Effective Target Thickness	$1 \cdot 10^{15}$ atoms/cm ²	$5 \cdot 10^{15}$ atoms/cm ²
Target Thickness Adjustable	yes (0–max)	yes (by reduction of pellet rate)
Volume Density Distribution	homogeneous	granular
Size Transversal to p Beam	2 – 3 mm	≤ 3 mm
Size Longitudinal to p Beam	15 mm	≤ 3 mm
Target Particle Size	nm scale	20 μ m
Mean Vertical Particle Distance	≤ 10 μ m	2 – 20 mm
Target Material	H ₂ , D ₂ heavier gases optional	H ₂ , D ₂ , N ₂ , Ar heavier gases optional

Table 10.2: Overview of the properties of the two target systems for \bar{P} ANDA [89]

Target Systems

The target density directly influences the luminosity. In order to achieve the peak luminosity of $2 \cdot 10^{32} \text{cm}^{-2} \text{s}^{-1}$ with a number of 10^{11} antiprotons stored in the HESR, the target should have a density of $4 \cdot 10^{15}$ atoms/cm², which corresponds to a mono-layer of atoms. Taking into account that the ultra-high vacuum of a storage ring must not be polluted, the target must be a jet of nano- to micro-sized condensed matter particles (clusters, droplets or pellets) traversing the stored antiproton beam. Actually two target systems, a cluster target system and a pellet target system are planned to be used at the \bar{P} ANDA experiment. Table 10.2 lists the already achieved values for relevant properties, further improvements are to be expected. The cluster jet target provides a homogeneous volume target density, and absence of time structure, but on the downside the interaction point can only be defined by the intersection with the beam. Transversely this is quite precise through the small focal size of the stored beam but longitudinally the uncertainty is at the order of 10 mm. In contrast to that, a pellet target will result to strong fluctuations of the luminosity, but on the upside it is possible to measure the interaction point to a precision at the order of 100 μ m by means of an optical pellet tracking system. At the beginning the cluster-jet target will be used. [89]

Superconducting Solenoid

Except for the outer most detector, which is dedicated to muon identification, all other sub-detectors of the target spectrometer are comprised by a superconducting solenoid magnet with an external iron return yoke. The design is based on internal winding and indirectly cooled aluminum stabilized NbTi cables. The accommodation of the target system, which traverses the magnet upstream of its center is a particular challenge. For symmetry reasons the coil will hence be divided into three sub-coils. The solenoid magnet provides a homogeneous magnetic field with a field strength of 2 T and encloses a cylindrical volume of 2.8 m length with an inner diameter of 1.05 m. In the innermost region, where the tracking detectors are located a homogeneity of better than 2% is foreseen. [86]

Due to the Lorentz force the magnetic field causes charged particles to move on curved tracks according to $|q\vec{v} \times \vec{B}| = |\vec{F}_L| = |\vec{F}_Z| = v \frac{p}{R}$. Thus the curvature provides information about the absolute value of the momentum fraction transverse to the magnetic field.

Micro Vertex Detector

Most hadrons decay so fast, that the location of their decay is indistinguishable from the point, where they were produced. Some particles as for example for D mesons decay slower so that the location of their decay, from which the tracks of all their decay products emerge, is a short distance of some hundred micrometers away from the production point for typical Lorentz boosts of $\beta\gamma \approx 2$. The micro vertex detector (MVD) is optimized for the detection of such secondary vertices. Furthermore the micro vertex detector (MVD) will also strongly increase the transverse momentum resolution by contributing information on the tracks close to the IP. The detector consists of radiation hard silicon detectors which are arranged in four cylindrical shaped barrel layers around the beam pipe with an innermost radius of 2.5 cm and an outermost radius of 13 cm and six layers of disks, which are located at distances of 2 cm up to 23 cm downstream from the IP. The innermost two barrel layers and the four disks closest to the IP consist of hybrid-pixels, whereas for the outer barrel layers and disks double-sided micro-strips are used. In total a polar angle range of 3° to 150° is covered by the MVD. The silicon detectors provide a fast response and a low material budget. The former is important for coping with the high expected interaction rates so that the time resolution must be in the order of 10 ns. The latter is important to avoid multiple scattering of low-energy particles, bremsstrahlung and pair production caused by high-energy particles or loss of photons due to conversion or absorption. The arrangement is chosen such that any track will hit the MVD at least at four different locations and a resolution for the location of secondary vertices of $100 \mu\text{m}$ along the beam axes and few $10 \mu\text{m}$ perpendicular to the beam axis can be achieved. [90]

Straw Tube Tracker

In radial direction the MVD is followed by the straw tube tracker (STT). The STT consists of tubes of $27 \mu\text{m}$ thick aluminized mylar foil filled with an Ar/CO₂ gas mixture. With a diameter of 1 cm and a length of 150 cm the tubes evoke of straws, thus the name. A gold-plated tungsten-rhenium wire with a diameter of $20 \mu\text{m}$ diameter is tensioned at the center. For mechanical stability the straw tubes are operated at an overpressure of 1 bar. [91]

Using the wire as anode and the inner aluminum coating as cathode the straw tubes become in principle proportional counters: Charged particles transversing the tube ionize the gas and create free electrons. Due to the applied voltage the ions drift towards the cathode and the electrons drift towards the anode wire. Close to the wire the electrons are accelerated and ionize the gas themselves thus creating an avalanche effect, which results in an electric signal proportional to the energy deposited by the transversing charged particle.

The straw tubes are arranged in six equal segments with 27 layers each, of which the central eight layers are skewed by $\pm 3^\circ$. These segments form a cylindrical volume with an inner radius of 15 cm, an outer radius of 42 cm and a total length of 165 cm. The in total 4636 straws thus cover a polar angle range from about 10° to 140° . The shape of the signal indicates in which radial distance to the anode wire a charged particle traversed the straw tubes, so that a resolution of better than $150 \mu\text{m}$ can be achieved transverse to the beam axis. The association with hits in the skewed layers provides information on the track position along the beam axis with a resolution of about 3 mm. Besides the tracking information the STT also contributes to the PID by measuring the deposited energy of

the traversing particles. The specific energy loss dE/dx is characteristic for different kinds of particles. From prototype measurements a relative resolution of 8% is expected for the energy loss measurement in the $\overline{\text{PANDA}}$ experiment. [91]

Tracking Stations with Gas Electron Multiplier Based Detectors

Along the beam axis the MVD is followed by three tracking stations with GEM based detectors, which complement the STT for angles below 22° . These stations will be located at distances of 1.1 m, 1.4 m and 1.9 m downstream of the IP, respectively. Due to the relativistic boost of the reaction products these stations have to cope with especially high count rates. The maximal value of $3 \times 10^4 \text{cm}^2 \text{s}^{-1}$ is to be expected for the first station in the vicinity of the beam pipe at a diameter of 5 cm. Compared to drift chambers gaseous micro-pattern detectors based on GEM foils as amplification stages have three orders of magnitude higher rate capabilities. Each tracking station consists of three double planes with two projections per plane. [79]

Detectors Based on Detection of Internally Reflected Cherenkov Light

When a charged particle passes through a solid radiator with refractive index n and its speed $v = \beta c$ is larger than the speed of light in that medium $\frac{c}{n}$, Cherenkov light is emitted on a cone with half opening angle $\cos(\theta_C) = \frac{1}{\beta n}$. For a highly polished rectangular radiator bar the magnitude of the Cherenkov angle will be conserved during all internal total reflections until the Cherenkov photons exit the radiator into the expansion volume. In the expansion volume the Cherenkov ring expands and the position information of the photons can be transformed to a direction measurement. For the analysis of the data the tracking information is needed, as the Cherenkov angle is measured between the Cherenkov photon direction and the momentum vector of the radiating particle. From the Cherenkov angle the velocity can be determined so that the mass of the particle can be estimated from the ratio between momentum and velocity. Two ring imaging cherenkov light (RICH) counters based on the detection of internally reflected cherenkov light (DIRC) principle are planned for the PID at momenta above $1 \text{ GeV}/c$, in particular the distinction between pions and kaons. The barrel DIRC has a radial distance of 50 cm from the beam axis and covers polar angles from 22° to 140° , whereas the end cap disc DIRC covers angles below 22° . [92]

Due to the limited available space within the superconduction solenoid a compact expansion volume material, focusing optics and small pixel sensors are needed. Thus the 16 flat sections which comprise the barrel DIRC contain each three fused silica bar radiators of 240 cm length. At the front end of each bar a flat mirror is attached to reflect photons toward the backward end, where a solid fused silica prism serves as expansion volume. At the back of the 30 cm deep prism the photons are focused by a multi-component spherical lens on an array of lifetime-enhanced microchannel plate photomultiplier tubes (MCP-PMTs) with 8×8 pixels of $6.5 \text{ mm} \times 6.5 \text{ mm}$. The arrival time of the photons can be determined with a precision of 100 ps. [92]

The end cap disc DIRC consists of four independent quadrants of fused silica Cherenkov radiators with a thickness of 20 mm. At the outer rim of each quadrant 96 focusing elements are attached via bars. On the backside the focusing elements have a cylindrical mirror coating on the backside to reflect the photons towards the MCP-PMTs with 3×100 pixels. [93]

Barrel Time-of-Flight Detector

The barrel time-of-flight (TOF) detector has the task to measure the time at which charged particles traverse the detector with a better precision than all other subdetectors. The distinction of kaons from pion can thus be extended to momenta below the threshold of Cherenkov emission. The detector is located at a radial distance of about 50 cm from the beam axis and covers the polar angle range from 22.5° to 140° . It consists of 16 flat so-called supermodules, which exactly match with the DIRC radiators from the outside. Each supermodule contains 120 very fast organic scintillator tiles arranged in two columns of 60 scintillators, which are read out by four silicon photomultipliers (SiPMs) on both ends, that is 960 SiPMs per supermodule. Various geometries, photo sensors and sensor configurations were tested. With the tile geometry $87 \text{ mm} \times 29.4 \text{ mm} \times 5 \text{ mm}$ and the four SiPMs at both ends the best single tile resolution of 60 ps has been obtained, which is well below the originally intended resolution of 100 ps. [94]

Electromagnetic Calorimeter

The purpose of the electromagnetic calorimeter is the efficient reconstruction of electrons, positrons and photons by measuring the deposited energy and the flight direction via the point of impact. The electromagnetic calorimeter of the target spectrometer (TS EMC) is a homogeneous crystal calorimeter. Improved PbWO_4 , lead tungstate (PWO) is chosen as scintillator material due to its good energy resolution, fast response and high density, which allows for a compact setup. In order to achieve a low energy threshold the light yield is increased by operating the TS EMC at -25°C . The TS EMC is subdivided into a barrel part, a forward and a backward endcap, which cover the angular ranges 22° to 140° , 5° horizontally and 10° vertically to 23.6° , and 151.4° to 169.7° , respectively. A more comprehensive description will follow in chapter 11. [95]

Muon System

The aim of the muon system is to identify primary muons with optimal separation from primary low-momenta pions and secondary decay muons. The range system technique is used with mini drift tube (MDT) detectors with fiberglass strip boards and preamplifiers closely integrated into the iron yoke of the superconducting solenoid. Similar as other detectors in the target spectrometer also the muon system comprises a barrel and an end cap in forward direction. Additionally, the so-called muon filter is foreseen as a third part of the muon system in the target spectrometer. It not only increases the depth of absorber for intermediate angles for better detection of muons, but also provides an additional magnetic screen between the solenoid and the dipole. The slots for the accommodation of the MDTs and strip boards in the iron absorbers are chosen to be 3 cm thick for the whole muon system. There are 13 sensitive layers in the barrel part, six in the end cap and five in the muon filter. Besides the inner and outer plates, which are thicker for mechanical reasons the iron absorber layers in the barrel are chosen to be also 3 cm thick, whereas for the end cap and the muon filter a thickness of 6 cm is preferred due to higher average energies for particles in forward direction. Due to the typical multiple scattering of minimal ionizing particles in the iron absorber a pitch of 1 cm for both coordinates given by wires and strips is reasonable. [96, 90]

10.3.2 Forward Spectrometer

The forward spectrometer measures the properties of particles, which emerge under an angle below 5° vertically and below 10° horizontally. The subdetectors are all planes perpendicular to the beam axis.

Dipole Magnet

The dipole magnet has a large aperture of about $1\text{ m} \times 3\text{ m}$ to allow for the angular acceptance of $\pm 5^\circ$ vertically and $\pm 10^\circ$ horizontally at a distance of 3.9 m downstream from the IP. The design is based on resistive race-track coils. With an integrated field strength of 2 Tm it deflects the antiproton beam by 2.2° at the maximum momentum of $15\text{ GeV}/c$. As mentioned above two correcting dipole magnets compensate for the resulting beam deflection. [86]

Forward Tracking System

The Forward Tracking (FT) system consists of three pairs of tracking stations, the first pair is placed upstream of the dipole magnet in the muon filter, the second pair is placed in the aperture of the dipole magnet and the third pair is placed downstream of the dipole magnet. The tracking stations consist each of four double layers with a modular layout. Each module comprises 32 self-supporting straw tubes with a diameter of 1 cm like the ones used in the STT, which are arranged as two staggered layers. The straw tubes of the first and the fourth layer are oriented vertically and the straw tubes of the two intermediate layer are inclined at $+5^\circ$ and -5° , respectively. The active area ranges from $134\text{ cm} \times 64\text{ cm}$ for the first pair to $392\text{ cm} \times 120\text{ cm}$ for the third pair. [97]

Forward Ring Imaging Cherenkov Counter

For the separation between protons, charged pions and kaons in forward direction a ring imaging cherenkov light (RICH) detector is proposed. Using two radiators of silica aerogel with a refraction index of $n = 1.0304$ and perfluorobutane gas (C_4F_{10}) with a refraction index of $n = 1.00137$, respectively, enables a significant separation in the broad momentum range from $2\text{ GeV}/c$ up to $15\text{ GeV}/c$. The material budget of the detector is reduced by using a lightweight mirror, which focuses the Cherenkov light on an array of photo-tubes outside the active volume. [95]

Forward Time-of-Flight Wall

The purpose of the forward time-of-flight (FToF) wall is to measure the time of flight of charged particles emitted with small angles in the acceptance of the forward spectrometer. Thus the sensitive area measures $560\text{ cm} \times 140\text{ cm}$ at a distance of about 7.5 m downstream of the IP. In combination with the information on the particle momentum provided by the Forward Tracking (FT) system the forward time-of-flight (FToF) wall enables reliable p/K and K/π separation momenta below $4.3\text{ GeV}/c$ and $3\text{ GeV}/c$, respectively, and thus complements the RICH detector at low momenta. The wall consists of 66 plastic scintillation counter slabs with a length of 140 cm and a thickness of 2.5 cm. In test measurements a timing resolution below 100 ps has been obtained. [98]

Forward Shashlyk Calorimeter

In the forward spectrometer a shashlyk-type sampling calorimeter fulfills the task of measuring the energy of photons, electrons and positrons over a large energy range from some MeV up to about 15 GeV. Lead plates of a thickness 0.275 mm doped with 3% of antimony to improve their rigidity are stacked alternating with scintillator plates of doped polystyrene in a thickness of 1.5 mm to form modules of in total 380 layers. The effective radiation length is determined to 34 mm and the effective Moliere radius to 35 mm. The total length of 675 mm corresponds hence to about 20 radiation lengths. In total 378 modules each composed of four independent cells of 55 mm \times 55 mm size cover an area of 3 m \times 1.5 m. Since the forward shashlyk calorimeter (FSC) is not located in a magnetic field PMTs are the most proper photosensors. Different prototypes were built and tested with beams. A prototype consisting of 64 cells arranged in a 8 \times 8 matrix has demonstrated that the stochastic energy resolution is with 3% below the required 4% and also the stochastic position resolution of 8 mm fulfills the requirements. With the implementation of additional reflector material and wavelength shifting fibers the light yield could be almost doubled and a satisfying reproducibility and homogeneity of the cells have been achieved. [79]

Forward Muon Range System

At a distance of about 9 m downstream from the IP a further muon range tracking system consisting of interleaved absorber layers is dedicated to the identification of muons in the forward spectrometer. The design of the muon system in the forward spectrometer is similar to the muon system of the target spectrometer, but for higher momenta, as 16 iron absorber plates of 6 cm thickness and a 380 cm \times 256.5 cm surface alternate with 16 detector layers of 3 cm thickness. Besides the discrimination of pions from muons the system also serves as a hadronic calorimeter with a moderate energy resolution. [96]

Luminosity Monitor

Precise knowledge of the integrated luminosity is crucial for absolute cross section measurements and scanning experiments. The luminosity can be determined by using the differential cross section of elastic $\bar{p}p$ scattering in dependence of the scattering angle. Since there are large systematic uncertainties for the cross section dependence on the scattering angle previously measured, the measurement is performed at very small scattering angles, where the Coulomb part of the elastic cross section dominates so that this part can be calculated precisely. [99]

The luminosity monitor is located about 10 m downstream of the IP and covers a polar angle range from 3 mrad to 8 mrad. As mentioned above at the end of section 10.2 parameters for the description of the differential elastic cross section will be measured by the KOALA experiment, because for high energies the hadronic contribution cannot be neglected anymore even at small angles. [87, 99]

The luminosity monitor comprises four sensor planes with 10 cm or 20 cm between them. Each plane contains 10 diamond wafers with a thickness of 200 μ m as support modules. The high voltage monolithic active pixel sensors (HV-MAPS) sensors with a pixel size of 80 μ m \times 80 μ m and a thickness of 50 μ m are glued on the modules from both sides. [99]

10.3.3 Detector Control System and Data Acquisition

Even though it is not included in the brief descriptions of the subdetectors of course also dedicated front end electronics (FEE) as well as monitoring and control systems have been developed, too. Hence, besides the signals generated by the subdetectors for the purpose of four-momentum determination for final state particles, most subdetectors also generate data from sensors monitoring detector conditions as currents, voltages, temperatures, humidity and so on and require according control, e.g. of supply voltages or cooling systems. The \bar{P} ANDA detector slow control (DCS) has the purpose to monitor and control all the experimental equipment of the \bar{P} ANDA detector and ensure the safe and efficient operation of the \bar{P} ANDA experiment.

The core software of the DCS is the experimental physics and industrial control system (EPICS) framework. Since an EPICS-based control system has a distributed architecture it is possible to test each subdetector autonomously and combine the individual control systems successively to one system. All the data transmitted to the DCS as well as the issued alarms will be stored in databases. [100]

In order to reduce the enormous data rates to be recorded at accelerator based experiments, usually a subset of specially instrumented detectors is used as trigger already on the hardware level, followed by one or several following software level triggers. In contrast to that the \bar{P} ANDA experiment adopts a free-running data acquisition (DAQ) concept, in order to fully exploit the high interaction rate of up to $2 \cdot 10^7$ events per second and allow as much flexibility as possible to match the complexity of the experiment and diversity of the physics objectives. That means, that every subdetector system runs autonomously in a self-triggering mode. All subdetectors perform a continuous online calibration with data, to maintain high data quality. The recorded signals are preprocessed by the respective subdetector and the relevant information is extracted and transmitted, which substantially reduces the data rate. That means algorithms for hit-detection, noise-suppression and cluster finding have to be provided by the FEE. The data related to a particle hit is buffered by data concentrators and marked by a precise time stamp provided by the synchronization of data acquisition (SODA) system, which has also access to information on beam structure, which for technical reasons contains $2 \mu\text{s}$ bursts and $500 \mu\text{s}$ super bursts. At this level a data rate of 200 GB/s is expected. Compute nodes employing fast FPGAs provide feature extraction, event building and event selection according to the current trigger scheme. The association of data fragments to events is a particular challenge, as the event data delivered from the various subdetectors with different timing must not be mixed up even at high interaction rates. The precise timing of the TOF detectors is a key to overcome this challenge by determining the collision time of the event and perform sound pattern recognition, online tracking and PID, which iteratively increase the accuracy. The data reduced to a rate of 100-200 MB/s will then be saved to mass storage. [86, 90, 94]

11 The Electromagnetic Calorimeter of the Target Spectrometer

Before going into the details of the PANDA TS EMC layout, the relevant physics are described briefly.

11.1 Physics Relevant for Calorimetry

The main purpose of an EMC is the measurement of the energy of photons, electrons and positrons. In order to measure the energy of an incident particle, all its energy must be transferred to the surrounding material. In particular materials a flash of light is generated with an intensity proportional to the transferred energy, which can then be measured by suitable photosensors. Sampling calorimeters split these two tasks between different materials, whereas homogeneous calorimeters fulfill both tasks with the same material. The TS EMC is a homogeneous crystal calorimeter, whereas the electromagnetic calorimeter of the forward spectrometer is a shashlyk-type sampling calorimeter.

11.1.1 Interaction with Matter

Three different processes are relevant for the energy loss of photons in matter: The photoelectric effect is dominant for photon energies below 1 MeV. The effect occurs, when an electron absorbs the energy of the photon, so that its energy exceeds the binding energy of the respective material and it is ejected. When a photon scatters elastically on a free particle, its energy decreases. This effect is called Compton scattering and dominates for medium photon energies from 1 MeV to 5 MeV. Pair production is the dominating effect for photon energies above 5 MeV. The energy of the photon can be converted into an electron-positron pair in the presence of a Coulomb field, for example of an atomic nucleus. The kinetic energy of electron and positron correspond to the energy excess of the photon energy compared to their rest masses.

Electrons and positrons loose energy in matter due to collisions, for example with electrons which will then be excited or even knocked out of from the atom or molecule, but also due to radiative processes, such as bremsstrahlung. Positrons annihilate after losing most of their energy by the processes described above.

11.1.2 Electromagnetic Cascades

When a high-energy electron or photon enters an absorber, bremsstrahlung and pair production recur alternating and generate more electrons and photons with lower energy. Hence an electromagnetic cascade is created as illustrated in figure 11.1 (left). The dimension of electromagnetic cascades depends on the respective material. In longitudinal direction it is described by the radiation length X_0 , which is defined as the mean distance over which a high-energy electron loses all but $\frac{1}{e}$ of its initial energy by bremsstrahlung.

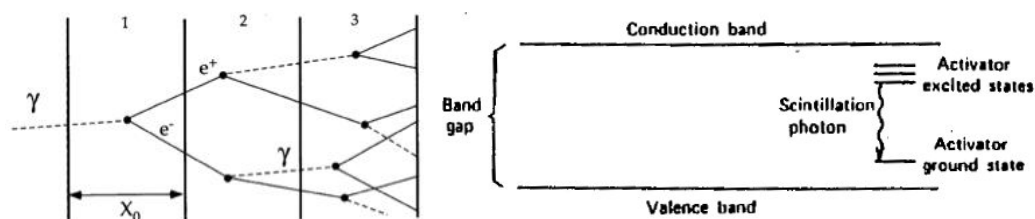


Figure 11.1: Formation of an electromagnetic cascade [102] (left); Energy band structure of an activated crystalline scintillator [101] (right)

For a high-energy photon one radiation length equals the fraction of $\frac{7}{9}$ of the mean free path for pair-production. The Molière radius describes the transverse size of an electromagnetic cascade and is defined as the radius of a cylinder, which contains 90% of its energy. [1]

11.1.3 Scintillation

The phenomenon, that certain materials flash when ionizing radiation is absorbed, is called scintillation. This property depends on the existence of excitation levels with an energy difference that corresponds to a wavelength for which the material is transparent. In case of organic materials the electronic structure can provide such a characteristic. For inorganic crystals as used for the PANDA TS EMC the bandstructure is relevant for the scintillation process. After the formation of an electromagnetic cascade numerous electrons will populate the conduction band instead of the valence band, resulting to electron-hole pairs which migrate along the lattice. Most of these pairs deexcite due to collisions with phonons, but some deexcite by the emission of a photon. Since the energy of the photon corresponds to the energy difference between valence and conduction band, such a photon is most likely absorbed by an electron being lifted to the conduction band, before it leaves the material. At the sites of imperfections for example due to doping, the bandstructure is changed and additional energy states in the gap between valence and conduction band become accessible. Such locations are called activator site. As shown in figure 11.1 (right) the transition energy from an excited state to a ground state in the activator is smaller than at a typical lattice site, the crystal is thus transparent for photons generated by a deexcitation at an activator site. The number of emitted photons corresponds strongly to the energy deposited by the incident particle. [101]

11.2 Layout of the PANDA TS EMC

In many decay channels of interest for the PANDA physics program numerous photons, electrons or positrons occur in the final state. In order to fulfill the purpose of detecting electron, positron and photon energies with high efficiency, it is important to cover at best the full solid angle and have a minimal energy threshold, to miss particles neither spatially nor because their energy is out of range. [95]

11.2.1 Requirements on the Energy Measurement

The acceptance of low energy photons is determined by the minimum photon energy E_{thres} , which is accessible with the TS EMC. The dependence of the photon energy threshold on

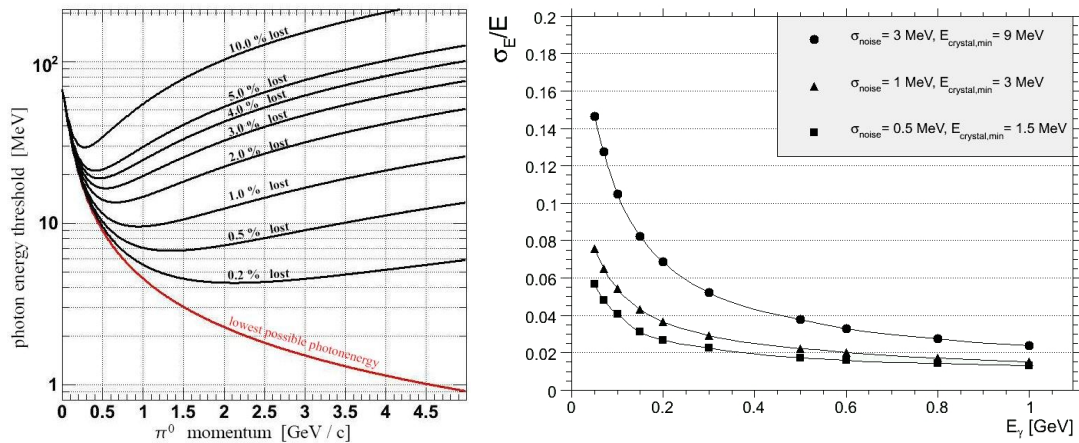


Figure 11.2: Energy threshold vs. π^0 momentum for different π^0 loss rates [95] (left) Comparison of the energy resolutions for different single crystal thresholds [95] (right)

the π^0 momentum is shown in figure 11.2 (left) for different π^0 loss rates. In order to lose not more than 1% of the π^0 mesons, a photon energy threshold of $E_{\text{thres}} = 10$ MeV is aimed for. [95]

The precise measurement of electron and positron energies is not only important for its own sake, but also for a very accurate E/p determination, in order to distinguish electrons and positrons from charged hadrons. Hence the energy resolution should be small compared to the momentum uncertainty from the tracking detectors. A resolution of $\frac{\sigma_E}{E} \leq 1.0\%$ is thus envisaged at high energies. [95]

Since π^0 and η mesons decay into two photons, an undetected photon results into background issues. Thus especially for radiative decay channels with an isolated photon, the efficient identification of π^0 and η mesons is crucial. From experiences of former experiments it is known, that a π^0 width of less than 8 MeV and an η width of less than 30 MeV is mandatory for a sound final state decomposition. At low energies the width of π^0 and η mesons is constituted by the $\frac{1}{\sqrt{E}}$ dependence of the energy resolution, while it is described by a constant term at high energies. In order to tackle the envisaged physics goals of the \bar{P} ANDA experiment, the energy resolution should be

$$\frac{\sigma_E}{E} = \leq 1\% \oplus \frac{\leq 2\%}{\sqrt{E[\text{GeV}]}}$$

where \oplus represents addition in quadrature and the energy should be put in the equation in GeV. Figure 11.2 (right) shows, that a single crystal threshold of $E_{\text{xtl}} = 3$ MeV must be achieved to obtain the intended energy resolution. [95]

Usually the energy resolution of an electromagnetic calorimeter is parametrized as

$$\frac{\sigma_E}{E} = \frac{a}{\sqrt{E[\text{GeV}]}} \oplus b \oplus \frac{c}{E}.$$

The term scaled with a represents statistics-related fluctuations such as intrinsic shower fluctuations, photoelectron statistics, and sampling fluctuations. The constant term scaled with b represents the systematic uncertainty for example due to detector non-uniformity and calibration uncertainty. The term scaled with c covers the uncertainty caused by electronics noise of the readout channels involved in the respective cluster. [1]

11.2.2 Hit Rate and Radiation Hardness Requirements

Instantaneous hit rates of up to 50 MHz per crystal are to be expected. Thus the resolution for the hit time may at most be 3 ns. In order to collect the whole signal, the shaping time of the preamplification stage should be longer than the actual decay time of the scintillation mechanism. Larger shaping times also reduce the noise level, but on the other hand too long shaping times lead to pile-up. With a pile-up hit recovery system pile-up rates up to 10% can be tolerated, resulting to an envisaged shaping time of ≈ 100 ns for the forward endcap and ≈ 400 ns for the barrel and backward endcap, respectively. [95]

Simulations of generic $p\bar{p}$ annihilation events have shown that for the highest beam momenta the innermost crystals accumulate an energy of 25 mJ/h. For a crystal weight of 1 kg and a typical annual operation of at most 5000 h, that corresponds to a maximal annual dose of 125 Gy for the forward crystals. For the backward endcap a maximal energy dose of 30 μ J/h (0.15 Gy annually) and for the barrel 1.4 mJ/h (7 Gy annually) is obtained, respectively. [95]

11.2.3 Properties of the Scintillator Material PWO

Since the $\bar{\text{P}}\text{ANDA}$ TS EMC is located inside the superconduction solenoid, the scintillator material must have a short radiation length to enable a compact design. Due to the high interaction rate a fast responding and radiation hard material is needed. A high light yield is necessary to fulfill the ambitious requirements for the energy resolution and efficiency. PWO as an extremely fast, compact and radiation hard scintillator material meets most of these requirements. Due to the usage in several calorimeters of large scale experiments such as CMS or ALICE at the LHC at CERN procedures for mass production have already been developed. In another extended research and development program the light yield could be increased drastically, especially combined with an operation at a low temperature. The choice of the operation temperature is a trade-off between increasing the light yield and decreasing the radiation hardness with decreasing operating temperature. As a compromise -25°C is chosen as operating temperature. Table 11.1 lists the relevant parameters of the original scintillator material PWO and the improved scintillator material PbWO_4 , lead tungstate with increased light yield (PWO-II). [95]

Parameter	PWO	PWO-II
ρ [g/cm ³]		8.28
X_0 [cm]		0.89
R_M [cm]		2.00
τ_{decay} [ns]		6.5
λ_{max} [nm]		420
n at λ_{max}	2.24	2.17
Relative LY [% (LY NaI)] at RT	0.3	0.6
Relative LY [% (LY NaI)] at -25°C	0.8	2.5
Hygroscopic		no
$\frac{d(\text{LY})}{dT}$ [%/ $^\circ\text{C}$] at RT	-2.7	-3.0
$\frac{dE}{dx}$ [MeV/cm]		10.02

Table 11.1: Relevant properties of PWO and PWO-II [74]

11.2.4 Geometric Layout

Since undetected photons are an important cause for background events, it is crucial to cover at best the full solid angle with the detector. As shown in figure 11.3 the TS EMC is composed of three parts, the backward endcap, the barrel and the forward endcap. The forward endcap has a hole around the beam pipe through which particles can escape unaffected, so that they can be measured with higher spatial resolution in the forward spectrometer. It covers azimuthal angles $5^\circ \leq \theta \leq 23.6^\circ$ in the horizontal direction and $10^\circ \leq \theta \leq 23.6^\circ$ in vertical direction. The barrel covers azimuthal angles $22^\circ \leq \theta \leq 140^\circ$. Thus the barrel and the forward endcap parts overlap so that all particles can be measured by at least one of them. The backward endcap also has a hole around the beam pipe and covers only azimuthal angles $151.4^\circ \leq \theta \leq 169.7^\circ$. The gap between the backward endcap and the barrel cannot be avoided, because this space is needed to feed through cooling pipes, voltage supply and signal cables from the inner tracking detectors. [95]

To avoid the escape of photons or charged particles through gaps between neighboring scintillator crystals, the crystals are not aligned with the interaction point, but are arranged in an offpointing geometry. The crystals of the barrel are tilted along the beam axis and transversal to the beam axis by 4° compared to the interaction point so that they are pointing to a ring around the beam axis. The crystals of the backward endcap are aligned with a point on the beam axis and 200 mm downstream of the target, while the crystals of the forward endcap are aligned with a point on the beam axis and 950 mm upstream of the target. [95]

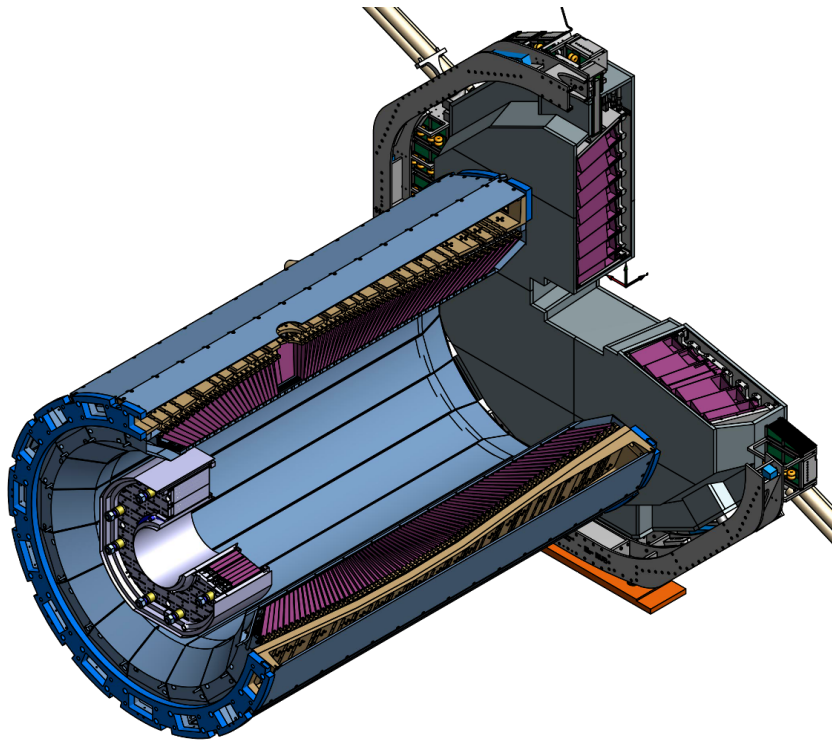


Figure 11.3: Composition of the TS EMC in backward endcap, barrel and forward endcap [103]

The spatial resolution of the TS EMC is mainly determined by the granularity in individual crystals. In order to distinguish two overlapping clusters, which originate for example from π^0 decays into two photons with a small opening angle, from a single cluster, the points of impact must be separated by at least two crystals so that two local maxima appear in the energy deposition. The lateral size of an individual crystal should thus not exceed the smallest π^0 opening angle to be expected. Also the mass resolution of for example the π^0 depends on the granularity. In a dedicated study the requirements on the lateral crystal size have been determined for all three parts of the TS EMC.

The crystals used in the barrel have eleven different shapes, whereas the crystals used in the forward and backward endcap have all the same shape each. The length of the crystals is 200 mm, which corresponds to 22 radiation lengths for lead tungstate with $X_0 = 0.89$ cm, to ensure that the electromagnetic showers caused by photons, electrons or positrons are fully contained. The lateral size is in the order of the Moliere radius $R_M = 2$ cm, so that the shower shape can be determined by the varying energy deposit of different crystals in the cluster. This information is needed for both, obtaining a good spatial resolution and discriminating electrons and positrons from charged hadrons.

The crystals used in the backward endcap are of rectangular shape, with a front face of $24.4 \text{ mm} \times 24.4 \text{ mm}$ pointing towards the interaction point. The crystals used in the barrel are significantly tapered with different angles varying along the beam axis. The lateral size of the front faces varies only very little between 21.18 mm and 22.02 mm, whereas the lateral size of the rear faces varies between 24.35 mm and 29.04 mm.

The crystals used in the forward endcap have two slightly tapered neighboring side faces. The other two crystal side faces have a right angle between each other and to the front and the rear faces, so that four crystals form a right square frustum. The front faces measure $24.4 \text{ mm} \times 24.4 \text{ mm}$ and the rear faces $26 \text{ mm} \times 26 \text{ mm}$. [95]

Table 11.2 compiles the main requirements put on the TS EMC.

Common properties	Required performance value		
Energy resolution σ_E/E	$\leq 1\% \oplus \frac{\leq 2\%}{\sqrt{E[\text{GeV}]}}$		
Energy threshold (photons) E_{thres}	10 MeV		
Energy threshold (single crystal) E_{xtl}	3 MeV		
RMS noise (energy equiv.) $\sigma_{E,\text{noise}}$	1 MeV		
Angular coverage % of 4π	99%		
Subdetector specific properties	backward ($151.4^\circ - 169.7^\circ$)	barrel ($22^\circ - 140^\circ$)	forward ($5^\circ - 23.6^\circ$)
Energy range from E_{thres} to	0.7 GeV	7.3 GeV	14.6 GeV
Angular equivalent of crystal size θ		4°	1°
Spatial resolution σ_θ	0.5°	0.3°	0.1°
Maximum signal load f_γ ($E_\gamma > E_{\text{xtl}}$)		60 kHz	500 kHz
Shaping time t_s		400 ns	100 ns
Radiation hardness	0.15 Gy	7 Gy	125 Gy

Table 11.2: Main requirements for the TS EMC [95]

11.2.5 Photosensors

Besides the scintillator material the most crucial components of an electromagnetic calorimeter are the photosensors, which convert the scintillation light into an electrical signal.

Avalanche Photodiodes

Since the TS EMC is located in the magnetic field of the superconducting solenoid, no conventional PMTs can be used. Even after increasing the light yield by a factor of four by operating at a temperature of -25°C , the light yield of PWO-II is relatively low so that the photosensors must provide internal amplification. Additionally they should be radiation hard at -25°C .

Silicon avalanche photo diodes (APDs), which fulfill these requirements and are insensitive to magnetic fields, have already been developed in cooperation between compact muon solenoid (CMS) and Hamamatsu Photonics. By investing more research and development time it has been possible to enlarge the photosensitive area to the size of $14\text{ mm} \times 6.8\text{ mm}$, resulting in the large area avalanche photo diodes (LAAPDs) used in the TS EMC. A technical drawing of such an LAAPD and its different layers is shown in figure 11.4.

Photons, which enter the LAAPD via the p^{++} doted layer, are absorbed in the following p^+ doted layer by exciting electrons so that electron-hole pairs are generated. A reverse bias voltage is applied so that the electrons are accelerated in direction of the pn transition. Due to the acceleration they have enough energy to create new electron-hole pairs themselves and an avalanche of electrons is created. When the avalanche of electron-hole pairs reaches the n^{++} doted layer, it results in an electric signal.

The quantum efficiency, which is defined as the ratio of electron-hole pairs produced in the p^+ doted layer to incident photons of the APDs, is approximately 70% at the wave length of lead tungstate scintillation photons. As to be expected for a semiconductor the LAAPD gain is strongly temperature dependent. Figure 11.5 shows the LAAPD gain versus supply voltage at different temperatures. For the same applied voltage the gain increases with decreasing temperature, since there are less lattice oscillations decelerating the electrons.

Defects caused by ionizing radiation result in a reduced gain and can thus be compensated to a certain level by applying a higher voltage. Thus LAAPDs are well suited for usage in the barrel and backward endcap, but only partly suitable for usage in the forward endcap, which is especially radiation exposed at its inner most region. [95, 61]

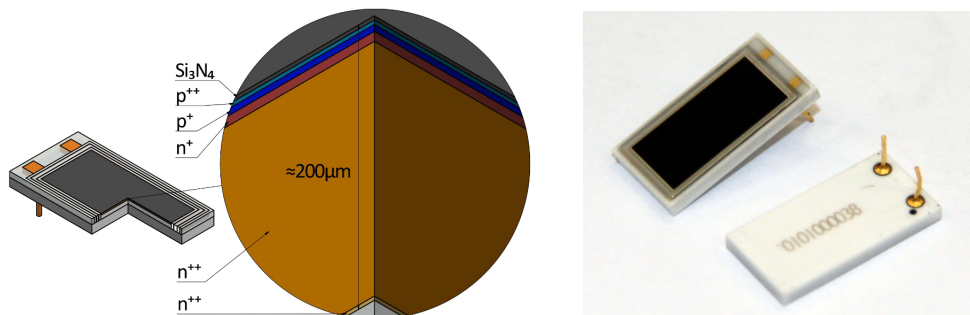


Figure 11.4: LAAPD as used for reading out the scintillator crystals of the \bar{P} ANDA TS EMC shown with its different layers in a CAD [104] (left) and in a photograph [62] (right)

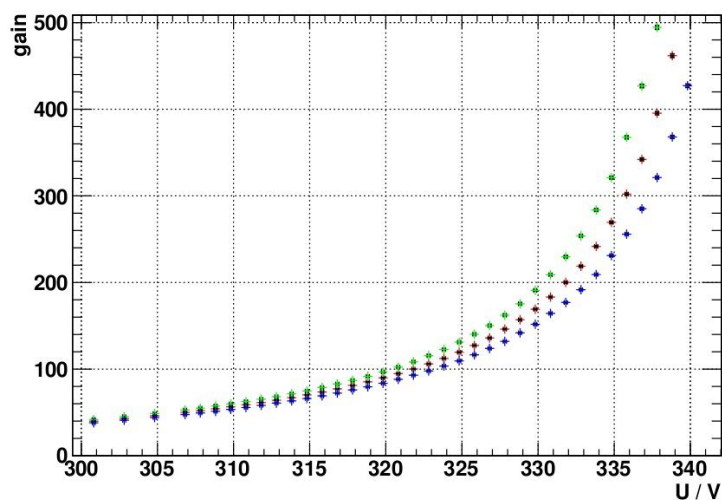


Figure 11.5: APDs gain vs. voltage at -23°C (blue), -25°C (purple) and -27°C (green) [61]

Vacuum Phototetrodes

For the crystal readout of the innermost region of the forward endcap vacuum phototetrodes (VPTTs) developed by Hamamatsu Photonics are used. These consist of a vacuum glass tube with a photo cathode applied to their front face, a mesh anode and two dynodes arranged parallel behind each other as shown in figure 11.6. The use of special fused silica for the glass body enhances their radiation hardness.

A photon that hits the cathode material, ejects an electron via the photo effect. This electron is then accelerated towards the first mesh dynode passes through it and is accelerated further towards the mesh anode. At both meshes secondary electrons are ejected and as well accelerated. Some electrons pass the anode and hit the second dynode, where further secondary electrons are ejected. These are accelerated back towards the anode, where they generate a signal. The gain of VPTTs is almost independent of the operating temperature, but depends significantly on the strength and orientation of external magnetic fields. [95, 61]

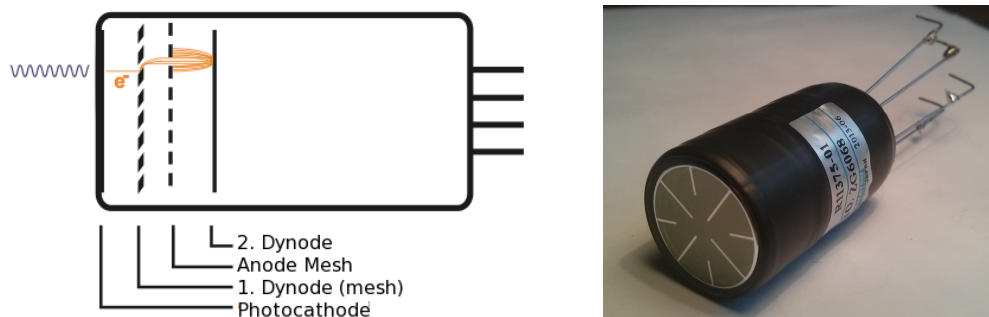


Figure 11.6: Functional principle of a VPTT [61] (left) and a photograph of a VPTT [62] (right)

11.2.6 Thermal Requirements

Since both the light yield of lead tungstate and the gain of APDs is temperature dependent, not only the operation temperature should be chosen reasonably, but also temperature variations should be avoided, because these worsen the energy resolution.

As shown in figure 11.7 the light yield increases at lower temperatures to a factor of approximately 3.5 at -25°C compared to $+25^\circ\text{C}$. Similarly the derivative gets more negative, so that the absolute temperature dependence increases at lower temperatures. At -25°C the temperature dependence of the light yield is $\frac{d(LY)}{dT} = -3\%/^\circ\text{C}$.

Variations of the light yield due to temperature variations result in a systematic uncertainty. As stated at the end of subsection 11.2.1, such an uncertainty is accounted by a constant term of the relative energy uncertainty. A decline of the energy resolution due to temperature variations should thus be small compared to the intended limit for the constant term of approximately 1%. Requiring the energy uncertainty caused by temperature variations to be less than $\sigma E, \sigma_T < 0.2\%$, a temperature deviation of at most

$$\sigma_{E, \sigma_T} \approx \frac{d(LY)}{dT} \sigma_T \Rightarrow \sigma_T \approx \frac{\sigma_E, \sigma_T}{\frac{d(LY)}{dT}} = 0.07^\circ\text{C}$$

would still be acceptable. This deviation corresponds to the second momentum of a uniform distribution with the peak-to-peak variation

$$\Delta T = \sqrt{12} \sigma_T \approx 0.24^\circ\text{C},$$

so that the temperature variation within the TS EMC should not exceed $\pm 0.1^\circ\text{C}$. [60]

Besides temporal instability also spatial inhomogeneities of the temperature distribution influence the energy resolution. Simulation studies have shown that the temperature gradient should not exceed $0.1^\circ\text{C}/\text{mm}$, which corresponds to 2°C along the length of a crystal [105]. Figure 11.8 shows results of this simulation study, where e.g. 10% inhomogeneity means that the light yield differs from the front side to the rear side of the crystal by 10% due to the temperature gradient along the crystal. These 10% correspond to a temperature difference of approximately 3.3°C between front and rear face at an operating temperature of -25°C .

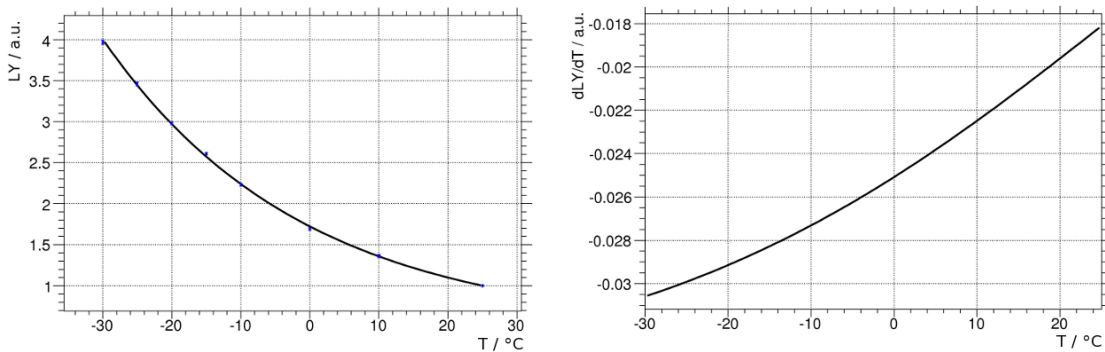


Figure 11.7: Light yield of PWO-II in dependence of temperature normalized to one at 25°C (left) and the first derivative of its temperature dependence (right) [105]

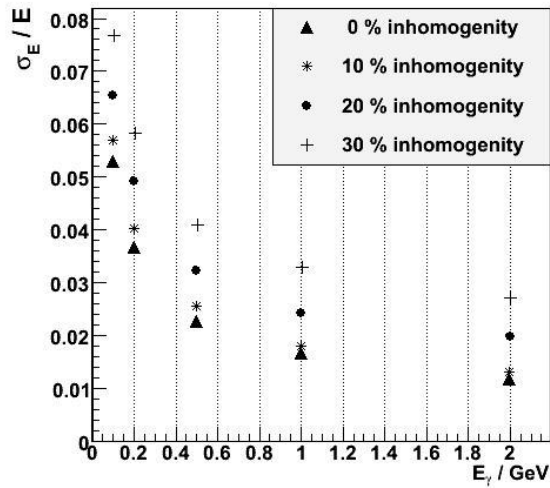


Figure 11.8: Energy resolution of the TS EMC against different incident photon energies for differently severe inhomogeneities of light yield along the scintillator crystals due to a temperature gradient [105]

12 The Forward Endcap of the TS EMC

The group of Prof. Wiedner at the Institut für Experimentalphysik I of the Ruhr-Universität Bochum is responsible for designing and manufacturing the forward endcap of the TS EMC. A prototype named Proto192 has been built so that several tests could be performed and the design of the forward endcap has been finalized to the version presented in the following. By several beam times at different accelerators the energy threshold and resolution have been determined [62, 106].

12.1 Mechanics, Cooling and Insulation

The core component of the forward endcap from the mechanical point of view is the aluminum backplate. With a diameter of 2.1 m and a thickness of 30 mm this aluminum plate is not only the central support structure to which the submodules containing crystals and photosensors will be mounted, but it also incorporates the main cooling system. A lot of holes and drills for feeding through cables, locking submodule positions and mounting them are visible in figure 12.1. In addition the backplate has long vertical drills and U-turns through which a 60:40 methanol-water mixture will be pumped to cool the forward endcap down to -25°C .

At the inner and outer edge of the backplate the so-called inner and outer stiffener rings are attached, which increase the stability of the forward endcap. In addition to the main cooling system, there will also be three cooling pipes mounted into grooves at the inside of the outer stiffener ring as shown in figure 12.2 (left) and hoses with cooling liquid in front of the crystals, which are glued to the 0.8 mm thin aluminum front cover plate. The space between the crystals and the front cover plate is so small, that the tilted alignment of the submodules is exploited to find space for the hoses. The foreseen course of the two front cooling hoses is depicted in figure 12.2 (right). The complete liquid cooling system is working at pressures below the atmospheric pressure, so that even in case of leakage, the cooling liquid does not flood the detector.

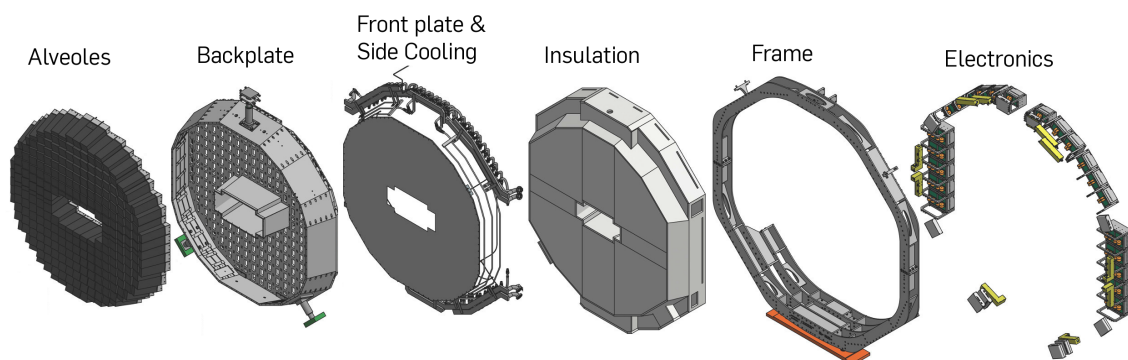


Figure 12.1: Exploded view of the components of the TS EMC forward endcap

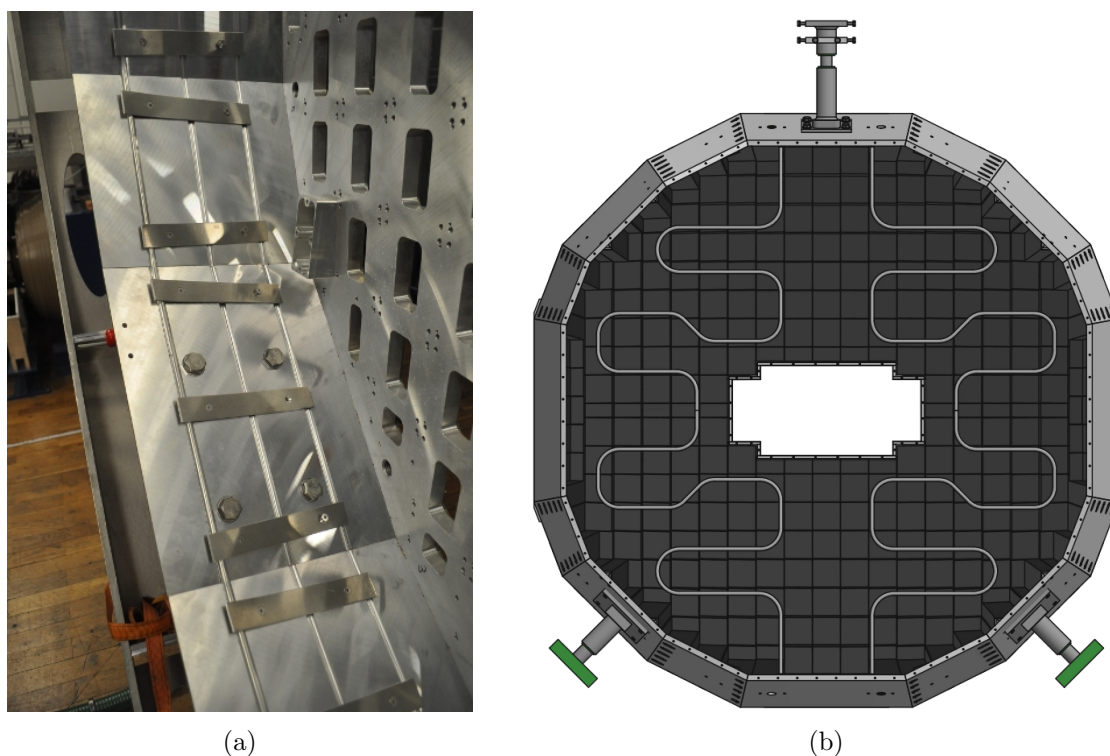


Figure 12.2: Grooves and clamps for the side cooling pipes (a) and course of the front cooling hoses (b) [21]

Also the backside of the backplate is covered with a 3 mm thick aluminum plate with the 30 mm thick electronics frame in between to leave space for cables. The airtight enclosed volume is flushed with cooled, dried air as a fourth cooling system, which prevents condensation and the formation of ice.

The insulation of this cooled volume is realized with vacuum insulation panels based on a fumed silica core. Besides the very low thermal conductivity which allows for a compact design, the vacuum insulation panels can not only be easily machined, but provide also many advantages for the usage in the forward endcap: sufficient radiation hardness, low mass density, and temperature resistance over a sufficient range of -70°C to $+70^{\circ}\text{C}$ enabling production of exceptional shapes with tilted edges. Due to spacial limitations the front insulation consists of only one layer which has a thickness of 15 mm. In contrast to that the back insulation consists of two layers which each have a thickness of 10 mm. The division into tiles is chosen differently for the two layers to avoid thermal bridges. For a total thickness of 20 mm a thermal conductivity of $\lambda \leq 5 \text{ mW}/(\text{m K})$ is expected. More details concerning the layout of the cooling systems and the insulation are presented in [21].

The mechanical support of the cooled volume is achieved by three massive bolts which connect the outer stiffener ring with the support frame. These bolts are made of two parts with a layer of PET in between them to provide thermal insulation.

The electronics components, which need to be mounted in close proximity to the submodules, are presented in the next section.

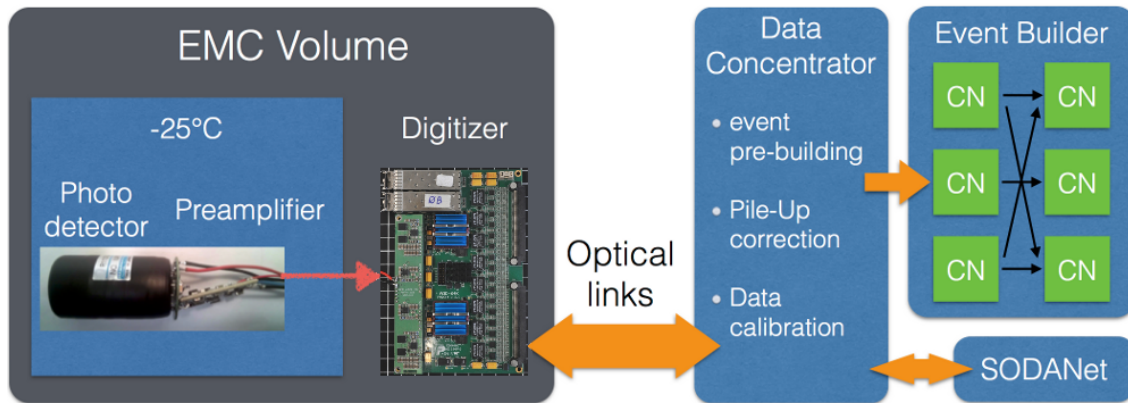


Figure 12.3: Scheme of the EMC readout[62]

12.2 Electronics

The front-end electronics, which needs to be as close as possible to the detector but is unsuited for operation at a temperature of -25°C , is directly mounted to the support frame. In the following only the readout-chain and the light pulser system are presented, the THMP will be presented in detail in chapter 14.

12.2.1 Readout-Chain

Once the signal cables are routed out of the cooled volume, they are connected to the backplane of crates customized for the forward endcap, which contain seven to fifteen digitizer boards. After an analog filtering the signals on these boards are split, with one branch being further amplified (high gain) and leaving the other one unmodified (low gain). Splitting the signals hence enables to achieve a good energy resolution even for small signals, whereas the full dynamic range can still be covered. In order to be able to perform an online feature extraction, the digitization boards based on Kintex-7 FPGAs continuously sample the output of a 14-bit ADC at a rate of 80 MHz. The extracted information is transmitted via optical fibers to data concentrators for further analysis, these pass the data on to the network of computer nodes, where event building based on the data received from different subdetectors is performed. After the event building, the data is transferred to an online computing farm and then finally gets permanently stored. The SODA protocol provides precise timestamps attached to the data. The concept of the readout chain is shown in figure 12.3.

12.2.2 Light Pulser System

A decrease of the signal yield can be caused at any stage of the readout chain, which includes the scintillator crystals, the photosensors, the preamplifiers, and the digitization board. The transparency of the crystals decreases with increasing radiation damage in such a way that the absorption of red light is less affected than the absorption of blue light. To monitor the complete readout chain, a system consisting of several light pulser modules which generate blue, green and red light distributes the light pulses via light fibers to all scintillator crystals (cf. figure 12.4). Thus different causes for decreased light yield of an individual readout channel can be identified.

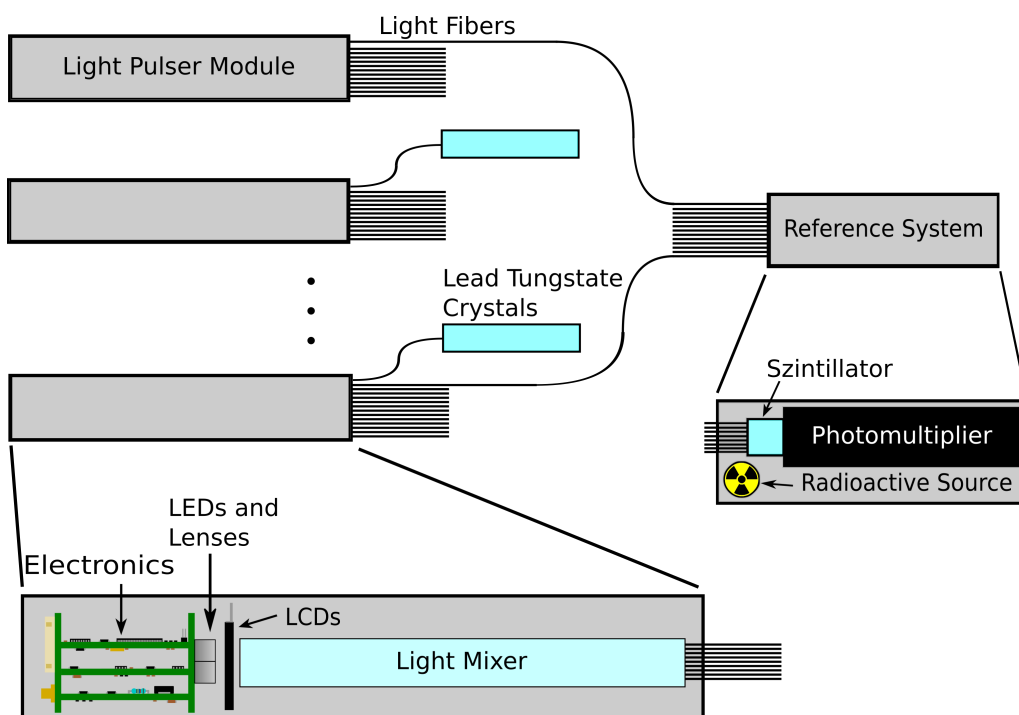


Figure 12.4: Schematic overview of the light pulser system [63]

The light pulser system consists of light pulser modules, light fibers and a reference system. The intensity of the light pulses can be varied by the transparency of two Liquid Crystal Displays (LCDs) with orthogonal orientation. As the light pulser system shall mimic the signals of scintillation light corresponding to energies between 10 MeV and 12 GeV, it is designed to cover a contrast ratio of 1:1000.

One light pulser module consists of four electronic boards with drivers for the LEDs and the LCDs and a microcontroller, the corresponding LEDs and LCDs, a perspex light mixer which homogenizes the intensity distribution and an aluminum casing including the light fiber coupling to up to 1696 light fibers. The electronics of a light pulser module is shown in figure 12.5 (a). It is designed such that the shape of a pulse matches the shape of a lead tungstate scintillation light pulse at the preamplifier output.

The light is guided to the lead tungstate crystals by four 245 μm thin light fibers per crystal, which are attached to the PWO crystals at the same side as the photosensors. Figure 12.5 (right) shows four sockets with four fibers each and their plugs.

A reference system monitors the light pulser intensity and thus provides a normalization. Light pulses from light pulser modules are transferred via light fibers to the reference system, which contains a radioactive ^{22}Na source, a lanthanum bromide scintillator and a photomultiplier. The sodium isotope ^{22}Na decays via β^+ decay into excited ^{22}Ne , so that the spectrum contains a peak at 511 keV from the electron-positron annihilation and another peak at 1275 keV originating from γ -radiation from the de-excitation of the ^{22}Ne nucleus. These two peaks are used to calibrate the reference system.

More details concerning the light pulser system are presented in [63].

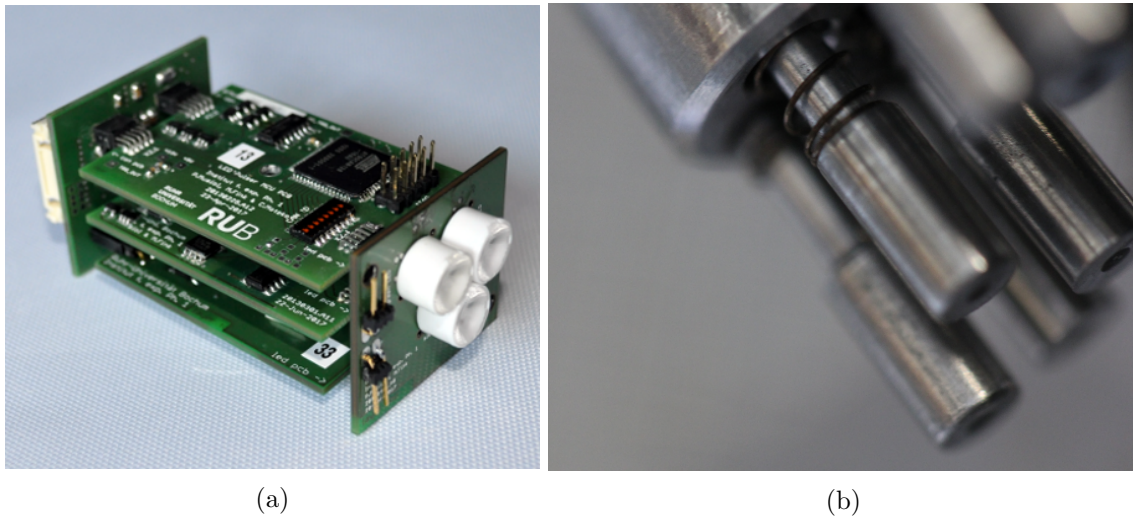


Figure 12.5: The light pulser electronics (a) and four light fiber sockets in their plug (b) [63]

12.3 Assembly of Submodules

The innermost submodules will be equipped with VPTTs as shown in figure 12.6 (a), since they are capable of processing higher signal rates than APDs due to lower detector capacitance and are additionally less sensitive to radiation damage. In order to obtain comparable signal outputs behind the preamplifiers, an algorithm is implemented to find the ideal combination of crystal, VPTT and preamplifier for each position. The light yield and radiation hardness of the crystals, the gain of the preamplifiers, the magnetic field dependency and sensitivity of the VPTTs are considered in a combined quality factor. First of all the crystals are assigned to positions in the endcap according to their radiation hardness so that the crystals with the best radiation hardness are placed at the innermost position, where the highest radiation doses are to be expected. In the next step photosensor-preamplifier combinations are assigned to positions by means of the Hungarian algorithm. Finally a Markov chain algorithm is used to randomly swap the positions of photosensor-preamplifier combinations in order to optimize the homogeneity of photosensor-preamplifier groups, which are connected to the same power supply.

When the parts needed to assemble a submodule are known, the first step of the assembly procedure is to solder the readily prepared preamplifier, and in case of a VPTT also the voltage divider, to the photosensor. The photosensor-preamplifier combination will be tested, shielded and tested again. In case of a VPTT first the electronics will be enclosed by a shrinking tube, which then is casted with Elastosil RT 601 and then wrapped with a copper tape, to which a ground strap is attached, and aluminum tape. In case of APDs, two APDs are glued into a customized nylon capsule before the preamplifiers are connected to them, and then an aluminum tube with an attached ground strap is put around the preamplifiers. The crystals are then wrapped in mirror foil to increase the amount of light, which reaches the photosensor. After that the matched crystals are placed in gluing jigs, cleaned and prepared with a primer before the exact amount of glue is applied with a pneumatic dispenser. Photosensor and preamplifier are put precisely in position in a customized capsule on the rear face of the crystal with another jig and pressed on the crystal with defined force by means of a customized weight. The bonding is inspected

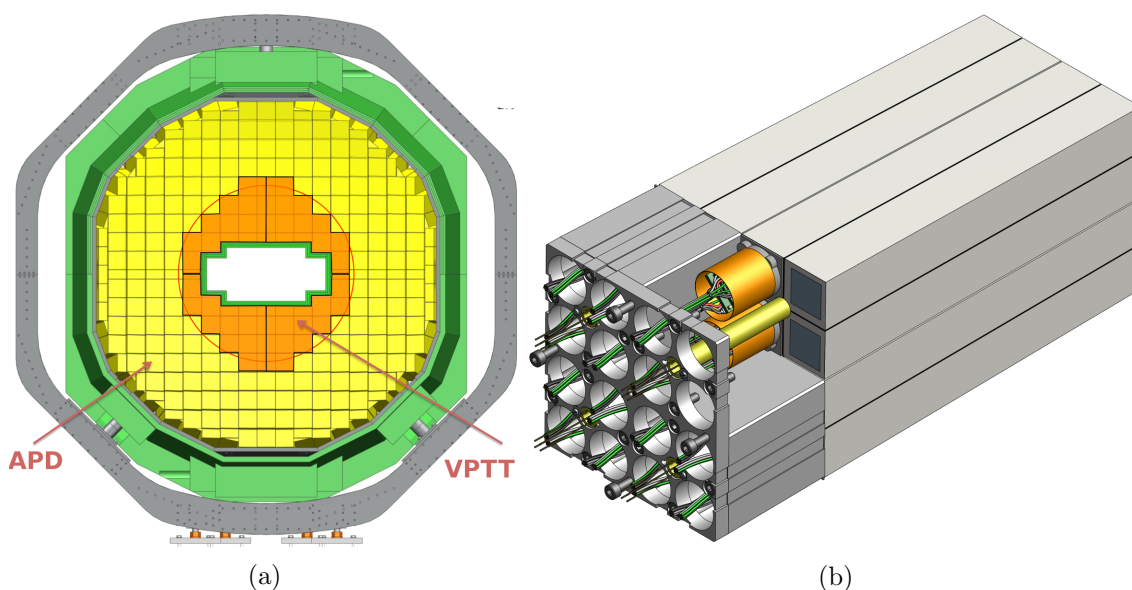


Figure 12.6: Distribution of VPTT and APD submodules [107] (a) and inner parts of an APD-channel submodule [103] (b)

with a camera through the crystal and in case air bubbles or any other kind of apparent impurities in the bond is visible, it can be resolved within the first few hours. After seven days of curing the bonding is fully hardened and the units can be removed safely from the gluing jigs and tested again.

Once all photosensor-crystal units are built and tested, they can be placed in the carbon fiber alveole. The alveole for a 16-channel submodule has the shape of a right square frustum with an inner cross, which separates the alveole into four compartments in the shape of oblique square frustums. Four photosensor-crystal units can be placed into each one of these compartments. Between the crystals two slotted layers of carbon fiber are placed, so that they form a cross and each pair of neighboring crystals is separated by the same amount of carbon fiber. Aluminum inserts with four holes, which enclose the photosensor in its capsule and the preamplifier, and a fifth central hole, which encloses the light fiber plug, are used to mechanically stabilize the four photosensor-crystal units in the alveole. Figure 12.6 (right) shows all the parts within the alveole. The light fiber plug contains four sockets, one for each of the crystals in the respective compartment. An aluminum part called mountplate is attached to all four insert pieces and has holes at the according positions to feed through the cables from the preamplifiers and the light fibers. The size of the inserts and the alveole are matched so that the alveole is set in mechanical tension and thereby stabilized, when the crystals and inserts are at the right position. Finally the ground straps of all photosensor shieldings are joined on a threaded bolt in the center of the mountplate.

The pairs of slots at the side faces of the insert pieces and the mountplate are intended for cables of temperature sensors. One out of eight crystals will have a temperature sensor attached at its side face, half of them close to the front face of the crystal and the other half close to the rear end of the crystal. Figure 12.7 shows the naming scheme for the crystal positions within a submodule. The front faces of the alveoles are closed. In order to indicate the correct orientation of the submodule afterwards, the production date of the

3	2	1	0
7	6	5	4
B	A	9	8
F	E	D	C

B	A	9	8
F	E	D	C

Figure 12.7: Naming scheme for crystal positions within a 16-channel submodule (left) and an 8-channel submodule (right) viewed the photosensor side towards the interaction point according to [59]

alveole is written on its front face. The alveoles for the 8-channel submodules are halves of alveoles for the 16-channel submodules. The side face which would be at the inside for a 16-channel submodule is orthogonal to the front and rear faces, whereas the opposite side face is slightly tilted. To avoid confusion during the assembly the crystal positions of an 8-channel submodule are named regardless of the submodule position in the forward endcap in such a way, that it corresponds to the lower half of a 16-channel submodule.

In order to obtain a homogeneous distribution, the position of the sensors within the submodule differs for the upper and the lower half of the forward endcap as shown in figure 12.9. For 16-channel submodules in the upper half the temperature sensor is attached to the top side face of the crystal at position 2 and the left side face of the crystal at position 8. For 16-channel submodules in the lower half the temperature sensor is attached to the left side face of the crystal at position 4 and the bottom side face of the crystal at position E.

For the 8-channel submodules the scheme is more complicated not least because of the crystal position naming scheme. Table 12.1 lists the submodule positions for which the temperature sensors is placed at a certain position within the submodule. The submodule positions are named according to the quadrant, the row (X) and column (Y) as shown in figure 12.8.

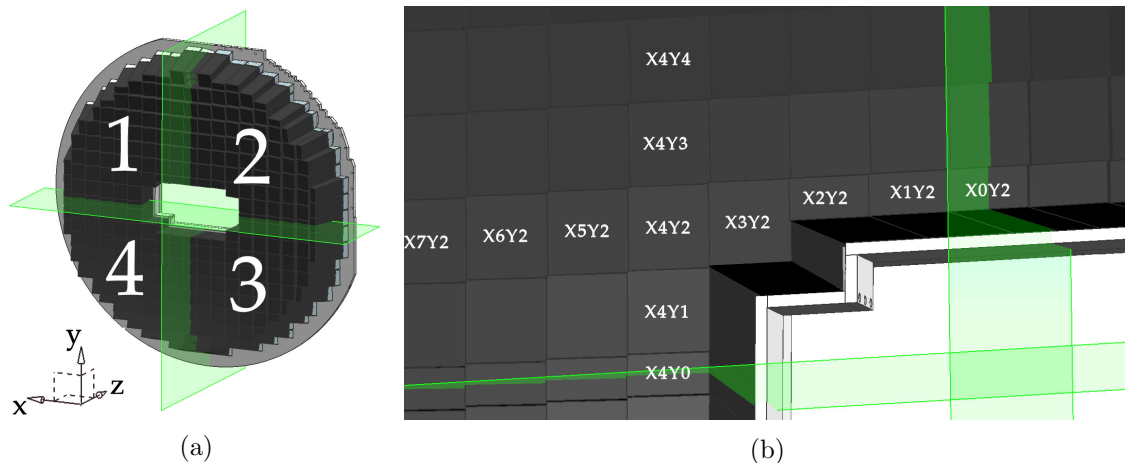


Figure 12.8: Naming scheme for the quadrants of the forward endcap (a) and the submodule positions (b) [59]

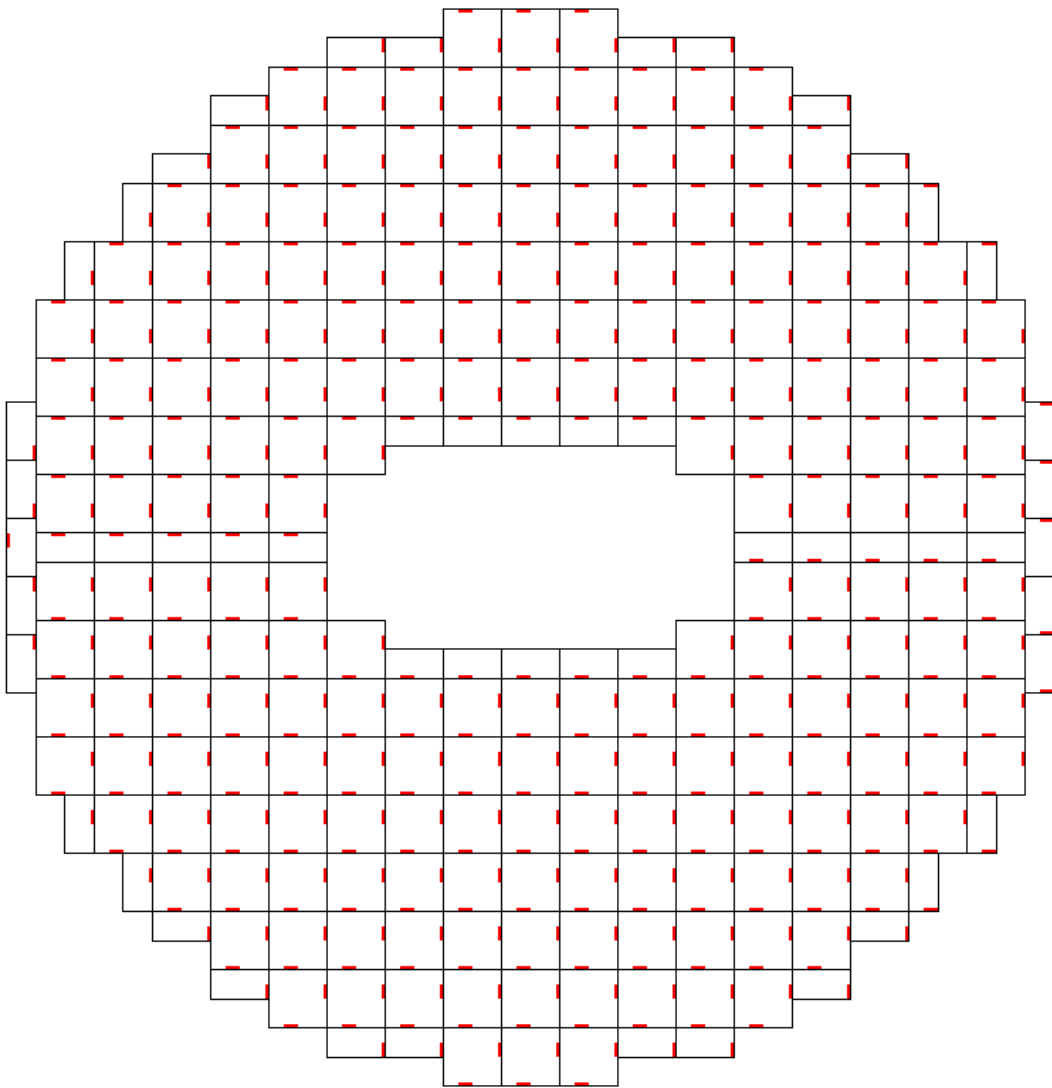


Figure 12.9: Positions of ultrathin temperature sensors spread over the TS EMC forward endcap as seen from behind the EMC forward endcap looking towards the interaction point

Crystal Position in Submodule	Transversal Position on Crystal	Longitudinal Position on Crystal	Submodule Position
D	bottom	back	1/4-X8Y0, 1/4-X7Y0, 1/4-X6Y0, 1/4-X5Y0, 1/4-X4Y0, 1-X2Y2, 1-X1Y2, 1/2-X0Y2, 2-X1Y2, 2-X2Y2
D	bottom	front	4-X7Y6, 4-X8Y5
E	bottom	back	2/3-X5Y0, 2/3-X6Y0, 2/3-X7Y0, 2/3-X8Y0, 2/3-X4Y0, 3-X2Y2, 3-X1Y2, 3/4-X0Y2, 4-X1Y2, 4-X2Y2
E	bottom	front	1-X8Y5, 1-X7Y6
8	right	front	1-X6Y7, 1-X5Y8, 1-X3Y9, 1-X2Y9, 2-X2Y9, 2-X3Y9, 2-X5Y8, 2-X6Y7
8	right	back	3-X9Y1, 3-X9Y2, 3-X8Y5, 3-X7Y6
B	left	front	3-X6Y7, 3-X5Y8, 3-X3Y9, 3-X2Y9, 4-X2Y9, 4-X3Y9, 4-X5Y8, 4-X6Y7
B	left	back	2-X7Y6, 2-X8Y5, 2-X9Y2, 2-X9Y1, 2/3-X9Y0
F	bottom	front	1-X9Y2, 1-X9Y2
C	bottom	front	4-X9Y2, 4-X9Y1
			1/4-X9Y0

Table 12.1: Temperature sensor positions for 8-channel submodules

12.4 Mounting of Submodules

For each position of a submodule an aluminum interface piece is used to obtain the desired alignment towards a point upstream of the interaction point. Alignment pins are used to ensure exact positioning. This tilted alignment of the submodules with respect to the backplate means, that submodules mounted at outer positions overlap with the inward neighboring submodules as shown in figure 12.10. Due to the alignment pins the submodules must be moved orthogonal to the backplate at least for the last millimeters. Hence the submodules must be mounted starting with the innermost ones and it will not be possible to remove any individual submodule once the mounting is completed. Thus when mounting the submodules to the backplate of the forward endcap, each submodule must be tested right away, so that in case something does not work properly, it can be fixed immediately. Therefore each submodule should be connected to all needed power supplies, a THMP, and a test fiber bundle connected to a light pulser module.

An adapter board is used to connect all the cables of the submodule with cables, which are routed out off the cooled volume and connected to the front end electronics and voltage supplies. These cables and light fibers are mostly routed between the backplate and the adapter boards, as shown in figure 12.11. The space between neighboring adapter boards increases as the angle between the according submodules increases so that space along the vertical and horizontal symmetry axes is particularly scarce. This circumstance makes the routing quite challenging since the electronics and the openings in the insulation are placed mostly at the upper half of the backplate so that many cables from the lower half have to be routed outwards close to the horizontal axis.

Figure 12.12 shows the routing scheme for cables and light fibers. The Arabic numerals corresponds to the different strands and the openings in the electronics frame are indicated by the endpoints of the red lines, but the openings in the insulation are not shown. More details concerning the routing are presented in [104].

Preferably the light fibers should be readily prepared at the according position, when mounting a submodule. Fixing the light fiber plug in a submodule works best when the fibers can be pulled through the openings in the backplate and attached to the submodule before it is mounted. To avoid mechanical stress on the fibers these should be routed first,

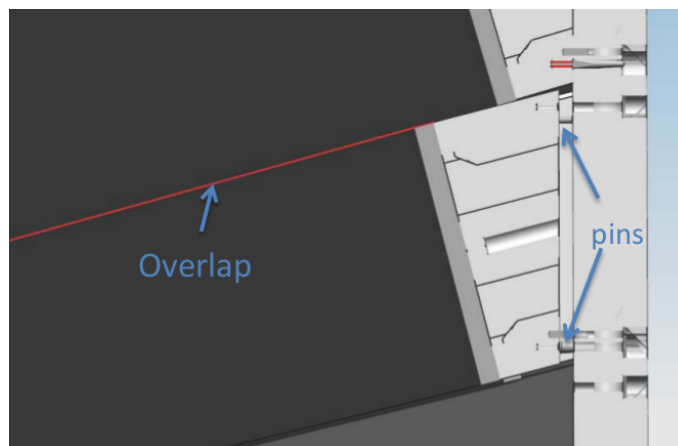


Figure 12.10: Overlap of submodules due to their tilt with respect to the backplate [108]

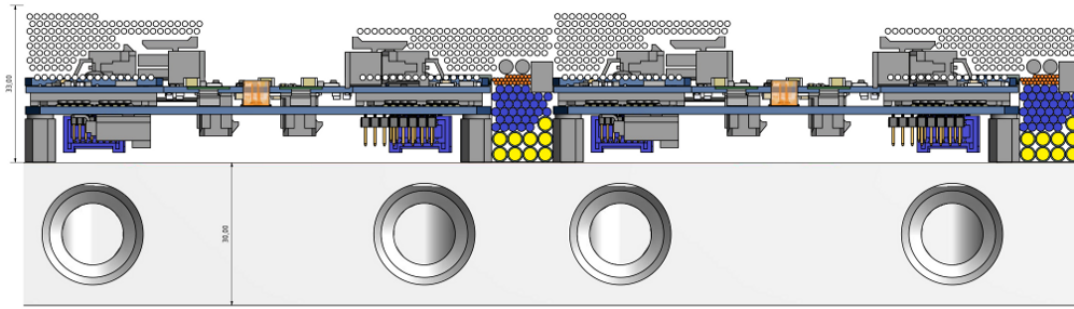


Figure 12.11: Cross section of cables and light fibers routed between adapter boards and backplate [104]

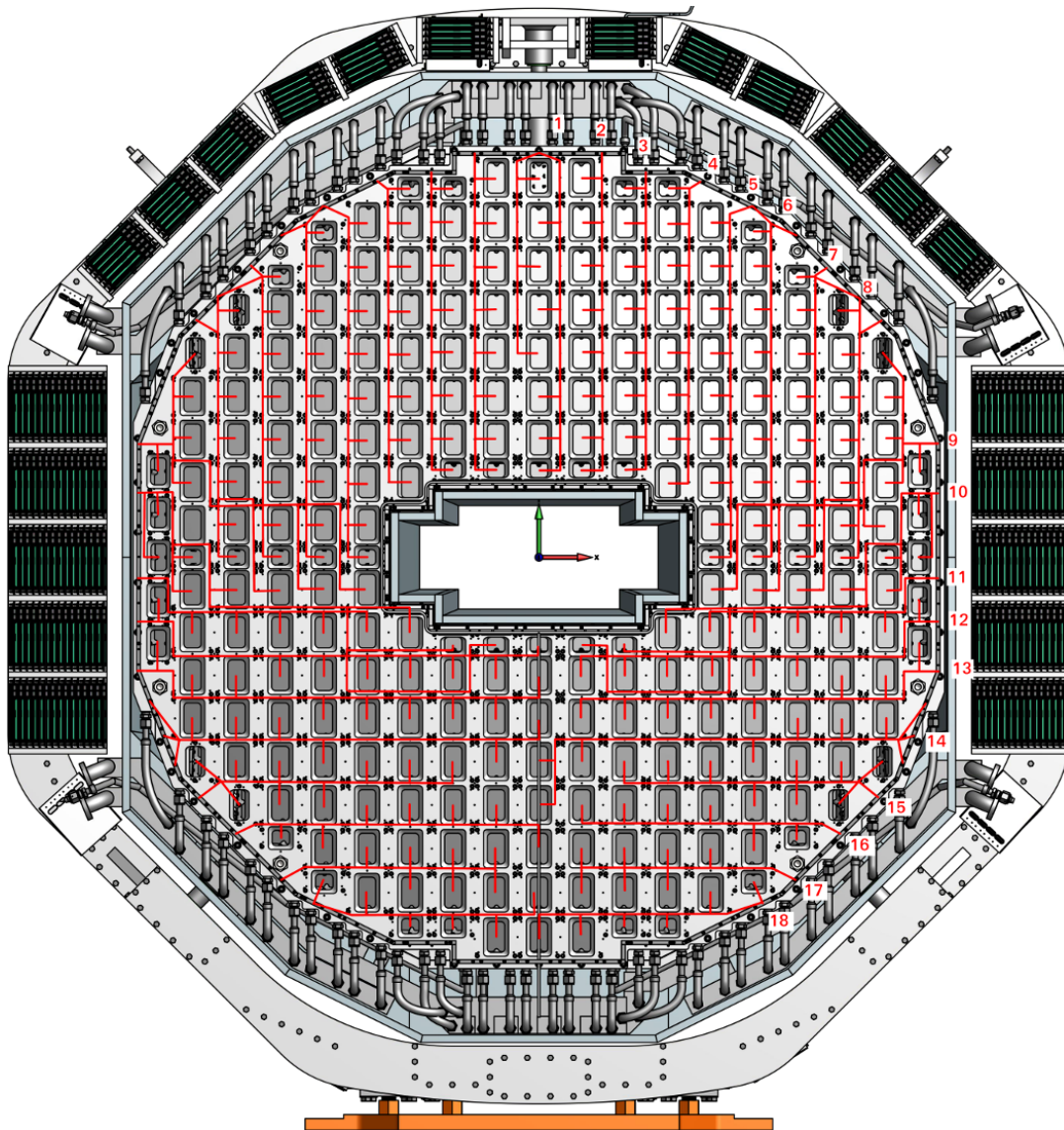


Figure 12.12: Routing scheme for light fibers, voltage supply and signal cables [103]

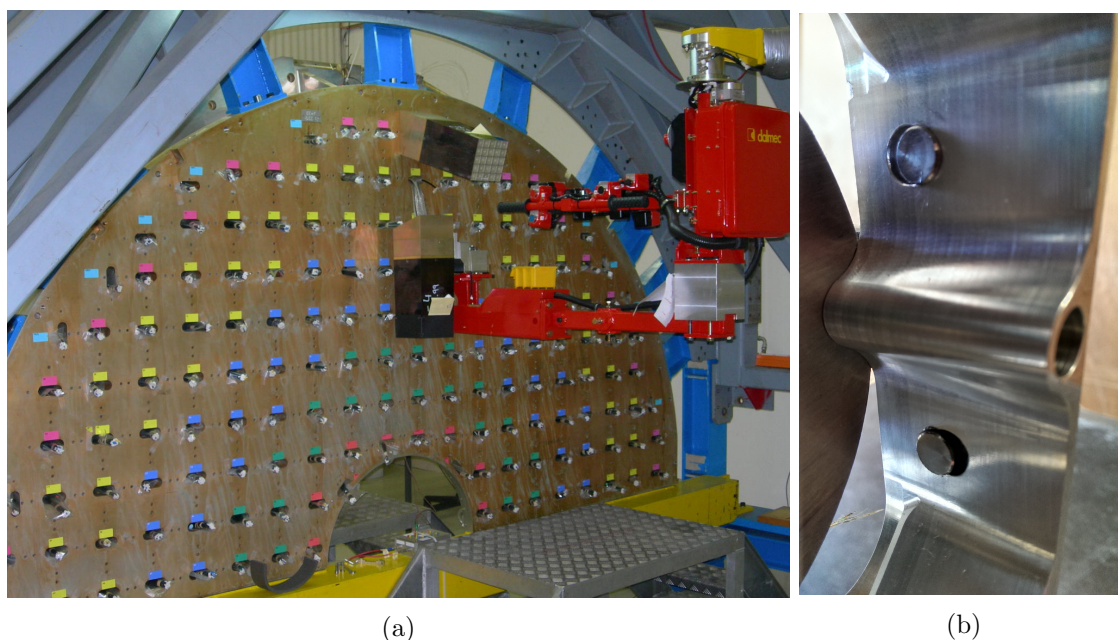


Figure 12.13: (a) Hydraulic manipulator arm used to assemble the end caps of the electromagnetic calorimeter of the CMS detector [109]
 (b) Interlocked interface [108]

before routing all other cables. Routing the cables after the adapter boards are already attached will also reduce the mechanical stress for both adapter boards and cables.

During the mounting procedure the submodules will be supported by a hydraulic manipulator arm from Dalmec, which has been purchased by the CMS collaboration for the assembly of the electromagnetic calorimeter of the CMS detector (figure 12.13, left) and will be lent to the PANDA collaboration for the assembly of the EMC. The manipulator arm is capable of carrying a load of 50 kg in total, which includes not only the submodules but also a customized holder.

Each interface has two holes at its outer side wall. Putting a holder with two studs through these holes the submodule will tilt due to its weight and interlock with the studs' notches as a quick lock system as shown in figure 12.13 (right). When the submodule is attached to the backplate and the weight is released from the holder, it can easily be loosened again.

Besides the geometric constraint on the mounting sequence, it is also important to keep the mounting sequence symmetric to avoid torque. Furthermore it is probably more convenient, to mount a sequence of neighboring submodules instead of changing the position with each mounted submodule. In addition the holder for submodules mounted on the right side will be a mirrored version of the holder for submodules mounted on the left side and for horizontally oriented submodules with eight crystals the stubs have a different distance, so again different holders are needed and it is preferable to minimize the number of holder exchanges. For testing it might be sensible to first mount all the VPTT submodules and in the following the APD submodules because a different amount of high voltage cables and signal cables needs to be connected per submodule.

With all these considerations in mind the mounting sequence depicted in figure 12.14 has been developed. VPTT submodules are shown in spring green and APD submodules in

Package	Module Type	Side	Mounting No.
1	h8-VP TT	L/R	1-10
2	h8-/16-VP TT	L/R	11-18
3	16-VP TT	L/R	19-24
4	16-VP TT	L/R	25-30
5	16-VP TT	L/R	31-38
6	16-VP TT	L/R	39-46
7	16-VP TT	L/R	47-54
8	16-APD	L/R	1-8
9	16-APD	L/R	9-16
10	16-APD	L/R	17-24
11	16-APD	L/R	25-32
12	16-APD	L/R	33-40
13	h8-/16-APD	R	41-47
14	h8-/16-APD	L	48-54
15	h8-/16-APD	L	55-61
16	h8-/16-APD	R	62-68
17	16-APD	R	69-74
18	16-APD	L	75-80
19	16-APD	L	81-86
20	16-APD	R	87-92
21	h8-APD	L/R	93-100
22	16-APD	R	101-107
23	16-APD	L	108-114
24	16-APD	L	115-121
25	16-APD	R	122-128
26	h8-/16-APD	R	129-136
27	h8-/16-APD	L	137-144
28	h8-/16-APD	L	145-152
29	h8-/16-APD	R	153-160
30	16-APD	R	161-167
31	16-APD	L	168-174
32	16-APD	L	175-181
33	16-APD	R	182-188
34	v8-/16-APD	L/R	189-196
35	v8-/16-APD	L/R	197-204
36	v8-APD	L/R	205-214

Table 12.2: Assignment of sequence steps to packages, which might be handled in one day

13 Ultrathin Platinum Resistance Temperature Sensors for $\overline{\text{PANDA}}$

Due to spatial limitations and high precision requirements it is not possible to use commercially available temperature sensors to monitor the TS EMC temperature. Therefore, ultrathin platinum resistance temperature sensors have been developed at the Institut für Experimentalphysik I at the Ruhr-Universität Bochum.

13.1 Requirements for $\overline{\text{PANDA}}$ TS EMC Temperature Sensors

Since the light yield of lead tungstate is temperature dependent, not only the operating temperature should be chosen reasonably, but also too large temperature variations should be avoided, because they worsen the energy resolution. As explained in subsection 11.2.6 the temperature dependence of the light yield which amounts to $\frac{d(LY)}{dT} = -3\%/^{\circ}\text{C}$ at -25°C means, that the temperature of the TS EMC should vary at most by $\Delta T = \pm 0.1^{\circ}\text{C}$ to keep the decline of energy resolution due to temperature instabilities below 1%. In order to ensure an appropriate temperature regulation the temperature sensors thus need to have an even higher precision of $\sigma_T < 0.02^{\circ}\text{C}$ [60].

Besides the strong requirements on the precision of the temperature sensors there are strict requirements on the dimensions of the sensors, too. Since they are to be placed in between the scintillators, they must fit in the tight geometry of the submodules, so their thickness has to be below $150\ \mu\text{m}$ [59]. Obviously, the width of the sensors must be smaller than 20 mm in order to not extend the width of the crystals. Also the length of the sensitive sensor area should not be too large so that the spatial temperature distribution along the crystals can be determined to ensure that the temperature gradient along the crystal length does not exceed 2°C .

13.2 Platinum Resistance Temperature Sensors

There are several ways to measure temperature, basically any temperature dependent property can be utilized. Compared to other materials the resistance of platinum has a quite linear temperature dependence, which makes it the most popular material for resistance temperature sensors.

The temperature dependence is characterized by the temperature coefficient, which is $\alpha_{\text{Pt}} = 3.851 \cdot 10^{-3}^{\circ}\text{C}^{-1}$ for platinum [110]. Hence, the resistance at a certain temperature can be estimated by

$$R(T) \approx R(0^{\circ}\text{C})(1 + \alpha_{\text{Pt}} \cdot T). \quad (13.1)$$

Resistance temperature sensors are thus characterized by their resistance at 0°C , as for example Pt100 or Pt1000 sensors.

For commercially produced platinum resistance temperature sensors the resistance at a given temperature is determined in the DIN EN 60751 standard [110] as

$$\begin{aligned} R(T) &= R(0^\circ\text{C})(1 + AT + BT^2 + C(T - 100^\circ\text{C})T^3) \quad \text{for } -200^\circ\text{C} \leq T \leq 0^\circ\text{C} \text{ and} \\ R(T) &= R(0^\circ\text{C})(1 + AT + BT^2) \quad \text{for } 0^\circ\text{C} \leq T \leq 600^\circ\text{C} \\ \text{with } A &= 3.9083 \cdot 10^{-3} \text{ }^\circ\text{C}^{-1}, \quad B = -5.775 \cdot 10^{-7} \text{ }^\circ\text{C}^{-2}, \quad C = -4.183 \cdot 10^{-12} \text{ }^\circ\text{C}^{-3}. \end{aligned}$$

Deviation limits from this function and the application limits for different precision classes are determined by this standard, too. For the highest precision class AA the deviation limit is $\pm(0.10^\circ\text{C} + 0.0017 \cdot T)$ over the temperature range -50°C to $+250^\circ\text{C}$. The comparison of this deviation limit to the required temperature resolution of only 0.02°C shows just how demanding the requirements put on the temperature sensors for the \bar{P} ANDA TS EMC actually are.

13.3 Design of Ultrathin Platinum Resistance Temperature Sensors

Both, the ultrathin temperature sensors for the \bar{P} ANDA TS EMC as well as commercial Pt100 temperature sensors are read out with the same electronics (THMP, cf. chapter 14), so that it is desirable to obtain similar properties.

The specific resistance of platinum is $\rho_{\text{Pt}} = 106 \cdot 10^{-9} \text{ } \Omega \text{ m}$ at 20°C . The length of a platinum wire with a diameter of $25 \text{ } \mu\text{m}$, which is needed to obtain the same resistance as for a Pt100 sensor of $R(20^\circ\text{C}) = 107.79 \text{ } \Omega$ at 20°C , can thus be estimated as

$$R(20^\circ\text{C}) = \rho_{\text{Pt}} \frac{l}{A} = \rho_{\text{Pt}} \frac{l}{\pi r^2} \quad \Rightarrow \quad l = \frac{R(20^\circ\text{C}) \pi r^2}{\rho_{\text{Pt}}} \approx 0.5 \text{ m}.$$

Using nine loops of approximately 2.7 cm length, the platinum wire can be stored compactly. The wound wire is attached to the sticky side of self-adhesive polyimide tape to fixate it and prevent short-circuits due to overlapping loops.

The cable with which the resistance of the wound platinum wire is measured has to be ultrathin, too. A very thin flexible cable can be realized by conductor paths etched in $18 \text{ } \mu\text{m}$ thick copper layers, which are coated on a $25 \text{ } \mu\text{m}$ thick polyimide foil. A part of that foil can also be used to cover the platinum wire on the sticky side of the polyimide tape. Figure 13.1 shows the schematic design of such a temperature sensor. To prevent corrosion the conductor paths are covered with another layer of polyimide foil and the contact pads are gold plated.

The platinum wire is electrically connected to the contact pads by a conductive adhesive. Each of the contact pads is connected to two conductor paths. This way it is possible that a constant current flows through one pair of conductor paths connected to the platinum wire, but the resulting voltage drop over the platinum wire can be measured with a very small current via the other pair of conductor paths in parallel. Thanks to this four-wire measurement the influence of the cable resistance and thus the cable length cancels out.

Table 13.1 summarizes the materials needed and their respective thicknesses. Since the conductor paths and the platinum wire sink into the adhesive film the actual thickness of a sensor is lower than the sum of the layer thicknesses. The thickness at the contact pads depends on the thickness of the manually applied adhesive, without the conduction adhesive the thickness is determined by the thickness of the copper coated polyimide foil

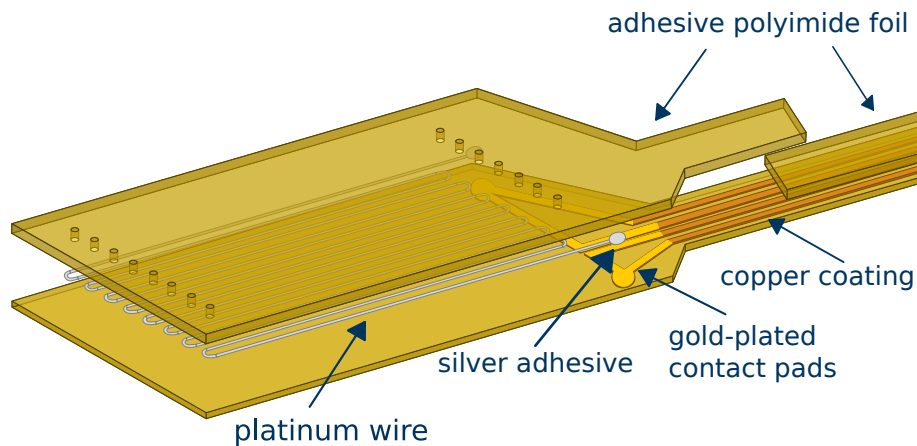


Figure 13.1: Design of a temperature sensor [111]

Material		Thickness / μm
Platinum Wire		25
Polyimide Tape	Carrier Layer	25
	Adhesive Film	30
Polyimide Toil	Carrier Layer	25
	Copper Coating	18
	Gold Plating	2

Table 13.1: Materials needed to manufacture an ultrathin temperature sensor and their thicknesses

and the polyimide tape as $45\ \mu\text{m} + 55\ \mu\text{m} = 100\ \mu\text{m}$. The thickest part is where the polyimide tape covering the conductor paths and the polyimide tape on which the platinum wire has been wound overlap. There a thickness of $45\ \mu\text{m} + 2 \cdot 55\ \mu\text{m} = 155\ \mu\text{m}$ is to be expected. This calculation could be approved by measurements yielding a thickness of $(160 \pm 10)\ \mu\text{m}$ [112].

13.4 Production Procedure

The individual steps of the production have changed over time and became more and more outsourced to external companies or automatized.

At the very beginning the polyimide foil has been bought with a continuous copper coating, so that it still needed to be coated with an additional light sensitive cover, exposed and etched. Each sheet of 500 mm \times 270 mm surface area yields 24 cables. After some first own trials, this procedure has been commissioned to the electronics engineering institute. The finished conductor paths are covered with polyimide tape and cut to individual cables with a sensor area as depicted in figure 13.2. Both, the contact pads as well as the open conductor paths at the opposite side of the cable are galvanized with gold to prevent corrosion and ensure a good electrical connection. Later on, when more cables were needed, all these steps could be omitted, because it was possible to obtain gold plated and polyimide covered conductor paths with the cable shape already prepunched.

For a long time the platinum wire has been wound on the polyimide tape manually. Therefore the tape was pushed onto two parallel rows of needles with the adhesive side facing upwards. The rows consisted of eight and nine needles each, with approximately 2 mm distance between the needles and approximately 27 mm between the rows.

The platinum wire was then wound around one needle after the other from alternating rows so that a meandering shape of nine loops could be obtained as shown in figure 13.3. The wire had to be pulled carefully so that it was neither so loose that loops overlap, nor torn apart. Since the wire sticks to the adhesive side of the tape it was not always obvious if the wire had already been torn. Hence, the resistance needed to be checked after the winding was finished.

Then the tape with the wires was lifted carefully and evenly from the needles. At this step the wire was often torn when the tape got skewed, which resulted in tensioning of the wire, or the wire was caught at a needle. Therefore the resistance was checked again after the tape had been removed from the needles.

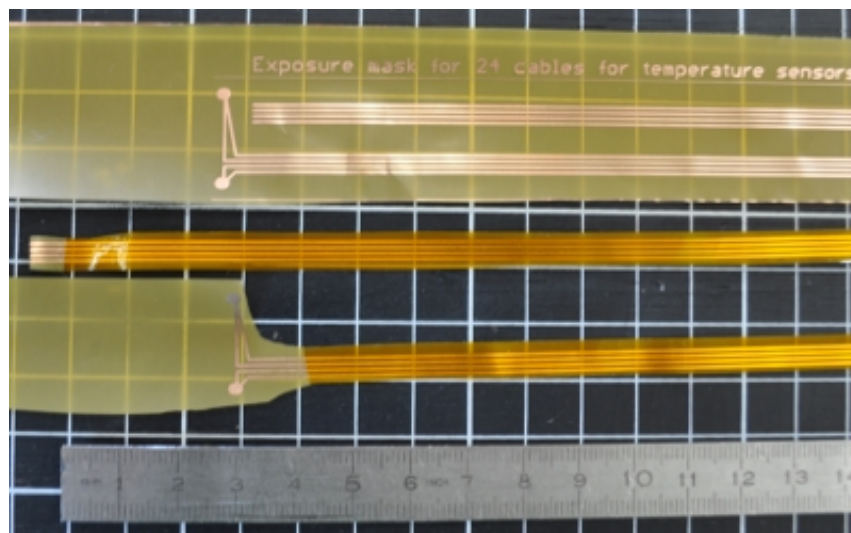


Figure 13.2: Strip of polyimide foil with conductor paths etched out of the copper coating (top), covered with polyimide tape and cut to individual cables [111] (bottom)

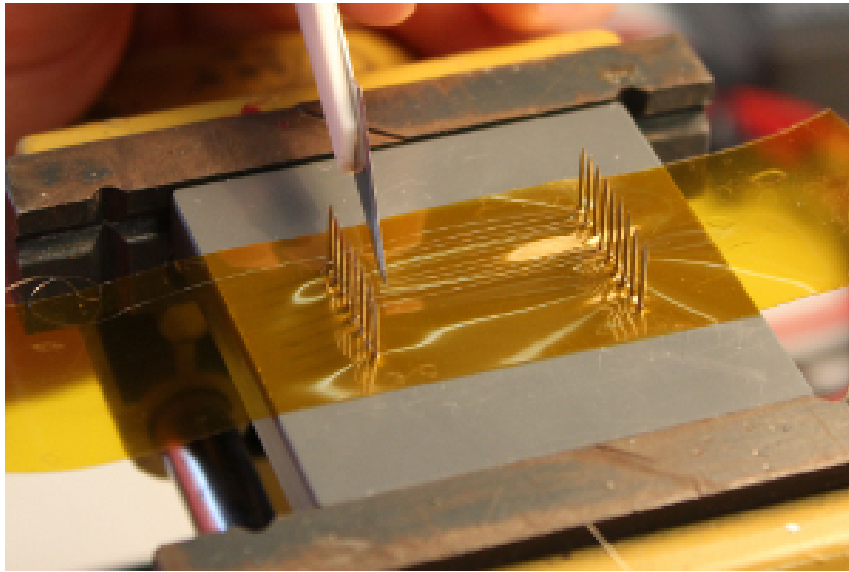


Figure 13.3: Winding the platinum wire alternating around needles from opposite rows to obtain a meandering shape [59]

Finally a 3D printer is utilized to automatically wind the platinum wire on the adhesive side of the polyimide tape in the scope of a Bachelor's thesis [113]. Instead of an extruder a stepper motor unrolls the platinum wire coil by driving a belt which is connected to the bearing of the platinum wire coil. The platinum wire is then led to the polyimide tape by a hollow needle with flattened opening. Figure 13.4 (left) shows the platinum wire coil, the stepper motor and the hollow needle in a customized 3D-printed holder.

The 3D printer moves the needle in windings above the tape so that the platinum wire is placed in the intended meandering shape. In order to pull the platinum wire into the adhesive film of the polyimide tape, a voltage supply is connected to the end of the platinum wire and the hollow needle under current control. Thus a constant electrical current flows through the platinum wire and induces a magnetic field. Below the tape, small magnets are arranged in an array which generate a magnetic field fitting to the intended meandering shape of the platinum wire. In figure 13.4 (right) the magnet arrays and some first platinum wire windings can be seen. The full setup is shown in figure 13.5.

After the platinum wire is placed on the adhesive side of the polyimide tape the next step is to attach the tape to the foreseen area at the end of the ultrathin cables, so that the wound platinum wire is covered by the foil, but the contact pads are still left free, as shown in figure 13.6 (left). Both ends of the wound platinum wire must then be connected to the contact pads of the wire.

After several tests the conductive adhesive H37MP, which is based on epoxy resins blended with silver particles, had been chosen since it turned out to provide connections with the best long time stability [59]. Figure 13.6 (left) shows how the adhesive is applied to the contact pads. After the platinum wire ends are connected with the contact pads also the remaining part of the tape can be attached to the cable. Protruding tape must be removed, before the temperature sensors are baked at 150 °C for at least 75 minutes to cure the adhesive.

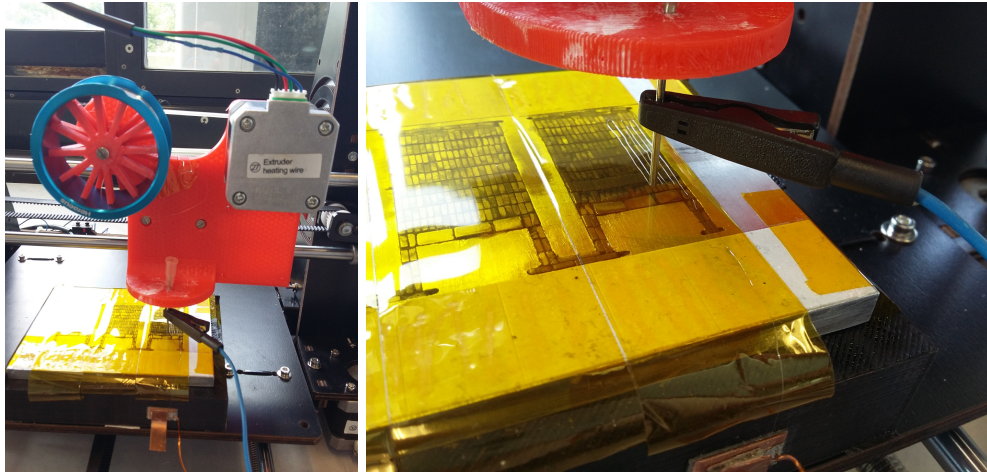


Figure 13.4: Customized holder for platinum wire coil, stepper motor, and hollow needle (left) and magnet arrays below the polyimide tape and some platinum wire windings on top of the polyimide tape (right)

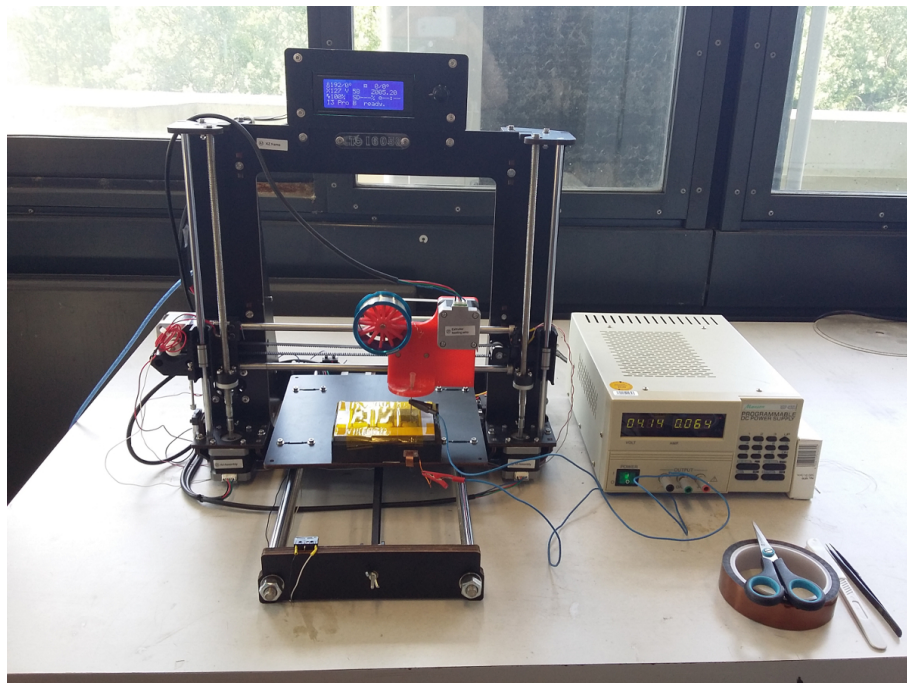


Figure 13.5: 3D printer based setup for winding a platinum wire on adhesive polyimide tape

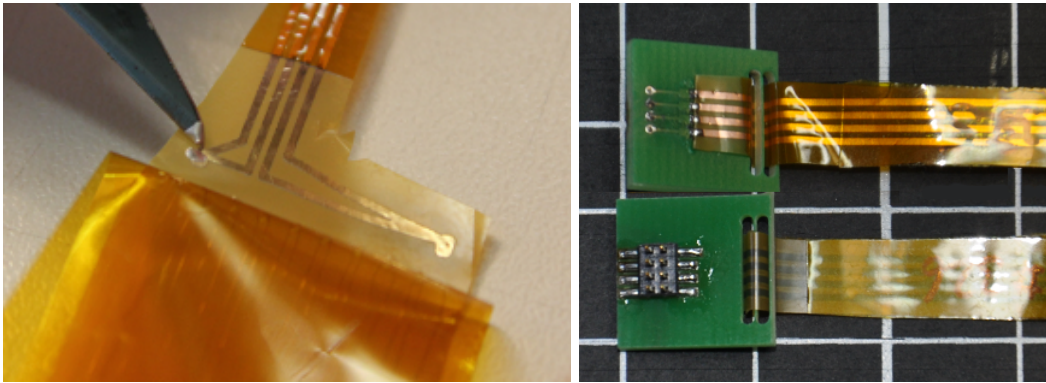


Figure 13.6: Attaching the polyimide tape with the wound platinum wire to the intended area of the polyimide foil based cable and applying conductive adhesive to the contact pads [59] (left), top and bottom side of the PCBs with pin headers and two slits for tension relief of the soldering joints connected to the temperature sensor cables as a plug [111] (right)

The resistance of the finalized sensor is then noted in the logbook and its cable is labeled with the corresponding sensor ID on both sides. A small PCB with a 2×4 pin header is soldered to the end of the cable as shown in figure 13.6 (right) to provide mechanically stable plugs. Two slits in the PCB shape the cable into a chicane to provide tension relief for the soldering joints.

13.5 Required Amount of Temperature Sensors

The use of ultrathin temperature sensors is planned for all three subdetectors of the $\bar{\text{P}}\text{ANDA}$ TS EMC.

As described in section 12.3, submodules comprised of 16 or of 8 crystal-photosensor units are used in the forward endcap. One temperature sensor is foreseen per eight units, so that the submodules are equipped with one or two sensors depending on their size. That yields a sum of 482 ultrathin temperature sensors to be distributed over the forward endcap as shown in figure 12.9.

In the barrel part of the TS EMC, which hosts the largest number of crystals, it is foreseen to supply each slice containing 720 crystals with 72 temperature sensors, which corresponds to one sensor per ten crystals. Depending on how the distribution around the integration of the target pipe is planned, that yields a total amount of up to 1152 temperature sensors for the full barrel TS EMC consisting of 16 slices.

The backward endcap as the smallest compound of the $\bar{\text{P}}\text{ANDA}$ TS EMC consists of 524 crystals, of which each fourth one shall be equipped with one of the ultrathin temperature sensors. That results in 131 sensors in total.

Since the temperature sensors for the backward endcap are produced by other collaborators, the amount of 1634 temperature sensors remains under the responsibility of the group in Bochum.

13.6 Calibration of the Ultrathin Platinum Resistance Temperature Sensors

Since all temperature sensors are at least partly manually produced, they must be calibrated to determine their individual characteristics.

13.6.1 Calibration Setup

The circulation thermostat FP50HL from Julabo is used to control the temperature during the calibration measurement [114]. A 50:50 methanol-water mixture is circulated through two cooling plates. Each of these plates consists of a copper block with meander shaped mills, a thin copper plate is soldered onto it to cover the mills. The temperature sensors are stacked with 0.5 mm thick copper plates in between them and put in a copper box, which is fixated between the two cooling plates. The side walls of the box provide a slit to let through the temperature sensor cables as shown in figure 13.7. Up to 15 of the ultrathin temperature sensors fit in this box at once. A commercial Pt100 sensor is tucked into the 5 mm thick bottom and lid of the box for reference. The Pt100 sensors are glued into small copper tubes with a thermally but not electrically conducting adhesive for mechanical protection, and the two pins are soldered to a pair of shielded cables each, to enable four-wire measurements [115].

For insulation against the environmental temperature the cooling plates are surrounded by a box made of vacuum insulation panels and rigid polymethacrylimid foam [59]. The cooling hoses from the thermostat are fed through holes in the rigid foam sidewall to the cooling plates, the reference sensor cables are routed through a small hole in the lid, while the cables of ultrathin temperature sensors pass through the slit between the rigid foam sidewall and the lid. The space between the insulation box and the copper box is filled with styrofoam beads to avoid convection.

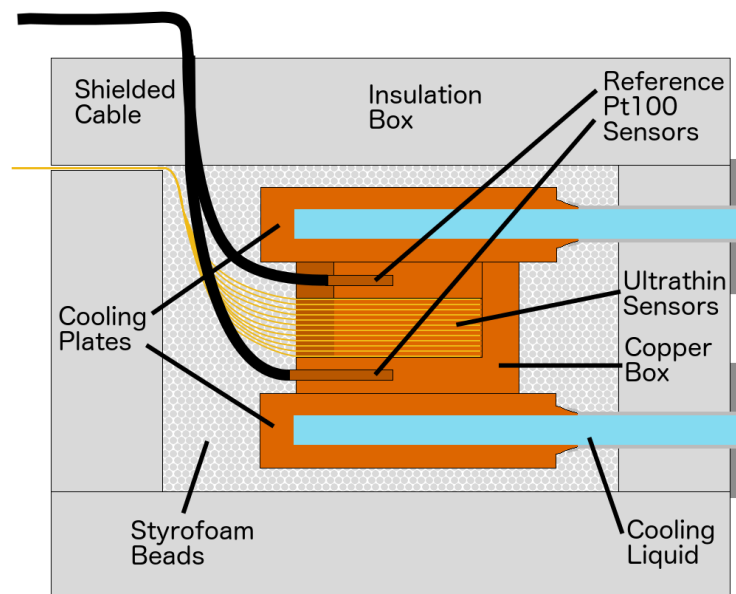


Figure 13.7: Cross-sectional side view of the temperature sensor calibration setup, schematically

Outside of the insulation box, the reference sensors and temperature sensors are connected to a THMP via adapter PCBs. These PCBs are the latest available version of the adapter board mentioned in section 12.4. Thus the full setup is as close as possible to the situation in the TS EMC forward endcap, including even the length of the flat ribbon cables between the adapter PCBs and the THMP.

13.6.2 Calibration Procedure

The calibration setup is situated in an air-conditioned laboratory. After previously connected temperature sensors are removed and new sensors are connected, the connections must be checked. The temperature sensors should then be stacked with copper plates in between them according to the sockets they are connected to as indicated by the labels. After the copper box is closed and fixated between the cooling plates, styrofoam beads are filled in for insulation, as shown in figure 13.8.

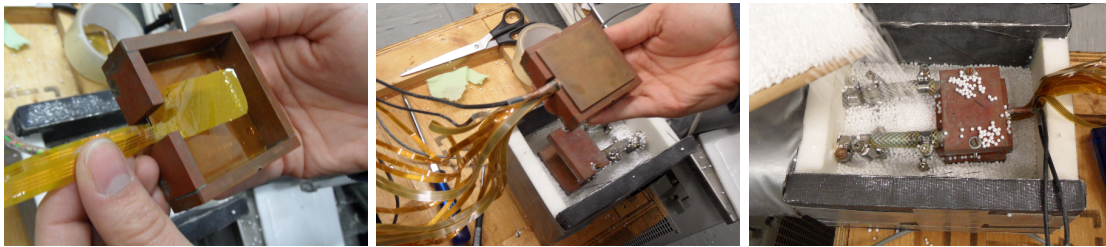


Figure 13.8: Stacking temperature sensors in the copper box with thin plates between them (left), covering the stack with the lid with an embedded reference temperature sensor (center) and filling the space around the copper box, which is fixed between the cooling plates, with styrofoam beads (right) [112]

Compared to the description in [112], additional tape has been attached to the lid of the insulation box to reduce thermal bridges, so that it should be closed carefully to not harm the attached tape. As the insulation box got closed the AC can be turned on again and the measurement can be started.

A checklist helps to remember all the steps in the right order and also serves as a lab log, where the IDs of the calibrated sensors and any incidents are noted. The sensor IDs must also be saved digitally in the order corresponding to the connected sockets to enable an automated analysis of the measurement. Before exchanging the calibrated temperature sensors, it should be checked that the measurement finished as planned by checking the temperature of the thermostat. Running the analysis script for the most recent measurement reveals if there were e.g. contact problems during the measurement so that it should be repeated.

13.6.3 Data Taking and Treatment

During a calibration measurement, the thermostat is set to different temperatures between -30°C and $+30^{\circ}\text{C}$ in steps of 5°C . Starting at 20°C , the set temperatures are decreased to -30°C , then increased to $+30^{\circ}\text{C}$, and decreased again to $+25^{\circ}\text{C}$, so that except for the minimum and maximum temperature each temperature is set twice to check for hysteresis effects.

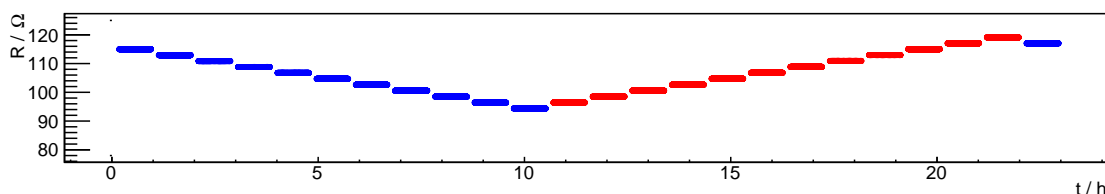


Figure 13.9: Considered resistance values of a temperature sensor over time, colored in blue for decreasing set temperatures and in red for increasing set temperatures

The thermostat is controlled via RS-232 with the same software that also retrieves the data from the THMP via controller area network (CAN) bus, so that the data set for each point consists of a timestamp, the ADC conversions of all 64 THMP readout channels, the THMP board temperature as well as the set temperature and the measured bath temperature of the thermostat. After reading out the data, a sleep time of ten seconds is passed before reading the next data. If communication problems with the CAN bus occur, a wait time of one second is passed before a second trial. Taking 310 data points per set temperature results in a total measurement time of approximately 23 hours, so that there is enough time to exchange sensors and keep a regular schedule.

For processing of the data, first all ADC conversions are converted to resistance values according to the THMP calibration parameters of the corresponding readout channel.

The two reference temperature sensors are commercial Pt100 sensors of the highest available precision class AA. In order to obtain an even better (relative) precision, the reference sensors have been calibrated in the calibration setup with a dedicated calibration measurement for temperatures between -30°C and $+30^{\circ}\text{C}$ varied in steps of only 1°C , each set for one hour. For consistency reasons, a polynomial of third order has been fitted to describe the set temperature in dependence of the measured resistance, just as intended for the manufactured temperature sensors. Hence it is possible to convert the resistances of the reference sensors $R_i^{\text{ref1}}, R_i^{\text{ref2}}$ to temperatures $T_i^{\text{ref1}}, T_i^{\text{ref2}}$ and the fit parameter uncertainties are propagated to temperature uncertainties $\Delta T_i^{\text{ref1}}, \Delta T_i^{\text{ref2}}$. The temperature values are averaged $T_i^{\text{ref}} = \frac{1}{2}(T_i^{\text{ref1}} + T_i^{\text{ref2}})$ and the root mean square of the two uncertainties estimates the uncertainty $\Delta T_i^{\text{ref}} = \sqrt{\frac{1}{2}((\Delta T_i^{\text{ref1}})^2 + (\Delta T_i^{\text{ref2}})^2)}$ of the respective data point.

It is not sensible to relate measured resistances and reference temperatures if the thermal equilibrium has not yet been reached. From experience that takes almost ten minutes after the set temperature has been changed by 5°C . Thus the first 60 data points that are recorded just after changing the set temperature are discarded. Figure 13.9 shows the considered resistance values exemplary for a temperature sensor calibration.

For each set temperature, the mean value and standard deviation of the corresponding resistance and reference temperature values are determined and a third order polynomial

$$f(R) = p_0 + p_1 R + p_2 R^2 + p_3 R^3$$

is fitted to the obtained mean values. According to the documentation of the software used for fitting, the error Δx_i along the x -axis is projected to the y -axis by evaluating the fit function at $x_i - \Delta x_i$ and $x_i + \Delta x_i$. In order to obtain good start parameters, the parameters p_2 and p_3 are fixed to 0 in the beginning, so that a first order polynomial is fitted, and then released one after the other.

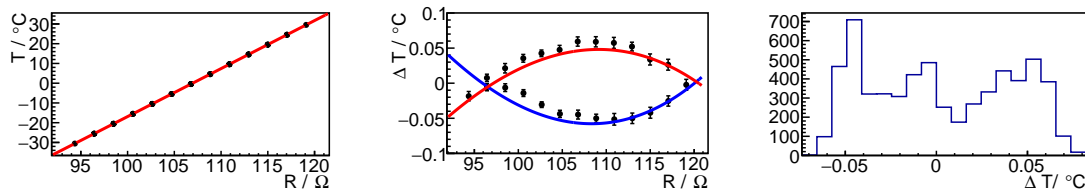


Figure 13.10: Fit of a third order polynomial to the full data sample (left), differences between means and fit function against measured resistance (center) and differences between individual data points and fit function (right)

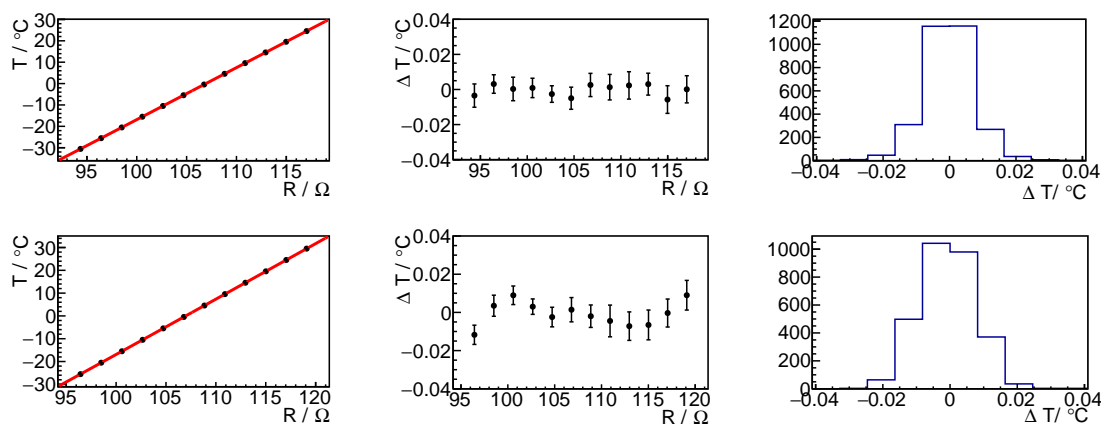


Figure 13.11: Fit of a third order polynomial (left) to the sample with decreasing (top row) and increasing (bottom row) set temperatures, differences between means and fit function against measured resistance (center) and one-dimensionally distributed differences between individual data points and fit function (right)

Figure 13.10 (left) shows the fit to all data points, which seem to lie all on one straight line. Looking at the differences between the fitted polynomial evaluated at the measured resistance values and the reference temperatures shown in figure 13.10 (center), the hysteresis effect of the manufactured temperature sensors becomes obvious.

It is known also for commercial Pt100 sensors, that a hysteresis effect occurs. It is traced back to mechanical tension between the platinum wire and the carrier material caused by different expansion coefficients. It may not be larger than the limiting deviation as specified for the according precision class in the norm.

Splitting the data into two subsamples as indicated by the colored markers in figure 13.9 and fitting each of them individually with a third order polynomial, the data can be described much better. The sample with decreasing set temperatures is in the following referred to as cooling sample and the sample with increasing temperatures is referred to as heating sample. The blue and red curves visible in figure 13.10 are the difference between the polynomial fitted to the full sample and the polynomial fitted to the respective subsample. The fit results for the individual subsamples are shown in figure 13.11.

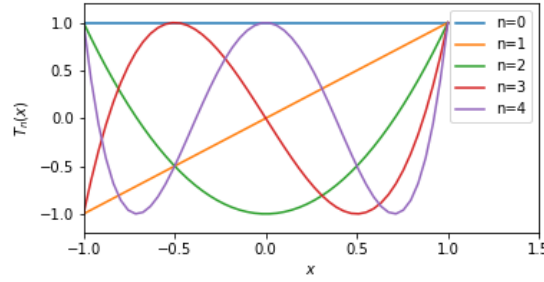


Figure 13.12: First five Chebyshev polynomials

Some of the fits failed to converge due to technical reasons, even though the data had obviously a good quality. In order to improve the fit stability, Chebyshev polynomials are used to prefit the data. The Chebyshev polynomials are recursively defined

$$\begin{aligned} T_0(x) &= 1 \\ T_1(x) &= x \\ T_n(x) &= 2xT_{n-1}(x) - T_{n-2}(x) \end{aligned}$$

such, that the maximum of their absolute value in the interval $[-1,1]$ is one, as shown in figure 13.12.

The second and third Chebyshev polynomials are given by

$$\begin{aligned} T_2(x) &= 2xT_1(x) - T_0(x) = 2x^2 - 1 \\ T_3(x) &= 2xT_2(x) - T_1(x) = 4x^3 - 2x - x = 4x^3 - 3x. \end{aligned}$$

These polynomials are orthogonal, which basically means that there is a unique linear combination of them for any polynomial defined on the interval $[-1,1]$, so that no ambiguities disturb the fitting process. Hence the resistance values need to be transformed accordingly.

Therefore, $\xi = \frac{2}{R_{\max} - R_{\min}}$ and $\zeta = \frac{R_{\max} + R_{\min}}{R_{\max} - R_{\min}}$ are defined with $R_{\min} = 83 \Omega, R_{\max} = 123 \Omega$ so that the resistance values are mapped to the interval $[-1,1]$ by $x = \xi R + \zeta$.

At the beginning the parameters τ_2 and τ_3 for the second and third Chebyshev polynomials are fixed to zero and then released iteratively. The Chebyshev coefficients are then translated to the parameters of an ordinary polynomial of third order. The parameters p_0, p_1, p_2, p_3 for which

$$p_0 + p_1 R + p_2 R^2 + p_3 R^3 = \tau_0 T_0(x) + \tau_1 T_1(x) + \tau_2 T_2(x) + \tau_3 T_3(x)$$

holds, are determined by the coefficients $\tau_0, \tau_1, \tau_2, \tau_3$ of the Chebyshev polynomials as

$$\begin{aligned} p_0 &= \xi^0 (\tau_0 + \zeta \tau_1 + (-1 + 2\zeta^2) \tau_2 + (-3\zeta + 4\zeta^3) \tau_3) \\ p_1 &= \xi^1 (\tau_1 + 4\zeta \tau_2 + (-3 + 12\zeta^2) \tau_3) \\ p_2 &= \xi^2 (2\tau_2 + 9\zeta \tau_3) \\ p_3 &= \xi^3 (3\tau_3) . \end{aligned}$$

By an iterative fitting procedure it is tested, how many parameters are necessary to yield a good description of the data, so that parameters consistent with zero are fixed to zero.

13.7 Quality Assessment

For a temperature sensor calibration to be considered successful in accordance with the requirements stated in section 13.1, the standard deviation of the data points from the fit function (cf. figure 13.11 (right)) should be smaller than $0.02\text{ }^\circ\text{C}$ for both subsamples.

This standard deviation is estimated by the root mean square of the distances of the reference temperatures T_i^{ref} from the fit function evaluated at the measured resistances R_i and thus given by

$$\text{RMS} = \sqrt{\frac{1}{n} \sum_{i=1}^n (T_i^{\text{ref}} - f(R_i))^2}.$$

This value corresponds to the statistical uncertainty of the measurement. Figure 13.13 shows the standard deviation of the data points (only values below $0.2\text{ }^\circ\text{C}$ are visualized) against the sensor ID with the corresponding fit status indicated by color.

Figure 13.14 shows the distributions for both subsamples individually as well as for the full sample. For the two subsamples the most probable value of $0.01\text{ }^\circ\text{C}$ is about a factor of two smaller than the limit value. Taking the full sample into account the most probable value of $0.03\text{ }^\circ\text{C}$ is significantly larger due to the hysteresis.

The correlation between the standard deviations of the two subsamples is displayed in figure 13.15. Since both distributions are quite asymmetric and not well described by a Gaussian distribution, the Pearson correlation coefficient is not suited as a measure for the statistical correlation. Therefore the Spearman's rank correlation coefficient is calculated instead, which is just the Pearson correlation of the data points ranked according to their values. The rank correlation is even sensitive to monotonic relations not only to linear relations. The obtained rank correlation coefficient of 0.045 is rather small, hence the RMS should be considered rather as a property of the measurement than of the calibrated temperature sensor itself. Thus a large RMS value is not conclusive to decide on the quality of this sensor. Although they have not been selected according to the criterion introduced above, some sensors may still be of good quality, which could be revealed by performing additional measurements.

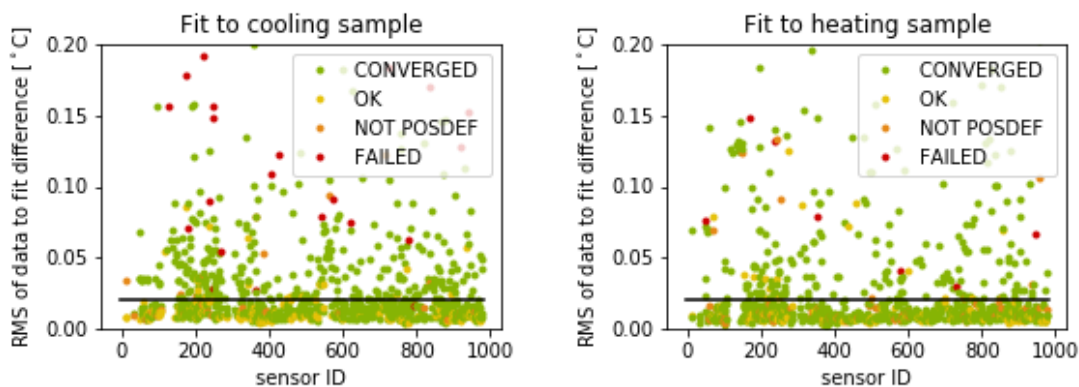


Figure 13.13: Standard deviation of the data points from the fit function against sensor ID for all fits marked with colors representing the fit status

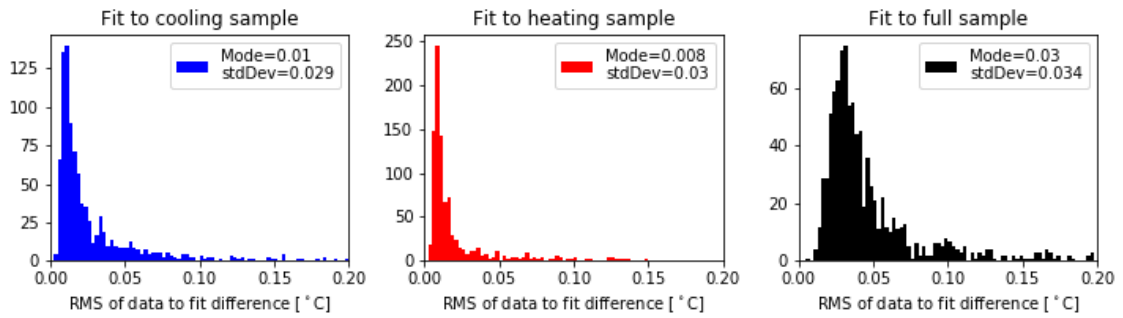


Figure 13.14: Standard deviation of the data points from the corresponding fit function for the cooling sample (blue), the heating sample (red) and the full sample (black)

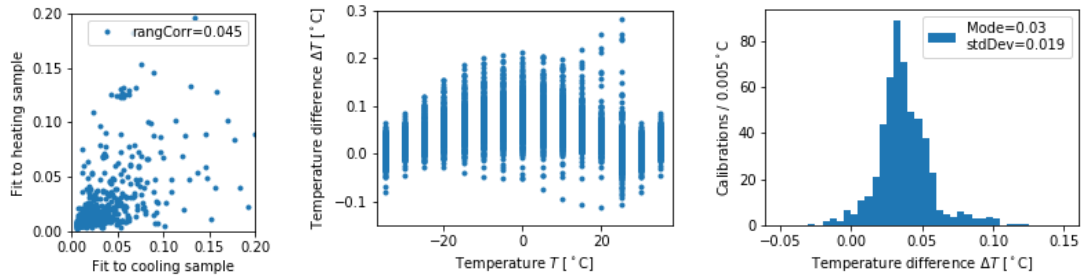


Figure 13.15: Correlation between the standard deviations for the two subsamples (left), difference between the fit functions at certain set temperatures (center), distribution of temperature differences for a set temperature of -25°C

The extent of the hysteresis varies for different sensors. Typically the fit function of the heating sample is above the one for the cooling sample. Figure 13.15 (center) displays the difference values of all calibration measurements at certain temperatures. The maximum of 0.2°C is located at 0°C . The distribution of the differences values at -25°C is shown in figure 13.15 (right). The most probable value of this distribution is 0.03°C , like for the standard deviation of the data points from the fit function to the full sample.

13.7.1 Reproducibility

Even more important than a low statistical uncertainty is a low systematic uncertainty, since the temperature sensors should reliably deliver the same results when exposed to the same temperature. In order to analyze the reliability of a temperature sensor, it needs to be measured several times, so that the difference between the resulting fit functions can

be quantified. The mean of several polynomials $f_j = d_j R^0 + c_j R^1 + b_j R^2 + a_j R^3$ can be determined easily by just using the mean of the individual parameters

$$\begin{aligned}\alpha &= \frac{1}{n} \sum_{j=1}^n a_j, \quad \beta = \frac{1}{n} \sum_{j=1}^n b_j, \quad \gamma = \frac{1}{n} \sum_{j=1}^n c_j, \quad \delta = \frac{1}{n} \sum_{j=1}^n d_j, \text{ since} \\ \bar{f} &= \frac{1}{n} \sum_{j=1}^n f_j = \frac{1}{n} \sum_{j=1}^n (d_j R^0 + c_j R^1 + b_j R^2 + a_j R^3) \\ &= \frac{1}{n} \sum_{j=1}^n d_j R^0 + \frac{1}{n} \sum_{j=1}^n c_j R^1 + \frac{1}{n} \sum_{j=1}^n b_j R^2 + \frac{1}{n} \sum_{j=1}^n a_j R^3 = \delta R^0 + \gamma R^1 + \beta R^2 + \alpha R^3\end{aligned}$$

To determine a standard deviation of several polynomials, it is necessary to define a distance between two polynomials. The area between the two polynomials is a natural choice for such a distance. Since the sign of the integral changes depending on which of the polynomials has higher values, the square root of the integral of the squared function

$$\begin{aligned}\text{dist}(f_j, \bar{f}) &= \sqrt{\int_{R_{\min}}^{R_{\max}} (f_j - \bar{f})^2 dR} \quad \Rightarrow \quad \text{dist}(f_j, \bar{f})^2 = \int_{R_{\min}}^{R_{\max}} (f_j - \bar{f})^2 dR \\ \Rightarrow \text{dist}(f_j, \bar{f})^2 &= \int_{R_{\min}}^{R_{\max}} ((d_j R^0 + c_j R^1 + b_j R^2 + a_j R^3) - (\delta R^0 + \gamma R^1 + \beta R^2 + \alpha R^3))^2 dR \\ &= \int_{R_{\min}}^{R_{\max}} ((d_j - \delta)R^0 + (c_j - \gamma)R^1 + (b_j - \beta)R^2 + (a_j - \alpha)R^3)^2 dR\end{aligned}$$

over the accessible resistance range from $R_{\min} = 85 \Omega$ to $R_{\max} = 122 \Omega$ is used. Defining $m = a_j - \alpha$, $n = b_j - \beta$, $k = c_j - \gamma$ and $l = d_j - \delta$, the integration yields

$$\begin{aligned}\text{dist}(f_j, \bar{f})^2 &= \left[m^2 \frac{R^7}{7} + 2mn \frac{R^6}{6} + (n^2 + 2mk) \frac{R^5}{5} + (2nk + 2ml) \frac{R^4}{4} \right. \\ &\quad \left. + (k^2 + 2nl) \frac{R^3}{3} + 2kl \frac{R^2}{2} + l^2 \frac{R^1}{1} \right]_{R_{\min}}^{R_{\max}}.\end{aligned}$$

The integrals are scaled by the value dist_1 obtained for $m = 0$, $n = 0$, $k = 0$, and $l = 1$, which corresponds to a constant difference of 1°C between two polynomials, such that the result is unitless but corresponds to the average temperature difference in $^\circ\text{C}$. The standard deviation is then calculated by

$$\sigma_f = \sqrt{\frac{1}{n} \sum_{j=1}^n \left(\frac{\text{dist}(f_j, \bar{f})}{\text{dist}_1} \right)^2}.$$

Figure 13.16 shows the standard deviation of the fit functions against the average time distance between the corresponding calibration measurements. Even though the rank correlation is rather small, the standard deviation values obtained for measurements which are separated in average less than 100 days are all small. Larger values are only obtained for calibrations between which longer time periods passed. Possibly, for those sensors which are not reproducible, the effect worsens over time. Therefore, there should be an adequate time distance between two calibration measurements, in order to be sure that a temperature sensor behaves reproducibly.

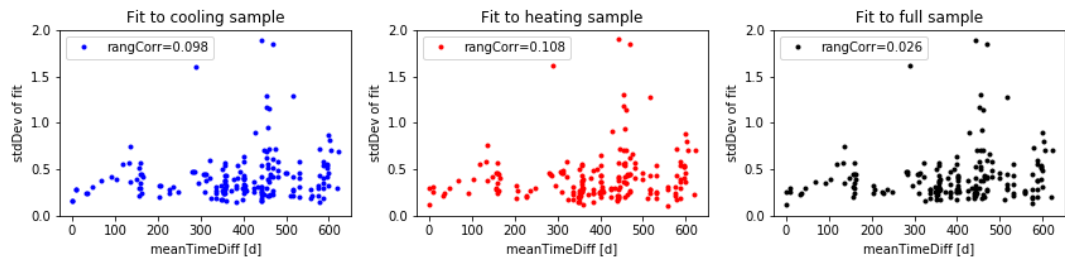


Figure 13.16: Standard deviation between the fit functions from different calibration measurements against averaged time difference between them

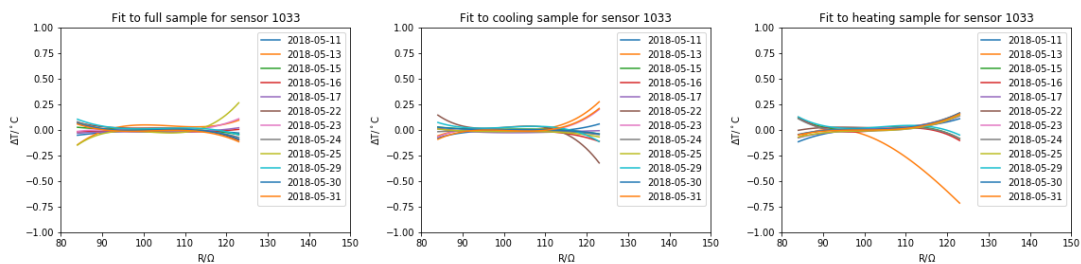


Figure 13.17: Difference of the fit functions obtained from several calibration measurements to the averaged fit function for the same sensor

None of the sensors has a standard deviation below 0.02°C between the fit functions, but as can be seen exemplary in figure 13.17 for a sensor, the largest difference between the fit functions occurs at the beginning and the end of the resistance range. Since the high precision of 0.02°C is actually not required for the full spectrum but just at -25°C , it is sensible to determine the standard deviation just at that point.

For that purpose, the resistance which is measured at -25°C , gets determined numerically for each fit function. For each sensor the standard deviation of these resistances is determined and then transformed into a temperature value by using the slope of the mean polynomial, which is displayed in figure 13.16. For about half of the sensors this transformed standard deviation is below 0.02°C which is indicated by the black line in figure 13.16. A detailed overview of the amount of reliable sensors is provided in section 13.9.

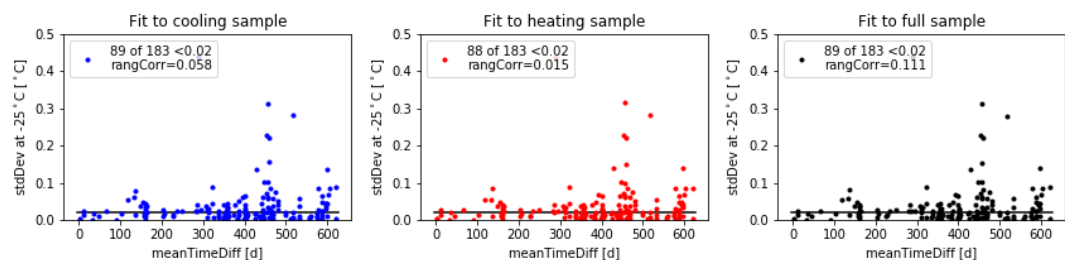


Figure 13.18: Standard deviation of the resistances at -25°C from the different fit functions of a sensor transformed to a temperature against the averaged time difference between these, the black line indicates the upper limit of 0.02°C

13.8 Dedicated Studies

Besides evaluating the data obtained from calibration measurements, the properties of the ultrathin temperature sensors have also been investigated in dedicated measurements, which will be presented in the following to subsections.

13.8.1 Hysteresis Effect

Naturally the question arises, if the strength of the hysteresis effect depends on the step size between the set temperatures or the minimal and maximal set temperatures of the calibration measurement. Those two parameters have been varied independently so that for twelve temperature sensors which fit at once in the calibration setup the resulting strength of the hysteresis effect could be studied.

Figure 13.19 shows the results for varying step sizes between the set temperatures from 10°C , over 5°C down to 1°C . In contrast to the expectation, the hysteresis effect is increased for the smallest step size tested between the set temperatures.

Figure 13.20 shows the results for varying minimal and maximal set temperatures from $\pm 35^\circ\text{C}$, over $\pm 30^\circ\text{C}$ down to $\pm 25^\circ\text{C}$, but with a constant step size of 5°C between the different set temperatures. The error bars correspond to the uncertainty of the reference temperature ΔT^{ref} , which is determined as described in section 13.6.3. Large errors typically occur if the thermal equilibrium has not yet been reached for all data points. Additionally, the effect on the hysteresis of baking the temperature sensors for a second time has been studied.

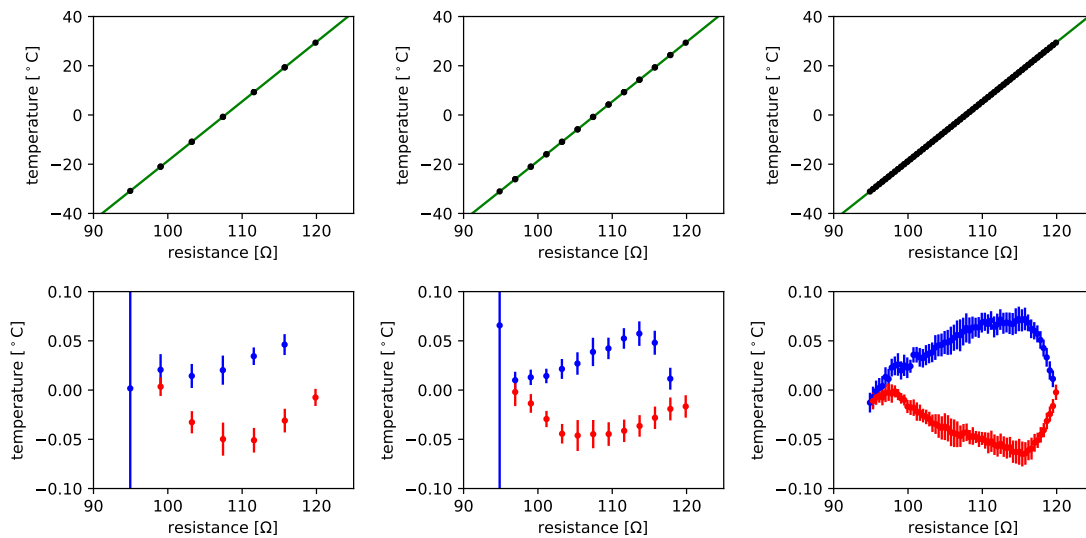


Figure 13.19: Three measurements (top row) of the same sensor with set temperatures between -30°C and $+30^\circ\text{C}$ with varying step sizes of 10°C (left), 5°C (center), and 1°C (right) between the set values, each kept for 1 h and the corresponding differences from the data points of the cooling sample (blue) and the heating sample (red) to the fit function obtained from fitting all data points at once (bottom row)

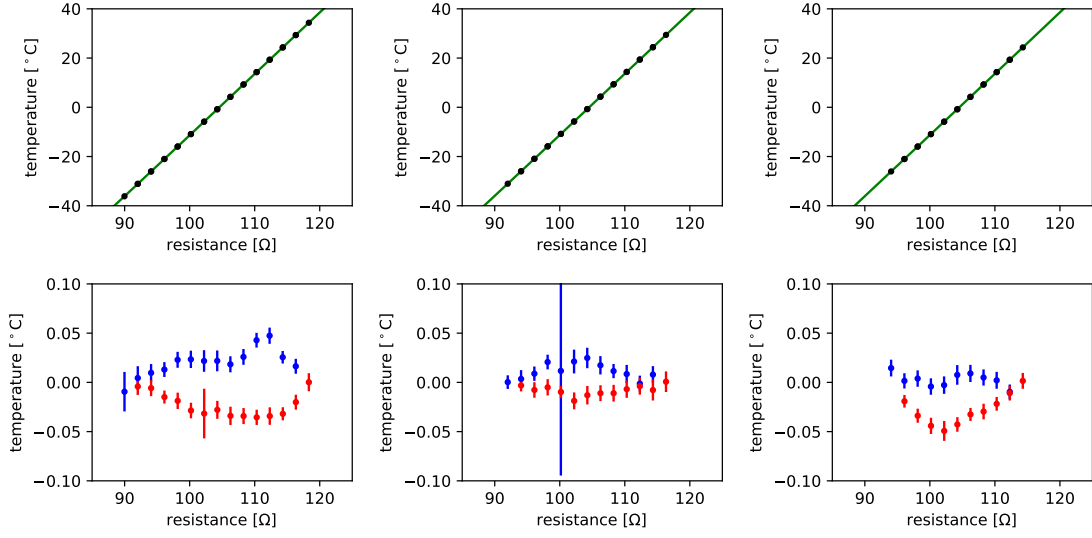


Figure 13.20: Three measurements of the same sensor for which the set temperatures were varied in steps of 5°C and kept constant for 1 h between varying minimal and maximal temperatures of $\pm 35^\circ\text{C}$ (left), $\pm 30^\circ\text{C}$ (center), and $\pm 25^\circ\text{C}$ (right); the lower row shows the corresponding differences from the data points of the cooling sample (blue) and the heating sample (red) to the fit function obtained from fitting all data points at once

For a more quantitative analysis of the results the hysteresis η is quantified by averaging over the distances between the evaluation of the data points from the cooling sample and the heating sample with the fit function f^{comb} obtained from fitting the combined sample

$$\begin{aligned}\eta &= \frac{1}{N} \sum_i^N \left([T_i - f^{\text{comb}}(R_i)] - [T_{i+k_i} - f^{\text{comb}}(R_{i+k_i})] \right) \\ &= \sum_i^N \frac{f^{\text{comb}}(R_{i+k_i}) - f^{\text{comb}}(R_i)}{N},\end{aligned}$$

where k_i is the respective index shift for which $T_i = T_{i+k_i}$. The uncertainty of this value is estimated by

$$\begin{aligned}\Delta\eta &= \sqrt{\sum_{k=0}^3 \left(\sum_i^N \left[\left. \frac{\partial f^{\text{comb}}}{\partial p_k} \right|_{R_i} - \left. \frac{\partial f^{\text{comb}}}{\partial p_k} \right|_{R_{i+k_i}} \right] \frac{\Delta p_k}{N} \right)^2 + \dots} \\ &\quad \dots + \sum_i^N \left[\left(\left. \frac{\partial f^{\text{comb}}}{\partial R} \right|_{R_i} \frac{\Delta R_i}{N} \right)^2 + \left(\left. \frac{\partial f^{\text{comb}}}{\partial R} \right|_{R_{i+k_i}} \frac{\Delta R_{i+k_i}}{N} \right)^2 \right].\end{aligned}$$

Figure 13.21 provides an overview of the hysteresis values obtained for the studies mentioned above. The observation that the hysteresis is larger for the smallest tested step size of 1°C than for the larger step sizes of 5°C or 10°C can be clearly confirmed. The uncertainties for small step sizes are smaller and for big step sizes are larger, which is to

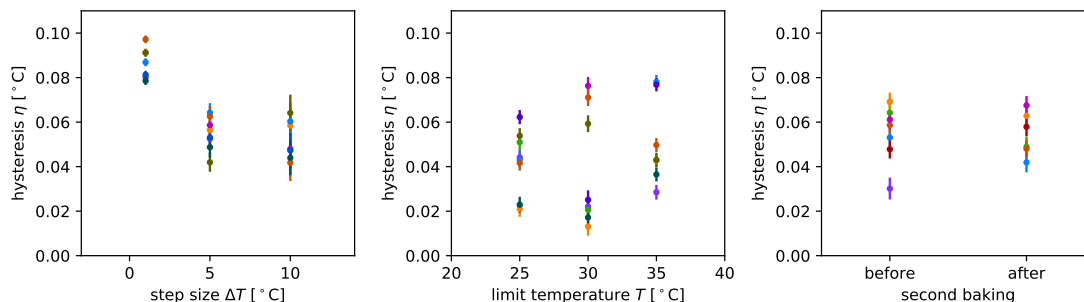


Figure 13.21: Hysteresis values obtained for the different step sizes between the temperature set values (left), for different maximal and minimal temperature values (center) and before and after a second baking (right); points of the same color correspond to the same sensor

be expected as a smaller step size corresponds to more different temperature set values and thus larger statistics for the determination of the hysteresis. Besides that no clear conclusion can be drawn.

The actually interesting question is not so much how the hysteresis effect can or cannot be influenced, but how to obtain the most reasonable temperature value when the detector is cooled down and then keeps the same temperature for a long time except maybe for small temperature fluctuations caused by the temperature regulation or load changes. To answer this question another series of measurements has been carried out. For these measurements the temperature is varied from -25°C to different extents, that is $\pm 5^{\circ}\text{C}$, $\pm 1^{\circ}\text{C}$, $\pm 0.5^{\circ}\text{C}$, and $\pm 0.1^{\circ}\text{C}$ and each set temperature is kept for nearly an hour. Figure 13.22 shows the results of these measurements. Besides the set temperature and the current value measured by the thermostat, the recorded ADC conversion, as well as the temperature recorded by the sensor on the THMP mainboard, and the corresponding resistance values according to the calibration of the respective THMP channel are shown. Furthermore also the corresponding temperature values according to the two different fit functions obtained from fitting the two different subsamples of the calibration measurement of the respective temperature sensor are displayed.

Unfortunately for none of these measurements the temperature measured by the THMP temperature sensor has been stable. The reason for the unstable temperature is the usage of the air conditioning, which might have failed, been turned off and on again and so on. The temperature sensor calibration setup is situated quite close to the air conditioning and the THMP itself is usually located directly in the airflow. Large changes of the environmental temperature have an influence on the recorded ADC conversion as it is obvious especially for the second and fourth measurement displayed in figure 13.22.

The influence of the environmental temperature can be compensated by taking into account the temperature measured by a sensor on the THMP mainboard (cf. section 14.4). The resistance values obtained after application of the THMP calibration should thus be independent of the THMP board temperature.

As visible in the fourth row of figure 13.22, the temperature dependence is not fully compensated but in comparison to the statistical fluctuations clearly decreased. The remaining temperature dependence might be caused by the circumstance, that the thermal distribution is different for the THMP in the airflow compared to that in the climate chamber

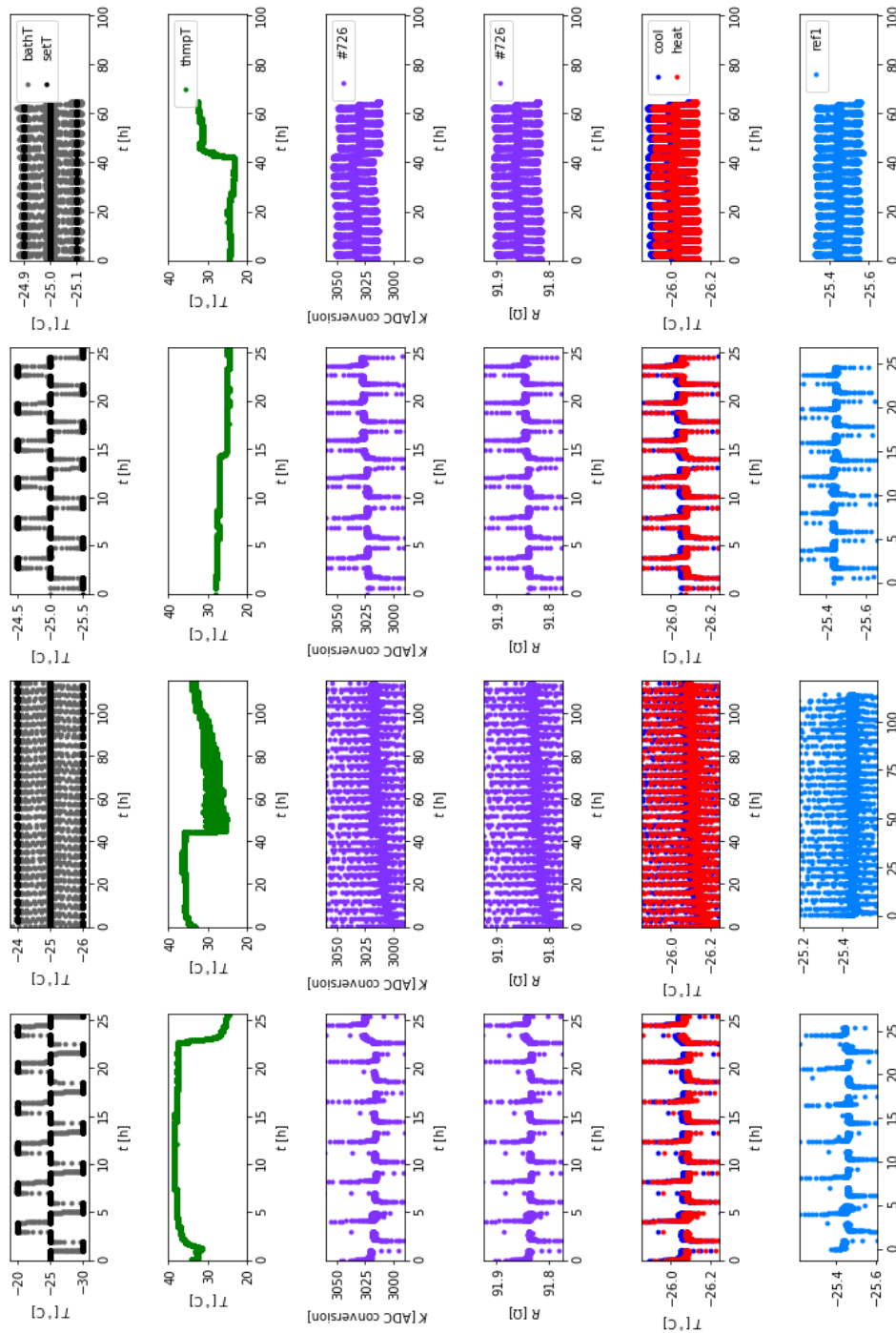


Figure 13.22: Recorded thermostat temperature and set value (1st row), temperature recorded by the sensor on the THMP mainboard (2nd row), ADC conversion values (3rd row), corresponding resistance values (4th row), temperature values of an ultrathin temperature sensor (5th row) and of a reference sensor (6th row) obtained from measurements with set temperatures varying by 5°C (1st column), 1°C (2nd column), 0.5°C (3rd column), and 0.1°C (4th column) around -25°C

during the calibration of the THMP \bar{P} . The actual temperature of the relevant electronic components thus might be different for the same measured THMP \bar{P} board temperature.

Considering the hysteresis effect it is surprising that the values measured at the temperature set value of -25°C do not seem to depend on whether the former temperature set value has been below or above.

Nonetheless, neither the ADC conversions nor the resistance values corresponding to periods during which the temperature set value has been -25°C are stable. The temperatures measured by a reference sensor simultaneously seem to be more stable, especially during the measurement with variations by 1°C . Nonetheless, also for the reference temperature the measured values vary over the course of the measurement.

For a clear overview figure 13.23 shows only these data points for all four measurements. Besides the ADC conversion values over time (1st row), also the correlation between the ADC conversion and the recorded THMP \bar{P} temperature (2nd row) as well as between the resistance values and the recorded THMP \bar{P} temperatures (3rd row) and the temperature recorded by the reference sensor (4th row) are shown, not only for the individual measurements but also for all measurements at once (5th column).

Constant resistance values but varying environmental temperatures should result in a line with a slope corresponding to the temperature dependence of the respective THMP \bar{P} channel in the ADC conversion versus THMP \bar{P} temperature plots shown in the second row in figure 13.23. If the temperature dependence is properly accounted for, the corresponding lines in the resistance versus THMP \bar{P} temperature plot should be flat. Different resistance values result in parallel lines.

As mentioned above, a slight temperature dependence is still observable for the resistance values obtained by applying the THMP calibration. The data points obtained for the measurements with set value variations of 5°C and 0.5°C seem to correspond to the same resistance value, whereas the data points obtained for the measurements with set value variations of 1°C and 0.1°C seem to correspond to different resistance values each. The temperature measured by the reference sensor and by the ultrathin temperature sensor do not show a clear correlation, at least for such small variations.

The successive display of the ADC conversions over time for all measurements given in the top row of the rightmost column of figure 13.23 shows a clear upwards trend beyond the temperature dependency, which could be caused by a slow drift of the resistance of the temperatures sensor. A clearer picture can be obtained with a longterm measurement with the constant set value -25°C without any fluctuations as presented in the following subsection.

The obtained temperature values are significantly separated from -25°C so that it does not make sense to decide on which of the two calibration functions obtained by fitting the two different subsamples should be used to obtain the most reasonable temperature value. In the end it should be considered to use the calibration function obtained by fitting the full data sample and use the known extent of the hysteresis effect of 0.03°C at -25°C just for the uncertainty estimation.

13.8.2 Longterm Stability

A longterm measurement using the calibration setup at a temperature -25°C kept for a duration of approximately 305 hours, which corresponds to almost 13 days has been performed. This way the stability of the temperature sensors can be qualified. Figure 13.24 shows some of the obtained results.

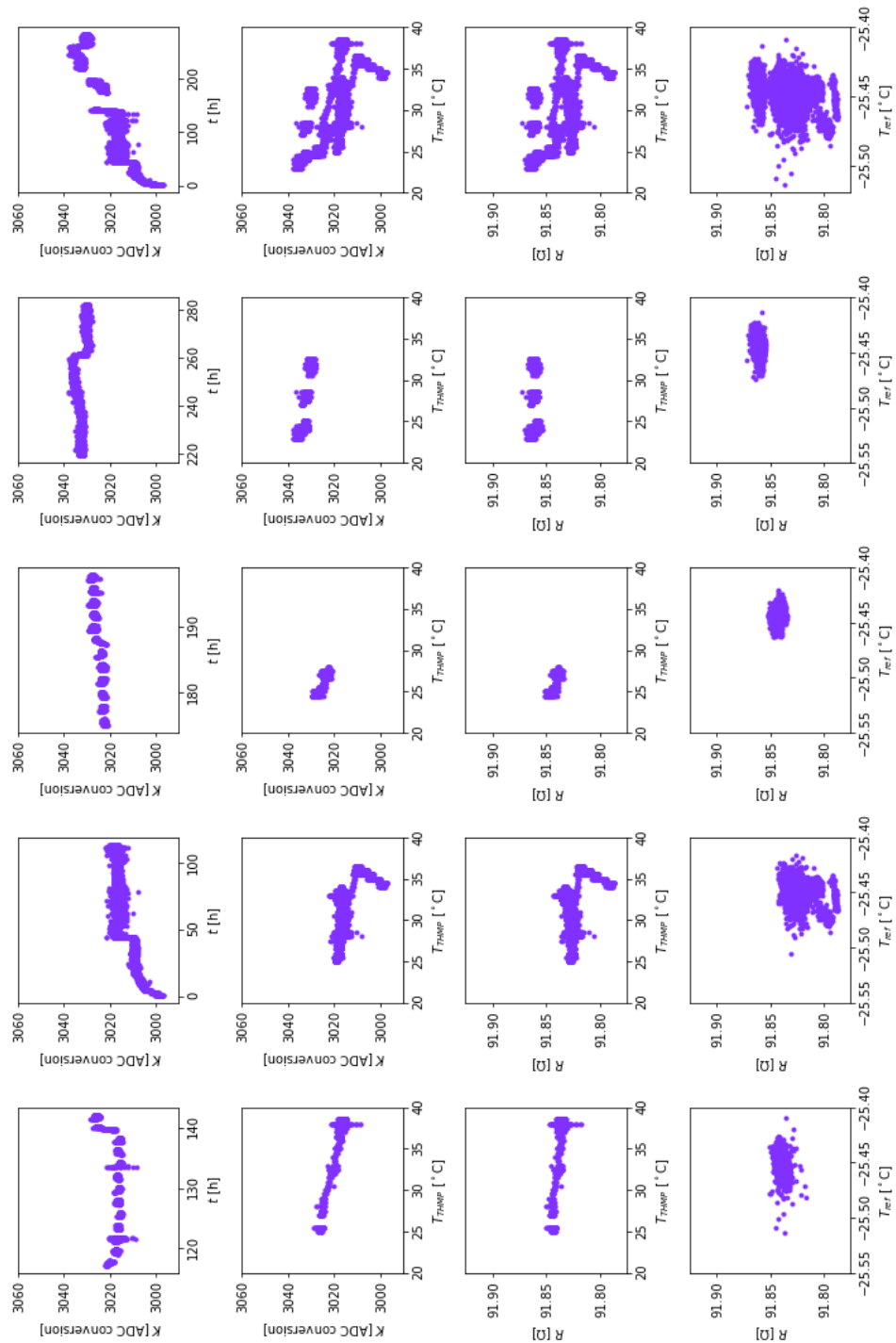


Figure 13.23: ADC conversions vs. time (1st row), ADC conversions vs. THMP board temperature (2nd row) as well as the corresponding resistances vs. THMP board temperature (3rd row) and vs. the temperature measured by the reference sensor (4th row) for the measurements with set temperatures varying by 5°C (1st column), 1°C (2nd column), 0.5°C (3rd column), and 0.1°C (4th column) around -25°C and for all these measurements together (5th column)

The bath temperature of the thermostat varies by no more than 0.02°C from the set value after it is reached, at the start of the measurement the setup is at $+20^\circ\text{C}$. Over the entire runtime of the measurement also the temperature sensor of the THMP mainboard recorded stable temperature values at 30°C .

A resistor has been soldered directly onto the piggyback board (PBB) so that in case of fluctuations concerning all readout channels an effect caused by a change of temperature can be distinguished from one caused by the electronics. Since the values obtained for that resistor stay stable over the entire measurement as shown in the last row of figure 13.24, the THMP may be considered as longterm stable.

Similar to the temperature values recorded by the thermostat the values of the reference temperature sensor displayed in the 7th row of figure 13.24 stay at the same temperature once it is reached, except for a small shift after approximately 240 hours. The temperature values of the reference sensor shown in figure 13.24 are slightly below -25.4°C , whereas the temperature values of the other reference sensor are slightly above -25.3°C and also show a small shift at the same time.

The cause of the observed shift has been investigated and could be reproduced by disconnecting the cable, which is connected with the shielding of the reference sensor cable, from the thermostat housing.

The temperatures measured by the ultrathin sensors all show a limited growth after a minimal temperature value is reached. A function describing the limited growth

$$g(t) = L - (L - g(0)) \cdot \exp(-k \cdot t)$$

is fitted to the resistance values in the time period from 90 minutes after the measurement start, when the minimal temperature is reached, to 48 hours after the start of the measurement, when the limit seems to be reached, but the limit line is as well shown for all remaining data points in figure 13.24. In comparison with that line, it becomes obvious that the limited growth is followed by a slight upwards drift over the runtime of the measurement. The two temperature sensors for which the measurement results are exemplary shown in figure 13.24 are the extreme cases for the extent of the drift. Since the temperature growth and the drift are only observed for the ultrathin temperature sensors but not for the reference sensors it is most probably not caused by a varying temperature but some characteristic of the temperature sensor.

The growth rates k are scattered around approximately 0.1h^{-1} and the limit values L transformed by the calibration functions of the respective sensor to a temperature $\frac{1}{2}(f^{\text{cool}} + f^{\text{heat}})$ are scattered around -26°C as shown in figure 13.25. For all sensors the obtained temperature values lie significantly below -25°C . It might be that the temperature sensor of the thermostat changed its behavior over time, so that the cooling liquid actually has a temperature below -25°C . Even if that is the case, still the ultrathin temperature sensors yield significantly lower temperature values than the reference sensors, which can only be explained with a similarly changed behavior of the ultrathin temperature sensors.

It is not practical to perform a longterm measurement with all ultrathin temperature sensors to check if they show drifting behavior at stable temperatures and to what extent. The assumption is, that drifting temperature sensors would yield different results when calibrated at two different times, so that demanding a good reproducibility yields sensors which provide stable measurement results.

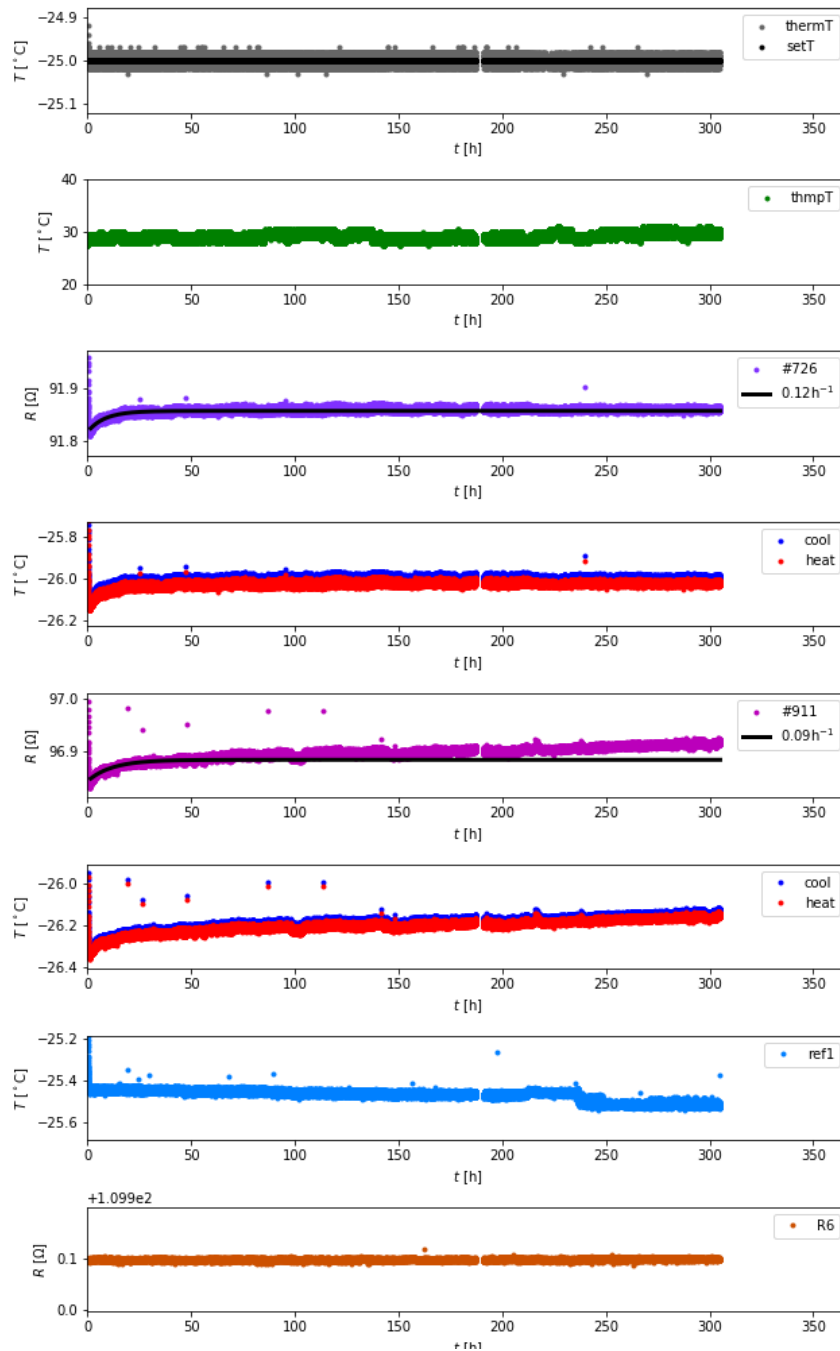


Figure 13.24: Recorded thermostat temperature and set value (1st row), temperature recorded by the sensor on the THMP mainboard (2nd row), resistance values corresponding to the recorded ADC conversions according to the calibration of the respective THMP channel and temperature values according to the calibration of the respective sensor for the most (3rd and 4th row) and least (5th and 6th row) stable sensors, temperature values of a reference temperature sensor (7th row), and resistance values of a resistor soldered directly on the PBB (8th row) obtained from a longterm measurement starting at +20°C with a temperature set value of -25°C over 305 h

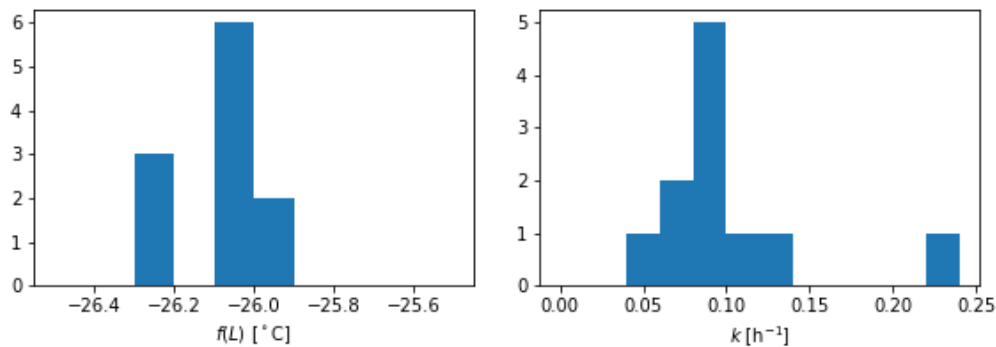


Figure 13.25: Limit values obtained from fitting a limited growth function to the resistance values between 1.5 h and 48 h of the longterm measurement for the different sensors transformed to temperatures according to their respective calibration function (left) and the obtained time constants (right)

13.9 Supply Status and Outlook

After the prototype of the TS EMC forward endcap called Proto192 had been equipped with numerous temperature sensors, 826 temperature sensors (ID #152 to #977) have been produced for the TS EMC forward endcap using the exposed and etched copper coated polyimide foil cables and manually wound platinum wire. In total 104 of the sensors were unfortunately broken unnoticed during the production or have too low or too high resistances to be read out with the THMP, so that they cannot be used further. At a comparably early stage of the temperature sensor production and calibration the 83 temperature sensors, which were considered to be best, have been provided for the first TS EMC barrel slice. To that time another THMP has been used, so that the temperature dependence had not been accounted for yet, neither had the reproducibility of the sensors been tested. Therefore 639 ultrathin temperature sensors remain for potential use in the forward endcap.

After many useful tests had been performed with the Proto192, it was disassembled. In total 75 ultrathin temperature sensors were retrieved, from which 28 sensors were broken or had too low or too high resistances to be read out with the THMP. Therefore the number of sensors potentially usable for the TS EMC forward endcap has been increased to 686.

Most of the temperature sensors have been calibrated twice with the intention to study reproducibility with high statistics as presented in subsection 13.7.1. Table 13.2 provides an overview on how many temperature sensors haven been calibrated how often and for how many of these calibrations the RMS of both fit functions to the two subsamples is smaller than 0.02°C . As the RMS values have a continuous distribution it might be interesting to check how many more sensors are below a slightly increased limit value of 0.022°C for example.

The reproducibility could be checked for all 380 sensors, which have been calibrated more than once, but of course it only makes sense to check the reproducibility for the $150+33+0=183$ sensors or $159+34+0=193$ sensors, respectively, for which at least two calibration measurements yielded a good result. Table 13.3 gives the amounts of temperature sensors, which yield reproducible calibration results, separately for the different

		n_{RMS}								n_{RMS}					
		0	1	2	3	4	total			0	1	2	3	4	total
n_{cal}	1	269	37	—	—	—	306	n_{cal}	1	255	51	—	—	—	306
	2	92	88	128	—	—	308		2	87	84	137	—	—	308
	3	7	8	21	29	—	65		3	6	8	21	30	—	65
	4	2	0	1	4	0	7		4	2	0	1	4	0	7
total		370	133	150	33	0	686	total		350	143	159	34	0	686

Table 13.2: Numbers of ultrathin temperature sensors, which have been calibrated n_{cal} times and fulfilled the criterion $\text{RMS} < 0.02^\circ\text{C}$ (left) or $\text{RMS} < 0.022^\circ\text{C}$ (right) for the fits to both subsamples n_{RMS} times

$n_{\text{RMS}}/n_{\text{cal}}$	Total	$n_{\text{rep}}^{\text{all}}$	$n_{\text{rep}}^{\text{last}}$	$n_{\text{RMS}}/n_{\text{cal}}$	Total	$n_{\text{rep}}^{\text{all}}$	$n_{\text{rep}}^{\text{last}}$
2/2	128	60	60	2/2	137	68	68
2/3	21	7	7	2/3	21	7	7
2/4	1	0	0	2/4	1	0	0
3/3	29	17	22	3/3	30	17	23
3/4	4	2	3	3/4	4	2	3
total	183	86	92	total	193	94	101

Table 13.3: Numbers of ultrathin temperature sensors, which have been calibrated n_{cal} times, fulfilled the criterion $\text{RMS} < 0.02^\circ\text{C}$ (left) or $\text{RMS} < 0.022^\circ\text{C}$ (right) for the fits of both subsamples n_{RMS} times and all fits are reproducible $n_{\text{rep}}^{\text{all}}$ or at least the last two fits are reproducible $n_{\text{rep}}^{\text{last}}$

numbers of performed measurements n_{cal} and numbers of measurements n_{RMS} , which fulfilled $\text{RMS} < 0.02^\circ\text{C}$ or $\text{RMS} < 0.022^\circ\text{C}$. Assuming, that the behavior of temperature sensors changes over time and reaches a stable point eventually, it makes sense to compare the measurements not with the mean, but with the last measurement. The sensor can then be assumed to have reached stable behavior, if the last two measurements fulfill the reproducibility criterion. That should not change anything for the sensors with only two considered calibrations, but some more sensors with three considered calibrations turn out reproducible with that criterion. With the loosened limit for the RMS that yields in total 101 of the 686 analyzed calibrated temperature sensors, that is 14.7%.

The assumption on an increasingly stable behavior should be tested with a high statistics of temperature sensors being calibrated at least three times, but better even more often. With the improved temperature calibration setup described in subsection 13.9.2, 30 temperature sensors instead of 12 can be calibrated in parallel so that such a study gets feasible.

Recalibrating the 51 sensors, which have been calibrated only once yet and yielded an RMS below 0.022°C , will probably increase the number of suitable temperature sensors a bit. Taking into account the ratio $\frac{137}{137+84} = 0.620$ of sensors, which have been calibrated twice and fulfilled the RMS limit for both measurements from those which fulfilled it at least once, and taking into account the ratio of the reproducible ones $\frac{68}{137} = 0.496$ one might expect $51 \cdot 0.620 \cdot 0.496 \approx 16$ more suitable sensors. The ratio would then be increased to $\frac{117}{686} = 17.1\%$.

13.9.1 Testing Contacting Methods

In order to increase the ratio of suitable sensors a series of sensors is produced with different preparation and connecting methods.

Preparation in that context means cleaning or surface roughening of the wire and/or the contact pads, in order to increase the surface tension and thus improve the connection between them. The contact pads are anyway cleaned with isopropanol before the tape with the wound platinum wire is attached, so this is not explicitly mentioned. After consultation with chemists acetone is used in addition for cleaning the contact pads and also the platinum wire itself to remove potential oil and grease deposits, which hinder a good connection.

The group of Prof. Keudell kindly allowed us to use their setup for treatment of platinum wires and the contact pads with cold plasma for the test series.

Additionally, a gadget for applying silicate nanostructures to roughen the surface and thereby increasing surface tension has been leased from the company Polytec for two weeks and used on the platinum wire for several sensors.

Connecting methods considered include also bonding and welding techniques besides applying a conductive adhesive.

Table 13.4 lists the properties of the considered conductive adhesives. Not all properties are given by all providers, so a question mark indicates that the respective property is not known. The volume resistivity should be as small as possible, whereas the thermal conductivity should be as high as possible. The temperature stability should cover the intended working range of the ultrathin temperature sensors of about $\pm 35^\circ\text{C}$. Long pot life times are preferable since only very small amounts of the adhesive are needed per sensor, so that most probably the pot life time is exceeded before the adhesive is used up.

Name	Epotek H37MP	Elecolit 414	Elecolit 3661	Polytec EC 242-frozen
Basis	Epoxy	Polyester	Epoxy	Epoxy
Viscosity [mPas]	22000-26000 (23°C, 10 rpm)	200000-25000 (25°C, 6 rpm)	20000-40000 (25°C, 10.5 s ⁻¹)	35000 (23°C, 10.5 s ⁻¹)
Temperature Stability	≤ 300°C	-55°C- 200°C	-40°C- 180°C	-55°C- 220°C
Volume Resistivity	≤ 5 · 10 ⁻⁴ Ω cm	5 · 10 ⁻⁵ Ω cm	5 · 10 ⁻³ Ω cm	5 · 10 ⁻⁵ Ω cm
Thermal Conductivity	1.6 W/m·K	?	?	4.2 W/m·K
Cure Condition	150°C/ 60 min	150°C/ 5 min	150°C/ 10 min	150°C/ 5 min
Shelf Life (Bulk)	12 months at -40°C	6-12 months at 0°C- 10°C	2-4 months at 0°C- 10°C	12 months at -40°C
Pot Life	28 days	?	14 days	48 hours at 23°C

Table 13.4: Properties of the used conducting adhesives

Cleaning	Preparation	Connection	# Sensors	Serial IDs
—	Wire: He plasma	H37MP	7	#1063,#1067,#1068 #1071-#1074
—	Both: He plasma	H37MP	5	#1064-#1066, #1069,#1070
Wire: with acetone	—	H37MP	5	#1075-#1079
—	—	welded & H37MP	1	#1080
Both: with acetone	—	H37MP	5	#1081-#1085
—	—	Elecolit 414	11	#1086-#1096
—	silicatized	Elecolit 414	12	#1097-#1108
Both: with acetone	silicatized	Elecolit 414	14	#1109-#1122
Both: with acetone	silicatized	Elecolit 3661	12	#1023-#1134
—	silicatized	Elecolit 3661	10	#1135-#1144
Both: with acetone	silicatized	H37MP	12	#1145-#1156
—	silicatized	H37MP	12	#1157-#1168
Both: with acetone	—	Elecolit 3661	4	#1169-#1172
Both: with acetone	—	H37MP	3	#1173-#1175
Both: with acetone	—	varyingly welded	22	#1176-#1197
Both: with acetone	blow dried at 60°C	welded with 30 V for 256 ms	8	#1198-#1205

Table 13.5: Number of sensors produced with different cleaning, preparation and connecting methods

The group of Advanced Chip and Wire Bonding of the Fraunhofer IZM system integration and interconnection technologies (SIIT) has been contacted for consultation of bonding methods and offered to perform bonding tests with the platinum wire and the gold contact pads on the polyimide cables. Bonding of this combination is quite challenging not only because of the hardness of platinum and its high melting point but also because of the softness of the polyimide tape underneath. In house tests some years ago just resulted in holes in the contact pads. Unfortunately the trials did not succeed. At first welding seemed to have similar problems, but after measures have been taken to control the introduced energy more reliably the connections could be produced successfully.

Table 13.5 provides an overview of the numbers of sensors produced with different combinations of preparation and connection methods.

Most important in the end is the performance of the temperature sensors. In order to detect potential drifting or other unstable behavior all the sensors should be calibrated at least twice before a reasonable decision can be taken on which method yields the best results. The project is still ongoing.

13.9.2 Improved Calibration Setup

In order to speed up the calibration of temperature sensors for the remaining measurements beyond the scope of this thesis, the layout of the calibration setup has been reconsidered. With little effort an improvement can be achieved by keeping almost everything the same but turn the stack of temperature sensors by 90 degrees. Thus the thermal flow from the cooling plates has not to pass all the sensors but can approach each sensor directly from its sides. Sideways there is so much space that up to 30 of the ultrathin temperature sensors can be calibrated simultaneously with copper plates of twice the thickness as before

between two sensors. To achieve a good thermal contact, the side walls of the new copper box, which incorporates the stack of sensors, are covered with a heat conduction pad. The box itself is divided into two shells, so that the side walls can be pressed on the side faces of the copper plates in the stack, as shown in figure 13.26 (left). The two shells are aligned precisely by means of pin bolts, which is especially beneficial when stacking the temperature sensors into the box. To ensure a good thermal contact between the copper plates and the temperature sensors, the stack is compressed by a lid plate with two oppositely arranged spring sheets. These spring sheets press against a C-shaped frame so that the lid gets pushed evenly towards the stack. The produced setup including reference sensors is shown in figure 13.26

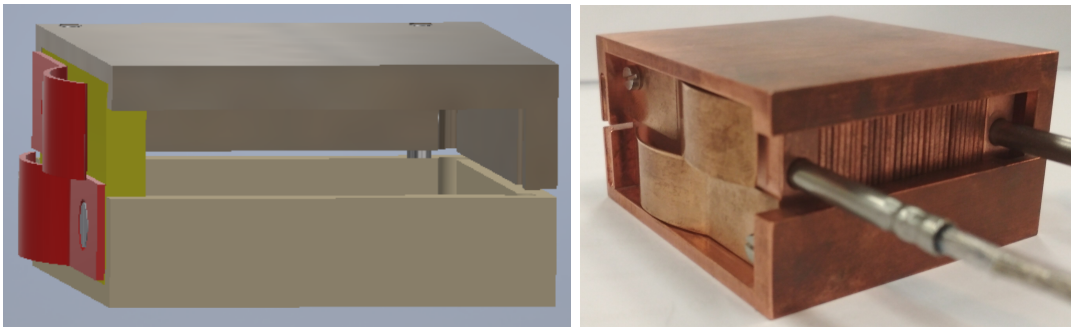


Figure 13.26: New design of the copper box, which incorporates the sensors stacked horizontally instead of vertically as CAD [116] (left) and photograph (right)

14 Temperature and Humidity Monitoring Board for $\overline{\text{PANDA}}$

In order to obtain highly accurate temperature measurements, not only the temperature sensors but also the readout electronics must provide a high precision. Therefore custom electronics dedicated for the readout of sensors, which monitor slowly varying environmental parameters as for examples humidity sensors, pressures sensors and the ultrathin platinum resistance temperature sensors have been developed at the Institut für Experimentalphysik I at Ruhr-Universität Bochum. To achieve an exceedingly high accuracy not only high precision electronic components are used but all readout channels are individually calibrated. The calibration procedure even takes the influence of the environmental temperature into account. Studies to determine the achieved precision are presented in this chapter.

The Temperature and Humidity Monitoring Board for $\overline{\text{PANDA}}$ (THMP $\overline{\text{P}}$) is designed modularly so that besides the resistance temperature sensors also humidity and pressure sensors can be read out. For the humidity and pressure sensor readout the precision requirements are not as ambitious as for the temperature sensors, so that the following chapter will focus on the temperature sensor readout with the THMP $\overline{\text{P}}$.

14.1 Requirements for the THMP $\overline{\text{P}}$

The requirements imposed on the THMP $\overline{\text{P}}$ board are driven by the requirements on the temperature measurement accuracy. By means of the temperature coefficient of platinum the measurement accuracy σ_T for temperature sensors translates to a measurement accuracy σ_R for the THMP $\overline{\text{P}}$ as

$$\sigma_R \approx \frac{\partial R(T)}{\partial T} \cdot \sigma_T \approx R(0^\circ\text{C}) \cdot \alpha_{\text{Pt}} \cdot \sigma_T \approx 7.8 \text{ m}\Omega \quad (14.1)$$

as follows from equation (13.1) with $R(0^\circ\text{C}) = 100 \Omega$, $\alpha_T = 3.851 \cdot 10^{-3} \text{ }^\circ\text{C}^{-1}$ and $\sigma_T = 0.02^\circ\text{C}$. That corresponds to a relative accuracy of $\frac{\sigma_R}{R} \approx 0.08\% = 80 \text{ ppm}$. To obtain that accuracy not only a low statistical uncertainty is needed, but also long-term stability of the readout is crucial. The longterm stability of the THMP $\overline{\text{P}}$ has already been demonstrated in the scope of the long-term measurements of the temperature sensors. The results are presented in section 13.8.2.

Besides that, further requirements are imposed on the THMP $\overline{\text{P}}$ due to its foreseen position in the detector. For measurements of the resistance temperature sensors the electronics should not be too far away from the sensors, which means that the THMP $\overline{\text{P}}$ must be mounted to the support frame of the forward endcap and in the support beams of the barrel slices. This still results in varying cable lengths of up to 2 m. Therefore it is crucial to base the measurement on 4-wire sensing not only for accuracy, but also to be independent of the varying line resistances.

Another requirement arises due to the positioning on the support frame and inside the support beam, all electronic components must be radiation hard. The radiation hardness of different electronic components has been investigated with a radiative γ source in Gießen and a proton beam at KVI in Groningen, the Netherlands [117]. The irradiation dose was chosen to be higher than the life time dose to be expected behind the TS EMC crystals and actually radiation damage has been observed, but at doses which will not be reached within ten years of data taking with the $\overline{\text{PANDA}}$ detector at full luminosity.

14.2 Layout of the THMP $\overline{\text{P}}$

The modular design of the THMP $\overline{\text{P}}$ consists of a mainboard with a microcontroller, an ADC and eight connectors to mount piggy-back boards (PBBs) as the key components. The PBBs have eight input channels which are transferred to an ADC on the mainboard. Hence, up to 64 sensors can be read out in parallel with one THMP $\overline{\text{P}}$.

By using different kinds of PBBs, the THMP $\overline{\text{P}}$ can read out different kinds of sensors. Two different kinds of PBBs are dedicated for the $\overline{\text{PANDA}}$ TS EMC. The one kind provides 4-wire sensing to read out resistance temperature sensors and the other kind serves for reading out humidity and pressure sensors. Figure 14.1 shows a THMP $\overline{\text{P}}$ with two PBBs attached.

Several theses [118, 119, 24, 120, 121, 112] have been concerned with developments of the THMP $\overline{\text{P}}$ and presented the layout at different stages. In the following the final layout of the mainboards and the PBBs will be presented.

14.2.1 Mainboard

Compared to the layout presented in [112] some changes have been made, which do not involve the key components, but are relevant for the THMP $\overline{\text{P}}$ usage. The THMP $\overline{\text{P}}$ uses CAN-bus for communication and for mechanical safety lockable USB-B connectors are used as according connectors. The openings in the casing of the THMP $\overline{\text{P}}$ are adjusted accordingly.

The Philips PCA82C251T is used as the CAN transmitter and receiver. The control logic of the THMP $\overline{\text{P}}$ is provided by an Atmel AT90CAN128 micro processor. It can be programmed either via a joint test action group (JTAG) debug port or an in-system programming (ISP) interface.

For digitization of analog signals a MAX1148 8-channel, 14-bit ADC with serial output and an internal reference voltage of $V_{\text{ref}} = 4.096 \text{ V}$ is used. For each PBB one channel is provided. The analog signals of the individual channels of each PBB first pass their respective active low-pass filters before the micro processor routes them via a 1×8 multiplexer through an additional low-pass passive filter to the ADC. Since the board temperature influences the electronics behavior, the mainboard is equipped with a temperature sensor for monitoring. Figure 14.2 depicts the scheme.

Since every readout channel of the THMP $\overline{\text{P}}$ is calibrated individually, it is important to identify each board unambiguously. Thus each mainboard and piggy-back board is equipped with a 64-bit ROM chip called DS2401, which provides a six byte digital serial number.

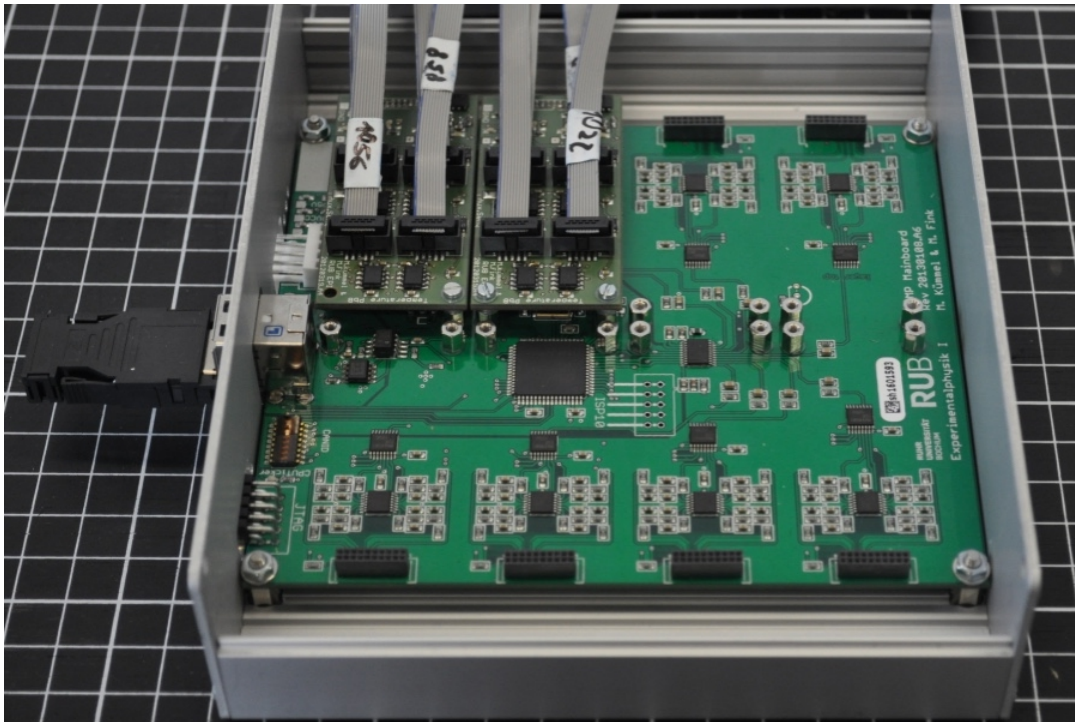


Figure 14.1: Opened THMP case equipped with a mainboard and two PBBs dedicated for temperature sensor readout

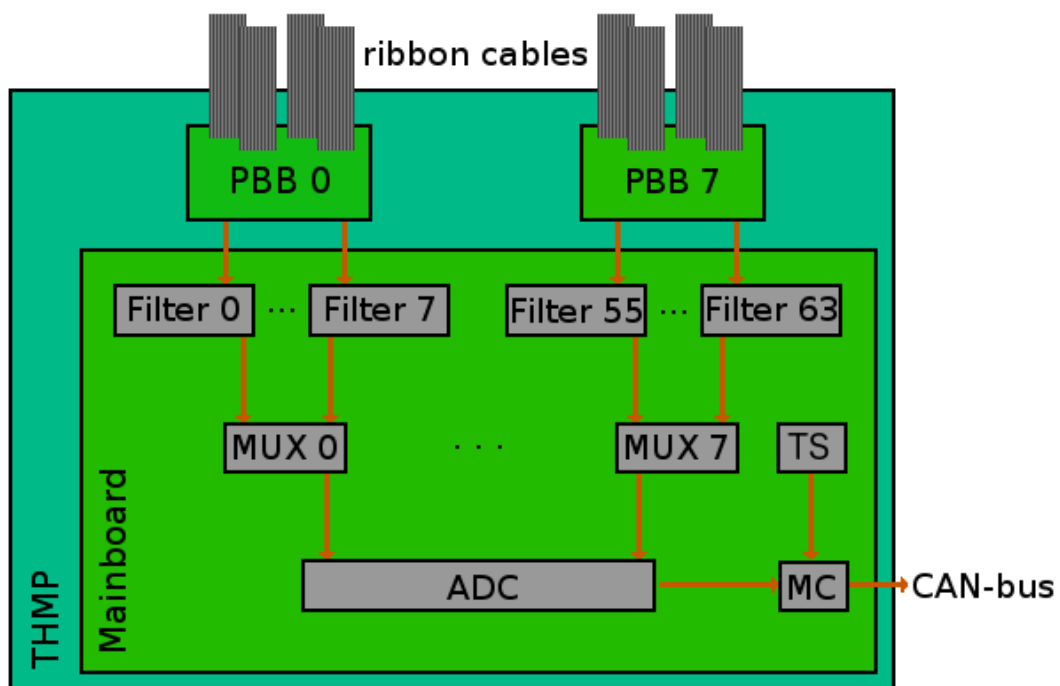


Figure 14.2: Schematic overview of the THMP mainboard components

14.2.2 Piggyback Boards

The PBBs are connected to the mainboard via 2×10 pin header contacts, which feed through the input voltages of ± 12 V to the PBBs and transfer the analog signals from the PBBs to the mainboard. On the PBB the voltages are regulated down to the actually required voltages and filtered. It has proven to be useful to use LEDs during assembly and testing, which indicate the status of each power rail. Before performing the calibration the series resistors of the LEDs are removed because their power dissipation is a significant heat source, which should be avoided.

The sensors are connected to the PBBs via 2×5 connector headers SHF-105-01-L-D-SM from Samtec with a pitch of 0.05 in. The counterpart can be pinched to a 10-pole flat ribbon cable with 0.025 in pitch. One cable can connect two sensors via 4-wire sensing, two leads are unused. The header connector features a keying slot, but for safety the routing scheme is designed in a rotational invariant way with the outermost contacts unused.

Piggy-Back Boards Dedicated for Temperature Sensors

The layout of the PBBs dedicated for the readout of resistance temperature sensors is almost unchanged in comparison to the layout presented in [112]. The measurement is based on 4-wire sensing, that means two separate pairs of wires are connected to the respective resistor in parallel. One pair carries the known constant current and the other pair is used for sensing the voltage. This way the current through the voltage sensing wires is negligibly small and the voltage drop in the current carrying wires is neglectable, so that the line resistance of the wire does not influence the measurement.

The constant current is realized by two stabilized voltage sources for four channels each, which are supplied with 5 V and provide $U_I = 2.5$ V and two operational amplifiers combined with a precise and temperature stable resistor of $R_I = 2.49$ k Ω . The current yields thus $I = \frac{U_I}{R_I} = 1.004$ mA. In order to optimally exploit the ADC input range of 0 V to 4.096 V the sensed voltage drop $U = R \cdot I$ is amplified by the instrumentation amplifier INA122 and shifted by a reference voltage U_{off} provided by high precision voltage sources. The gain of the instrumentation amplifier is set by the choice of the resistor R_G according to $G = 5 + \frac{200 \text{ k}\Omega}{R_G}$. On the mainboard the amplified and shifted voltage drop is digitized into the 2^{14} channels of the ADC (figure 14.3), corresponding to a conversion factor $C = \frac{2^{14}}{4.096 \text{ V}} = 4000 \text{ V}^{-1}$, so that the ADC conversion is determined by

$$K(R) = (R \cdot I \cdot G + U_{\text{off}}) \cdot C = R \cdot I \cdot G \cdot C + \cdot C = n + m \cdot R. \quad (14.2)$$

The resistor R_G and the high precision voltage sources are the only changes besides the new connectors compared to the layout presented in [112] in order to even better exploit the ADC input range. Two similar options have been considered and tested, finally the resistance value $R_G = 1.96$ k Ω and the offset voltage $U_{\text{off}} = -9.1$ V have been chosen. According to the nominal values the resistance is converted to an integer with a slope of $m = 429.9$ ADC channels/ Ω and an offset of $n = -36400$ ADC channels so that the resistances in a range from $R_{\text{min}} = 84.67$ Ω to $R_{\text{max}} = 122.79$ Ω can be read out by the THMP. For a commercial Pt100 temperature sensor that corresponds to a temperature range from $T_{\text{min}} = -38.98$ $^{\circ}\text{C}$ to $T_{\text{max}} = 58.82$ $^{\circ}\text{C}$ according to equation (13.1). Since the manually produced ultrathin resistance temperature sensors usually have a lower resistance at 0 $^{\circ}\text{C}$, the range is shifted downwards for them. The desired resistance precision σ_R corresponds to 3.3 ADC channels for the nominal values of U_I , R_I , R_G and U_{off} .

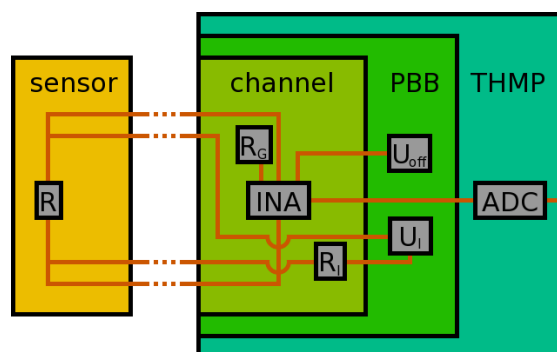


Figure 14.3: Schematic overview of the PBBs dedicated for the readout of temperature sensors

14.3 Required Amount and Supply Status

The required number of THMPs obviously scales with the number of sensors foreseen to be mounted. Besides the ultrathin temperature sensors, also commercial temperature sensors are going to be used and also humidity and pressure sensors are needed for monitoring all the environmental conditions in the subdetectors of the PANDA TS EMC. Table 14.1 summarizes the number of required mainboards (MBs) and PBBs dedicated for temperature sensor readout (T -PBB) and dedicated for humidity and pressure sensor readout (p -PBB). The first TS EMC barrel slice is listed separately, because the electronics for it are needed earlier than for the other slices. In case any kind of problem occurs it is desirable to have a fully equipped, tested and calibrated THMP for quick exchange at hand. The cause of the problem can then be investigated thoroughly without time pressure.

The first 15 THMP mainboards of the final design are already equipped and tested, these are intended for the usage in the forward endcap and the first slice. To maximize the measurement throughput the 84 equipped and tested PBBs are distributed so that 10 THMP mainboards are fully equipped and one THMP with 4 PBBs can be used for the calibration of ultrathin temperature sensors. Furthermore, 25 PBBs dedicated for the readout of humidity and pressure sensors are already equipped and tested. The remaining PCBs and the electronic components are already ordered and mostly delivered and will be assembled as soon as all needed components are received.

Purpose	MBs	T -PBBs	p -PBBs
Forward Endcap	10	74	6
First Slice	2	12	4
Remaining Slices	26	180	28
Backward Endcap	3	20	4
Spare	5	35	5
Total	46	321	47

Table 14.1: Required PCBs for the different parts of the PANDA TS EMC

14.4 Calibration of PBBs Dedicated for Temperature Sensors

The PBBs dedicated for the readout of temperature sensors must fulfill particularly strong requirements. The required resolution for the temperature measurement of $\sigma_T = 0.02^\circ\text{C}$ translates via the relation $R(T) = R(0^\circ\text{C})(1 + \alpha T)$ with the platinum temperature coefficient $\alpha_{\text{Pt}} = 3.85 \cdot 10^{-3}^\circ\text{C}$ to a relative resistance resolution of $\frac{\sigma_R}{R} = \alpha_T \sigma_T = 7.16 \cdot 10^{-5}$. At -25°C , where the temperature sensors have a resistance of typically $93\ \Omega$, the required absolute resistance resolution is $\sigma_R = R(0^\circ\text{C})\alpha_T \sigma_T = 6.7\ \text{m}\Omega$. In comparison, the production accuracy of high precision resistors is at least 0.1%. Thus a calibration of the temperature sensor PBBs on the THMP is crucial to obtain the required resolution.

The basic concept of the calibration is to measure the resistances of resistors with well-known values in the appropriate range. For this purpose calibration boards have been designed, which will be introduced in the following subsection.

At an early stage of the THMP calibrations it became apparent, that the measured values depend on the environmental temperature of the electronics. Hence a climate chamber is used not only to provide a stable environmental temperature, but to provide different stable temperatures, so that the temperature dependence of the electronics can be studied. The accordingly implemented calibration procedure is presented in subsection 14.4.2. After it turned out, that the operation in the climate chamber causes signal disturbances, an offline data treatment has been developed to get remove the corrupt parts of the data, which will be presented in subsection 14.4.3.

Subsections 14.6 and 14.7 show the results of the several THMP calibrations conducted in the scope of this thesis and assess the calibration quality in terms of uncertainties and reproducibility.

14.4.1 Calibration Boards

The first two calibration boards of the final layout were developed and produced in 2013 [121]. Each board provides resistors for all eight readout channels of one PBB. By bridging suitable pins of the corresponding pin headers, five different resistors can be connected to each channel enabling a 4-wire measurement. The first two calibration boards provide the nominal resistances $80\ \Omega$, $90\ \Omega$, $100\ \Omega$, $110\ \Omega$, $120\ \Omega$ and $86\ \Omega$, $93\ \Omega$, $96\ \Omega$, $105\ \Omega$, $115\ \Omega$, respectively. Thus by swapping the calibration boards in total ten resistances are available. In 2014 six more calibration boards of the same layout were produced [112], to obtain a more efficient calibration procedure by calibrating all PBBs of a THMP in parallel. For supply reasons instead of $96\ \Omega$ a nominal resistance value of $95\ \Omega$ was used for these boards. Two-rowed pin headers with the appropriate neighboring pins soldered together are used for efficient bridging of resistors for two PBB readout channels at once. Due to an adjustment of the resistance range the lowest two resistances are not used for the calibration.

In order to obtain the required resolution each resistor on each calibration board has been measured with an Agilent 34980A Multifunction Switch/Measure Unit for three hours. A Gaussian is fitted to each obtained distribution and the mean values and standard deviations are saved and used as references for all calibrations.

Since the production of the calibration boards, the layout of the THMP connectors has been changed twice. At first adapters were used to connect the two different kinds of ribbon cables with the respective connector. After the final connectors and cables were decided, these were implemented on the calibration boards, too. Even though the connectors are

protected against polarity reversal still there are two options how the plugs are squeezed on the cable or in case of the calibration boards which side of the connector is joint with which soldering points. The pin assignment is chosen such, that both connected channels can be read out via 4-wire measurement independent of the plug/cable orientation. Swapped channel orders are accounted for in the offline analysis of the calibration measurement.

14.4.2 Calibration Procedure

For the calibration of the temperature sensor PBBs the ADC conversions of all channels are read out for different input resistances and different environmental temperatures. Changing the environmental temperature can be automatized by programming the climate chamber, whereas for a change of the resistance the bridging pin headers need to be moved manually. Thus for a set resistance value the climate chamber varies the temperature according to the program, before the procedure is repeated for the next resistance value. The chosen program varies the temperature between $+30^{\circ}\text{C}$ and $+9^{\circ}\text{C}$ at eight different temperatures, each is kept constant for three hours, so that the program takes 24 hours of runtime in total. The program starts at $+24^{\circ}\text{C}$ and ends at $+18^{\circ}\text{C}$ so that the temperature difference is not too large, when opening the door of the climate chamber after performing a calibration measurement.

Since there are two different kinds of calibration boards, not all but only half of the PBBs can be connected to the same resistance at once. Swapping the calibration boards is rather time-consuming, so the order of measurements is chosen such, that the calibration boards need to be swapped only once. In total eight measurements have to be performed.

Before starting a calibration measurement the THMP \bar{P} should be powered up for at least one hour so that the board is in a thermal equilibrium. The cables should then already be attached to the THMP \bar{P} . It turned out to be useful to have a case lid with cables fixed by the strain relief permanently in the climate chamber so that all 32 plugs are at their intended positions. All cables are fed out of the climate chamber through an insulated feedthrough. A checklist is used to keep track of the conducted measurements. Time and date of turning on the power supply is noted, and the equipped PBB positions and the serial IDs of the PBBs and the mainboard are saved. For each measurement the ADC conversions returned by the THMP \bar{P} should be checked before the measurement is started. The start time, the name of the operator and the date when the conversions have been checked (cf. subsection 14.4.3) are noted, which should be done at best before the next measurement is conducted.

The channels connected to different cables are set to different resistance values each: When for example channels 0 and 1 are set to $90\ \Omega$, channels 2 and 3 are set to $100\ \Omega$, channels 4 and 5 to $110\ \Omega$ and channels 6 and 7 are set to $120\ \Omega$, respectively. This way swapped cabling is obvious, when comparing the ADC values returned by the THMP \bar{P} with the values to be expected, and can be corrected before the measurement is started. For the next measurement the set resistances are permuted, so that again after four measurements each channel has been set to each resistance, before the calibration boards are swapped.

14.4.3 Data Treatment

For every conducted measurement some checks and filters are applied to determine if a measurement is usable or needs to be repeated, otherwise all relevant information is extracted.

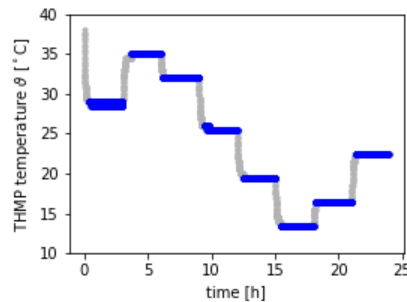


Figure 14.4: Temperatures measured with the sensor on the THMP \overline{P} mainboard over time, with stable data points marked in blue

Summing successive conversion values results in reduced fluctuations. Using two 8 bit words of the microcontroller results in values, that are a factor of four larger than the 14 bit ADC conversions. The THMP \overline{P} output is corrected for this factor before any further processing.

As a first and very rough test it is checked if any conversion value equals the maximum ADC conversion or is so low that a short-circuit must be assumed. All conversion values are compared with roughly estimated expectation values. Discrepancies above a threshold of 150 ADC conversions result in an alarm message, discrepancies of more then 1000 ADC channels most probably originate from wrongly set resistances and result in an error message, the status for the corresponding channel is set to invalid for the respective measurement.

In order to make reliable statements on the temperature dependence of the THMP \overline{P} only those values are to be considered, for which the board temperature has been stable. Since the climate chamber and the readout of the THMP \overline{P} are controlled independently, the information on when the temperature has been stable is retrieved from the data recorded by the temperature sensor on the THMP \overline{P} mainboard. For each data point the variance of the following 55 data points is determined. The difference between the variance values belonging to successive data points is compared to a limit value to determine if the temperature can be considered stable or cannot be considered stable any more starting from that data point on. Only if at least 100 successive data points can be considered stable, the start and stop data point are saved, where the stop point is chosen to be the last of the 55 following data points which were considered for the determination of the variance instead of the one for which the difference of variance values is over the limit itself. In case a start point is before the stop point of the precessing start point, the intermediate start and stop points are removed. Now the sequences of stable temperature data points must be matched with the set temperatures. An instability might occur during the time a temperature is set, resulting in too separate sequences of stable temperature data points. Such cases are identified by comparing the end points of the sequences, if less than 500 data points are in between, the shorter sequence is then removed. The blue parts in figure 14.4 shows the result of this procedure for the recorded THMP \overline{P} temperature.

For further analysis the data is compressed by using mean and standard deviation of the approximately 500 data points for each temperature set value and connected resistor.

It turned out, that even though THMP \overline{P} measurements have low statistical fluctuations and are stable over time (cf. section 13.8.2) there occur different kinds of disturbances during

the calibration measurements in the climate chamber, which may result in systematically displaced mean values. Many of the observed disturbances occur similarly in several readout channels at the same time. Sometimes there is a single data point or some few data points significantly larger or lower than the other data points taken under the same conditions. Especially for single data points that might be caused by a bit flip at some point of the digital data processing. Sometimes just the deviations are increased significantly for some time and later on the data shows the same deviations as usual. It was also observed that increased deviations occur systematically in only one direction. Rarely, the mean of the data points is suddenly shifted by some ADC channels and sometimes even shifted forth and back within the period of one set temperature.

Obviously it would be favorable to avoid the cause of these disturbances once it has been identified, but as long as this is not the case the information contained in the data should be retrieved and used. With eight 24 h measurements of 64 readout channels per THMP calibration it is too tedious, to look through all the data by hand and check whether it is reasonable or not.

In order to identify periods for which the data is not usable, an obvious ansatz is to evaluate the momentary extent of deviations. The point of reference for the deviations should not be floating, but fixed because actually the data should be constant with only statistical deviations. The mean value is no good choice for the reference point, because due to e.g. only few points far off, the mean could be shifted and the deviation would be large even for reasonable data just due to the shifted mean. Instead the mode is used, which is simply the value occurring most frequently in the considered sample, thus the most probable value.

For each data point the momentary deviation is determined by considering the next 20 data points and calculating the difference to the mode, summing over the squared differences, taking the square root and dividing through the number of considered data points. These momentary deviation values are compared to the limit value of 1.0. If data points deviate significantly from the mode, this should affect the momentary deviation values for all cases where these data points were considered for the calculation. Thus only if at least 20 data points in a row exceed the limit they are discarded, starting from the 20th data point after the first one for which the limit has been exceeded. An exception must be made for the end of the considered data, where no longer 20 momentary deviation values follow after the point currently under consideration. If there are less than 100 data points between two sequences of discarded data points, these are discarded, too, because they might be unreliable.

Figure 14.6 shows for illustration two channels from the same measurement as displayed in figure 14.4. For each channel the upper two plots show the respective ADC conversions over time as well as one-dimensionally distributed, which are recorded for the considered temperature step at a set temperature of +9 °C in the climate chamber, the respective mode is indicated by a black line. The lower plots contain the respective absolute of the difference to the mode and the corresponding momentary deviation values in dark gray. The data points which are discarded due to the evaluation described above are depicted in brighter colors. For channel 0 of PBB0 most of the data points are discarded as there is an increased deviation systematically below the mode during the whole measurement. At the end of the considered period the deviation is a bit smaller, so that these data points are considered for further analysis. In addition there is a period where the data points deviate even more from the mode in both directions, which is also the case for the data points

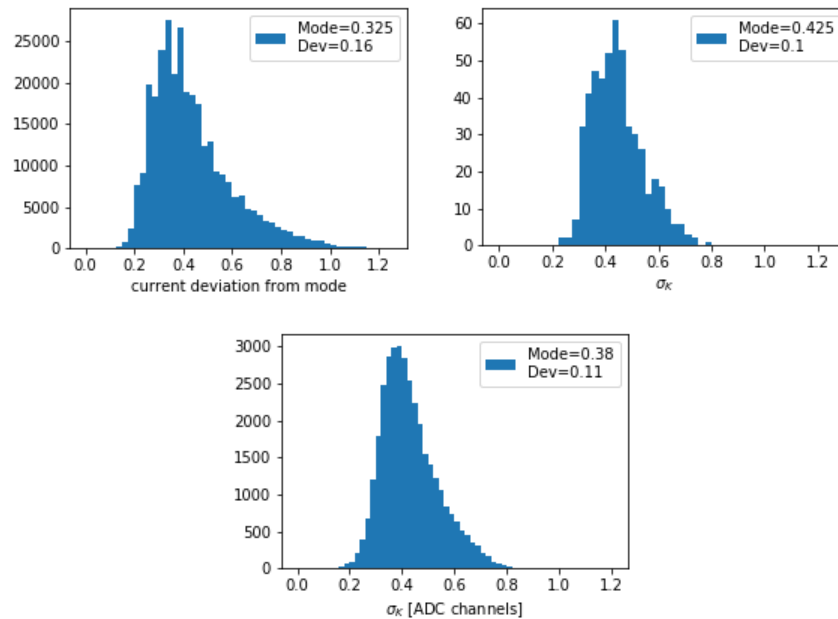


Figure 14.5: Momentary deviations from the mode of the ADC conversions of all considered data points (top left) and standard deviation from the mean of the ADC of the calibration measurement displayed in figure 14.4 (top right) as well as for all performed calibrations (bottom)

recorded at the same time for channel 1 of PBB2. Similarly also the other readout channels show an increased deviation during that period, but to convey an accurate picture, e.g. for PBB0 no data points had to be discarded for any other set temperature.

For the remaining data points mean and standard deviation are determined, and used for the calibration fits. If most of the data points are discarded and less than 100 remain for further analysis the data of that channel for that temperature step is not taken into account at all, because it is unlikely that the data is reliable. Figure 14.5 (top row) shows the momentary deviations from the respective mode and the standard deviation of the considered data points. The distribution of the momentary deviations from the mode with a most probable value of 0.34 and a standard deviation of 0.16 show, that the limit of 1.0 is a reasonable choice. On the one hand the distribution has already dropped to almost zero at 1.0 and on the other hand this limit is more than four standard deviations above the most probable value of the momentary mode distribution. Even though the distribution is asymmetric, this distance to the mode affirms, that momentary deviations of the mode of more than 1.0 are quite unlikely to occur statistically. The standard deviations for the full sample corresponding to a certain set temperature is narrower with a deviation of only 0.07, the mode delivers comparable results.

Figure 14.5 (bottom) shows the distribution of ADC conversion standard deviations determined for all 8 set temperatures, all 8 different connected resistances and all 64 readout channels of all 10 calibrations. The most probable value for all calibration measurements is determined to be 0.38, which is slightly larger than for the measurement discussed above. Even the largest statistical uncertainty of the averaged samples (0.8 ADC conversions) is quite small.

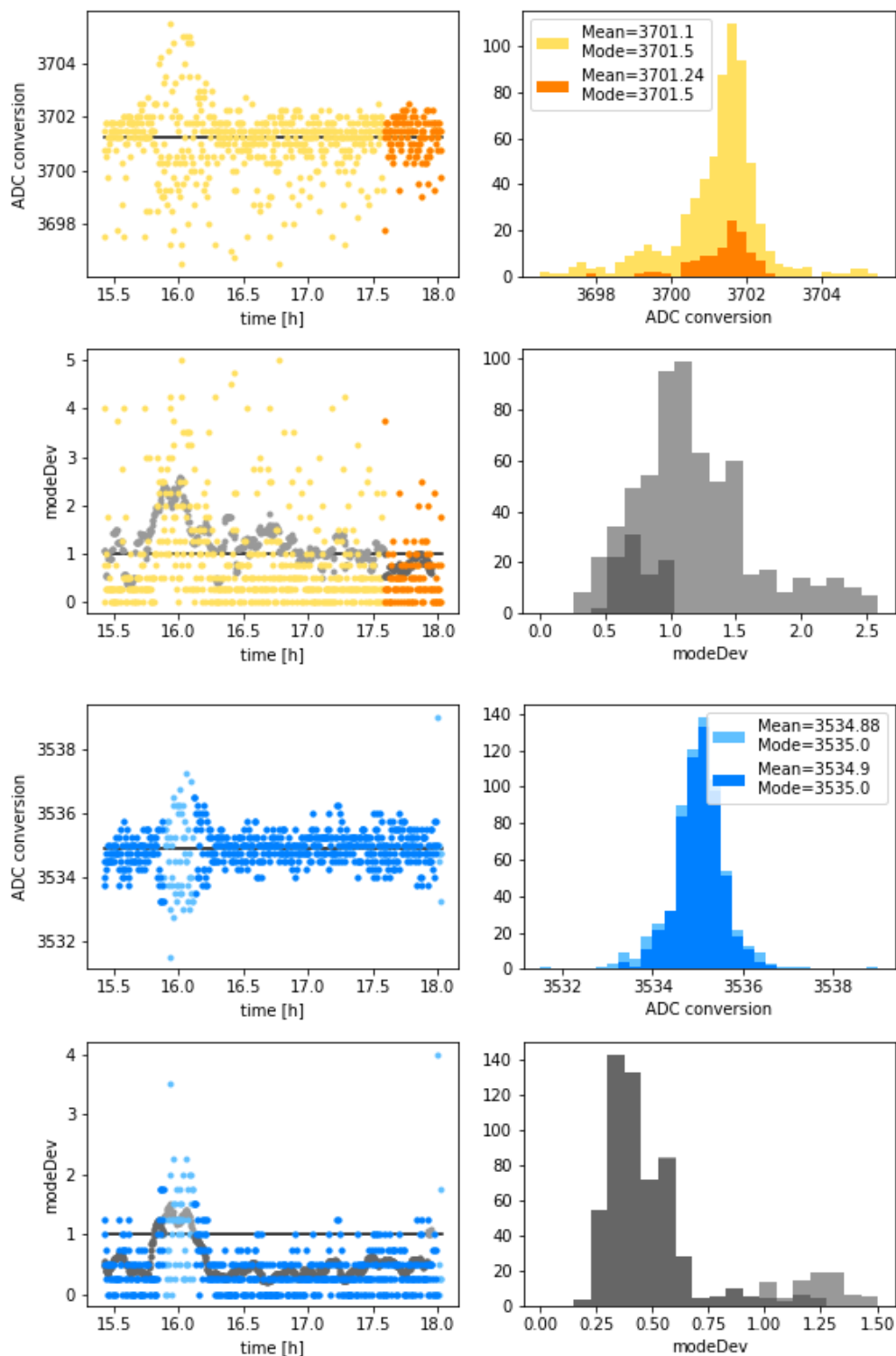


Figure 14.6: ADC conversion over time and in a histogram (1st and 3rd row) for one set temperature and the difference to the mode and its local deviation in gray (2nd and 4th row) for two different channels (blue, yellow)

14.4.4 Fitting Procedure

With the retrieved data the calibration fits can be performed. According to the relations given in equation (14.2) the ADC conversion K of a readout channel depends linearly on the connected resistance value

$$K(R, \vartheta) = n(\vartheta) + m(\vartheta) \cdot R,$$

where the parameters can differ for different environmental temperatures ϑ . Combining the data of the different calibration measurements at the same set temperatures, the dependence on the resistance can be fitted. Since the temperature dependency is also linear as visible in figure 14.4, the dependence of the obtained parameters on the different set temperatures can be fitted by

$$n(\vartheta) = n_0 + n_1 \cdot \vartheta \quad \text{and} \quad m(\vartheta) = m_0 + m_1 \cdot \vartheta.$$

Figure 14.7 shows exemplary fit results for the resistance dependence of one channel at a certain set temperature as well as the fit results for the temperature dependence of the fit parameters $m(\vartheta)$ and $n(\vartheta)$ for this channel.

Additionally, for each calibration measurement the temperature dependence of the ADC conversions

$$K(R, \vartheta) = b(R) + a(R) \cdot \vartheta$$

is fitted, where the obtained parameters then both depend linearly on the resistance connected during the respective calibration measurement as

$$b(R) = b_0 + b_1 \cdot R \quad \text{and} \quad a(R) = a_0 + a_1 \cdot R.$$

Figure 14.8 shows exemplary fit results for the temperature dependence of the same channel as in 14.7 for a certain connected resistance and the fits for the resistance dependence of the fit parameters a and b for this channel.

The distributions of the obtained fit parameters for all performed calibrations are shown in the appendix. A somewhat distorted distribution is to be expected, when blending the results for different set temperatures even though it is known that the parameters differ for different set temperatures. But it turns out that the distortion of the distribution of the parameter $m(\vartheta)$ (figure B.1) is instead caused by blending the results of different THMP calibrations. Figure B.3 shows the distribution of the parameter $m(\vartheta)$ separately for different THMP calibrations. As the differences depend on the respective THMP they might be caused by differences in the conversion factor of the respective ADC chip. The temperature dependence of the parameters $m(\vartheta)$ and $n(\vartheta)$ is so small compared to the spread of the values that it does not distort the distributions significantly. On the contrary, the resistance dependence especially for the parameter $b(R)$, which describes the offset of the temperature dependency, is so significant that it does not make sense to show the blended distribution, instead the distribution is shown separately for the different connected resistances in figure B.4. The two bumps in the distributions of $b(R)$ for the nominal resistance values 96Ω and 115Ω occur because the calibration boards 3, 5 and 7 were produced with slightly different nominal resistor values than calibration board 1. The distribution of the obtained parameters $a(R)$ is shown in figure B.2, its resistance dependence is so small compared to the spread that it has no significant effect on the distribution.

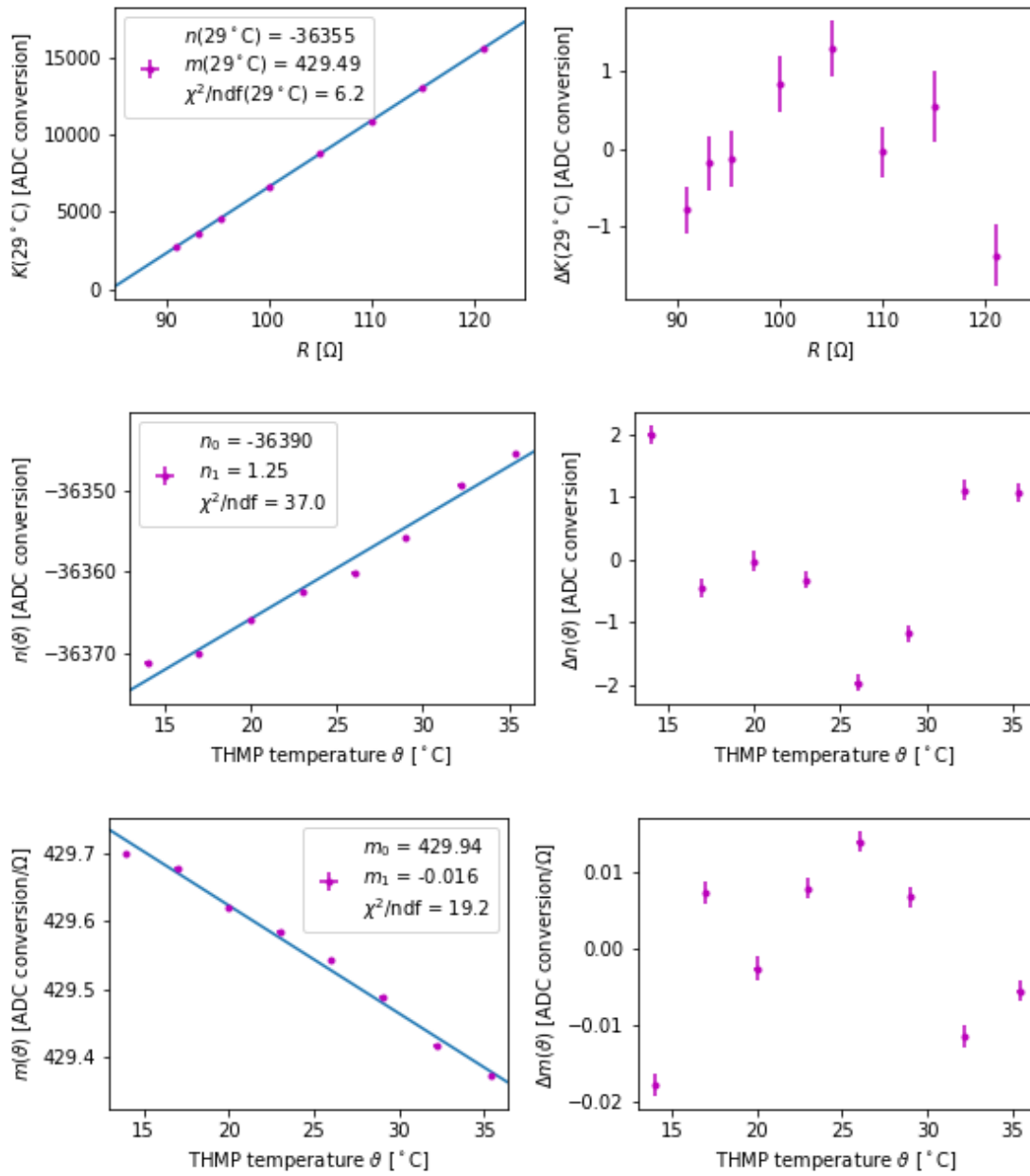


Figure 14.7: Fitted resistance dependence for the ADC conversions of one channel at a measured THMP temperature of 29°C (top) and fitted temperature dependence for the obtained offset (mid) and slope (bottom) for the different set temperatures

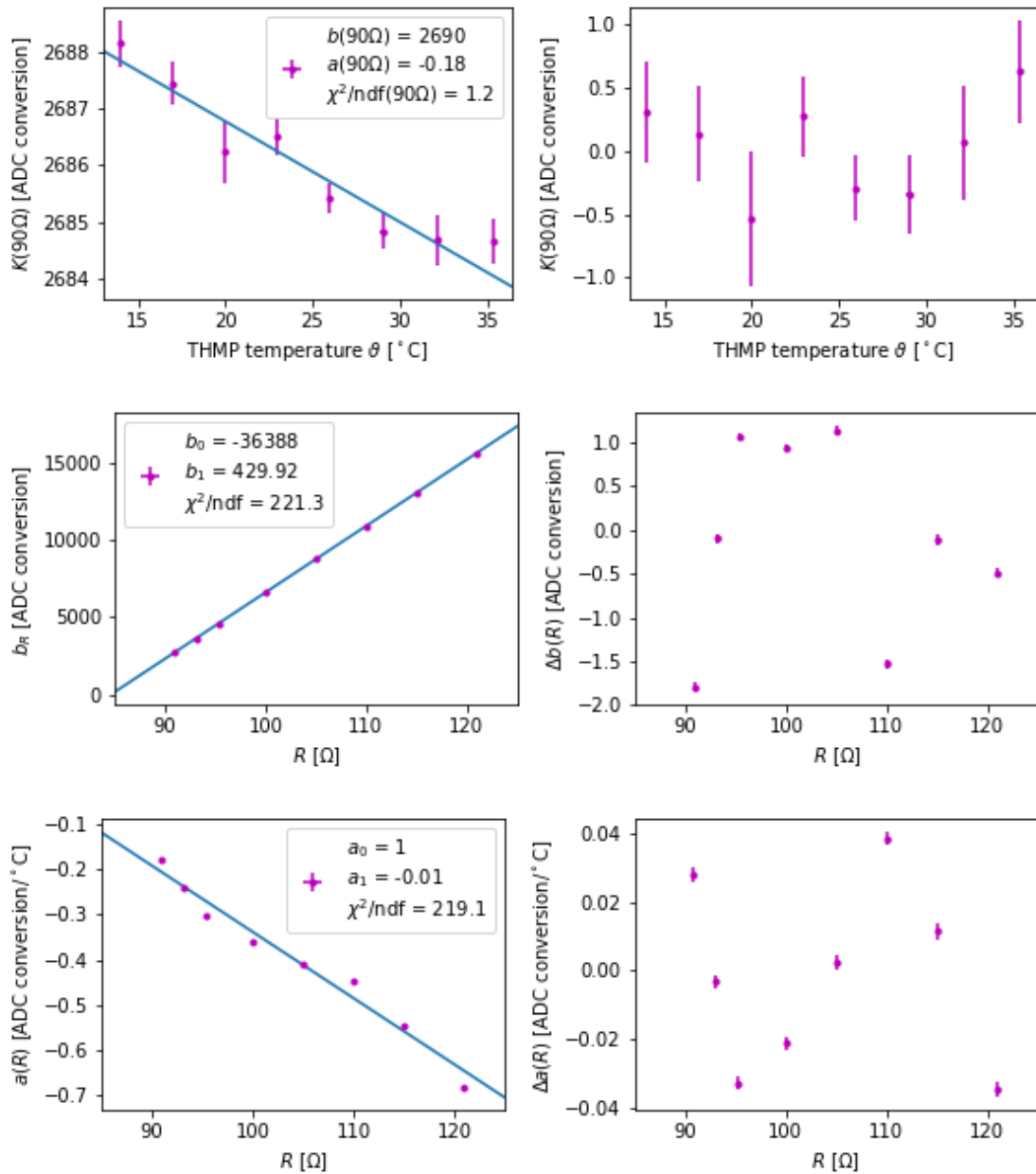


Figure 14.8: Fitted temperature dependence for the ADC conversions of one channel for a connected resistance of 90Ω (top) and fitted resistance dependence for the obtained offset (mid) and slope (bottom) for the different connected resistances

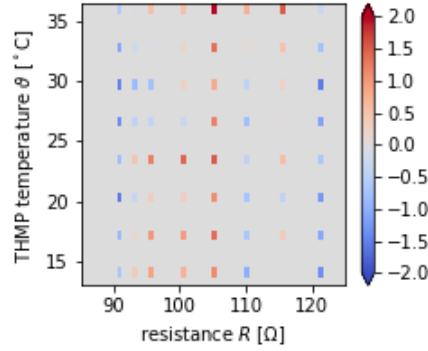


Figure 14.9: Difference of the 64 measured data points to the two-dimensional fit obtained from the same measurement as the results shown in figures 14.7 and 14.8

For all the fits described above the least squares method is used, where

$$\chi^2(m,n) = \sum_{i=1}^N \frac{(K_i - (n + mR_i))^2}{\sigma_{K_i}^2} \quad \text{and} \quad \chi^2(a,b) = \sum_{i=1}^N \frac{(K_i - (b + a\vartheta_i))^2}{\sigma_{K_i}^2}.$$

In order to account for the uncertainty of R_i and ϑ_i as well, not just the statistical measurement uncertainty is used but $\sigma_{K_i} = \sqrt{(\Delta K_i)^2 + (m\Delta R_i)^2}$ and $\sigma_{K_i} = \sqrt{(\Delta K_i)^2 + (a\Delta \vartheta_i)^2}$, respectively. The linear dependence is used to propagate the uncertainties ΔR_i and $\Delta \vartheta_i$ to an uncertainty of the same dimension as ΔK_i .

Considering both, the resistance and the temperature dependency simultaneously in a two-dimensional fit, the ADC conversion is thus determined by four independent parameters p_{00} , p_{01} , p_{10} and p_{11} as

$$\begin{aligned} K(R,\vartheta) &= n(\vartheta) + m(\vartheta) \cdot R = (n_0 + n_1 \cdot \vartheta) + (m_0 + m_1 \cdot \vartheta) \cdot R \\ &= b(R) + a(R) \cdot \vartheta = (b_0 + b_1 \cdot R) + (a_0 + a_1 \cdot R) \cdot \vartheta \\ &= p_{00} + p_{01} \cdot \vartheta + p_{10} \cdot R + p_{11} \cdot \vartheta \cdot R. \end{aligned}$$

This way the correlation between the two dependencies can be determined more precisely. The average of the results of fitting the temperature dependence and resistance dependence of the parameters, respectively,

$$p_{00}^{\text{start}} = \frac{n_0 + b_0}{2}, \quad p_{01}^{\text{start}} = \frac{n_1 + a_0}{2}, \quad p_{10}^{\text{start}} = \frac{m_0 + b_1}{2}, \quad p_{11}^{\text{start}} = \frac{m_1 + a_1}{2},$$

can be used as reasonable start parameters for a two-dimensional fit. For the two-dimensional fit thus

$$\chi^2(p_{00},p_{01},p_{10},p_{11}) = \sum_{i=1}^N \frac{(K_i - (p_{00} + p_{01} \cdot \vartheta_i + p_{10} \cdot R_i + p_{11} \cdot \vartheta_i \cdot R_i))^2}{\sigma_{K_i}^2}$$

is used for minimization with $\sigma_{K_i} = \sqrt{(\Delta K_i)^2 + (p_{10}\Delta R_i)^2 + (p_{01}\Delta \vartheta_i)^2}$. The correlation between R_i and ϑ_i scaled by p_{11} is assumed to be neglectable. Figure 14.9 shows exemplary the difference between the data points and the result of such a fit.

If the variances used for constructing the χ^2 are underestimated, then this will lead to χ^2 values larger than n_{df} and underestimated statistical uncertainties for the fitted parameters. The uncertainty of R_i is estimated by the uncertainty of the multimeter measurement $\Delta R_i \approx 0.17 \text{ m}\Omega$. The uncertainty of ϑ_i is estimated by the second central moment of a uniform distribution

$$\Delta\vartheta_i = \sqrt{\frac{(x_{\text{up}} - x_{\text{low}})^2}{12}} = \sqrt{\frac{(0.5^\circ\text{C})^2}{12}} \approx 0.14^\circ\text{C},$$

which corresponds to the resolution of 0.5°C of the temperature sensor on the THMP mainboard, because most often the measured values do not vary as long as the temperature in the climate chamber is stable. With these estimations rather high χ^2 values are obtained as shown in figure B.5. Thus a more sophisticated estimation of the uncertainties as presented in the following section is needed in order to correctly determine the uncertainties of the obtained fit parameters.

14.5 Estimation of Uncertainties

To simplify the estimation, the results from the one-dimensional fits are considered. The uncertainty of the resistance measurements is estimated by comparing the resistance values obtained by the multimeter measurement with the value retrieved from inverting the fit function to the resistance dependence

$$R(K, \vartheta) = \frac{K - n(\vartheta)}{m(\vartheta)} \quad (14.3)$$

for all set temperatures, all connected resistances and all calibrations.

Due to the design of the calibration boards every resistor is connected twice during a full calibration (cf. subsection 14.4.2) and different ADC conversions are obtained for each of the eight set temperature values for both assignments. Figure 14.10 (left) shows exemplary the comparison between the resistance values, which were determined with a multimeter and the values retrieved from the inversed fit function evaluated for the recorded ADC conversions.

The difference and the standard deviation are saved, so that they can be used to correct the values determined by the 4-wire measurement with the multimeter. For some resistors the retrieved values are systematically below or above the ones determined by the multimeter, so such systematic uncertainties are reduced as well. The most probable value of the standard deviations is $2.6 \text{ m}\Omega$ as shown in figure 14.10 (right). For further fits the uncertainty of each resistor is estimated individually.

For the temperature measurement not only the precision of the temperature sensor is relevant, but also how informative this value is regarding the temperature of the individual electronics chips on the PBB used for the readout of the resistances. Similarly as for the estimation of the resistance uncertainty, the temperature uncertainty is estimated by comparing the temperature values obtained by the THMP temperature sensor with the values retrieved from inverting the fit function to the temperature dependence

$$\vartheta(K, R) = \frac{K - b(R)}{a(R)} \quad (14.4)$$

for all set temperatures, all connected resistances and all calibrations.

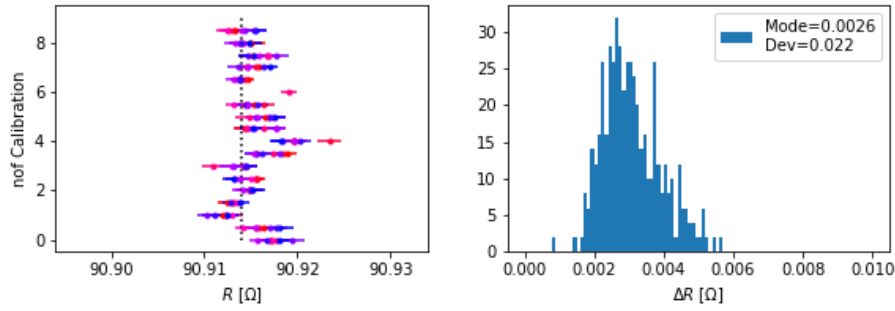


Figure 14.10: Resistance value from a 4-wire measurement performed with a multimeter (dashed black line) and the resistance values retrieved from all calibrated THMPs according to equation (14.3) at different set temperatures (indicated by color) for the same resistor plotted for the individual calibration measurements (left) and the distribution of the uncertainties obtained for all resistors (right)

In contrast to the resistance dependence, the temperature dependence is distributed around zero and in some cases even changes the sign for the same channel for different connected resistances. As the propagated uncertainty for the retrieved temperature is given by

$$\Delta\vartheta(K,R) = \sqrt{\left(-\frac{K-b(R)}{a(R)^2}\Delta a(R)\right)^2 + \left(\frac{-b(R)}{a(R)}\Delta b(R)\right)^2 + \left(\frac{1}{a(R)}\Delta K\right)^2}, \quad (14.5)$$

the uncertainty is quite large for low values of the parameter a . Figure 14.11 illustrates this effect with data points retrieved from a measurement with a set temperature of 24 $^{\circ}\text{C}$ in the climate chamber and 27 $^{\circ}\text{C}$ measured by the THMP temperature sensor as reference value depicted by a dashed black line. Figure 14.12 (left) shows the correlation between the parameter a and the retrieved temperature uncertainty for all set temperatures, all connected resistances and all calibrations for decreasing ranges.

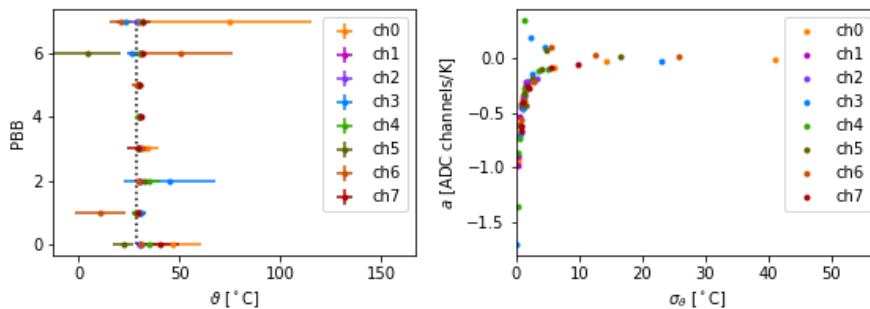


Figure 14.11: THMP temperature (dashed black line) and retrieved temperature values and uncertainties according to equations (14.4) and (14.5) (left) and the correlation between the temperature uncertainty and the fit parameter a for the same data sample (right)

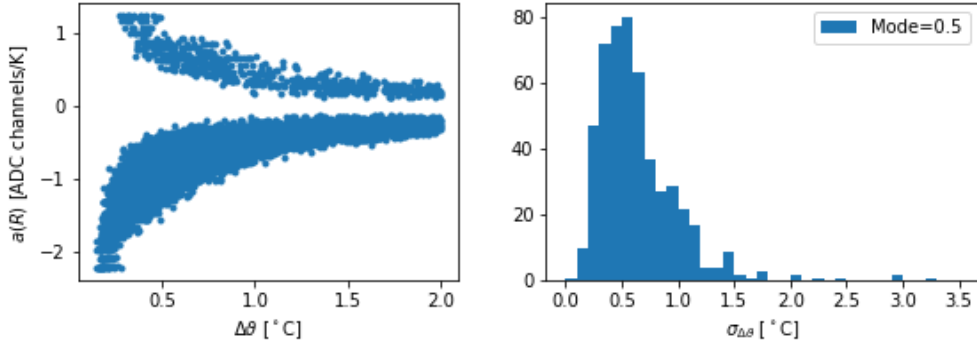


Figure 14.12: Correlation between temperature uncertainty $\Delta\vartheta$ and parameter a (left) and averaged deviation of the difference between the retrieved temperature and the THMP temperature $\sigma_{\Delta\vartheta}$ (cf. equation 14.6) for all set temperatures and connected resistances (right), the red dot shows the respective mode

It is not reasonable, to just determine the deviation of all the values obtained that way, in order to estimate the uncertainty of the temperature. Temperatures retrieved from the inversed fit function with an uncertainty of more than 2°C are thus not considered.

To take the very different uncertainties into account each value is weighted according to its uncertainty and the weighted average is determined. This procedure is also used by the Particle Data Group to reasonably average values obtained by different experiments with different statistical and systematic errors [1]. Specifically the weighted average of the distance between the retrieved temperature and the temperature measured by the THMP temperature sensor is determined and used to estimate the average deviation by

$$\sigma_{\Delta\vartheta} = \sqrt{\sum_i \frac{((\vartheta(K_i) - \vartheta_i) - \overline{\Delta\vartheta})^2}{(\Delta\vartheta(K_i))^2}}, \quad \text{where} \quad \overline{\Delta\vartheta} = \sum_i \frac{\vartheta(K_i) - \vartheta_i}{(\Delta\vartheta(K_i))^2}. \quad (14.6)$$

Figure 14.12 (right) shows the distribution of the averaged deviations, which has a mode of 0.5°C . This value is used to estimate the uncertainty of the temperature ϑ measured by the THMP temperature sensor.

The χ^2 distributions obtained by using these newly estimated uncertainties are shown for an exemplary THMP calibration in figure B.6. Especially for the one-dimensional fits describing the resistance dependency of the ADC conversions and the successive fits describing the temperature dependence of the thereby obtained parameters m , n the newly estimated uncertainties yield the desired effect, the modes are basically one. The fits describing the temperature dependence of the ADC conversions yielded already too small χ^2 values and with the newly estimated uncertainties these are even further decreased. For the fits describing the resistance dependence of the thereby obtained offset b the effect is most impressive: The most probable value is decreased from 160 to only 1.2. For the corresponding slope a not much is achieved. Comparing the most probable values of the χ^2 distributions for a in figure B.5 and figure B.6, it seems as if the most probable value has increased, but this is just caused by a binning effect. For the χ^2 distribution corresponding to the two-dimensional fits the most probable value is decreased slightly from 2.4 to 1.9.

14.6 Quality Assessment

The parameter values and uncertainties obtained by the two-dimensional fit respecting resistance and temperature dependence simultaneously is shown in figure B.7. Very loose criteria are used to remove those cases for which the fit does not yield reasonable results. First of all at least one of the two successively one-dimensionally fitted parameter sets n_0 , n_1 , m_0 , and m_1 or b_0 , b_1 , a_0 and a_1 should be valid, i.e. with χ^2 values below the limits indicated by the plotted ranges in figure B.6. The χ^2 value of the two-dimensional fit should be below the limit of 5. Of course a result is also discarded if the fit did not converge. Besides that a fit is discarded if $p_{00} > 0$, $\sigma_{00} > 30$ or $\sigma_{01} > 10^5$.

Compared to the distributions of the one-dimensionally fitted parameters shown in figures B.1, B.2, B.3, B.4 the distributions of the two-dimensionally fitted parameters show long flat tails. That might be an indication, that there are still technical issues with the fitting, maybe some of the parameters which control the fit behavior of iminuit [122] should be adjusted. Therefore in the following also the parameters obtained from the one-dimensional fit considered, besides the parameters obtained from the two-dimensional fit.

More interesting than the obtained parameter values themselves are the minimal and maximal resistances R_{\min} , R_{\max} , that define the input range, and the propagated uncertainty of the resistance value ΔR determined by the measured ADC conversion and THMP temperature. All these quantities are determined by the fit parameters by evaluating the inverse function

$$R(K, \vartheta) = \frac{K - (p_{00} + p_{01}\vartheta)}{p_{10} + p_{11}\vartheta} \approx \frac{K - n(\vartheta)}{m(\vartheta)}.$$

To determine the propagated uncertainty the partial derivatives

$$\begin{aligned} \frac{\partial R}{\partial p_{00}} &= \frac{-1}{p_{10} + p_{11}\vartheta}, & \frac{\partial R}{\partial p_{10}} &= \frac{-(K - (p_{00} + p_{01}\vartheta))}{(p_{10} + p_{11}\vartheta)^2}, \\ \frac{\partial R}{\partial p_{01}} &= \frac{-\vartheta}{p_{10} + p_{11}\vartheta}, & \frac{\partial R}{\partial p_{11}} &= \frac{-\vartheta(K - (p_{00} + p_{01}\vartheta))}{(p_{10} + p_{11}\vartheta)^2}, \\ \frac{\partial R}{\partial K} &= \frac{1}{p_{10} + p_{11}\vartheta}, & \frac{\partial R}{\partial \vartheta} &= \frac{-p_{01}}{p_{10} + p_{11}\vartheta} - \frac{p_{11}(K - (p_{00} + p_{01}\vartheta))}{(p_{10} + p_{11}\vartheta)^2} \\ & & &= -\frac{p_{01} + p_{11}R}{p_{10} + p_{11}\vartheta} \end{aligned}$$

have to be calculated so that the total uncertainty can be estimated by

$$\Delta R \approx \sqrt{\left(\frac{\partial R}{\partial p_{00}} \Delta p_{00}\right)^2 + \left(\frac{\partial R}{\partial p_{01}} \Delta p_{01}\right)^2 + \left(\frac{\partial R}{\partial p_{10}} \Delta p_{10}\right)^2 + \dots} \quad (14.7)$$

$$\dots + \left(\frac{\partial R}{\partial p_{11}} \Delta p_{11}\right)^2 + \left(\frac{\partial R}{\partial K} \Delta K\right)^2 + \left(\frac{\partial R}{\partial \vartheta} \Delta \vartheta\right)^2.$$

Similarly the total uncertainty can be estimated by the parameters obtained from the one-dimensional fit to the resistance dependence at different set temperatures

$$\begin{aligned}\Delta R_T &\approx \sqrt{\left(\frac{\partial R}{\partial n(\vartheta)}\Delta n(\vartheta)\right)^2 + \left(\frac{\partial R}{\partial m(\vartheta)}\Delta m(\vartheta)\right)^2 + \left(\frac{\partial R}{\partial K}\Delta K\right)^2} \\ &= \sqrt{\left(\frac{\Delta n(\vartheta)}{m(\vartheta)}\right)^2 + \left(\frac{\Delta m(\vartheta)}{m(\vartheta)^2}\right)^2 + \left(\frac{\Delta K}{m(\vartheta)}\right)^2},\end{aligned}\quad (14.8)$$

but then obviously the uncertainty caused by the temperature dependence is neglected. Figure 14.13 (top row) shows the distribution of the total resistance uncertainty obtained by all the numerous performed fits to the resistance dependence at different set temperatures with the roughly estimated temperature and resistance measurement uncertainties and the distribution obtained with the more sophisticated estimation presented in the previous section. As to be expected the propagated uncertainty for the resistance increases with the increased uncertainty estimation for the connected resistances and the THMP temperature. Actually the increase of the most probable value by a factor of two is small compared to the difference between the differently estimated uncertainties. Figure 14.13 (bottom) shows the distribution obtained for the two-dimensional fit with the sophisticated uncertainty estimation. This way the most probable value is increased by yet another factor of two.

Table 14.2 lists the most probable parameter values and uncertainties obtained by the two-dimensional fit as depicted in figure B.7. The listed temperature and ADC conversions are chosen more or less arbitrarily, they should reflect a reasonable scenario for the usage of the THMP in the \bar{P} ANDA detector. The uncertainty for the ADC conversion is estimated by the most probable value of the distribution shown in figure 14.5 (bottom). The individual uncertainties are propagated to a resistance uncertainty and their fraction of the squared uncertainty is shown to demonstrate their impact on the total propagated uncertainty. The total resistance uncertainty determined this way is slightly decreased compared to the most probable value of the distribution shown in figure 14.13 (bottom). Either way the propagated uncertainty of the resistance determined by THMP temperature and ADC conversion is well below the maximal uncertainty value of 7.7 m Ω for which the envisaged temperature precision can still be achieved.

Quantity	Value x	Uncertainty Δx	$\left \frac{dR}{dx}\Delta x\right $ [m Ω]	$\left(\frac{dR}{dx}\Delta x\right)^2 / (\Delta R)^2$ [%]
p_{00}	-36386	0.6	1.4	20
p_{01} [($^{\circ}\text{C}$) $^{-1}$]	1.8	0.025	1.4	20
p_{10} [(Ω) $^{-1}$]	429.5	0.0054	1.2	14
p_{11} [($^{\circ}\text{C}\Omega$) $^{-1}$]	-0.034	0.00022	1.2	13
K	3800	0.38	0.9	8
ϑ [$^{\circ}\text{C}$]	24	0.5	1.6	26
R [Ω]	93.64	0.0032	3.2	100

Table 14.2: Propagated uncertainties from the different input parameters and their fraction of the squared total uncertainty of the resistance

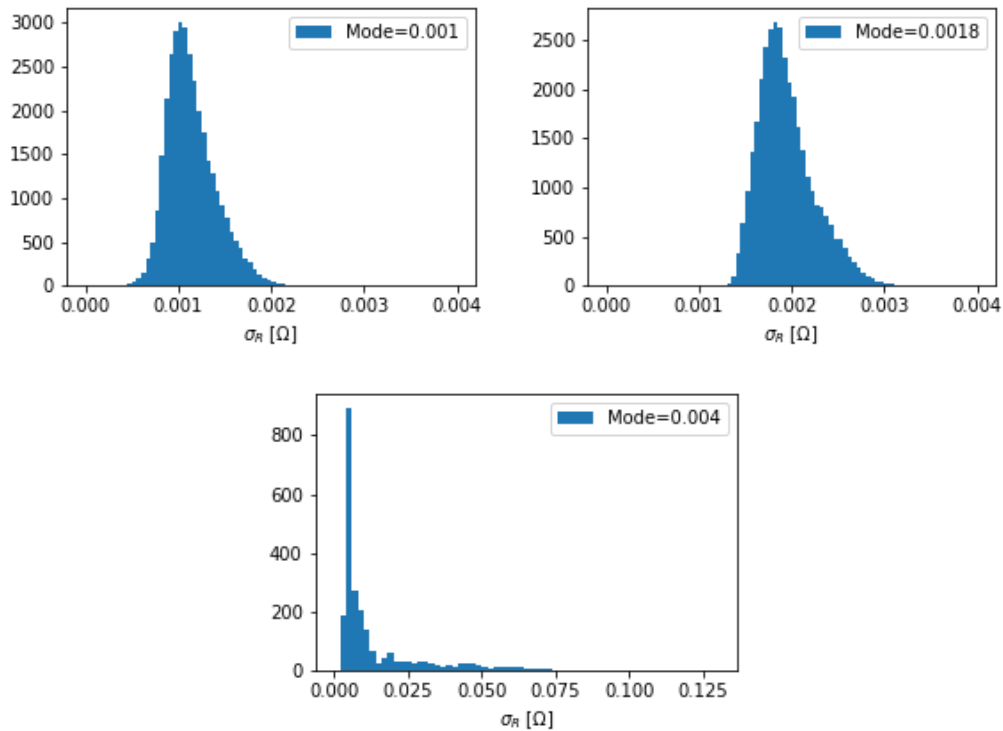


Figure 14.13: Propagated uncertainty of the retrieved resistance according to equation (14.8) (top) and equation (14.7) (bottom) from fits using the naive (top left) and the sophisticated resistance and temperature uncertainty estimation (top right, bottom)

The uncertainty introduced by the temperature measurement is the largest, but it is still on the same scale as the uncertainty introduced by individual fit parameters. As discussed earlier the uncertainty might rather originate from the fact, that the temperature is not measured at the actual point of interest, than from the uncertainty of the measured value itself. Therefore it should not be expected, that the uncertainty of the retrieved resistance can be improved significantly by using a more precise temperature sensor. As the uncertainties are summed quadratically the effect would be at most a reduction by 14% if there was no uncertainty on the temperature at all.

The minimal resistance and the maximal resistance which can be read out by the individual channels of all PBBs and all THMPs are shown correlated with each other in figure 14.14 determined by the one-dimensionally fitted parameters m and n as well as for the two-dimensionally fitted parameters. It is not visible for the first case, but in both plots the individual data points do have error bars. For the two-dimensionally fitted parameters the minimal and maximal resistances seem to be less correlated, but on the other hand the further the values are apart from the correlation region obtained by the one-dimensionally parameters, the larger is the uncertainty. This impression of less correlated values might thus just originate from the data points in the tails of the parameter distributions shown in figure B.7.

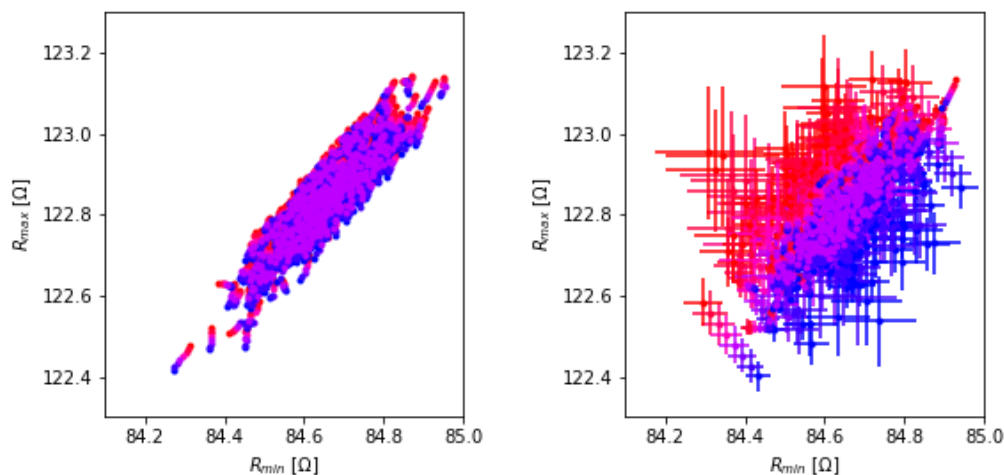


Figure 14.14: Minimal versus maximal resistances that can be read out by the individual channels of all PBBs and THMPs according to their temperature dependence fit parameters m and n (left) and according to their two-dimensionally fitted parameters p_{00} , p_{01} , p_{10} , and p_{11} (right) with the values obtained for increasing temperatures depicted from blue to red

14.7 Reproducibility

Even though the uncertainty of the retrieved resistance is already determined, the question remains if consistent fit parameters are obtained when a THMP is calibrated twice. Uncertainties of the method should already be taken into account by the discussed uncertainty estimation, but differences of the parameters obtained from different calibrations might occur due to for example aging effects or seasonal effects or maybe even a slow drift in the climate chamber calibration.

Figure B.8 shows the difference between the resistances retrieved from two calibrations of the same THMP, one performed according to an old scheme and the other one performed according to the scheme presented in section 14.4 for both kinds of uncertainty estimation. There are approximately six months between these two calibration measurements.

Actually, the difference between the obtained parameters is larger when using the larger uncertainties. The range is chosen to $\pm 7.8 \text{ m}\Omega$, which is the limit resistance uncertainty for which the envisaged temperature uncertainty can still be achieved as determined in equation (14.1). Values out of this range are shown in a constant deeper red or blue depending on the direction of the deviation but no longer on the size.

Figure 14.15 shows exemplary the distribution of the absolute difference between the resistances retrieved from the two different calibrations for all readout channels of all PBBs of an arbitrary THMP, except for two PBBs for which cabling issues occurred in the previous calibration. The THMP temperature and the ADC conversion range are binned into 50 bins each. For the parameter sets obtained from fits with the naive uncertainty estimation the largest difference of the determined resistance values amounts to $20 \text{ m}\Omega$, whereas for parameter sets obtained from fits with the larger estimated uncertainties differences up to $60 \text{ m}\Omega$ occur. Correspondingly, for the former case more differences lie in the acceptable region below $7.8 \text{ m}\Omega$, approximately 93.5% compared to 91.1%.

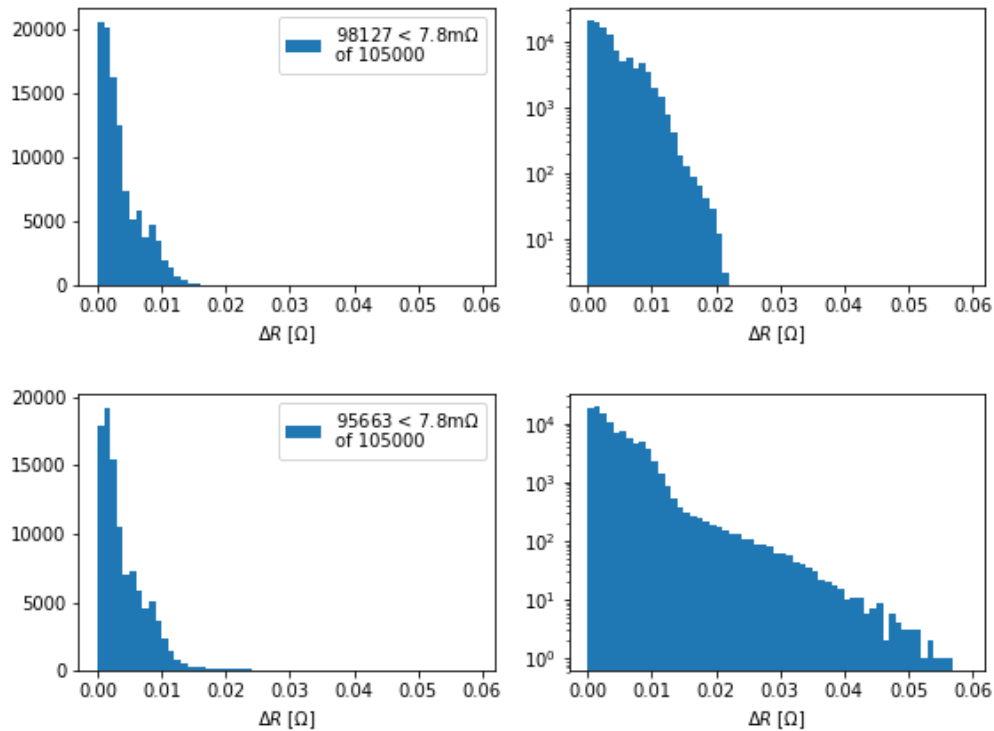


Figure 14.15: Distributions of resistance differences obtained from a 50 times 50 grid of points within the $\overline{\text{THMP}}$ temperature range from 10°C to 35°C and the ADC conversion range from 0 to 16383 for parameters for all valid PBBs obtained from two different calibrations of the same $\overline{\text{THMP}}$ with the naive (top) and the sophisticated uncertainty estimation (bottom)

14.8 Temperature Measurements at the Submodule Test Station

There are several intermediate tests during the assembly of a submodule for the $\overline{\text{PANDA}}$ TS EMC forward endcap. After the assembly is finished besides the photo sensors also the temperature sensors are tested. For that purpose a $\overline{\text{THMP}}$ is used to read out the temperature sensors. These test measurements are performed at room temperature, just to check as early as possible if something is broken and the submodule has to be disassembled, repaired and reassembled.

A more sophisticated test setup for cosmics measurements at -25°C in a climate chamber is located in Bonn. Figure 14.16 shows the inner assembly of the test station with its electronics. For the first submodule to be measured in the test station several tests were made resulting in a measurement with a total length of 1440 hours, that is 60 days.

Two temperature sensors were incorporated into the submodule, the sensor with ID #161 was attached to the bottom face of the crystal at position 2 towards the photosensors (cf. section 12.3, figure 12.7) and preamplifiers and the sensor with ID #163 was attached to the right face of the crystal at position 8 towards the front face, which will show towards the interaction point.

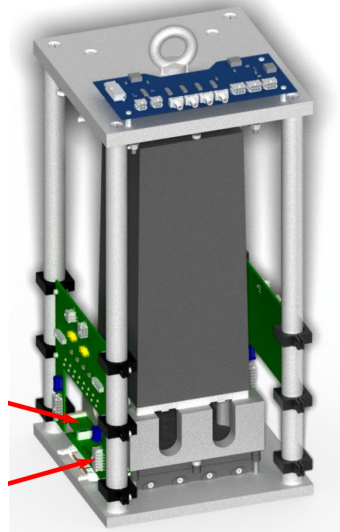


Figure 14.16: Inner assembly of the test station for cosmic measurements at -25°C performed at Bonn university, the red arrows point to a heat source of the electronics

Each of the sensors has been calibrated twice and a third order polynomial is fitted to the full sample, the subsample with decreasing set temperatures (cooling), and the subsample with increasing set temperatures (heating) as described in subsection 13.6.3. Hence the question arises, which of the in total six different calibration parameter sets should be taken into account. Figure 14.17 shows a comparison between these fit functions. As the differences between the fits to different samples for the same fit is rather small, the fit to the full sample is a reasonable choice. Especially for the sensor with ID #163 the fit results obtained for the two calibration measurements differ significantly. Assuming, that some kind of aging effect occurred, which hopefully reached its endpoint before the second calibration, the fit function obtained from the later calibration is used.

Similarly also for the THMP channels two calibration measurements exist and two sets of fit functions depending on how the uncertainties are estimated. Needless to say the calibration performed according to the new scheme with the uncertainties estimated with the more sophisticated method is considered the most reasonable.

As shown in figure 14.16 the submodule is placed pointing upwards with the photosensors and preamplifiers at the lower side, where some boards are located to provide power supply and pass the signals from the photosensors and the temperature sensors on for readout. Besides the photosensors and the preamplifiers, these electronics boards provide additional heat sources, the most significant one marked with red arrows in figure 14.16. The submodule is placed in the test station so that the crystals at positions 3, 7, B, and F are closest to these heat sources.

Figure 14.18 provides an overview over the recorded data after applying the THMP as well as the temperature sensor calibrations, whereas figure 14.19 provides zoomed views for the different interesting periods of the measurement. As the position of the sensor in the submodule is more important for the interpretation of the data than their ID, the measured temperatures are referred to as ‘rear temperature’ and ‘front temperature’ in the following.

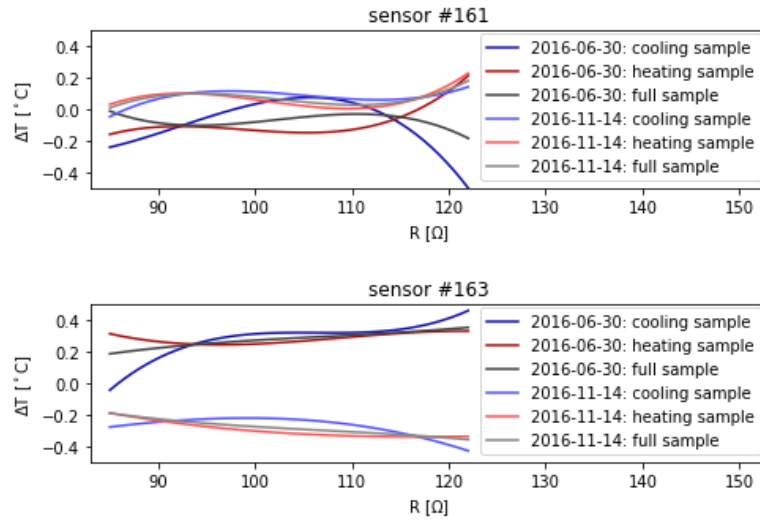


Figure 14.17: The fit functions obtained from fits to different data samples of different calibration measurements are represented by their difference to the mean of the fits to the combined data sample

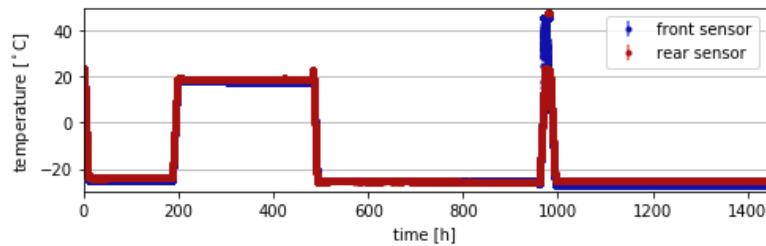


Figure 14.18: Temperatures measured by the two temperature sensors, which are incorporated in the first submodule with which cosmic measurements were made in the dedicated test stations at Bonn University

At the beginning of the measurement the climate chamber is still at room temperature because the test station with the submodule has just been mounted. The climate chamber starts cooling down to -25°C . The front temperature is quite exactly -25°C , whereas the rear temperature is -24°C . As the rear sensor is close to the preamplifiers and the electronics board, it is to be expected, that the rear temperatures are higher.

After 200 hours the climate chamber is warmed up again and several actions are taken, which are not connected with the temperature monitoring. Both temperatures reach a peak value and then decrease slowly until thermal equilibrium is reached. For the front temperature that takes significantly longer than for the rear temperature. Again the temperatures have a difference of 1°C as before.

After 482 hours the submodule is turned by 90° around the longitudinal axis, so that then the crystals on positions 0, 1, 2, and 3 are closest to the heat sources and the climate chamber is cooled down again to -25°C . Both temperatures are below -25.25°C and the front temperature is actually higher than the rear temperature. A slight decrease of

approximately 0.1°C over 400 hours is visible for the rear temperature, whereas the front temperature seems to increase slightly but then returns to the original value.

Approximately 472 hours later, in total after 954 hours, the power supplies were switched off for six hours so that no heat is dissipated in the climate chamber any more. As to be expected, both temperatures drop even lower to approximately -26°C , which is 1°C lower than the set temperature of the climate chamber. The front temperature is again lower than the rear temperature, however the distance between them is by a factor of about ten smaller than at beginning of the measurement. The difference to the set temperature might not only be caused by a change of the ultrathin temperature sensors over time, but also by a change of the temperature sensor of the climate chamber, which is used for the regulation.

Anyway these observations do not match with the above mentioned rotation. One would expect, that the rear temperature significantly higher than before, as the rear sensor sits on the side face of crystal 2 and would directly face the heat source. Nonetheless, the observations can be explained, by assuming that the submodule in the beginning has been oriented with the crystals on positions 0, 1, 2, and 3 closest to the heat source and is oriented with the crystals on positions C, 8, 4 and 0 closest to the heat source after the rotation. Under this assumption the rear temperature should be significantly lower than before. The front sensor would be on the side facing the heat source, but as it is placed at the front of the submodule it would be in some distance to the heat source and thus not be affected too much. Then it would even make sense that the front temperature is stronger affected by turning off the heat sources.

After 960 hours the climate chamber is heated up again to room temperature, at 981 hours the submodule is removed from the test stations and mounted into another test station. The submodule has again the usual orientation with the crystals on positions 3, 7, B, and F closest to the heat sources. The climate chamber cools again down to -25°C and stays at that temperature for the remaining 459 hours of the measurement, that is 19 days. The rear temperature is about -25°C and the front temperature is almost -27°C , thus the distance between them has increased to 2°C . Compared to the beginning of the measurement the rear temperature is decreased by 1°C and the front temperature even by almost 2°C . It is unlikely that reconnecting the temperature sensors or the THMP could have caused that, especially since the 4-wire-measurement is used. As observed in the longterm measurements presented in 13.8.2, temperature sensors might change their behavior over time, especially for the sensor with ID #163 with two significantly different calibration results that would not be surprising. On the other hand the temperatures seem quite stable, but slight drifts in the order of 0.1°C over 200 hours are visible in the third and fifth plot of figure 14.19, that might sum up to 0.5°C over thousand hours if the temperatures keep drifting constantly, but 2°C seems unlikely.

After 1230 hours since the start of the measurement the power supplies are once more switched off, but this time both temperatures decrease only by 0.2°C instead of 0.5°C or 0.75°C as before. Considering the submodule is oriented with the crystals on positions 3, 7, B, and F closest to the heat source, the front sensor would be on the opposite side of the submodule and the rear sensor on an orthogonal side. If at the beginning of the measurement the submodule has been oriented with the rear sensor towards the heat source and the front sensor on an orthogonal side, the change of orientation might explain why both temperatures are significantly lower and less affected by the voltage supply being switched off.

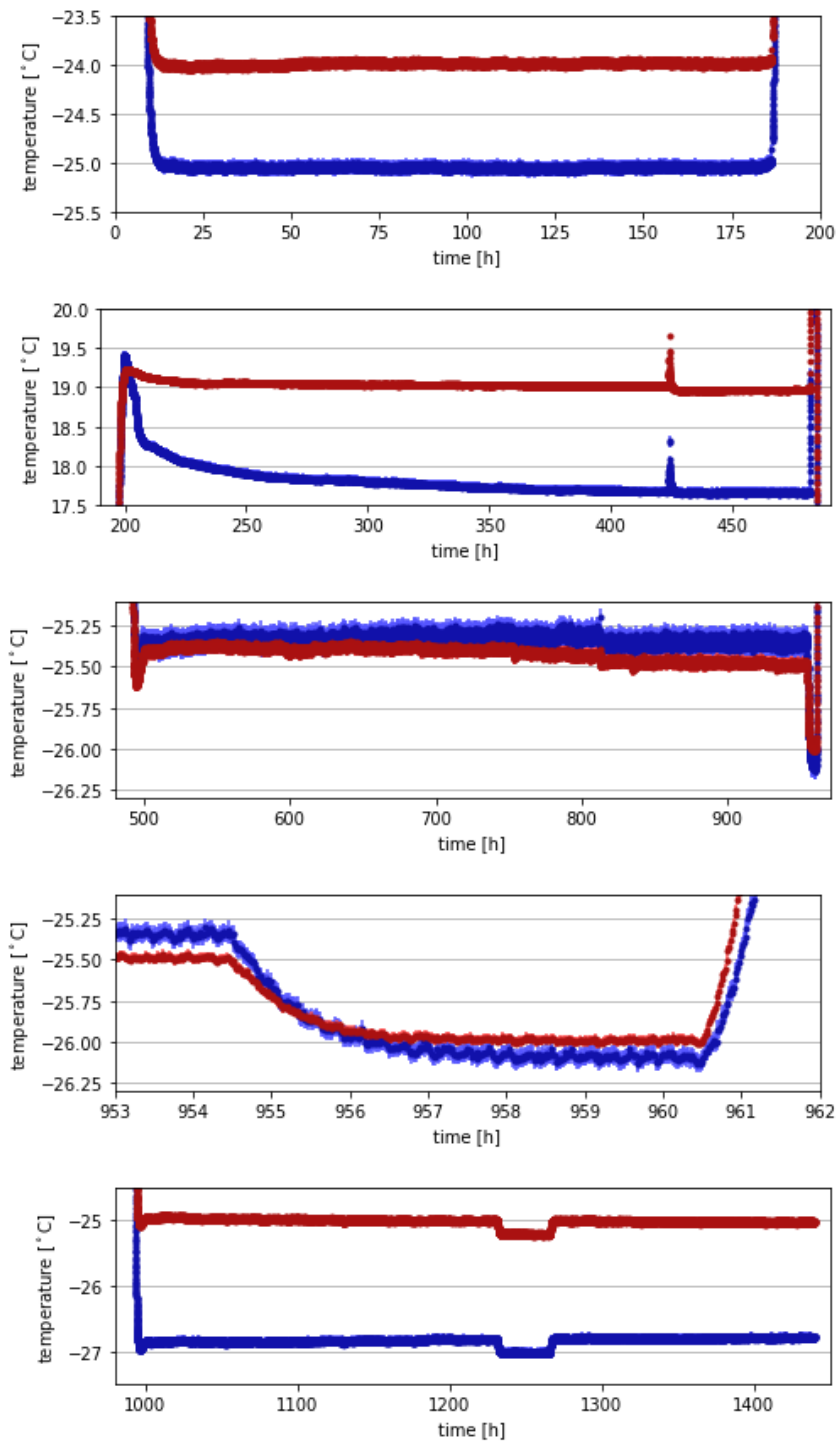


Figure 14.19: Zoomed views of the rear and front temperature, which are incorporated in the first submodule with which cosmics measurements were made in the dedicated test stations at Bonn University

15 Conclusion and Discussion

In order to precisely monitor the operating temperature of the EMC, dedicated ultrathin temperature sensors and corresponding readout electronics THMP have been developed at the Institut für Experimentalphysik I, Ruhr-Universität Bochum. In the forward endcap one ultrathin temperature sensor is foreseen per eight crystals, which amounts to 482 sensors in total, for the barrel it is one sensor per ten crystals, which amounts to 1152 sensors in total. The 131 ultrathin temperature sensors for the backward endcap will be produced at the University of Mainz.

An amount of 826 temperature sensors has been produced manually for the forward endcap of the EMC, of which 83 were provided for the first barrel slice. Additional 75 temperature sensors were retrieved from the prototype of the forward endcap Proto192. Measures are taken to decrease the manpower needed for the temperature sensors remaining to be produced for the barrel part, by outsourcing the cable production and utilizing a 3D printer for placing the platinum wire.

All 686 working temperature sensors have been calibrated at least once, most of them twice or more often. The data obtained by a calibration measurement is split into two samples, one with increasing set temperatures, the other one with decreasing set temperatures to take the hysteresis effect into account. A polynomial of third order is fitted to the full sample and also to the two subsamples. The fit convergence has been improved by employing a multi-staged fit approach, where Chebyshev polynomials are used in the first stages.

A calibration measurement for which the standard deviation of the data points from the fitted polynomial is below 0.02°C for both subsamples is considered suitable. The distribution of standard deviations for all calibration measurements has a most probable value of 0.01°C for the fits to the individual subsamples. For the fits to the full sample the most probable value is 0.03°C because the hysteresis effect results in greater deviations. The extent of the hysteresis is given by the difference between the functions fitted to the two subsamples. At -25°C the most probable value of the corresponding distribution amounts also to 0.03°C . For sensors, which have been calibrated with positive result more than once, the reproducibility is evaluated by determining the standard deviation of the fit functions at -25°C .

The hysteresis effect has been investigated by varying the temperature difference between successive set temperatures and by varying the minimal and maximal set temperatures. The smallest difference of 1°C between successive set temperatures increased the hysteresis effect. Apart from that, the hysteresis effect did not change significantly for the tested variations. Additionally the hysteresis effect has also been studied for temperature fluctuations around -25°C with varying extent. In contrast to the expectation, the measured value at the set temperature of -25°C was almost the same regardless of the former set value, so the hysteresis effect seems to be small for fluctuations around a constant temperature. However, the values changed over time and differed significantly from -25°C . Unfortunately the measurement setup has been exposed to strong environmental temperature changes during these measurements. It is known, that the electronics are influenced

by the environmental temperature, but this effect is taken into account in the calibration. The correlation between the resistance read out with the electronics and the temperature of the electronics revealed, that there are resistance changes, which are not correlated with the environmental temperature. This way no reliable conclusion can be drawn, which of the two fits to the different subsamples delivers the more realistic temperature value, instead the fit to the full sample should be used.

In a longterm measurement which started at $+20\text{ }^{\circ}\text{C}$ and kept the set temperature $-25\text{ }^{\circ}\text{C}$ for almost two weeks, all ultrathin temperature sensors showed a limited growth after they reached a minimal temperature. The temperature progress over the first 50 h has been fitted, in average the limit value was $-26\text{ }^{\circ}\text{C}$ and the time constant was 0.1 h^{-1} . In the further course of the measurement the temperatures measured by the ultrathin temperature sensors increased very slowly to different extent. The two commercial Pt100 sensors used as reference sensors did not show this behavior, hence it seems to be a characteristic of the ultrathin temperature sensors.

Nonetheless, there are temperature sensors which provide reproducible results. Out of the 686 calibrated sensors 380 ultrathin temperature sensors have been calibrated more than once, and for 183 of these sensors more than one calibration measurement has been suitable. For 86 temperature sensors the standard deviation of all suitable fit functions is less than $0.02\text{ }^{\circ}\text{C}$ at $-25\text{ }^{\circ}\text{C}$. When comparing only the last two suitable measurements, the deviation is less than $0.02\text{ }^{\circ}\text{C}$ for 92 sensors. Relaxing the limit to $0.022\text{ }^{\circ}\text{C}$, 94 and 101 sensors fulfill the above mentioned criteria for reproducibility, respectively. Thus 14.7% of the calibrated sensor yield suitable and reproducible results. The ratio might increase slightly by calibrating sensors again for which only one suitable measurement has been obtained yet.

In order to significantly increase the ratio of suitable and reproducible sensors different methods to contact the platinum wire with the pads of the ultrathin cable are tested. Furthermore the measurement setup was redesigned, so that it will be possible to calibrate 30 sensors in parallel instead of twelve.

The THMP design is modular and consists of a mainboard with a microcontroller and a 14-bit ADC as key components as well as connectors for PBBs which are dedicated for the readout of different kinds of sensors. Besides temperature sensors also pressure and humidity sensors can be read out by the THMP, but the requirements for the precision of the temperature sensor readout are by far the strongest and thus the main focus of this thesis. The resistance of the temperature sensors is measured by a four-wire-measurement and the voltage drop is amplified and shifted by an offset voltage to optimally exploit the input range of the ADC. The ADC conversion depends thus linearly on the measured resistance. The nominal parameters of the used components result in a covered resistance range from $R_{\min} = 84.67\ \Omega$ to $R_{\max} = 122.79\ \Omega$. For commercial Pt100 temperature sensors this corresponds to a temperature range from $T_{\min} = -38.98\text{ }^{\circ}\text{C}$ to $T_{\max} = +58.82\text{ }^{\circ}\text{C}$, but for the ultrathin temperature sensors the resistance is typically higher, so that the range is shifted towards lower temperatures.

Including spare units, in total 46 THMP mainboards, 321 PBBs dedicated for the readout of temperatures sensors, and 47 PBBs dedicated for the readout of humidity and pressure sensors are needed. In the course of this thesis 15 THMP mainboards, 84 temperature sensor PBBs, and 25 pressure sensor PBBs have been equipped and tested. The THMP used for the calibration setup of the ultrathin temperature sensors is equipped with four PBBs

and the remaining 80 temperature sensor PBBs are distributed to ten THMP mainboards for efficient calibration.

For the calibration of the PBBs calibration boards with precisely measured resistors for each readout channel of the PBB are used. In total eight different resistance values are provided. During the measurement the THMP is exposed to eight different temperatures in a climate chamber, so that also the temperature dependence of the electronics can be taken into account. When the THMP is operated in the climate chamber, signal disturbances occur. The corresponding data points are removed by an algorithm before those data points belonging to one set temperature are averaged for fitting.

The read out ADC conversions depend also linearly on the THMP temperature, which is measured by a dedicated sensor on the mainboard. In total 64 data points can be grouped in samples with fixed resistance (or temperature), for which a simple linear fit can be performed. In a second step the temperature (or resistance) dependence of the obtained slope and offset parameters can be fitted. This way good start parameters for a two-dimensional fit are obtained, which simultaneously takes the resistance and the temperature dependence of the ADC conversion into account. The fit function can easily be inverted to obtain a resistance value from the measured ADC conversion and THMP temperature.

The uncertainty of the resistances and the temperatures are estimated by determining the corresponding pull distributions from the fits of all calibrated readout channels. With these properly estimated uncertainties all fits are performed again. The uncertainty of the obtained fit parameters can be propagated to an uncertainty of the resistance measurement, which yields $1.8 \text{ m}\Omega$ for the successive linear fits. For the two-dimensional fit a resistance uncertainty of $4 \text{ m}\Omega$ is obtained. The largest fraction of the resistance uncertainty is caused by the uncertainty of the THMP temperature, which is measured on the mainboard and naturally not directly at the place of the respective electric components on the PBBs. However, the resistance uncertainty is well below the required precision of $7.8 \text{ m}\Omega$.

Furthermore the reproducibility of the THMP calibration is investigated by comparing the fit results of two successive calibrations of the same THMP. The absolute difference between the fit functions is determined using 2500 data points in the accessible range of the ADC conversions and THMP temperatures. With the proper uncertainty estimation, 91% of the differences are below the required precision.

A Results of the Partial Wave Analysis

A.1 First Results of the Iterative Approach

Additional Contribution	n_{free}	-NLL	-BIC	-AIC	-(BIC+AIC)	$\Delta\text{BIC} + \Delta\text{AIC}$
	33	1471.49	2652.64	2876.98	5529.62	0
phase space	34	1525.52	2751.91	2983.05	5734.96	205.34
$f_2(1270)$	43	1570.63	2762.95	3055.27	5818.22	288.60
$f_2(1430)$	43	1593.01	2807.69	3100.01	5907.70	378.08
$f_2(1565)$	43	1570.14	2761.96	3054.28	5816.24	286.62
$f_2(1640)$	43	1539.96	2701.59	2993.91	5695.50	165.88
$f_2(1810)$	43	1666.15	2953.98	3246.30	6200.28	670.66
$f_2(1910)$	43	1650.29	2922.26	3214.58	6136.84	607.22
$f_2(1950)$	43	1664.59	2950.87	3243.19	6194.06	664.44
$f'_2(2010)$	43	1661.60	2944.88	3237.20	6182.08	652.46
$f_4(2050)$	43	1540.12	2701.92	2994.24	5696.16	166.54
$h_1(1595)$	39	1394.59	2446.06	2711.18	5157.24	-372.38
$h_1(1965)$	39	1627.54	2911.95	3177.08	6089.03	559.41
$h_1(2215)$	39	1603.98	2864.84	3129.96	5994.80	465.18
$h_3(2025)$	39	1524.96	2706.78	2971.91	5678.69	149.07
$h_3(2275)$	39	1531.46	2719.79	2984.92	5704.71	175.09
$\phi(1680)$	35	1517.71	2722.49	2965.43	5687.92	158.30
$\phi(2170)$	35	1512.14	2716.34	2954.27	5670.61	140.99
$\phi_3(1850)$	35	1450.18	2502.43	2830.37	5332.80	-196.82
$\omega(1650)$	35	1535.75	2763.57	3001.51	5765.08	235.46
$\omega(1960)$	35	1512.41	2716.89	2954.83	5671.72	142.10
$\omega(2205)$	35	1472.39	2636.85	2874.79	5511.64	-17.98
$\omega(2290)$	35	1536.10	2764.27	3002.20	5766.47	236.85
$\omega(2330)$	35	1480.64	2653.35	2891.28	5544.63	15.01
$\omega_2(1975)$	39	1588.24	2833.36	3098.48	5931.84	402.22
$\omega_2(2195)$	39	1530.52	2717.91	2983.04	5700.95	171.33
$\omega_3(1670)$	35	1506.68	2705.42	2943.35	5648.77	119.15
$\omega_3(1945)$	35	1510.86	2713.79	2951.73	5665.52	135.90
$\omega_3(2255)$	35	1450.82	2593.71	2831.65	5425.36	-104.26
$\omega_3(2285)$	35	1482.64	2657.34	2895.27	5552.61	22.99
$\omega_4(2250)$	39	1492.55	2641.97	2907.10	5549.07	19.45
$\omega_5(2250)$	35	1504.81	2701.69	2939.62	5641.31	111.69
$X(1575)$	35	1503.08	2698.22	2936.16	5634.38	104.76
$X(1750)$	35	1499.92	2691.91	2929.85	5621.76	92.14

Table A.1: First step of the iterative approach with Breit-Wigner description for all contributions in addition to the base hypothesis consisting of the $(\pi\pi)_S$ wave described by a K -matrix and the $f'_2(1525)$ described by a Breit-Wigner distribution with masses and widths fixed to the values given in table 7.1 and 7.2

Additional Contribution	n_{free}	-NLL	-BIC	-AIC	-(BIC+AIC)	$\Delta\text{BIC} + \Delta\text{AIC}$
phase space	44	1696.64	3006.15	3305.27	6311.42	111.14
$f_2(1270)$	53	1707.63	2948.96	3309.27	6258.23	57.95
$f_2(1430)$	53	1696.81	2927.31	3287.61	6214.92	14.64
$f_2(1565)$	53	1707.00	2947.70	3308.00	6255.70	55.42
$f_2(1640)$	53	1694.75	2927.20	3287.50	6214.70	14.42
$f_2(1910)$	53	1624.53	2782.76	3143.07	5925.83	-274.45
$f_2(1950)$	53	1710.15	2954.01	3314.31	6268.32	68.04
$f_2'(2010)$	53	1705.21	2944.14	3304.44	6248.58	48.30
$f_4(2050)$	53	1713.78	2961.26	3321.57	6282.83	82.55
$h_1(1595)$	49	1676.03	2920.95	3254.06	6175.01	-25.27
$h_1(1965)$	49	1515.36	2599.61	2932.72	5532.33	-667.95
$h_1(2215)$	49	1615.05	2798.99	3132.10	5931.09	-269.19
$h_3(2025)$	49	1570.03	2708.96	3042.07	5751.03	-449.25
$h_3(2275)$	49	1691.17	2951.23	3284.34	6235.57	35.29
$\phi(1680)$	45	1681.39	2966.87	3272.78	6239.65	39.37
$\phi(2170)$	45	1669.76	2943.61	3249.52	6193.13	-7.15
$\phi_3(1850)$	45	1656.65	2917.38	3223.29	6140.67	-59.61
$\omega(1650)$	45	1682.89	2969.86	3275.77	6245.63	45.35
$\omega(1960)$	45	1603.82	2811.73	3117.65	5929.38	-270.9
$\omega(2205)$	45	1509.74	2623.57	2929.49	5553.06	-647.22
$\omega(2290)$	45	1682.89	2969.86	3275.77	6245.63	45.35
$\omega(2330)$	45	1515.89	2635.87	2941.78	5577.65	-622.63
$\omega_2(1975)$	49	1762.30	3093.49	3426.60	6520.09	319.81
$\omega_2(2195)$	49	1710.54	2989.98	3323.09	6313.07	112.79
$\omega_3(1670)$	45	1667.77	2939.62	3245.54	6185.16	-15.12
$\omega_3(1945)$	45	1581.01	2766.11	3072.02	5838.13	-362.15
$\omega_3(2255)$	45	1664.82	2933.73	3239.65	6173.38	-26.90
$\omega_3(2285)$	45	1588.81	2781.70	3087.61	5869.31	-330.97
$\omega_4(2250)$	49	1651.81	2872.51	3205.61	6078.12	-122.16
$\omega_5(2250)$	45	1669.99	2944.05	3249.97	6194.02	-6.26
$X(1575)$	45	1672.23	2948.53	3254.45	6202.98	2.70
$X(1750)$	45	1699.16	3002.40	3308.32	6310.72	110.44

Table A.2: Second step of the iterative approach with Breit-Wigner description for all contributions in addition to the base hypothesis consisting of the $(\pi\pi)_S$ wave described by a K -matrix, the $f_2'(1525)$ and $f_2(1810)$ resonances described by a Breit-Wigner distribution with masses and widths fixed to the values given in table 7.1 and 7.2

Additional Contribution	n_{free}	-NLL	-BIC	-AIC	-(BIC+AIC)	$\Delta\text{BIC} + \Delta\text{AIC}$
phase space	50	1787.16	3134.41	3474.31	6608.72	88.63
$f_2(1270)$	59	1663.28	2807.47	3208.56	6016.03	-504.06
$f_2(1430)$	59	1780.80	3042.51	3443.60	6486.11	-33.98
$f_2(1565)$	59	1681.92	2844.74	3245.83	6090.57	-429.52
$f_2(1640)$	59	1788.71	3058.34	3459.43	6517.77	-2.32
$f_2(1910)$	59	1809.30	3099.51	3500.60	6600.11	80.02
$f_2(1950)$	59	1808.87	3098.64	3499.73	6598.37	78.28
$f_2'(2010)$	59	1802.54	3086.00	3487.09	6573.09	53.00
$f_4(2050)$	59	1818.93	3118.77	3519.86	6638.63	118.54
$h_1(1595)$	55	1769.20	3054.50	3428.40	6482.90	-37.19
$h_1(1965)$	55	1790.95	3098.01	3471.91	6569.92	49.83
$h_1(2215)$	55	1699.87	2915.83	3289.73	6205.56	-314.53
$h_3(2025)$	55	1771.97	3060.04	3433.94	6493.98	-26.11
$h_3(2275)$	55	1780.66	3077.42	3451.32	6528.74	8.65
$\phi(1680)$	51	1815.23	3181.75	3528.45	6710.20	190.11
$\phi(2170)$	51	1779.46	3110.21	3456.92	6567.13	47.04
$\phi_3(1850)$	51	1742.03	3055.36	3382.07	6437.43	-82.66
$\omega(1650)$	51	1785.35	3121.99	3468.69	6590.68	70.59
$\omega(1960)$	51	1727.83	3006.96	3353.67	6360.63	-159.46
$\omega(2205)$	51	1782.17	3115.64	3462.34	6577.98	57.89
$\omega(2290)$	51	1782.93	3117.16	3463.86	6581.02	60.93
$\omega(2330)$	51	1785.25	3121.79	3468.50	6590.29	70.20
$\omega_2(2195)$	55	1732.97	2982.05	3355.95	6338.00	-182.09
$\omega_3(1670)$	51	1762.52	3076.34	3423.04	6499.38	-20.71
$\omega_3(1945)$	51	1746.60	3044.50	3391.20	6435.70	-84.39
$\omega_3(2255)$	51	1775.48	3102.25	3448.95	6551.20	31.11
$\omega_3(2285)$	51	1658.93	2869.16	3215.87	6085.03	-435.06
$\omega_4(2250)$	55	1763.37	3042.85	3416.75	6459.60	-60.49
$\omega_5(2250)$	51	1762.56	3076.42	3423.12	6499.54	-20.55
$X(1575)$	51	1764.15	3076.58	3426.29	6502.87	-17.22
$X(1750)$	51	1807.51	3166.31	3513.01	6679.32	159.23

Table A.3: Third step of the iterative approach with Breit-Wigner description for all contributions in addition to the base hypothesis consisting of the $(\pi\pi)_S$ wave described by a K -matrix, the $f_2'(1525)$, $f_2(1810)$ and $\omega_2(1975)$ resonances described by a Breit-Wigner distribution with masses and widths fixed to the values given in table 7.1 and 7.2

Additional Contribution	n_{free}	-NLL	-BIC	-AIC	-(BIC+AIC)	$\Delta\text{BIC} + \Delta\text{AIC}$
phase space	52	1829.72	3201.93	3555.43	6757.36	47.16
$f_2(1270)$	61	1819.13	3101.57	3516.26	6617.83	-92.37
$f_2(1430)$	61	1823.68	3110.68	3525.37	6636.05	-74.15
$f_2(1565)$	61	1811.88	3087.07	3501.75	6588.82	-121.38
$f_2(1640)$	61	1821.40	3106.11	3520.80	6626.91	-83.29
$f_2(1910)$	61	1819.13	3101.57	3516.26	6617.83	-92.37
$f_2(1950)$	61	1837.62	3138.55	3553.24	6691.79	-18.40
$f_2'(2010)$	61	1832.38	3128.07	3542.76	6670.83	-39.37
$f_4(2050)$	61	1850.72	3164.76	3579.44	6744.20	34.00
$h_1(1595)$	57	1820.50	3139.50	3526.99	6666.49	-43.71
$h_1(1965)$	57	1822.58	3143.67	3531.16	6674.83	-35.37
$h_1(2215)$	57	1838.50	3176.41	3563.90	6740.31	30.11
$h_3(2025)$	57	1818.44	3135.39	3522.88	6658.27	-51.93
$h_3(2275)$	57	1831.01	3160.52	3548.01	6708.53	-1.67
$\phi(2170)$	53	1819.34	3172.38	3532.68	6705.06	-5.14
$\phi_3(1850)$	53	1827.77	3189.24	3549.55	6738.79	28.59
$\omega(1650)$	53	1818.92	3171.43	3531.83	6703.26	-6.94
$\omega(1960)$	53	1809.70	3153.11	3513.41	6666.52	-43.68
$\omega(2205)$	53	1815.37	3164.44	3524.74	6689.18	-21.02
$\omega(2290)$	53	1810.75	3155.13	3515.43	6670.56	-39.64
$\omega(2330)$	53	1816.91	3167.53	3527.83	6695.36	-14.84
$\omega_2(2195)$	57	1825.15	3148.80	3536.30	6685.10	-25.10
$\omega_3(1670)$	53	1816.26	3166.22	3526.52	6692.74	-17.46
$\omega_3(1945)$	53	1819.87	3173.44	3533.74	6707.18	-3.02
$\omega_3(2255)$	53	1828.34	3190.38	3550.68	6741.06	30.86
$\omega_3(2285)$	53	1829.21	3192.12	3552.43	6744.55	34.35
$\omega_4(2250)$	57	1814.93	3128.37	3515.86	6644.23	-65.97
$\omega_5(2250)$	53	1789.09	3111.88	3472.18	6584.06	-126.14
$X(1575)$	53	1803.62	3140.94	3501.24	6642.18	-68.02
$X(1750)$	53	1813.43	3160.56	3520.86	6681.42	-28.78

Table A.4: Fourth step of the iterative approach with Breit-Wigner description for all contributions in addition to the base hypothesis consisting of the $(\pi\pi)_S$ wave described by a K -matrix, the $f_2'(1525)$, $f_2(1810)$, $\omega_2(1975)$ and $\phi(1680)$ resonances described by a Breit-Wigner distribution with masses and widths fixed to the values given in table 7.1 and 7.2

Additional Contribution	n_{free}	-NLL	-BIC	-AIC	-(BIC+AIC)	$\Delta\text{BIC} + \Delta\text{AIC}$
	51	1833.53	3218.36	3565.06	6783.42	73.22
phase space	52	1842.54	3227.57	3581.08	6808.65	25.24
$f_4(2050)$	61	1859.85	3183.01	3597.70	6780.71	-2.71
$h_1(2215)$	57	1849.76	3198.03	3585.52	6783.55	0.13
$\phi_3(1850)$	53	1827.77	3189.24	3549.55	6738.79	-44.63
$\omega_3(2255)$	53	1840.80	3215.30	3575.60	6790.90	7.48
$\omega_3(2285)$	53	1840.84	3215.39	3575.69	6791.08	7.66

Table A.5: Last step of the iterative approach with Breit-Wigner description for all contributions in addition to the base hypothesis consisting of the $(\pi\pi)_S$ wave described by a K -matrix, the $f'_2(1525)$, $f_2(1810)$, $\omega_2(1975)$ and $\phi(1680)$ resonances described by a Breit-Wigner distribution with masse and width fixed to the values given in table 7.4

Additional Contribution	n_{free}	-NLL	-BIC	-AIC	-(BIC+AIC)	$\Delta\text{BIC} + \Delta\text{AIC}$
phase space	52	1842.54	3227.57	3581.08	6808.65	25.24
$f_4(2050)$	61	1861.63	3186.57	3601.26	6787.83	4.41
$h_1(2215)$	57	1858.01	3214.53	3602.02	6816.55	33.13
$\phi_3(1850)$	53	1831.31	3196.32	3556.62	6752.94	-30.48
$\omega_3(2255)$	53	1843.64	3220.98	3581.28	6802.26	18.84
$\omega_3(2285)$	53	1844.63	3222.96	3583.26	6806.22	22.80
$h_1(2215)$	57	1860.41	3219.33	3606.82	6826.15	42.73

Table A.6: Last step of the iterative approach with Breit-Wigner description for all contributions in addition to the base hypothesis consisting of the $(\pi\pi)_S$ wave described by a K -matrix, the $f'_2(1525)$, $f_2(1810)$, $\omega_2(1975)$ and $\phi(1680)$ resonances described by a Breit-Wigner distribution with mass and width fixed to the values given in table 7.4 and optimized mass and width parameters for the additional resonances, the obtained values are shown in table A.7; the last hypothesis is with mass and width values optimized as given in table 7.5

Additional Contribution	Mass [MeV]	Deviation from PDG [σ]	Width [MeV]	Deviation from PDG [σ]
$f_4(2050)$	<u>2194</u> \pm 212	0.8	<u>416</u> \pm 358	0.5
$h_1(2215)$	2115 \pm 118	-2.4	118 \pm 20	-3.5
$\phi_3(1850)$	1894 \pm 18	2.1	174 \pm 26	2.3
$\omega_3(2255)$	2189 \pm 61	-1.1	<u>350</u> \pm 53	2.9
$\omega_3(2285)$	<u>2135</u> \pm 232	-0.6	<u>460</u> \pm 50	3.3

Table A.7: Mass and width values obtained for the fits listed in table A.6; underlined or overlined values indicate if an lower or upper limit has been reached

A.2 Results of K -Matrix Description for 2^{++} Contributions

Production Amplitudes		-NLL	-BIC	-AIC	-(BIC+AIC)
fixed	71	1723.29	2819.62	3304.59	6124.21
L dependent	75	1744.98	2827.67	3339.96	6167.53
LS dependent	87	1770.53	2772.81	3367.07	6139.88

Table A.8: Fit results for the hypotheses containing $(\pi\pi)_S$ wave, $\omega_2(1975)$, $\phi(1680)$ contributions and a K -matrix description for the dynamics of the 2^{++} contribution with three poles with and without individual description of the LS dependency of the production

Production Amplitudes		-NLL	-BIC	-AIC	-(BIC+AIC)
fixed	78	1754.40	2820.02	3352.80	6172.82
L dependent	86	1778.65	2797.88	3385.31	6183.19
LS dependent	102	1830.06	2759.41	3456.12	6215.53

Table A.9: Fit results for the hypotheses containing $(\pi\pi)_S$ wave, $\omega_2(1975)$, $\phi(1680)$ contributions and a K -matrix description for the dynamics of the 2^{++} contribution with four poles with and without individual description of the LS dependency of the production

Production Amplitudes		-NLL	-BIC	-AIC	-(BIC+AIC)
fixed	85	1763.67	2776.74	3357.34	6134.08
L dependent	97	1800.26	2743.96	3406.52	6150.48
LS dependent	117	1843.03	2652.89	3452.06	6104.95

Table A.10: Fit results for the hypotheses containing $(\pi\pi)_S$ wave, $\omega_2(1975)$, $\phi(1680)$ contributions and a K -matrix description for the dynamics of the 2^{++} contribution with five poles with and without individual description of the LS dependency of the production

A.3 Results of the Continued Systematic Survey for Contributions

Additional Contribution	n_{free}	-NLL	-BIC	-AIC	-(BIC+AIC)	$\Delta\text{BIC} + \Delta\text{AIC}$
$f_4(2050)$	112	1845.64	2702.26	3467.29	6169.55	-45.98
$h_1(1595)$	108	1834.51	2715.33	3453.03	6168.36	-47.17
$h_1(1965)$	108	1835.75	2717.81	3455.51	6173.32	-42.21
$h_1(2215)$	108	1836.86	2720.01	3457.71	6177.72	-37.81
$h_3(2025)$	108	1833.21	2712.72	3450.42	6163.14	-52.39
$h_3(2275)$	108	1833.92	2714.14	3451.84	6165.98	-49.55
$\phi(2170)$	104	1833.81	2749.24	3459.62	6208.86	-6.67
$\phi_3(1850)$	104	1836.49	2754.60	3464.97	6219.57	4.04
$\omega(1650)$	104	1830.88	2743.39	3453.76	6197.15	-18.38
$\omega(1960)$	104	1832.01	2745.65	3456.03	6201.68	-13.85
$\omega(2205)$	104	1830.78	2743.18	3453.56	6196.74	-18.79
$\omega(2290)$	104	1831.82	2745.27	3455.65	6200.92	-14.61
$\omega(2330)$	104	1831.43	2744.47	3454.85	6199.32	-16.21
$\omega_2(2195)$	108	1835.42	2717.14	3454.84	6171.98	-43.55
$\omega_3(1670)$	104	1830.35	2742.32	3452.69	6195.01	-20.52
$\omega_3(1945)$	104	1834.54	2750.70	3461.08	6211.78	-3.75
$\omega_3(2255)$	104	1833.56	2748.74	3459.11	6207.85	-7.68
$\omega_3(2285)$	104	1834.48	2750.58	3460.96	6211.54	-3.99
$\omega_4(2205)$	108	1834.13	2714.56	3452.26	6166.82	-48.71
$\omega_5(2250)$	104	1831.68	2744.98	3455.35	6200.33	-15.20
$X(1575)$	104	1832.98	2747.58	3457.96	6205.54	-9.99
$X(1750)$	104	1830.99	2743.61	3453.98	6197.59	-17.94

Table A.11: First step of the continued iterative approach with Breit-Wigner description for all contributions in addition to the base hypothesis consisting of the $(\pi\pi)_S$ wave and the 2^{++} contributions described by a K -matrix, the $\omega_2(1975)$ resonance and the $\phi(1680)$ described by a Breit-Wigner distribution with mass and width parameters fixed to the values given in table 7.1 and 7.2

Additional Contribution	n_{free}	-NLL	-BIC	-AIC	-(BIC+AIC)	$\Delta\text{BIC} + \Delta\text{AIC}$
$f_4(2050)$	114	1848.64	2689.98	3468.66	6158.64	-56.89
$h_1(1595)$	110	1836.15	2700.93	3452.29	6153.22	-62.31
$h_1(1965)$	110	1852.86	2734.37	3485.73	6229.10	4.57
$h_1(2215)$	110	1844.23	2717.10	3486.46	6185.56	-11.97
$h_3(2025)$	110	1845.20	2719.05	3470.41	6189.46	-26.07
$h_3(2275)$	110	1836.37	2701.38	3452.74	6154.12	-61.41
$\phi(2170)$	106	1835.43	2734.82	3458.86	6193.68	-21.85
$\phi_3(1850)$	106	1837.89	2739.75	3463.78	6203.53	-12.00
$\omega(1650)$	106	1831.72	2727.40	3451.43	6178.83	-36.70
$\omega(1960)$	106	1836.73	2737.42	3461.45	6198.87	-16.66
$\omega(2205)$	106	1835.43	2734.82	3458.86	6193.68	-21.85
$\omega(2290)$	106	1835.43	2734.82	3458.85	6193.67	-21.86
$\omega(2330)$	106	1835.43	2734.82	3458.86	6193.68	-21.85
$\omega_2(2195)$	110	1838.64	2705.92	3457.28	6193.20	-52.33
$\omega_3(1670)$	106	1831.40	2726.77	3450.81	6177.58	-37.95
$\omega_3(1945)$	106	1838.19	2740.35	3464.39	6204.74	-10.79
$\omega_3(2255)$	106	1837.21	2738.38	3462.42	6200.80	-14.73
$\omega_3(2285)$	106	1838.24	2740.45	3464.49	6204.94	-10.59
$\omega_4(2250)$	110	1837.42	2703.47	3454.83	6158.30	-57.23
$\omega_5(2250)$	106	1837.79	2739.55	3463.59	6203.14	-12.39
$X(1575)$	106	1840.42	2744.81	3468.85	6213.66	-1.87
$X(1750)$	106	1834.53	2741.02	3465.05	6206.07	-9.46

Table A.12: First step of the continued iterative approach with Breit-Wigner description for all contributions in addition to the base hypothesis consisting of the $(\pi\pi)_S$ wave and the 2^{++} contributions described by a K -matrix, the $\omega_2(1975)$ resonance and the $\phi(1680)$ described by a Breit-Wigner distribution with released mass and width parameters

Additional Contribution	Mass [MeV]	Deviation from PDG	Width [MeV]	Deviation from PDG
$f_4(2050)$	<u>2194</u> \pm 216	0.8	3 \pm 3	-12.8
$h_1(1595)$	1590 \pm 5	-0.1	<u>768</u> \pm 747	0.5
$h_1(1965)$	1979 \pm 8	0.3	59 \pm 15	-3.7
$h_1(2215)$	2212 \pm 3	-0.1	17 \pm 8	-5.5
$h_3(2025)$	2090 \pm 3	3.2	14 \pm 7	-4.3
$h_3(2275)$	2311 \pm 16	1.2	49 \pm 20	-2.9
$\phi(2170)$	2204 \pm 4	1.5	79 \pm 8	-4.9
$\phi_3(1850)$	1894 \pm 25	1.5	<u>174</u> \pm 115	0.7
$\omega(1650)$	1604 \pm 6	-2.2	13 \pm 14	-8.0
$\omega(1960)$	2007 \pm 10	1.7	40 \pm 20	-2.5
$\omega(2205)$	2204 \pm 3	0.0	12 \pm 5	-3.7
$\omega(2290)$	2204 \pm 4	-4.2	12 \pm 8	-7.3
$\omega(2330)$	2204 \pm 4	-4.2	12 \pm 8	-5.6
$\omega_2(2195)$	2023 \pm 12	-5.3	93 \pm 30	-2.6
$\omega_3(1670)$	1734 \pm 33	2.0	<u>346</u> \pm 210	0.8
$\omega_3(1945)$	1911 \pm 26	-1.0	<u>230</u> \pm 160	0.7
$\omega_3(2255)$	2141 \pm 55	-2.0	<u>350</u> \pm 41	3.4
$\omega_3(2285)$	2153 \pm 153	-0.8	<u>460</u> \pm 58	3.1
$\omega_4(2250)$	<u>2400</u> \pm 296	0.5	<u>300</u> \pm 209	0.7
$\omega_5(2250)$	<u>2100</u> \pm 21	-4.1	<u>640</u> \pm 68	2.7
$X(1575)$	1570.6 \pm 0.4	-13.5	23 \pm 11	2.1
$X(1750)$	1776.9 \pm 0.3	78.0	1.7 \pm 0.7	2.4

Table A.13: First step of the continued iterative approach with Breit-Wigner description for all contributions in addition to the base hypothesis consisting of the $(\pi\pi)_S$ wave and the 2^{++} contributions described by a K -matrix, the $\omega_2(1975)$ resonance and the $\phi(1680)$ resonance described by a Breit-Wigner distribution with free masses and widths; underlined or overlined values indicate if an lower or upper limit has been reached

Additional Contribution	n_{free}	-NLL	-BIC	-AIC	-(BIC+AIC)	$\Delta\text{BIC} + \Delta\text{AIC}$
$f_4(2050)$	122	1869.04	2660.76	3494.08	6154.84	-65.26
$h_1(1595)$	118	1861.07	2680.14	3486.15	6166.29	-53.81
$h_1(2215)$	118	1866.18	2690.35	3496.36	6186.71	-33.39
$h_3(2025)$	118	1867.68	2693.35	3499.35	6192.70	-27.40
$h_3(2275)$	118	1858.35	2674.69	3480.70	6155.39	-64.71
$\phi(2170)$	114	1857.99	2709.30	3487.98	6197.28	-22.82
$\phi_3(1850)$	114	1859.09	2711.49	3490.17	6201.66	-18.44
$\omega(1650)$	114	1854.16	2701.65	3480.33	6181.98	-38.12
$\omega(1960)$	114	1857.99	2709.30	3487.98	6197.28	-22.82
$\omega(2205)$	114	1857.99	2709.30	3487.99	6197.29	-22.81
$\omega(2290)$	114	1857.99	2709.30	3487.99	6197.29	-22.81
$\omega(2330)$	114	1857.99	2709.30	3487.98	6197.28	-22.82
$\omega_2(2195)$	118	1860.68	2679.36	3485.36	6164.72	-55.38
$\omega_3(1670)$	114	1860.34	2714.00	3492.68	6206.68	-13.42
$\omega_3(1945)$	114	1862.28	2717.88	3496.56	6214.44	-5.66
$\omega_3(2255)$	114	1862.28	2717.88	3496.56	6214.44	-5.66
$\omega_3(2285)$	114	1862.16	2717.63	3496.32	6213.95	-6.15
$\omega_4(2250)$	118	1859.23	2676.46	3482.47	6158.93	-61.17
$\omega_5(2250)$	114	1865.19	2723.70	3502.38	6226.08	5.98
$X(1575)$	114	1863.24	2719.80	3498.48	6218.28	-1.82
$X(1750)$	114	1861.82	2716.97	3495.65	6197.28	-7.48
$\omega_0(2195)$	118	1861.87	2717.06	3495.74	6212.80	-7.30
$h_2(2215)$	118	1857.99	2709.29	3487.97	6197.26	-22.84

Table A.14: Second step of the continued iterative approach with Breit-Wigner description for all contributions in addition to the base hypothesis consisting of the $(\pi\pi)_S$ wave and the 2^{++} contributions described by a K -matrix, $\omega_2(1975)$, $\phi(1680)$, and $h_1(1965)$ resonance described by a Breit-Wigner distribution with free mass and width values also for the additional resonances

Additional Contribution	Mass [MeV]	Deviation from PDG	Width [MeV]	Deviation from PDG
$f_4(2050)$	<u>2940</u> \pm 942	1.0	2.8 ± 0.5	-13.0
$h_1(1595)$	1592 \pm 4	0.0	<u>768</u> \pm 488	0.8
$h_1(2215)$	2212 \pm 3	-0.1	21 \pm 13	-5.4
$h_3(2025)$	2090 \pm 3	3.2	15 \pm 8	-4.2
$h_3(2275)$	2309 \pm 16	1.1	47 \pm 22	-2.9
$\phi(2170)$	2138 \pm 23	-2.0	72 \pm 36	-0.3
$\phi_3(1850)$	1782 \pm 9	-6.3	30 \pm 19	-1.9
$\omega(1650)$	1602 \pm 4	-2.2	9 \pm 13	-8.2
$\omega(1960)$	2138 \pm 23	5.2	72 \pm 37	-1.7
$\omega(2205)$	2138 \pm 22	-1.8	72 \pm 37	-2.9
$\omega(2290)$	2138 \pm 22	-5.1	72 \pm 37	-4.0
$\omega(2330)$	2138 \pm 23	-5.1	72 \pm 37	-4.3
$\omega_2(2195)$	2106 \pm 35	-1.9	297 \pm 85	0.8
$\omega_3(1670)$	1634 \pm 10	-3.1	<u>600</u> \pm 415	1.0
$\omega_3(1945)$	2180 \pm 50	4.4	<u>500</u> \pm 113	3.3
$\omega_3(2255)$	2195 \pm 54	-1.1	<u>500</u> \pm 318	1.0
$\omega_3(2285)$	2185 \pm 56	-1.2	<u>460</u> \pm 295	0.8
$\omega_4(2250)$	<u>2400</u> \pm 199	0.7	<u>300</u> \pm 213	0.7
$\omega_5(2250)$	2033 \pm 39	-4.4	<u>640</u> \pm 124	2.0
$X(1575)$	1570.6 \pm 0.5	-10.8	23 \pm 11	2.1
$X(1750)$	1777.0 \pm 0.3	78.3	1.8 \pm 0.7	2.6
$\omega_0(2195)$	2088 \pm 2	—	8 \pm 3	—
$h_2(2215)$	1823 \pm 7	—	25 \pm 14	—

Table A.15: Second step of the continued iterative approach with Breit-Wigner description for all contributions in addition to the base hypothesis consisting of the $(\pi\pi)_S$ wave and the 2^{++} contributions described by a K -matrix, the $\omega_2(1975)$ resonance, the $\phi(1680)$ resonance and the $h_1(1965)$ resonance described by a Breit-Wigner distribution with free masses and widths; underlined or overlined values indicate if an lower or upper limit has been reached

B Results of the THMP Calibrations

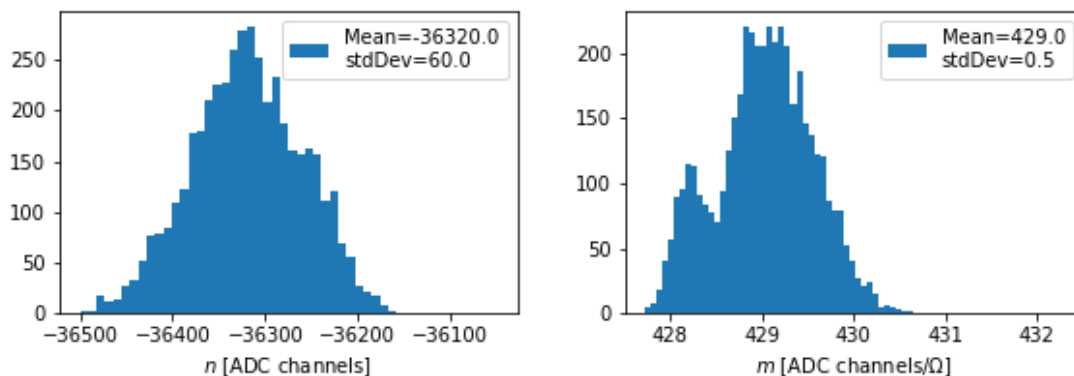


Figure B.1: Offset (top) and slope (bottom) values and uncertainties of the resistance dependence of the ADC conversions obtained by fits for all set temperatures, readout channels and calibrations

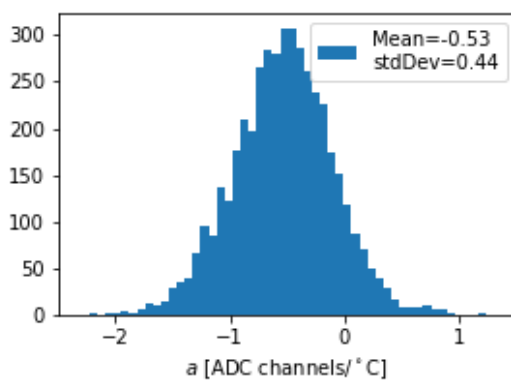


Figure B.2: Slope values and uncertainties of the temperature dependence of the ADC conversions obtained by fits for all readout channels and connected resistances for all calibrations

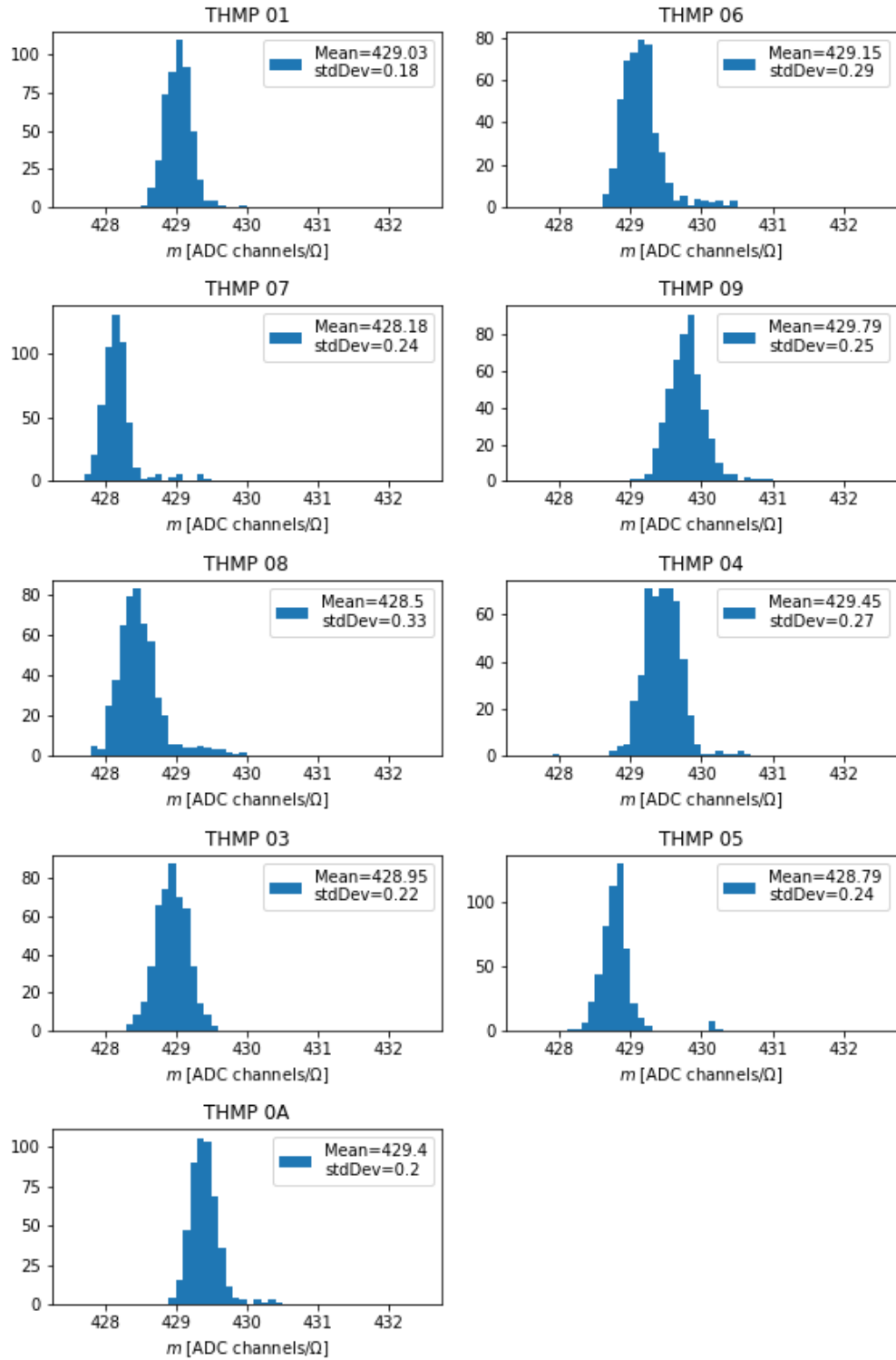


Figure B.3: Slope values of the resistance dependence of the ADC conversions obtained by fits for all temperature steps and readout channels separately for the different calibrations

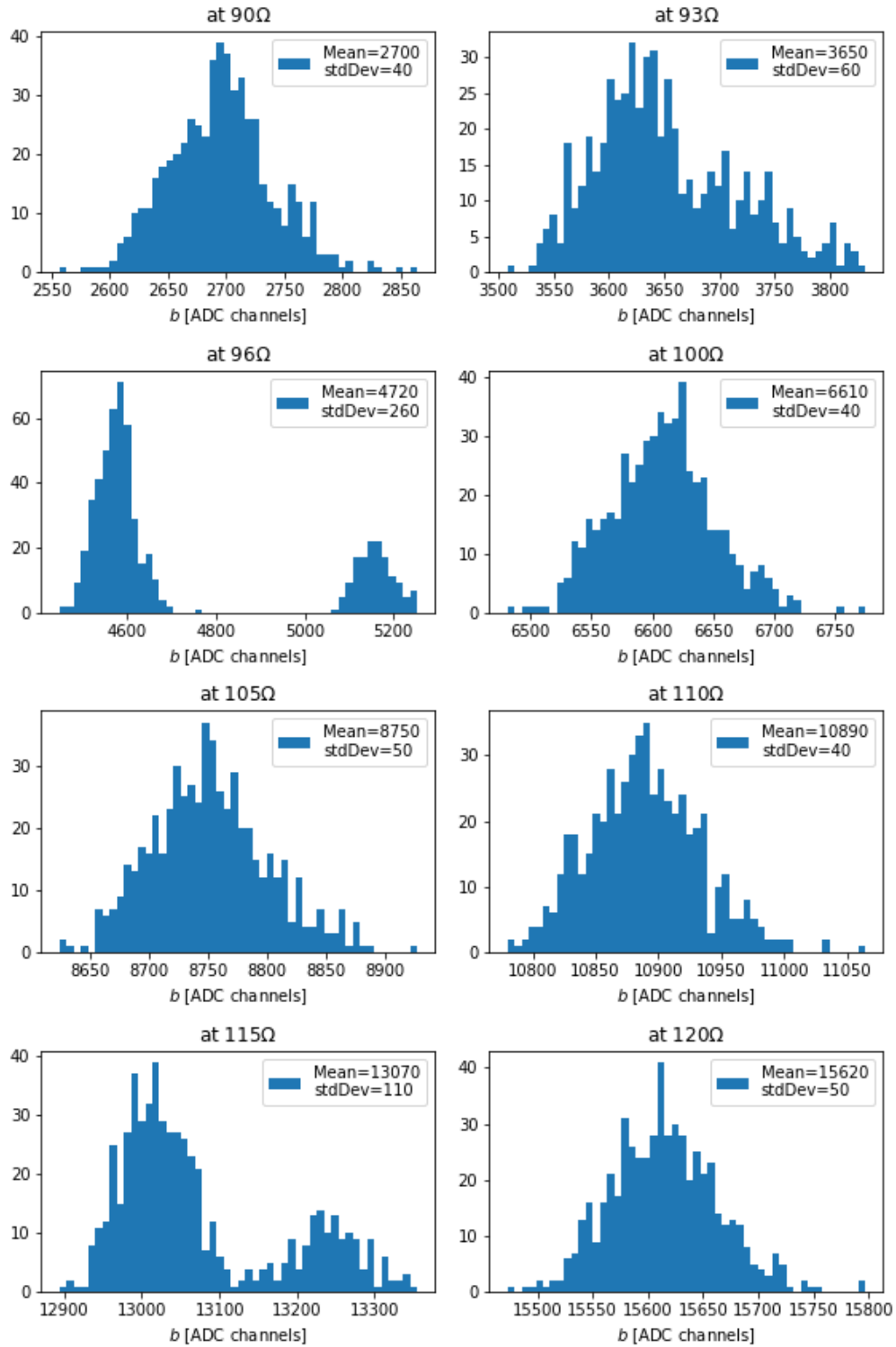


Figure B.4: Offset values of the temperature dependence of the ADC conversions obtained by fits for all readout channels separately for different connected resistances for all calibrations

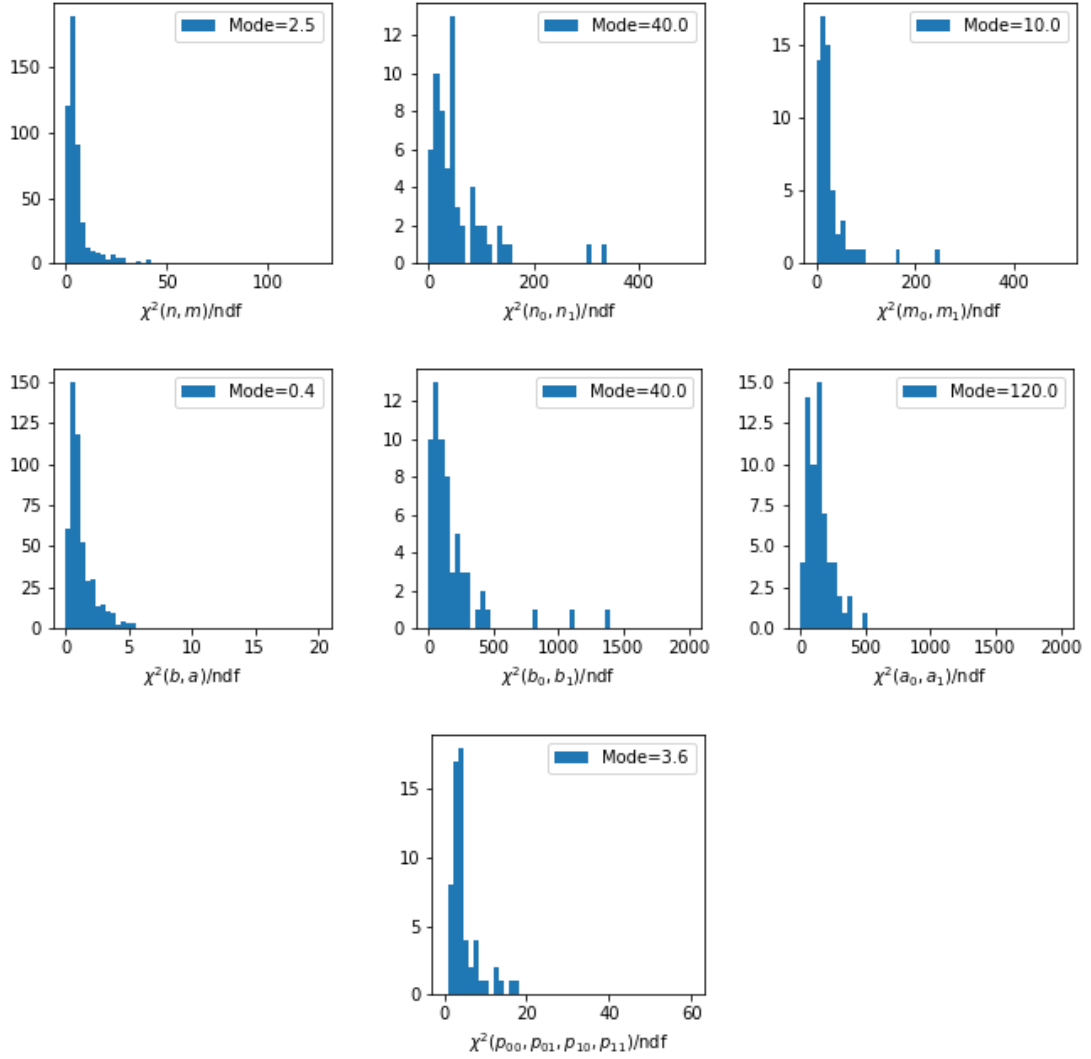


Figure B.5: Resulting χ^2 distributions exemplary for all channels of all PBBs of THMP 0A for the fit of the resistance dependence of the ADC conversions at certain set temperatures (top left) and the temperature dependence of the obtained offset n (top center) and slope m (top right), for the fit of the temperature dependence of the ADC conversions at certain connected resistances (mid left) and the resistance dependence of the obtained offset b (mid center) and slope a (mid right), and for the two dimensional fit describing resistance and temperature dependence of the ADC conversions simultaneously (bottom)

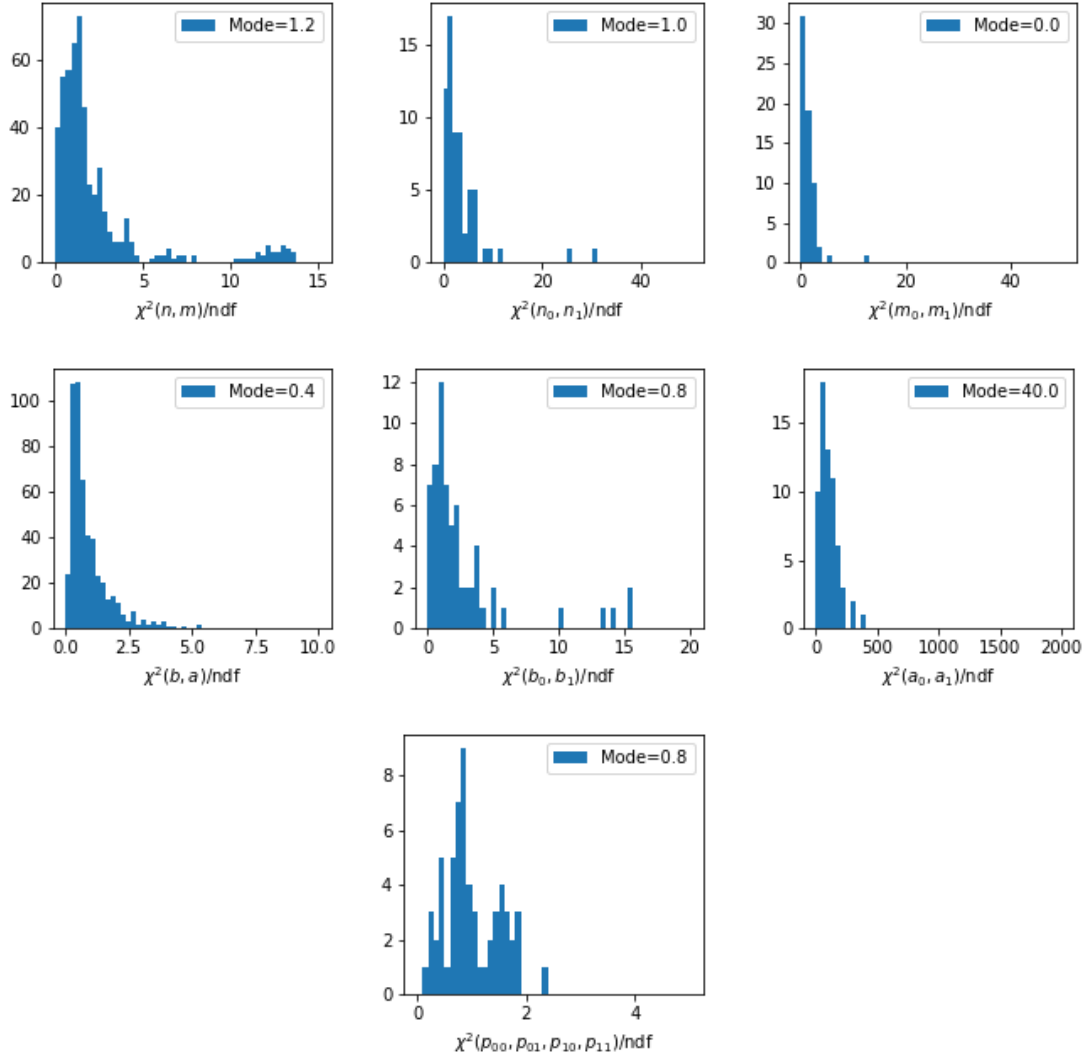


Figure B.6: Resulting χ^2 distributions exemplary for all channels of all PBBs of THMP 0A with the improved uncertainty estimation for the fit of the resistance dependence of the ADC conversions at certain set temperatures (top left) and the temperature dependence of the obtained offset n (top center) and slope m (top right), for the fit of the temperature dependence of the ADC conversions at certain connected resistances (mid left) and the resistance dependence of the obtained offset b (mid center) and slope a (mid right), and for the two dimensional fit describing resistance and temperature dependence of the ADC conversions simultaneously (bottom)

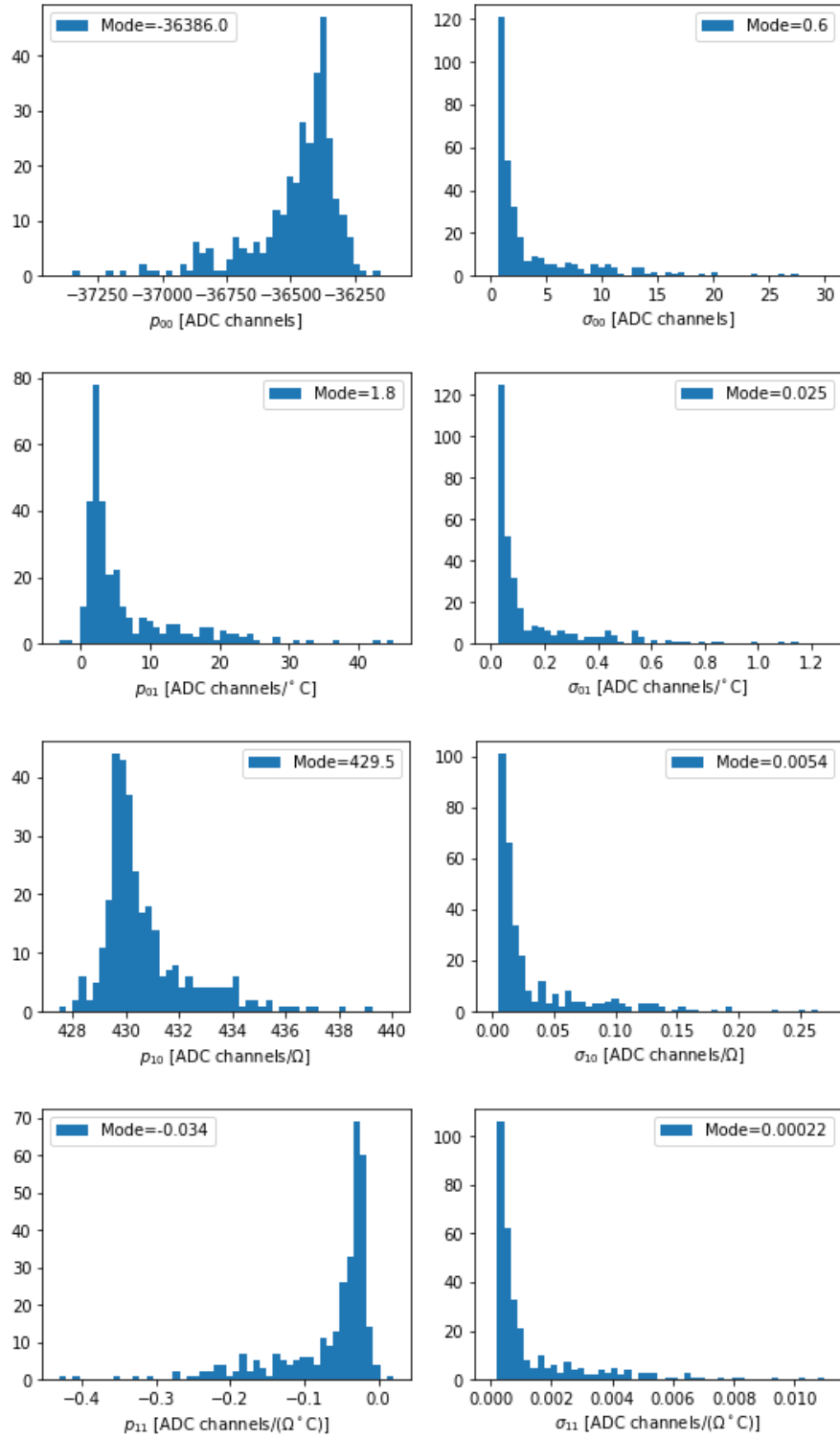


Figure B.7: Parameter values and uncertainties obtained by the two-dimensional fit for all readout channels and calibrations

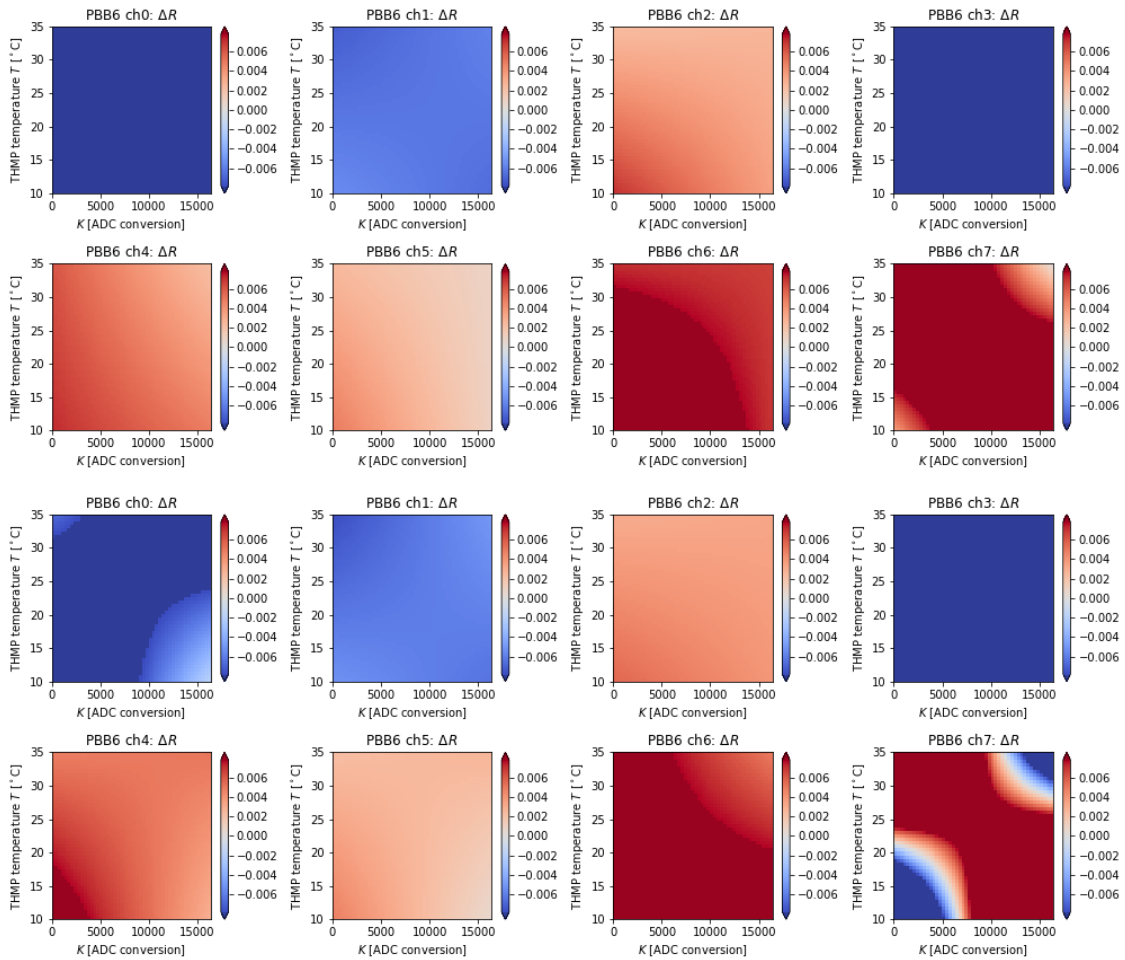


Figure B.8: Difference between the resistances retrieved from two different calibrations individually for the channels of one PBB using the naive (two upper rows) and the sophisticated uncertainty estimation (two lower rows); colors indicate the value of the resistance difference blue for negative and red for positive values the limit is chosen as $7.8\text{ m}\Omega$

List of Figures

2.1	Fermion masses depicted as spheres of corresponding volume	5
2.2	Simplest combinations composing a color neutral system	7
2.3	α_S as a function of the energy scale Q [8]	10
2.4	QCD potential obtained from lattice calculations	11
2.5	Predicted glueball mass spectrum from lattice QCD [20]	15
3.1	Lowest order diagrams for $J/\psi \rightarrow \phi X$	19
4.1	Layout of the BEPCII rings [27]	22
4.2	Overview of the BEPC facility [26]	22
4.3	Configuration of the BESIII detector [25]	23
4.4	TOF performance	26
4.5	Energy resolution for Bhabha scattering at $E_{\text{CMS}} = m_{J/\psi}$ [34]	28
5.1	Distribution of χ_{H0}^2 and $\chi_{4\text{C}}^2$ vs. χ_{H0}^2	33
5.2	Distribution of χ_{H1}^2 and χ_{H2}^2	34
5.3	Invariant K^+K^- and $\gamma\gamma$ mass distribution	34
5.4	Efficiency over invariant $\eta\eta$ and $\phi\eta$ mass	35
5.5	Efficiency over squared invariant $\phi\eta$ vs. $\phi\eta$ mass	36
5.6	Invariant $\eta\eta$ and $\phi\eta$ mass distribution for the selected data	36
5.7	Invariant $\eta\eta$ and $\phi\eta$ mass distribution for generic MC and recorded events	38
5.8	Invariant $\eta\eta$ and $\phi\eta$ mass distribution for individual contributions	38
5.9	$J/\psi \rightarrow \phi\eta\eta$ and $J/\psi \rightarrow \phi\pi^0\pi^0$ MC events discarded by the χ_{H1}^2 criterion	40
5.10	Distribution of χ_{H1}^2 for recorded and phase space MC events	40
5.11	Distribution of least vs. second least χ_{H0}^2 for miscombined events	42
5.12	Comparison of recorded events selected nominally and in the signal region	43
5.13	Sideband regions for recorded data	44
5.14	Sideband regions for signal MC	45
5.15	Comparison of recorded events in the signal and in the sideband region	47
5.16	Comparison of signal MC events in the signal and in the sideband region	47
5.17	Dalitz plot for recorded and signal MC events in the sideband regions	48
5.18	Comparison of generic MC events in the signal and sideband regions	49
5.19	Dalitz plot of all generic MC events and background in the sideband region	49
5.20	Distribution of χ_{H0}^2 for recorded and signal MC events	51
6.1	Coordinate transformation to the canonical and the helicity system [38]	57
7.1	Invariant $\eta\eta$ and $\phi\eta$ mass distributions for iteration steps 0, 1, 2	78
7.2	Invariant $\eta\eta$ and $\phi\eta$ mass distributions for iteration steps 3, a, b	79
7.3	Dalitz plots for iteration steps 0, 3, b and recorded data	80

7.4	Dalitz plots for individual contributions	81
7.5	Scattering data and fit result of a 4-pole K -matrix	83
7.6	Complex energy plane with f_2 -matrix poles	86
7.7	Invariant $\eta\eta$ and $\phi\eta$ mass distributions for iteration steps I and II	87
7.8	Dalitz plots of best hypothesis and recorded data	89
7.9	Production angle contributions of the best hypothesis	89
7.10	Decay angular distributions of the best hypothesis	90
7.11	Efficiency corrected Dalitz plot of the best hypothesis and recorded data	93
7.12	Efficiency corrected invariant $\eta\eta$ and $\phi\eta$ mass distributions	94
7.13	Efficiency corrected production angle contributions	94
7.14	Efficiency corrected decay angular distributions	95
10.1	Beam momentum and center of mass range accessible at HESR [74]	106
10.2	Overview of the FAIR complex [76]	108
10.3	Scheme of the HESR [85]	109
10.4	Layout of the \bar{P} ANDA detector	110
11.1	Formation of an EM shower and band structure of a scintillator	120
11.2	Energy resolution for different single crystal thresholds	121
11.3	Composition of the EMC in barrel, backward and forward endcap [103]	123
11.4	APDs used for readout of the TS EMC scintillator crystals	125
11.5	Temperature dependency of APD gain	126
11.6	Functional principle of a VPTT [61]	126
11.7	Temperature dependency of PWO-II light yield	127
11.8	Energy resolution for different temperature gradients	128
12.1	Exploded view of the components of the TS EMC forward endcap	129
12.2	Side and front cooling [21]	130
12.3	Scheme of the EMC readout[62]	131
12.4	Schematic overview of the light pulser system [63]	132
12.5	Light pulser electronics and light fiber sockets	133
12.6	Distribution of VPTT and APD submodules on the forward endcap	134
12.7	Naming scheme for crystal positions within a submodule	135
12.8	Naming scheme for submodule positions [59]	135
12.9	Distribution of ultrathin temperature sensors on the forward endcap	136
12.10	Overlap of submodules due to their tilt with respect to the backplate [108]	138
12.11	Cross section of routed cables and light fibers [104]	139
12.12	Routing scheme for light fibers, voltage supply and signal cables [103]	139
12.13	Hydraulic manipulator and interlocked interface	140
12.14	Submodule mounting sequence on the forward endcap	141
13.1	Design of a temperature sensor [111]	145
13.2	Polyimide foil with conductor paths cut to cables [111]	146
13.3	Winding the platinum wire manually	147
13.4	Hollow needle and magnet arrays guiding the wire	148
13.5	3D printer based setup for winding a platinum wire	148
13.6	Connecting the Pt wire and a plug to the cable	149
13.7	Cross-sectional side view of the calibration setup	150

13.8	Calibration preparations	151
13.9	Resistance values of a temperature sensor over time	152
13.10	Fit of a third order polynomial to the full data sample	153
13.11	Fit of a third order polynomial to two subsamples	153
13.12	First five Chebyshev polynomials	154
13.13	Standard deviation against sensor ID	155
13.14	Standard deviation for the three samples	156
13.15	Correlation between the standard deviations and hysteresis distribution	156
13.16	Standard deviation of the fit functions against time difference	158
13.17	Difference of fit functions obtained from several calibration measurements	158
13.18	Standard deviation of the resistances at -25°C	158
13.19	Measurements with varying set temperatures step sizes	159
13.20	Measurements with varying minimal and maximal set temperatures	160
13.21	Hysteresis values obtained for different measurements	161
13.22	Measurements with set temperatures varying around -25°C	162
13.23	ADC conversion and resistance correlated with temperature	164
13.24	Longterm measurement	166
13.25	Parameters obtained from fitting a limited growth function	167
13.26	New design of the copper box	171
14.1	THMP mainboard and PBBs	175
14.2	Schematic overview of the THMP mainboard components	175
14.3	Schematic overview of the PBBs dedicated for temperature sensors	177
14.4	THMP temperatures over time	180
14.5	Momentary deviations from the mode and standard deviations	182
14.6	Extraction of usable data	183
14.7	Fitted resistance dependence	185
14.8	Fitted temperature dependence	186
14.9	Difference of data points to a two-dimensional fit	187
14.10	Retrieved resistances compared to multimeter measurement	189
14.11	THMP temperature compared to retrieved temperature values	189
14.12	Correlation between $\Delta\vartheta$ and a and $\sigma_{\Delta\vartheta}$ distribution	190
14.13	Propagated uncertainty of the retrieved resistance	193
14.14	Minimal versus maximal resistances defining the input range	194
14.15	Distributions of resistance differences for two calibrations	195
14.16	Test station for cosmic measurements	196
14.17	Comparison of different temperature sensor calibrations	197
14.18	Rear and front temperatures of a tested submodule	197
14.19	Zoomed views of the rear and front temperatures	199
B.1	Offset and slope values and uncertainties of the resistance dependence	XIII
B.2	Slope values and uncertainties of the temperature dependence	XIII
B.3	Slope values of the resistance for different calibrations	XIV
B.4	Offset values of the temperature dependence for different resistances	XV
B.5	Resulting χ^2 distributions	XVI
B.6	Resulting χ^2 distributions with the sophisticated uncertainty estimation	XVII
B.7	Parameter values and uncertainties for the two-dimensional fit	XVIII
B.8	Difference between the resistances retrieved from two calibrations	XIX

List of Tables

2.1	Quantum numbers and masses [1] of the fundamental fermions	5
2.2	Lightest spin 0 mesons sorted according to isospin and strangeness	6
2.3	Lightest spin $\frac{1}{2}$ baryons sorted according to isospin and strangeness	6
2.4	Lightest spin $\frac{3}{2}$ baryons sorted according to isospin and strangeness	7
2.5	A possible classification of mesons into nonets [1, 17]	13
4.1	BEPCII design parameters compared to those of BEPC [25]	22
4.2	Summary of MDC performance values [29]	25
5.1	Decay chains of generic MC events	37
5.2	Categories of decay chain topologies for background events	38
5.3	Comparison of event numbers with and without $\pi^0\pi^0$ veto	40
5.4	Comparison of event numbers with and without ambiguity veto	41
5.5	Number of sideband regions in which certain background contributions occur	45
5.6	Event numbers found in the different sideband regions	46
5.7	Corrected background fraction estimations	50
5.8	Scaling factors to match the signal yield of different samples	51
6.1	Possible (L,S) combinations for accessible J^{PC}	62
6.2	\hat{K} -matrix parameters of the $(\pi\pi)_S$ wave description [48]	69
7.1	Intermediate resonances for the decay $J/\psi \rightarrow \phi X, X \rightarrow \eta\eta$	74
7.2	Intermediate resonances for the decay $J/\psi \rightarrow \eta Y, Y \rightarrow \phi\eta$	74
7.3	Fit results of the first iteration steps	75
7.4	Mass and width values for contributions of hypothesis (a)	76
7.5	Mass and width values for contributions of hypothesis (b)	77
7.6	Fit fractions of the individual contributions and their sum	82
7.7	Mass and width values for contributions of hypothesis I	84
7.8	Fit results with a K -matrix description of the f_2	85
7.9	Mass and width values for contributions of hypothesis II	86
7.10	Fit fractions of the individual contributions and their sum	88
7.11	Yield and efficiency of the individual contributions	93
7.12	Fit independent values for the determination of branching fractions	93
7.13	Systematic uncertainties independent of the hypothesis	97
7.14	Systematic uncertainties caused by the choice of hypothesis	97
7.15	Product branching fractions for the best fit with the Breit-Wigner description	98
7.16	Product branching fractions for the best fit with the K -matrix description	98
10.1	Intended parameters for the HL and HR mode [79]	109
10.2	Overview of of the cluster-jet and pellet target properties [89]	111

11.1	Properties of PWO and PWO-II	122
11.2	Requirements for the TS EMC	124
12.1	Temperature sensor positions for 8-channel submodules	137
12.2	Assignment of mounting sequence steps to packages	142
13.1	Materials needed to manufacture an ultrathin temperature sensor	145
13.2	Numbers of sensors, which fulfill the RMS criterion	168
13.3	Numbers of sensors, which fulfill the RMS and reproducibility criterion	168
13.4	Properties of the used conducting adhesives	169
13.5	Numbers of sensors produced with methods	170
14.1	Required PCBs for the different parts of the $\overline{\text{PANDA}}$ TS EMC	177
14.2	Propagated uncertainties from the different input parameters	192
A.1	Step 1 of the iterative approach	I
A.2	Step 2 of the iterative approach	II
A.3	Step 3 of the iterative approach	III
A.4	Step 4 of the iterative approach	IV
A.5	Step (a) of the iterative approach	V
A.6	Step (b) of the iterative approach	V
A.7	Masses and width values for iteration step (b)	V
A.8	K -matrix fits with three poles	VI
A.9	K -matrix fits with four poles	VI
A.10	K -matrix fits with five poles	VI
A.11	Step II of the iterative approach with fixed mass and width parameters	VII
A.12	Step II of the iterative approach with released mass and width parameters	VIII
A.13	Mass and width values for iteration step II	IX
A.14	Step III of the iterative approach with released mass and width values	X
A.15	Mass and width values for iteration step III	XI

List of Acronyms

- $\bar{\text{PANDA}}$** anti-Proton ANnihilation at Darmstadt
- THMP $\bar{\text{P}}$** Temperature and Humidity Monitoring board for $\bar{\text{PANDA}}$
- AC** Air Conditioning
- ADC** Analog to Digital Converter
- AIC** Akaike Information Criterion
- ALICE** A Large Ion Collider Experiment
- APD** Avalanche Photo Diode
- APPA** Atomic, Plasma Physics and Applications
- ATLAS** A Toroidal LHC ApparatuS
- BEPC** Beijing Electron-Positron Collider
- BEPCII** the second generation of the Beijing Electron-Positron Collider
- BES** Beijing Electron Spectrometer
- BESII** the second generation of the Beijing Electron Spectrometer
- BESIII** the third generation of the Beijing Electron Spectrometer
- BIC** Bayesian Information Criterion
- BNL** Brookhaven National Laboratory
- BOSS** BES Offline Software System
- BTOF** Barrel of the Time-of-Flight system
- CAN** Controller Area Network
- CERN** Conseil Européen pour la Recherche Nucléaire (engl. European Organization for Nuclear Research)
- CGEM** Central Gaseous Electron Multiplier
- CKM** Cabibbo-Kobayashi-Masukawa
- CMS** Compact Muon Solenoid
- COSY** COoler SYnchrotron
- CR** Collector Ring
- DAQ** Data AcQuisition
- DCS** Detector Slow Controll
- DIRC** Detection of Internally Reflected Cherenkov light
- DST** Data Summary Tape
- EMC** ElectroMagnetic Calorimeter
- EPICS** Experimental Physics and Industrial Control System
- ETOF** End cap of the Time-of-Flight system
- FAIR** Facility for Antiproton and Ion Research
- FEE** Front End Electronics
- FPGA** Field Programmable Gate Array

- FSC** Forward Shashlyk Calorimeter
FT Forward Tracking
FToF Forward Time-of-Flight
- GAMS** acronym stems from the Russian abbreviation for the experiment's large lead-glass array
GDML Geometry Design Markup Language
Geant4 GEometry ANd Tracking
GEM Gaseous Electron Multiplier
GSi research center founded as Gesellschaft für SchwerIonenforschung (engl. society for heavy ion research), now Helmholtz Center for Heavy Ion Research
- HESR** High Energy Storage Ring
HL High Luminosity
HR High Resolution
HV-MAPS High Voltage Monolithic Active Pixel Sensors
- IP** Interaction Point
ISP In-System Programming
IZM Institut für Zuverlässigkeit und Mikrointegration
- JTAG** Joint Test Action Group
- KOALA** Key experiment fOR \bar{P} ANDA Luminosity determinAtion
KVI Kernfysisch Versneller Instituut
- LAAPD** Large Area Avalanche Photo Diode
LCD Liquid Crystal Display
LEAR Low Energy Antiproton Ring
LED Light Emitting Diode
LHC Large Hadron Collider
LHCb Large Hadron Collider beauty
LINAC LINear ACcelerator
LY Light Yield
- MB** MainBoard
MC Monte Carlo
MCP-PMT Microchannel Plate PhotoMultiplier Tube
MDC Multilayer Drift Chamber
MDT Mini Drift Tube
MRPC Multigap Resistive Plate Chamber
MSV Modularized Start Version
MUC MUon Counter system
MVD Micro Vertex Detector
- NESR** New Experimental Storage Ring
NLL Negative Log-Likelihood
NUSTAR NUclear STructure, Astrophysics and Reactions
- PAWIAN** PArtial Wave Interactive ANalysis

-
- PBB** PiggyBack Board
PCB Printed Circuit Board
PDG Particle Data Group
PET PolyEthylene Terephthalate
PID Particle IDentification
PIN Positive Intrinsic Negative
PMT PhotoMultiplier Tube
PWO PbWO₄, lead tungstate
PWO-II PbWO₄, lead tungstate
- QCD** Quantum ChromoDynamics
QED Quantum ElectroDynamics
- RadFET** Radiation sensitive Field Effect Transistors
RESR Recuperated Experimental Storage Ring
RICH Ring Imaging CHerenkov light
RMS Root Mean Square
ROM Read Only Memory
RPC Resistive Plate Chamber
RT Room Temperature
- SC coil** SuperConducting coil
SCQ SuperConducting Quadrupole
SIIT System Integration and Interconnection Technologies
SiPM Silicon Photomultiplier
SIS-100 SchwerIonen Synchrotron (engl. heavy ion synchrotron) with a bending power of 100 Tm
SIS-18 SchwerIonen Synchrotron (engl. heavy ion synchrotron) with a bending power of 18 Tm
SODA Synchronization Of Data Acquisition
SPARC Stored Particles Atomic Research Collaboration
SPS Super Proton Synchrotron
STT Straw Tube Tracker
- TOF** Time-of-Flight
TS EMC Electromagnetic Calorimeter of the Target Spectrometer
- UNILAC** UNIversal Linear Accelerator
USB Universal Serial Bus
VPTT Vacuum Photo TeTrode

Bibliography

- [1] **Particle Data Group** Collaboration, C. Patrignani *et al.*, Review of Particle Physics *Chin. Phys.* **C40** no. 10, (2016) 100001.
- [2] A. Pais, On the Baryon-meson-photon System *Progress of Theoretical Physics* **10** no. 4, (1953) 457–469.
- [3] T. Nakano and K. Nishijima, Charge Independence for V-particles *Progress of Theoretical Physics* **10** no. 5, (1953) 581–582.
- [4] **ATLAS** Collaboration, G. Aad *et al.*, Observation of a new particle in the search for the Standard Model Higgs boson with the ATLAS detector at the LHC *Phys. Lett.* **B716** (2012) 1–29.
- [5] **CMS** Collaboration, S. Chatrchyan *et al.*, Observation of a new boson at a mass of 125 GeV with the CMS experiment at the LHC *Phys. Lett.* **B716** (2012) 30–61.
- [6] D. Griffiths, *Introduction to Elementary Particles*. Physics textbook. Wiley, 2008.
- [7] A. Jaffe and E. Witten, “Quantum Yang-Mills Theory.” Millenium Prize Problems, 2000.
- [8] S. Bethke, α_S in *QCD16*, vol. 282 – 284, pp. 149 – 152. Nuclear and Particle Physics Proceedings, 2017.
- [9] E. Eichten, K. Gottfried, T. Kinoshita, J. B. Kogut, K. D. Lane, and T.-M. Yan, The Spectrum of Charmonium *Phys. Rev. Lett.* **34** (1975) 369–372. [Erratum: *Phys. Rev. Lett.* **36**, (1976) 1276].
- [10] G. S. Bali, QCD forces and heavy quark bound states *Phys. Rept.* **343** (2001) 1–136.
- [11] M. Thomson, *Modern Particle Physics*. Cambridge University Press, 2013.
- [12] T. Blum, A. Denig, I. Logashenko, E. de Rafael, B. L. Roberts, T. Teubner, and G. Venanzoni, “The Muon ($g-2$) Theory Value: Present and Future.” arXiv:1311.2198 [hep-ph], 2013.
- [13] C. E. Carlson, The Proton Radius Puzzle *Prog. Part. Nucl. Phys.* **82** (2015) 59–77.
- [14] **BaBar** Collaboration, J. P. Lees *et al.*, Evidence for an excess of $\bar{B} \rightarrow D^{(*)} \tau^- \bar{\nu}_\tau$ decays *Phys. Rev. Lett.* **109** (2012) 101802.
- [15] **LHCb** Collaboration, R. Aaij *et al.*, Measurement of the ratio of branching fractions $\mathcal{B}(\bar{B}^0 \rightarrow D^{*+} \tau^- \bar{\nu}_\tau) / \mathcal{B}(\bar{B}^0 \rightarrow D^{*+} \mu^- \bar{\nu}_\mu)$ *Phys. Rev. Lett.* **115** no. 11, (2015) 111803.

- [16] **Belle** Collaboration, M. Huschle *et al.*, Measurement of the branching ratio of $\bar{B} \rightarrow D^{(*)}\tau^{-}\bar{\nu}_{\tau}$ relative to $\bar{B} \rightarrow D^{(*)}\ell^{-}\bar{\nu}_{\ell}$ decays with hadronictagging at Belle *Phys. Rev.* **D92** no. 7, (2015) 072014.
- [17] M. Battaglieri *et al.*, Analysis Tools for Next-Generation Hadron Spectroscopy Experiments *Acta Phys. Polon.* **B46** (2015) 257.
- [18] F. E. Close and A. Kirk, The Mixing of the $f(0)(1370)$, $f(0)(1500)$ and $f(0)(1710)$ and the search for the scalar glueball *Phys. Lett.* **B483** (2000) 345–352.
- [19] H.-Y. Cheng, C.-K. Chua, and K.-F. Liu, Revisiting Scalar Glueballs *Phys. Rev.* **D92** no. 9, (2015) 094006.
- [20] Y. Chen *et al.*, Glueball spectrum and matrix elements on anisotropic lattices *Phys. Rev.* **D73** (2006) 014516.
- [21] S. Leiber, *Analyse des Zerfalls $J/\psi \rightarrow \omega\pi^{+}\pi^{-}$ bei BESIII und Entwicklungen für das Kühlsystem und die thermische Isolierung des PANDA-EMC*. PhD thesis, Ruhr-Universität Bochum, 2018.
- [22] J. Frech, *Analyse des Zerfalls $J/\psi \rightarrow \gamma\eta\eta$ bei BESIII* Master’s Thesis, Ruhr-Universität Bochum, 2018.
- [23] **BESIII** Collaboration, M. Ablikim *et al.*, Amplitude analysis of the $\pi^0\pi^0$ system produced in radiative J/ψ decays *Phys. Rev.* **D92** no. 5, (2015) 052003. [Erratum: *Phys. Rev.*D93,no.3,039906(2016)].
- [24] P. Friedel, *Analyse des Zerfalls $J/\psi \rightarrow \gamma\phi\phi$ bei BESIII und Entwicklungen für den Prototyp des \bar{P} ANDA-EMC*. PhD thesis, Ruhr-Universität Bochum, 2012.
- [25] **BESIII** Collaboration, M. Ablikim *et al.*, Design and Construction of the BESIII Detector *Nucl. Instrum. Meth.* **A614** (2010) 345–399.
- [26] C. Zhang, Performance of the BEPC and Progress of the BEPCII in *APAC’04*, pp. 15–19. PAL, 2005.
- [27] C. Yu *et al.*, BEPCII Performance and Beam Dynamics Studies on Luminosity in *IPAC’16*, pp. 1014–1018. JACoW, 2016.
- [28] L. Malter, Thin Film Field Emission *Phys. Rev.* **50** no. 1, (1936) 48–58.
- [29] Z. Qin, Status and prospects for BESIII in *Charm 2013*. SLAC NAL, 2013.
- [30] Y.-j. Xie *et al.*, Construction and cosmic-ray test of the new inner drift chamber for BESIII *Chin. Phys.* **C40** no. 9, (2016) 096003.
- [31] L. Lavezzi *et al.*, The Cylindrical GEM Inner Tracker of the BESIII experiment: prototype test beam results in *INSTR17*. IOP, 2017.
- [32] X. Wang *et al.*, The Upgrade System of BESIII ETOF with MRPC Technology in *RPC 2016*, vol. 11. JINST, 2016.

- [33] Q. Gang *et al.*, Particle identification using artificial neural networks at BESIII *Chin. Phys.* **C32** no. 1, (2008) 1–8.
<http://stacks.iop.org/1674-1137/32/i=1/a=001>.
- [34] F. Feldbauer, Current Status and Performance of the BESIII Electromagnetic Calorimeter in *CALOR 2014*, vol. 587, BESIII Collaboration. Journal of Physics: Conference Series, 2015.
- [35] Q. Gao, J. Zhang, and C. Li, Alignment and measurement of the magnetic field for the BESIII muon counter *Chin. Phys.* **C40** no. 11, (2016) 116001.
- [36] **BESIII** Collaboration, M. Ablikim *et al.*, Determination of the number of J/ψ events with inclusive J/ψ decays *Chin. Phys.* **C41** no. 1, (2017) 013001.
- [37] J. D. Richman, An Experimenter’s Guide to the Helicity Formalism doe research and development report, California Institute of Technology, 1984. CALT-68-1148.
- [38] S. U. Chung, Spin Formalisms BNL preprint BNL-QGS-02-0900, Brookhaven National Laboratory, CERN, 8, 1971. Upadated 2014.
- [39] F. Von Hippel and C. Quigg, Centrifugal-barrier effects in resonance partial decay widths, shapes, and production amplitudes *Phys. Rev.* **D5** (1972) 624–638.
- [40] S. U. Chung, Formulas for Angular-Momentum Barrier Factors BNL preprint BNL-QGS-06-101, Brookhaven National Laboratory, 2015.
- [41] S. U. Chung, J. Brose, R. Hackmann, E. Klempt, S. Spanier, and C. Strassburger, Partial wave analysis in K matrix formalism *Annalen Phys.* **4** (1995) 404–430.
- [42] J. Pychy, *Gekoppelte Partialwellenanalyse von $\bar{p}p$ -Annihilationen im Fluge in die Endzustände $K^+K^-\pi^0$, $\pi^0\pi^0\eta$ und $\pi^0\eta\eta$* . PhD thesis, Ruhr-Universität Bochum, 2016.
- [43] J. L. Basdevant and E. L. Berger, Unstable-particle scattering and an analytic quasi-unitary isobar model *Phys. Rev. D* **19** no. 1, (1979) 239–245.
- [44] I. J. R. Aitchison, The K-matrix formalism for overlapping resonances *Nucl. Phys.* **A189** no. 2, (1972) 417 – 423.
- [45] A. Badalyan, L. Kok, M. Polikarpov, and Y. Simonov, Resonances in coupled channels in nuclear and particle physics *Phys. Rept.* **82** no. 2, (1982) 31–177.
- [46] V. Anisovich and A. Sarantsev, K-matrix analysis of the ($IJ^{PC} = 00^{++}$)-wave in the mass region below 1900 MeV *Eur. Phys. J.* **A16** (2003) 229–258.
- [47] S. L. Adler, Consistency Conditions on the Strong Interactions Implied by a Partially Conserved Axial-Vector Current *Phys. Rev.* **137** (1965) B1022–B1033.
- [48] **BaBar** Collaboration, B. Aubert *et al.*, Improved measurement of the CKM angle γ in $B^\mp \rightarrow D^{(*)}K^{(*)\mp}$ decays with a Dalitz plot analysis of D decays to $K_S^0\pi^+\pi^-$ and $K_S^0K^+K^-$ *Phys. Rev.* **D78** (2008) 034023.

- [49] V. V. Anisovich, L. G. Dakhno, and V. A. Nikonov, $D_s^+ \rightarrow \pi^+\pi^+\pi^-$ decay: The $1^3P_0s\bar{s}$ component in scalar-isoscalar mesons *Phys. Atom. Nucl.* **67** no. 8, (2004) 1571–1579.
- [50] V. A. Schegelsky, A. V. Sarantsev, V. A. Nikonov, and A. V. Anisovich, The $K_S^0K_S^0$ final state in two-photon collisions and SU(3) tensor nonets *Eur. Phys. J.* **A27** no. 2, (2006) 207–212.
- [51] J. Link *et al.*, Dalitz plot analysis of D_s^+ and D^+ decay to $\pi^+\pi^-\pi^+$ using the K -matrix formalism *Phys. Lett.* **B585** no. 3, (2004) 200 – 212.
- [52] B. Kopf, H. Koch, J. Pychy, and U. Wiedner, Partial wave analysis for $\bar{p}p$ and e^+e^- annihilation processes *Hyperfine Interactions* **229** no. 1, (2014) 69–74.
- [53] B. R. Ko and the Belle Collaboration, Charm CP violation and mixing at Belle *Journal of Physics: Conference Series* **556** no. 1, (2014) 012058.
- [54] **LHCb** Collaboration, R. Aaij *et al.*, Dalitz plot analysis of $B^0 \rightarrow \bar{D}^0\pi^+\pi^-$ decays *Phys. Rev.* **D92** no. 3, (2015) 032002.
- [55] A. Austregesilo, Light scalar mesons in central production at COMPASS *AIP Conference Proceedings* **1735** no. 1, (2016) 030012.
- [56] D. Bugg, A study in depth of $f_0(1370)$ *Eur. Phys. J.* **C52** no. 1, (2007) 55–74.
- [57] K. P. Burnham and D. R. Anderson, *Model Selection and Multimodel Inference. A Practical Information-Theoretic Approach*. Springer, second edition ed., 2002.
- [58] F. James and M. Roos, Minuit – a system for function minimization and analysis of the parameter errors and correlations *Comput. Phys. Commun.* **10** (1975) 343–367.
- [59] J. Schulze, *Analyse des Zerfalls $\chi_{c0} \rightarrow K^+K^-\pi^0\pi^0$ bei BESIII und Entwicklung von mechanischen Komponenten für einen Prototypen des $\bar{P}ANDA$ -EMC*. PhD thesis, Ruhr-Universität Bochum, 2012.
- [60] J. Becker, *Analyse des Zerfalls $\chi_{cJ} \rightarrow K^+K^-\eta$ bei BESIII und Entwicklung eines Kühlsystems für den Prototypen des $\bar{P}ANDA$ -EMC*. PhD thesis, Ruhr-Universität Bochum, 2012.
- [61] M. Leyhe, *Analyse des J/ψ - und $\psi(2S)$ -Zerfalls in $\gamma\pi^+\pi^-\eta$ bei BES III und Entwicklungen zur Auslese des $\bar{P}anda$ -EMC*. PhD thesis, Ruhr-Universität Bochum, 2013.
- [62] M. Albrecht, *Partial Wave Analysis of the Decay $J/\psi \rightarrow \gamma\omega\omega$ at BESIII and Developments for the Electromagnetic Calorimeter of the PANDA Detector*. PhD thesis, Ruhr-Universität Bochum, 2016.
- [63] P. Musiol, *Analyse der Kanäle $\chi_{c2} \rightarrow \pi^+\pi^-/K^+K^-$ in radiativen $\psi(2S)$ -Zerfällen bei BESIII und Entwicklung eines Monitorierungssystems für das elektromagnetische Kalorimeter des $\bar{P}ANDA$ -Experiment*. PhD thesis, Ruhr-Universität Bochum, 2018.

- [64] C. Patrignani *et al.*, “The review of particle physics.” <http://pdglive.lbl.gov/>. Accessed: 2016-11-11.
- [65] B. Hyams *et al.*, $\pi\pi$ Phase Shift Analysis from 600-MeV to 1900-MeV *Nucl. Phys.* **B64** (1973) 134–162.
- [66] **Serpukhov-Brussels-Annecy(LAPP)** Collaboration, F. G. Binon *et al.*, G (1590): A Scalar Meson Decaying Into Two eta Mesons *Nuovo Cim.* **A78** (1983) 313.
- [67] D. Alde *et al.*, Production of G(1590) and other mesons decaying into η pairs by 100 GeV/c π^- on protons *Nucl. Phys.* **B269** no. 2, (1986) 485 – 508.
- [68] R. Longacre *et al.*, A measurement of $\pi^- p \rightarrow K_S^0 K_S^0 n$ at 22 GeV/c and a systematic study of the 2^{++} meson spectrum *Phys. Lett.* **B177** no. 2, (1986) 223 – 227.
- [69] V. Prasad, Study of Photon Detection Efficiency and Position Resolution of BESIII Electromagnetic Calorimeter in *XXI DAE-BRNS High Energy Physics Symposium*, pp. 577–582. 2016.
- [70] **BESIII** Collaboration, M. Ablikim *et al.*, Study of χ_{cJ} radiative decays into a vector meson *Phys. Rev.* **D83** (2011) 112005.
- [71] A. Falvard *et al.*, Study of hadronic J/ψ decays involving φ and ω production *Phys. Rev.* **D38** no. 9, (1988) 2706–2721.
- [72] G. Gidal *et al.*, Observations of $S^* \rightarrow \pi^+ \pi^-$ in ψ decay *Phys. Lett.* **B107** no. 1, (1981) 153 – 158.
- [73] M. F. M. Lutz *et al.*, Physics Performance Report for PANDA: Strong Interaction Studies with Antiprotons tech. rep., PANDA collaboration, 2009. [arXiv:0903.3905](https://arxiv.org/abs/0903.3905) [hep-ex].
- [74] M. Kotulla, Technical Progress Report for: PANDA tech. rep., PANDA collaboration, 2005.
- [75] G. Brown and M. Rho, Chiral symmetry restoration and the Georgi vector limit *Phys. Lett.* **B338** (1994) 301–307.
- [76] FAIR GmbH, “The fair complex.” <https://fair-center.eu/public.html>. Accessed: 2018-11-04.
- [77] H. H. Gutbrod, I. Augustin, H. Eickhoff, K.-D. Gross, W. F. Henning, D. Krämer, and G. Walter, Executive Summary Tech. Rep. 1, FAIR, 2006.
- [78] FAIR Joint Core Team and Scientific and Technical Issues Working Group, Green Paper: The Modularized Start Version tech. rep., FAIR, 2009.
- [79] **PANDA** Collaboration, B. Singh *et al.*, Technical Design Report for the: PANDA Forward Spectrometer Calorimeter [arXiv:1704.02713](https://arxiv.org/abs/1704.02713) [physics.ins-det].
- [80] A. Dolinskii *et al.*, Antiproton complex at the FAIR project *Nucl. Instrum. Meth.* **A629** no. 1, (2011) 16 – 24.

- [81] R. Bär *et al.*, Technical Design Report on the Collector Ring tech. rep., Collector Ring working group, 2008.
- [82] O. Kester *et al.*, Status of the FAIR Accelerator Facility in *Proceedings, 5th International Particle Accelerator Conference (IPAC 2014)*. 2014.
- [83] R. Maier, The High-Energy Storage Ring (HESR) in *Proceedings, 24th Particle Accelerator Conference (PAC'11)*, vol. C110328, pp. 2104–2106. 2011.
- [84] V. Kamerdzhiev *et al.*, 2MeV Electron Cooler for COSY and HESR – First Results in *Proceedings, 5th International Particle Accelerator Conference (IPAC 2014)*. 2014.
- [85] M. Fritsch, Personal Communication 2018.
- [86] **PANDA** Collaboration, W. Erni *et al.*, Technical Design Report for the: PANDA Solenoid and Dipole Spectrometer Magnets [arXiv:0907.0169](#) [physics.ins-det].
- [87] Q. Hu *et al.*, A recoil detector for the measurement of antiproton-proton elastic scattering at angles close to 90° *Eur. Phys. J.* **A50** no. 10, (2014) 156.
- [88] **SPARC** Collaboration, T. Stöhlker *et al.*, SPARC Collaboration: New Strategy for Storage Ring Physics at FAIR *Hyperfine Interactions* **227** (2014) 45–53.
- [89] **PANDA** Collaboration, W. Erni *et al.*, Technical Design Report for the PANDA Internal Targets.
- [90] **PANDA** Collaboration, W. Erni *et al.*, Technical Design Report for the: PANDA Micro Vertex Detector [arXiv:1207.6581](#) [physics.ins-det].
- [91] **PANDA** Collaboration, W. Erni *et al.*, Technical Design Report for the: PANDA Straw Tube Tracker [arXiv:1205.5441](#) [physics.ins-det].
- [92] **PANDA** Collaboration, B. Singh *et al.*, Technical Design Report for the: PANDA Barrel DIRC Detector [arXiv:1710.00684](#) [physics.ins-det].
- [93] M. Schmidt *et al.*, Endcap Disc DIRC for PANDA at FAIR in *Proceedings of International Conference on Technology and Instrumentation in Particle Physics 2017 (TIPP 2017)*, pp. 275–278. 2018.
- [94] **PANDA** Collaboration, B. Singh *et al.*, Technical Design Report for the: PANDA Barrel Time-of-Flight.
- [95] **PANDA** Collaboration, W. Erni *et al.*, Technical Design Report for: PANDA Electromagnetic Calorimeter (EMC) [arXiv:0810.1216](#) [physics.ins-det].
- [96] **PANDA** Collaboration, W. Erni *et al.*, Technical Design Report for the PANDA Muon System.
- [97] **PANDA** Collaboration, F. Davi *et al.*, Technical Design Report for the: PANDA Forward Tracker.

- [98] **PANDA** Collaboration, B. Singh *et al.*, Technical Design Report for the: PANDA Forward Time of Flight Detector.
- [99] A. Karavdina *et al.*, Offline Software for the PANDA Luminosity Detector in *20th International Conference on Computing in High Energy and Nuclear Physics (CHEP2013)*, vol. 513 of 2, p. 022016. 2014.
- [100] **PANDA** Collaboration, F. Davi *et al.*, Technical Design Report for the: PANDA Detector Control System tech. rep., 2018. soon to be published.
- [101] G. F. Knoll, *Radiation Detection and Measurement*. John Wiley & Sons, 2nd ed., 1989.
- [102] C. Amsler, *Kern- und Teilchenphysik*. vdf Hochschulverlag AG, 2007.
- [103] C. Schnier. Personal Communication, 2018.
- [104] C. Schnier, *Analyse des Zerfalls $\eta_c \rightarrow \pi^+\pi^-\eta$ bei BESIII und Entwicklung von Komponenten für das elektromagnetische Kalorimeter des \bar{P} PANDA-Experimentes*. PhD thesis, Ruhr-Universität Bochum, 2018.
- [105] J. Schulze, Prototypenentwicklung für das elektromagnetische Kalorimeter des PANDA-Experiments Diplomarbeit, Ruhr-Universität Bochum, 2009.
- [106] M. Albrecht, The Forward Endcap of the Electromagnetic Calorimeter for the PANDA Detector at FAIR in *CALOR 2014*, vol. 587 of *Journal of Physics: Conference Series*, p. 012050. 2015.
- [107] M. Albrecht. Personal Communication, 2018.
- [108] M. F. Lindemulder. Personal Communication, 2013.
- [109] **CMS** Collaboration, A. P. L. Linssen, 2004.
<http://cds.cern.ch/record/1295575>.
- [110] Industrielle Platin-Widerstandsthermometer und Platin-Temperatursensoren 2009.
- [111] C. Sowa, Personal Communication 2014.
- [112] M. Kümmel, Investigations Concerning the Spatial and Energy Resolution of the PANDA Electromagnetic Calorimeter Master's Thesis, Ruhr-Universität Bochum, 2014.
- [113] N. Boelger, Automatisierung der Produktion von Platindraht-Temperatursensoren Bachelor's Thesis, Ruhr-Universität Bochum, 2018.
- [114] JULABO Ed., JULABO WEST, 2575 Pioneer Avenue, Suite 102, Vista, CA 92081, *Operating Manual*, 2010.
- [115] C. Schnier, Aufbau und Test von Kalorimeter-Moduln für PANDA Master's Thesis, Ruhr-Universität Bochum, 2014.
- [116] P. Meyer, Personal Communication 2018.

-
- [117] V. Freudenreich, Studien zur Strahlenhärte der Elektronikkomponenten für das elektromagnetische Kalorimeter des PANDA-Experiments Bachelor's Thesis, Ruhr-Universität Bochum, 2018.
- [118] P. Friedel, Studien zum Prototypaufbau des elektromagnetischen Kalorimeters für den PANDA-Detektor Diplomarbeit, Ruhr-Universität Bochum, 2009.
- [119] F. Feldbauer, Studien zur Strahlenhärte von Bleiwolframat-Kristallen Master's Thesis, Ruhr-Universität Bochum, 2009.
- [120] F. Feldbauer, *Analyse des Zerfalls $\chi_{cJ} \rightarrow K^+ K_s^0 \pi^- \pi^0 \eta$ bei BES-III und Entwicklung der Slow Control für das PANDA-Experiment.* PhD thesis, Ruhr-Universität Bochum, 2012.
- [121] A. Csapó, Präzise Temperaturmessung für das PANDA elektromagnetische Kalorimeter Master's thesis, Ruhr-Universität Bochum, 2013.
- [122] iminuit team, "iminuit – a python interface to minuit." <https://github.com/iminuit/iminuit>. Accessed: 2018-03-05.

Acknowledgments

Many people supported directly or indirectly the success of the presented thesis, whom I would like to thank here. First of all I want to thank Prof. Ulrich Wiedner for welcoming me in his group several years ago, entrusting me with the responsibility of calibrating temperature sensors and THMPs and giving me the opportunity to independently develop the necessary steps. I thank Prof. Wiedner and PD Fritz-Herbert Heinsius for supervising my Ph.D. project.

Numerous further colleagues also inspired the project with fruitful discussions and helpful suggestions, namely Matthias Steinke, Thomas Held, Malte Albrecht, Marc Pelizaeus, and Bertram Kopf must be mentioned. I would like to thank Malte Albrecht, Matthias Steinke, Bertram Kopf, Marc Pelizäus, Thomas Held, Cathrina Sowa, Jan Reher, Hendrik Vondracek, Markus Kuhlmann, Iman Keshk, Claudius Schnier, Tobias Holtmann, Stephan Leiber and Patrick Musiol for proof reading.

Mario Fink has drawn the circuit diagrams for the THMP mainboard and the PBBs he commissioned the production of the PCBs, acquired the necessary electronics components and their equipment, and he updated the firmware. Also Steffen Schuettler must be mentioned in this context, who dedicated several hours of diligent work on equipping, testing and if necessary repairing PBBs.

Cathrina Sowa, Lukas Sohl, Swetlana Mazarov, Niels Boelger and Vincent Freudenreich deserve my gratitude for the production of numerous temperature sensors. I thank Dennis Bootje and Thomas Schmidt for their inspirations concerning an efficient automatic temperature sensor production. Many colleagues participated in the continuation of the temperature sensor calibration measurements while I was staying in Beijing taking shifts at BESIII and during my research stay in Bloomington.

I thank my office mate Markus Kuhlmann with whom I could both concentrate on work and discuss fruitfully for the pleasant and productive time we spent together.

I would like to thank Prof. Matthew Shepherd and Ryan Mitchell for inviting me to a research stay at the Indiana University Bloomington and the Research School for funding my stay.

Last but not least I thank my family and my friends for their understanding whenever I did not join them, working on this thesis instead. In particular my partner deserves great gratitude, he kept any burden away from me so that I could focus all my efforts on the completion of this thesis.

Miriam Kümmel

Personal Data

Name Miriam Kümmel
Date of Birth 06.04.1987
Place of Birth Fulda

Education

since 2014 **Ph.D. Program**, *Ruhr-Universität Bochum*.
2012 – 2014 **M.Sc. Physics Program**, *Ruhr-Universität Bochum*.
2010 – 2012 **M.Sc. Mathematics Program**, *Ruhr-Universität Bochum*.
2008 – 2010 **B.Sc. Mathematics Program**, *Ruhr-Universität Bochum*.
2007 – 2010 **2-subject B.Sc. Mathematics and Physics Program**, *Ruhr-Universität Bochum*.
2006 – 2007 **Studium Generale**, *Leibniz-Kolleg*, Tübingen.
1997 – 2006 **High School**, *Rhenanus-Schule*, Bad Sooden-Allendorf.
2003 – 2004 **Student Exchange**, *Satri Sri Suriyothai School*, Bangkok, Thailand.

Grants

2017 **Research School PLUS**, *University of Indiana*, Bloomington IN, USA.
2015 **Heraeus Foundation**, *Lindau Nobel Laureate Meeting*, Lindau, Germany.
2007 – 2014 **German National Academic Foundation**.
2013 **Erasmus Grant**, *Uppsala Universitet*, Uppsala, Sweden.

Teaching

SS 18 **Tutor**, *Introduction to Particle and Nuclear Physics*.
SS 17 **Tutor**, *Introduction to Particle and Nuclear Physics*.
WS 16/17 **Tutor**, *Introduction to Particle and Nuclear Physics*.
WS 15/16 **Tutor**, *Introduction to Particle and Nuclear Physics*.
WS 14/15 **Tutor**, *Beginner's Laboratory Course in Physics*.
SS 12 **Tutor**, *Mathematics Freshman*.
WS 11/12 **Tutor**, *Linear Algebra I*.
WS 10/11 **Tutor**, *Mathematics Freshman*.
WS 09/10 **Tutor**, *Mathematics Freshman*.

Study-Related Activities

- 2013 **Summer School**, *Topic: Hadron Colliders (HASCO)*, Göttingen.
- 2012 **Summer Academy**, *Topic: Information and the Structure of the World*, Salem.
- 2008 – 2010 **Student Representative**, *Faculty of Mathematics*.
- 2009 – 2010 **Student Representative**, *Assessment Committee*.
- 2009 **Internship**, *Research Center*, Jülich.
- 2009 **Attendant**, *International Mathematics Olympiad*, Bremen.
- 2008 **Summer Academy**, *Topic: Resilience of Ecologic and Economic Systems*.

Languages

German	First Language
English	Fluent
Thai	Basic
Chinese	Basic